Thermal and Nonthermal Radiation Signatures in Solar Flares: Models and Observations

by

Sarah A. Matthews B.Sc. Hons.

Thesis
submitted to the
University of Glasgow
for the degree of
Ph.D.

Astronomy and Astrophysics Group
Department of Physics and Astronomy,
University of Glasgow,
Glasgow G12 8QQ

February 1996

ProQuest LLC.
789 East Eisenhower Parkway
P.O. Box 1346
Ann Arbor, MI 48106 – 1346

Acknowledgements

During the last 3 and a half years, and particularly the last six months, it has sometimes felt as if writing a thesis was a never ending process. In a way I suppose that it is, in the sense that there is always more that you could, and would like to do. However, an end of sorts has to be reached and this is it, so now seems an appropriate time to acknowledge some of the people who have helped me reach this point.

Firstly, I have to to thank my superviser, John Brown, for infinite patience, many research trips and, to steal a quote from Andrew, 'the ability to to identify the key issues in almost any problem'. I only hope that someday I can claim to have even a fraction of that ability. David Alexander (Montana State University) has over the last few years provided me with lots of inspiration, plenty of nagging, when and as required, and the answers to more stupid questions than most people deserve to be subjected to. And most of this from a distance - thanks David. I should also take this opportunity to point out that the work of Chapter 3 in this thesis was carried out in conjunction with him.

To Andrew Conway, who has been my friend and my office mate for the last 3 years I just want to say that life won't be the same without the smell of grapefruit and all the cat stories, amongst other things, when I leave. Thanks also have to go to Keith who has listened to me moan on more than one occasion; to Shashi, for computer type fixing and an inspiring dedication and genuine enthusiasm for almost every area of astronomy and to Aidan, who always volunteers to make the coffee when nobody else will and never complains about it. I'd also like to mention Richard- an amazing ability to sound knowledgeable on almost any subject, Giota, Moray, Kenny, Andy Wood, John Simmons (Greek dancing with tables in his mouth), Iain, Andy Newsam (Mr. Postscript) and Norman (the LaTex guru). Finally, the most important member of the Astronomy & Astrophysics group is definitely Daphne, who fixes anything bureaucratic and without whom the place would inevitably disintegrate. I'm sure that there is nobody to match Daphne anywhere else in the country.

Outside the department, I want to say thanks to Ailsa and Elaine, for keeping me sane and joining me in the consumption of large quantities of alcohol; Louise, who helped me get a job I really wanted - I owe you, and my parents, for feeding me most of the time, amongst other things.

Last, but by no means least I want to thank Mark, who has dug me out of more computer holes than he had time to, constantly reassured me that I am not stupid (although he could be wrong in this...), asked me lots of awkward questions and given me his unconditional support on (almost) every occasion.

Summary

The work of this thesis has been concerned with various aspects of the solar flare phenomenon, and covers a wavelength range from the optical to γ-ray, in varying degrees of depth. The approach taken has been a combination of modelling of physical processes and the application of these models to solar observations from the Solar Maximum Mission (*SMM*), and in particular the *Yohkoh* mission. Attempts have also been made, in Chapters 3 and 5, to relate nonthermal high energy phenomena such as γ-rays and hard X-rays to the lower energy thermal radiation signatures of soft X-ray and optical emission.

Chapter 1 provides an overview to the solar flare phenomenon, with particular emphasis on the observations. Where appropriate, the mechanisms responsible for the production of radiation signatures from flares has been described, and a brief and by no means complete, description of the possible mechanisms for flare energy release and transport are described. For those radiation signatures which are considered in further detail in later chapters the emphasis is on describing recent observations, particularly those from *Yohkoh*. A brief description of future up and coming satellite missions is also given.

Chapter 2 furnishes an introduction to the *Yohkoh* satellite and its instrumentation. Much of the work in later chapters involves the analysis of data from *Yohkoh* and it is necessary to have a basic understanding of how this data was collected, and its limitations to enable results based on it to be placed in a proper perspective.

Chapter 3 discusses the hypothesis that stochastic acceleration by Alfvén wave turbulence is responsible both for the acceleration of γ-ray producing protons, and for the observed nonthermal line broadening in coronal soft X-ray lines. A general background to the subjects of nonthermal line broadening, particle acceleration and γ-ray line production is presented and the model is described together with the results of its application to data from four flares observed by SMM and one flare observed by *Yohkoh*. This model is particularly interesting on the basis of its self-consistent approach to the problem of relating the thermal and nonthermal aspects of solar flares.

Chapter 4 investigates the posssibility that decreasing levels of Hydrogen ionization in the deep chromosphere of solar flares could cause the return current associated with a thick target electron beam to become unstable to the generation of ion-acoustic wave turbulence. To begin with the

background behind the need for a nearly co-spatial return current to exist is described, along with some observational evidence for the existence of electron beams in solar flares. A simple model is described and the results of its application to semi-empirical model solar atmospheres is described. We find that the possibility for such an instability to develop exists and that it can lead to the break up of the thick target electron beam and significant anomalous energy deposition at the level in the solar atmosphere where this occurs.

Chapter 5 follows on from Chapter 4 in considering that the generation of ion-acoustic wave turbulence via a return current instability can provide sufficient heating to power the white-light flare. To begin with, the white-light flare phenomenon is described in some detail, with emphasis on the various existing theories for its production. Then the analysis of the hard X-ray and white-light emission from four white-light flares observed by the *Yohkoh* satellite is described. The limitations of the results in respect to the available data are also described. It is found that there is a definite correlation between the hard X-ray and white-light flare and that the hypothesis of the white-light flare being powered by anomalous ohmic heating cannot be ruled out.

Chapter 6 draws together the results of the previous chapters, providing a summary of the work achieved in this thesis. It also points out some of the limitations of the approaches adopted and outlines possible improvements and new directions.

Contents

List of Tables

List of Figures

Chapter 1

Solar Flares: an Overview

"In the land of the dark, the Ship of the Sun is driven by the grateful dead"

-Egyptian Book of the Dead

1.1 Introduction

This chapter is intended to give a broad overview of the observations of solar flares at a variety of wavelengths and also, where appropriate, to indicate the probable mechanisms responsible for the production of the emission. For the cases of γ-rays, hard X-rays and white-light emission, a more detailed description is given at later and more relevant parts of this thesis.

By necessity, this is a brief and by no means comprehensive review of the phenomenon of solar flares. However, I have tried to address the salient points relating to flares and hopefully draw attention to some of the new and exciting results from the last decade's satellite missions. In deference to the fact that much of the work of this thesis hinges on results from missions such as *Yohkoh* and *SMM*, I have devoted some time to describing the next generation of solar satellites and addressing some of the questions that we hope these observations will help answer.

The classical definition of a solar flare is usually that of a sudden short-lived brightening of the chromosphere seen in H_α. Solar flares are not just confined to the chromosphere, however. A better description of impulsive flares might be that given by Sweet (1969):"Solar flares are complex transient excitations of the solar atmosphere above magnetically active regions of the surface enhancing thermal and radio emission, hard X-rays, cosmic rays and plasma ejecta."

What then does a solar flare look like? A flares covers less than 1% of the solar surface and is rarely seen in the visible wavelength range, despite the fact that the first recorded flare (observed independently by Carrington and Hodgson in 1859) was a white-light flare. They produce large amounts of radiation over a wavelength range from radio to γ-rays. Most of the $10^{28} - 10^{32}$ ergs of radiant energy is in the soft X-ray emission; but comparable or perhaps even larger, amounts

Last, but by no means least I want to thank Mark, who has dug me out of more computer holes than he had time to, constantly reassured me that I am not stupid (although he could be wrong in this...), asked me lots of awkward questions and given me his unconditional support on (almost) every occasion.

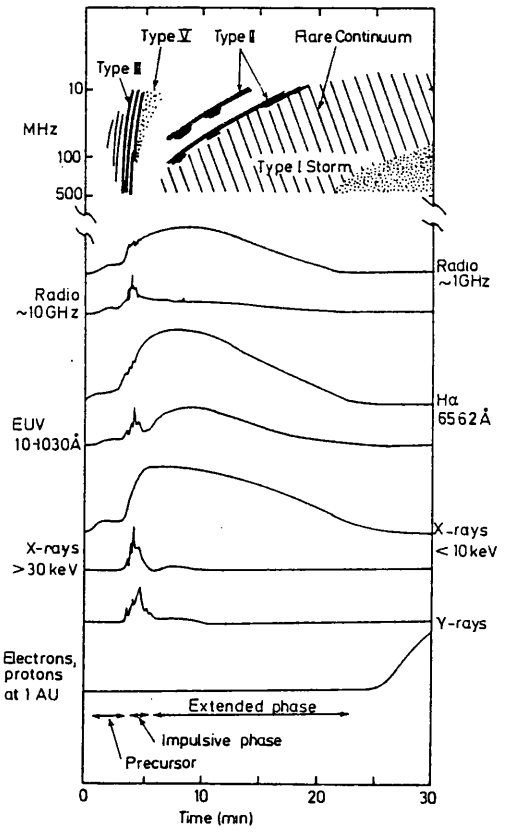

Figure 1.1: The temporal development of different types of flare emission during the different phases of the flare (after Kane (1974))

In the simple loop model free magnetic energy is dissipated in the current carrying loop by some undefined process, probably in the coronal region of the loop. As a result of this energy dissipation the plasma is heated to high temperatures, possibly in excess of 10^8 K, and electrons and protons are accelerated to high energies. Exactly what fraction of the flare energy goes into each of these processes- plasma heating and particle acceleration- is still a matter of some controversy, as are the exact details of the mechanisms. However, having been accelerated, the fast particles then propagate down the loop legs, guided by the magnetic field lines, and interact with the ambient plasma. The most energetic of these particles will reach the loop footpoints, producing hard X-ray and sometimes γ-ray emission. Figure 1.2 shows that different emission is produced from different parts of the loop.

The hard X-ray, γ-ray, radio and neutron emission provides the most direct information on the energy release process. All of these emissions are produced before the energetic particles lose their energy to the ambient atmosphere and thus carry the most information.

Flares always occur in active regions, so to begin with a description of the phenomena which characterize an active region on the Sun is appropriate.

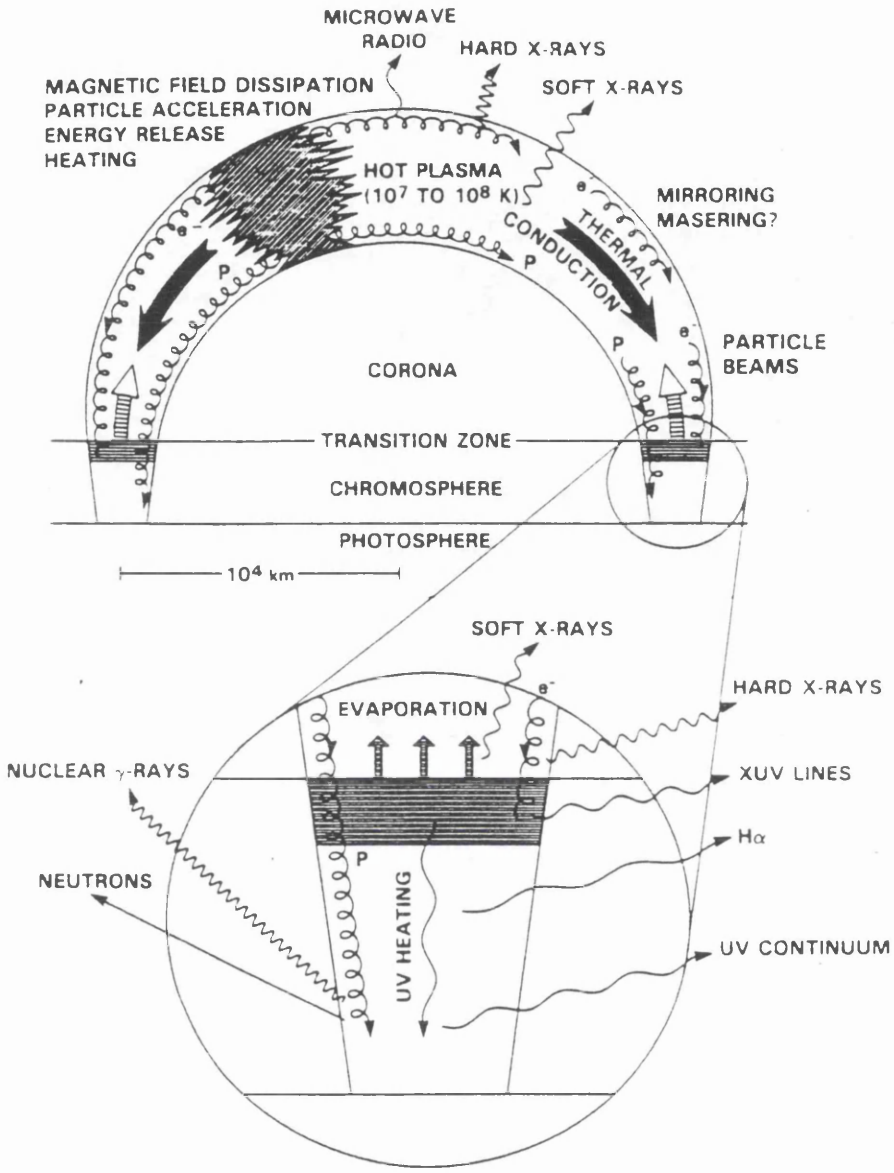

Figure 1.2: Schematic diagram of a simple flare showing some of the physicsl processes which occur and the position in the atmosphere they originate from (after Dennis and Schwartz, 1989).

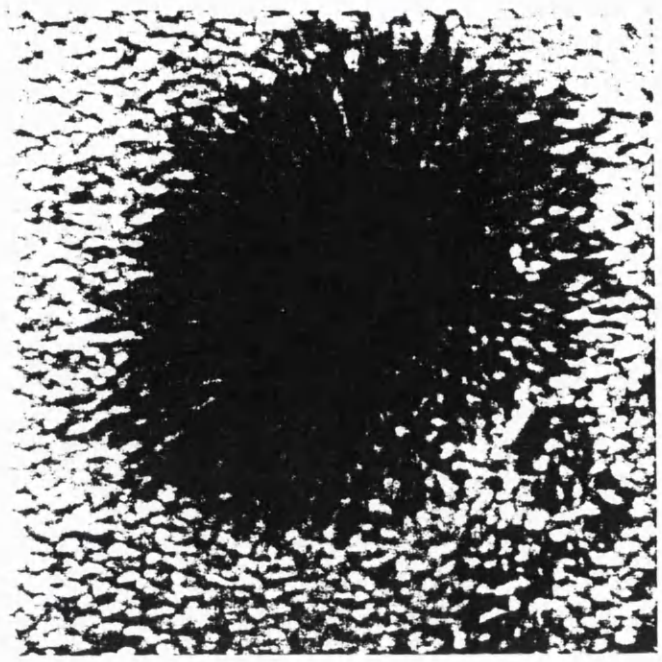

Figure 1.3: A broad-band white-light image of a sunspot. The dark interior is called the umbra and the mixed dark and light filamented exterior is the penumbra (after Gurman, 1992)

1.1.1 Active regions

Active regions are regions of the solar atmosphere which extend from the photosphere to the corona having enhanced magnetic field and coronal density. Observable phenomena of active regions include sunspots, plages, filaments, coronal loops and flares. In each of these layers of the Sun's atmosphere the active region is distinguishable by different effects. Undoubtedly the most obvious indication of an active region on the Sun is sunspots, see fig. 1.3. These are areas which are dominated by strong magnetic fields of $\sim 3000G$ which inhibit heat transfer resulting in sunspots appearing much darker than the surrounding photosphere. The temperature inside the sunspot is $\sim 4200K$. Other notable features of sunspots are their highly structured appearance- in the penumbrae this is probably due to arched filaments diverging from the sunspot- and the fact that they appear in pairs of opposite magnetic polarity.

After sunspots, plages are the next most obvious active region indicator. These are the areas surrounding the sunspots which appear bright when observed in H_α. They also, like sunspots, coincide with areas of high magnetic field strength. The enhanced brightness is a result of the higher density in these regions; the optical thickness of the chromospheric contribution to the line is increased relative to that of the photosphere. Because the energy loss per unit area of chromospheric plage is greater than that of the normal quiet Sun the energy input must also be higher, hence the plage appears bright. Flares always occur in plage regions, although rarely directly over sunspots.

Dark filaments are also common features of active regions when observed in, e.g. H_α. For example quiescent filaments are also observed near boundaries where the photospheric field changes polarity. Active region filaments are clouds of dense, relatively cool plasma ($T \sim 2 \times 10^4 K$) which are supported in the corona by almost horizontal magnetic fields. On the disk they appear dark in H_α, whilst on the limb they are bright and are called prominences.

Filaments are a dynamic phenomenon, often showing matter flowing down the field lines to the photosphere. They can show localised brightenings and often erupt or are ejected from the Sun completely. Some prominence eruptions are gradual, taking place over a number of hours, whilst others are very rapid with speeds of up to $\sim 10^3 kms^{-1}$ having been observed. These rapid eruptions are often associated with flares and are called flare sprays.

In the corona of active regions, above the chromospheric plage, are coronal condensations. These are regions of higher density and temperature which are largely composed of loop structures, as can be seen in soft X-rays. The temperatures of coronal active regions are in the range $2-3 \times 10^6 K$ and the electron density at the base of the corona has an average value of $\sim 3 \times 10^9 cm^{-3}$. Because the scale height is larger than the characteristic length scale of the active region corona, the pressure remains essentially constant at $n_e T \sim 3 \times 10^{15} cm^{-3} K$.

1.1.2 Magnetic fields in the active region corona

No reliable means of measuring magnetic field strengths in the corona yet exists, except for the Hanlé effect which can be used in solar prominence measurements. The best measurements available so far have been derived indirectly from radio observations, and below $1.5 R_\odot$ these are consistent with photospheric field measurements, which are reliably measured in e.g. sunspots. Dulk and McLean (1978) found that the relation

$$B \simeq 0.5 \times 10^{-5} [(R/R_\odot) - 1]^{-1.5} \, G \tag{1.1}$$

gives a reasonable fit over the range $1.02 < R/R_\odot < 10$.

However, fields in different active regions can differ by up to a factor of 3 and field strengths associated with different structures within the active region can vary even more.

1.1.3 Active region evolution

Active regions first make their appearance as emerging small bipolar magnetic regions surrounded by very bright and compact chromospheric plages and by X-rays from a coronal condensation (e.g. Zwaan, 1981). X-ray and H_α images show that there are loops connecting regions of opposite polarity. Less than 12 hours after this first appearance the field has spread apart, new flux has emerged and the active region has developed magnetic connections to other active regions or

Corrected Area		Relative Intensity Evaluation		
Square degrees	Millionths of hemisphere	Faint (f)	Normal (n)	Brilliant (b)
< 2.06	< 100	Sf	Sn	Sb
2.06 - 5.15	100 - 250	1f	1n	1b
5.15 - 12.4	250 - 600	2f	2n	2b
12.4 - 24.7	600 -1200	3f	3n	3b
> 24.7	> 1200	4f	4n	4b

Table 1.1: H_α flare classification scheme, from Zirin (1988).

magnetic elements which can be as far away as $0.3R_\odot$ (Dulk, 1985). Enough flux will have emerged within a day for sunspots to form, and over the space of about a week the region will continue to grow, usually becoming more magnetically complex. Prominences will form near the magnetic neutral line and flares will become more and more frequent.

The peak of the active region occurs about 10 days after its first appearance and after this it will begin to decay. The decay is a much longer and more gradual process which can take about one or two months. At this time all that remains of the active region is a slightly enhanced field and possibly a filament.

1.1.4 Flare classifications

As mentioned above, an important active region phenomenon is that of the solar flare. Solar flares are classified by importance mainly in the optical, X-ray and radio regions of the electromagnetic spectrum. Prior to the 1960's all flare classifications were based on observations in the visible range, and in particular H_α. This optical system was approved by the IAU in 1966 and utilizes measurements of the flare area in degrees of heliocentric latitude as the basis for the classification.

In Table 1.1, S denotes a subflare, and the letters *f, n, b* are added to provide information on the flare brightness. Although the area should be corrected for projection, height effects in practice make the areas of flares more than 65° from the central meridian passage rather uncertain.

Although the area is a quantity which can be relatively easily measured, it is not, however, particularly useful for classification purposes since it disregards impulsiveness and intensity and we often find impulsive or bright flares with strong radio and X-ray emission which have low importance because their area is small.

As well as the increase in optical flare patrols over recent years regular radio observations of the Sun are now also common; the great advantage of these ground based measurements being that they are unaffected by cloud. Single frequency fluxes are measured in solar flux units, where 1 sfu= 10^{-22} $Wm^{-2}Hz^{-1}$ = 10^4 Jansky. For frequencies > $2000MHz$ almost every event with a signal above 1 sfu is a flare. For impulsive flares, the area importance classification can be roughly related to the measured microwave flux, viz.

$$Imp = log_{10}S(sfu) - 0.5 \tag{1.2}$$

where S is the flux at 5 GHz. For impulsive events this classification scheme is much better than the optical since microwave fluxes can be measured with greater reliability than flare areas. The measured flux range is generally between about 5 sfu for a subflare, increasing to about 30,000 sfu for a class 4 flare at 5 GHz.

Other flare clssifications are based on observations taken in the soft and hard X-ray wavelength ranges. For soft X-rays, the *GOES* satellite data provides a scheme based on the measurement of the SXR flux in the $1-8\mathring{A}$ range. The *GOES* (Geostationary Operational Environmental Satellites) are owned and operated by the National Oceanic and Atmospheric Administration (NOAA) and provide continuous, dependable and high quality observations of the Earth and its environment; including the acquisition of Space Environment Monitor (SEM) data. The SEM consists of a three-axis magnetometer, an Energetic Particle Sensor (EPS) and associated High Energy Proton and Alpha Detector (HEPAD), plus the X-ray Sensor (XRS). XRS performs real time measurements of the solar X-ray emission in two channels covering the spectral ranges $0.5 - 3\mathring{A}$ and $1 - 8\mathring{A}$. Its sensitivity is such as to permit quiet Sun background measurements at as low a level of solar activity as possible while detecting events at the lowest practical threshold for early event warning. In this case flares are categorized under the scheme *Xn, Mn, Cn, Bn*, where *X, M, C, B* denote whether the measured flux at the Earth is greater than 10^{-1}, 10^{-2}, 10^{-3} or 10^{-4} erg cm^{-2} s^{-1} respectively, and *n* represents the actual flux value i.e. $M3 = 3 \times 10^{-2}$ erg cm^{-2} s^{-1}.

For hard X-ray classes defined by Tanaka (1983), see section 1.9.4.

The distribution of flare sizes has a range of several orders of magnitude, with small events occurring much more frequently than large events. In fact, (Dennis, 1985) the distribution of flare frequency with size actually has a power law form with spectral index $\delta = 1.8$. There is a turnover at low energies, most likely due to selection effects, and a high energy cut-off which is necessary so that the total energy release rate remains finite, i.e., such that $\int AF(A)dA$ remains finite, where F is the number of events in a given energy range per day, and A is the number of counts per second in hard X-rays. Lu and Hamilton (1991) have suggested that this power law form is consistent with the behaviour that is expected from avalanche or self organizing systems.

1.2 Flare theories

Solar flares are without question associated with the rapid release of up to 10^{32} ergs of stored magnetic energy over a timescale of a few minutes, and over an area of $\sim 10^{18}$ cm^2 (10 arc seconds square). Although this is an impressive amount of energy for such a small area and short timescale, it in fact only amounts to 1/40 of the Sun's normal radiative output. The energy released during

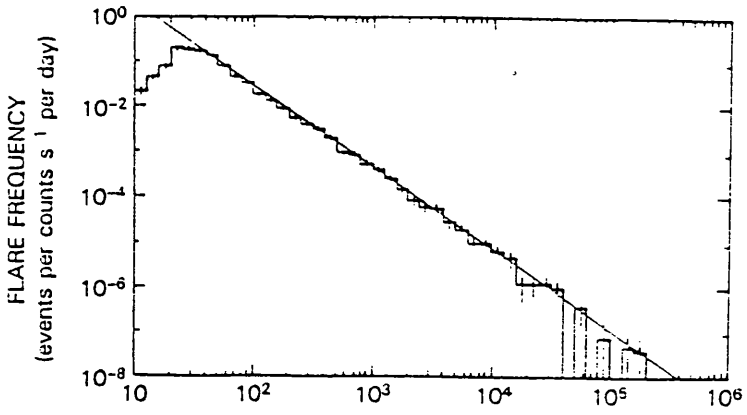

Figure 1.4: Distribution of flare frequency vs. size of event (After Dennis, 1985).

a flare is almost certainly stored in stressed magnetic fields in active regions over a period of hours to days preceding the actual energy release.

Sometimes this magnetic energy release is accompanied by a mass ejection of up to $10^{14} - 10^{16}$ g of plasma at speeds in excess of 10^3 kms^{-1}.

There is little doubt that solar flares are highly complex phenomena and as a result attempts to model them inevitably require the inclusion of certain simplifying assumptions. The basic building block of the flare model is an isolated magnetic flux tube rooted in the photosphere and extending into the corona. From this basic element there are two routes which may be travelled in the pursuit of a flare model. Firstly, a pre-flare magnetic field/plasma configuration can be assumed and the equations of MHD solved to yield the evolution of the system and the modes of energy release. The second, and more relevant approach to this thesis, is the inverse problem of attempting to infer details of the energy release process via relationships between flare observations at different wavelengths.

1.2.1 Energy storage

Firstly, it is perhaps appropriate to indicate why we are so certain that the only plausible energy source for solar flares is magnetic.

If one considers that the thermal energy in the corona above an active region is given approximately by

$$E_{th} = 3nk_BTV \tag{1.3}$$

then for the corona $nV \simeq 10^{38}$, if $n \simeq 10^{11}$ cm^{-3} is the coronal plasma density and $V \simeq 10^{27}$ cm^3 is a typical flare volume, and $T = 10^6K$, we find that $E_{th} \simeq 10^{28}$ ergs. This is obviously four

orders of magnitude lower than the the observed energy release in a flare. Also, the use of this thermal energy constitutes a violation of the Second Law of Thermodynamics since it would have to be converted into both a *hotter* corona and particle acceleration.

Secondly, we consider gravitational energy as the energy source. For a coronal loop, the gravitational potential energy is given by

$$E_{grav} = nghV \simeq 10^{28} ergs \tag{1.4}$$

The similarity between this value and that obtained from thermal considerations is a direct consequence of the Virial theorem for an atmosphere in hydrostatic equilibrium, i.e.

$$E_{th} = \frac{-E_{grav}}{3(\gamma - 1)} \tag{1.5}$$

for $\gamma = 4/3 \Rightarrow E_{th} = -E_{grav}$. Again we see that the energy available from the gravitational field is insufficient to account for the observed energy release during the flare.

Finally, we consider the energy available from the magnetic field and we see that for a field $B = 10^3 G$, the magnetic energy stored $\sim B^2 V/8\pi \simeq 10^{32} ergs$ would be sufficient to account for the flare energy. However, not all the energy stored in the magnetic field is 'free' energy, i.e. it cannot all be released. The ground state of the magnetic field is the potential or current free state and only energy in excess of this amount is free energy. Because of this restriction, it is clear that flares must occur in regions of non-potential field, that is, where there are currents or where magnetic shear exists.

Consider that the momentum equation for a single fluid plasma is

$$\rho \frac{d\mathbf{v}}{dt} = -\nabla p + (\nabla \times \underline{\mathbf{B}}) \times \underline{\mathbf{B}}/4\pi \tag{1.6}$$

The final term on the right hand side of this equation is the Lorentz force associated with charges which are moving perpendicular to the magnetic field direction. For currents which are very far from parallel to the field a force density of $\sim \nabla(B^2/4\pi)$ is produced, and since $B^2 \gg 4\pi p$ in the corona, equation 1.6 cannot hold unless the fields and currents are aligned, i.e.

$$(\nabla \times \underline{\mathbf{B}}) \times \underline{\mathbf{B}} = 0 \tag{1.7}$$

Magnetic fields which satisfy this criterion are called force-free fields.

The available solutions to equation 1.7 are the following:

1. $\underline{\mathbf{B}} = 0$ (trivial)
2. $\nabla \times \underline{\mathbf{B}} = 0$ - ground state potential case with no free energy available for release.
3. $\nabla \times \underline{\mathbf{B}} = \alpha \underline{\mathbf{B}}$ - linear force-free case

4. $\nabla \times \underline{\mathbf{B}} = \alpha(\underline{\mathbf{r}})\underline{\mathbf{B}}$ - the general case. $\alpha(\underline{\mathbf{r}})$ is a function of position but is still constant along any given field line.

For solar flare physics the most important element of any solution to $\nabla \times \underline{\mathbf{B}} = \alpha(\underline{\mathbf{r}})\underline{\mathbf{B}}$ is the value of α, which represents the 'shear' of each magnetic field line relative to the potential state.

In theory at least, $\nabla \times \underline{\mathbf{B}}$ can be deduced from observations of the transverse component of $\underline{\mathbf{B}}$. In practice, large uncertainties are introduced because of seeing effects and the atmospheric model used. A more reliable measurement of the shear of the field can be obtained from the angle between the observed transverse field and that deduced from a potential extrapolation of the observed line of sight field. Because $\nabla.\underline{\mathbf{B}} = 0$ and for a potential field $\underline{\mathbf{B}} = \nabla\Omega$, the potential field can be obtained by solving Laplace's equation, $\nabla^2\Omega = 0$ in a region where $\nabla\Omega$ is known on the boundary.

The results of calculations of the energy buildup when the footpoints of magnetic structures are sheared relative to one another (e.g. Wu et al, 1984) have shown that most of the energy *is* stored in the form of magnetic energy rather than in kinetic, thermal or gravitational forms, These calculations have also provided verification of the theory that photospheric shearing motions can provide the mechanism for the energy buildup - the rates of energy buildup are adequate to accumulate significant amounts of energy. Other proposed field stressing mechanisms involve the stressing of fields before they emerge from the photosphere. The measurement of the evolution of active region currents before a flare should, in principle, be capable of differentiating between whether the shearing occurs before or after flux emergence.

1.3 Energy release

The fundamental problem with explaining the energy release mechanism in solar flares is caused by the huge volume over which such an event occurs. As a direct result of this the region involved has both high inductance, L, and low resistance, R, which results in an inductive energy release timescale (L/R), of the order of years, seemingly irreconcilable with the observed timescale of seconds to minutes.

In modelling the energy release there are, as mentioned above, two primary approaches. The first of these is the direct approach in which an initial plasma and magnetic field configuration is assumed and the equations of magnetohydrodynamics (MHD) are solved to determine the evolution of the system. This is a rather complicated problem which requires the solution of 16 coupled, nonlinear PDEs in 16 unknowns (Chen, 1974). It also requires a prior knowledge of the pre-flare structure on length scales which are orders of magnitude smaller than those which are currently observable.

The second approach is the inverse problem of beginning with a set of flare observations in various different wavelength ranges and attempting to infer something about the energy release

mechanism from relationships between these different emissions. The biggest problem of this approach is that the physics of the energy release process is inevitably coupled to the physics of the energy transport over the source. As energy transport always involves an increase in entropy from that at the time of the energy release, and so information is irretrievably lost.

Because flares derive their energy from current dissipation in stressed magnetic fields the resistance of the dissipation region has to be high enough that the energy can be dissipated on the observed timescales. For this to be the case, in the corona, either the resistivity has to increase, possibly through turbulence, or the cross-sectional area through which the current flows has to decrease.

Consider the diffusion equation, which may be derived from the steady-state form of Ohm's law,

$$\frac{\partial \underline{\mathbf{B}}}{\partial t} = \nabla \times (\underline{\mathbf{v}} \times \underline{\mathbf{B}}) + \frac{\eta c^2}{4\pi} \nabla^2 \underline{\mathbf{B}} \tag{1.8}$$

if $\eta \rightarrow 0$ then we have the frozen-in field approximation which means that the plasma is confined by the magnetic field and essentially moves with it.

The first term on the right hand side of equation 1.8 describes the advection of field lines carried by the plasma and has associated with it an advection timescale,

$$\tau_a = \frac{L}{v} \tag{1.9}$$

while the second term on the right describes the diffusion of the field through the plasma, with its associated diffusion timescale,

$$\tau_d = \frac{4\pi L^2}{\eta c^2} \tag{1.10}$$

L is the characteristic length scale over which the magnetic field strength changes, η the resistivity and c the speed of light.

The ratio of these timescales is called the magnetic Reynolds or Lundquist number, R_m,

$$R_m = \frac{\tau_d}{\tau_a} = \frac{4\pi v L^2}{\eta c^2} \tag{1.11}$$

For the classical Spitzer (1962) resistivity, $\eta = 10^{-7} T^{-3/2}$ then the diffusion time and the Lundquist number reduce to:

$$\tau_d \simeq 10^{-13} T^{3/2} L^2 \tag{1.12}$$

$$R_m \simeq 10^{-5} T^{3/2} L \tag{1.13}$$

and at pre-flare coronal temperatures of $\simeq 3 \times 10^6$ K and a typical $L \sim 10^8 - 10^9$ cm, τ_d is of the order of millions of years with $R_m \simeq 10^{13}$.

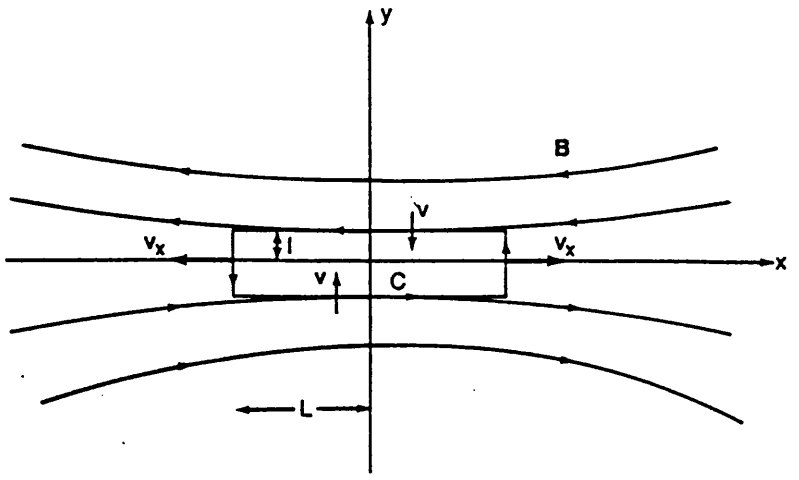

Figure 1.5: Neutral sheet magnetic reconnection. The magnetic field reverses direction along the x-axis, leading to a large current density in the z-direction. The inflow of the magnetic field at velocity v is balanced by fluid outflow at velocity v_x, since the fluid is incompressible. (After Tandberg-Hanssen and Emslie, 1986)

What this means is that the plasma in the corona is frozen in to the field to a very high degree. Really, this is a result of the very large length scales with which we are dealing rather than the value of the resistivity itself. So, to dissipate the magnetic energy on timescales commensurate with those observed in flares we must somehow reduce L and/or increase η. To do this two oppositely directed magnetic fields must approach one another, see fig. 1.5.

Figure 1.5 shows a neutral sheet model, from which one can calculate the rate of energy release in a current sheet, P, (Sweet, 1958; Parker, 1975), viz.

$$P = \frac{4B^2Lv}{8\pi} = \frac{B^2 v_A L}{\pi S^{1/2}}\ ergcm^{-1}s^{-1} \tag{1.14}$$

Typically, $B \simeq 10^3$ G, $v_A \simeq 10^8$ cms^{-1}, where v_A is the Alfvén speed, $L \simeq 10^9$ cm and $S \sim 10^{14}$ so that $P \simeq 3 \times 10^{15}$ erg cm^{-1}s^{-1},where S is the Lundquist number. So even for a sheet of dimension 10^9 cm this model only results in the release of 10^{24} erg s^{-1}.

In order to overcome this discrepancy Petschek (1964) studied the fluid flow near a current sheet and found that the velocity changes from a gradual inflow of $v \ll v_A$ to a rapid outflow at $\sim v_A$. Since the field and the plasma are frozen together the field inflow velocity is also v.

By considering a small fluid element with dimensions Δx, Δy Petschek showed that as a result of continuity for an incompressible flow, $\Delta x \rightarrow \infty$ as $\Delta y \rightarrow 0$. Since the flux in the x direction is also conserved, $B_x \rightarrow \infty$ as $\Delta y \rightarrow 0$. This unphysical behaviour is prevented by the formation of

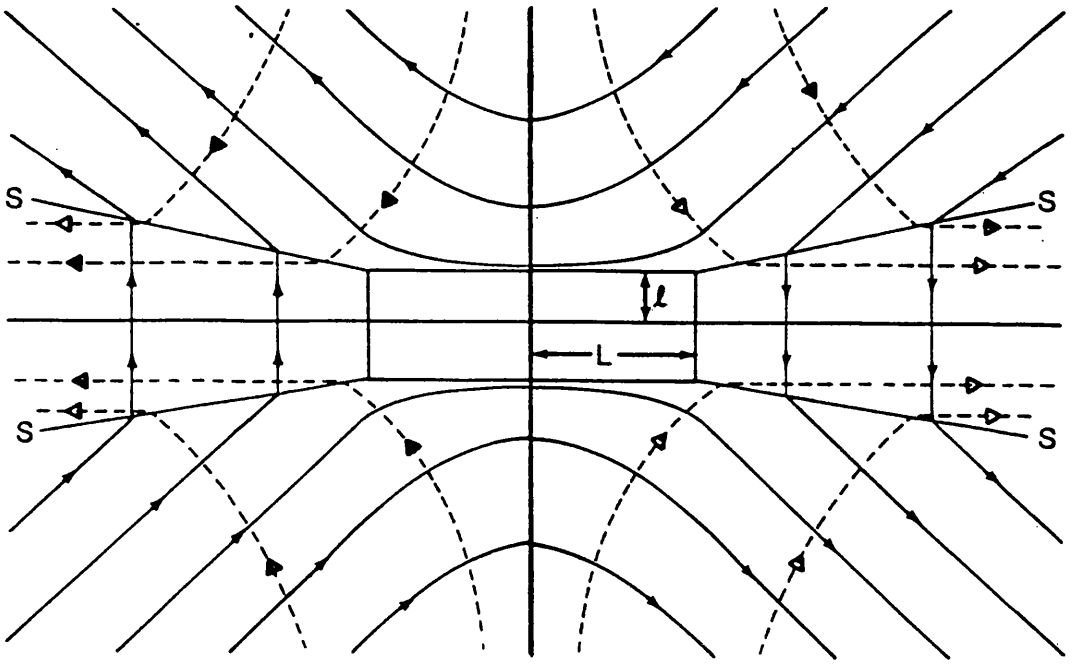

Figure 1.6: The Petschek mode of magnetic reconnection. The solid lines and arrows represent magnetic field lines and the dashed lines and open arrows velocity streamlines. (after Forman et al., 1985)

standing shocks where the fluid flow changes abruptly (see fig. 1.6).

There is a small region which surrounds the origin and becomes a stagnation or X-type neutral point. In this model the field lines truly reconnect and the topology of the magnetic field changes, producing a strong tension force which pushes fluid out at v_A. Sonnerup (1970) developed a variation of this model in which he employed two sets of standing shocks.

If a magnetic field configuration like that of fig. 1.5 is subject to a rippling disturbance in the x-direction then magnetic reconnection can occur at several points along the neutral line. This leads to the formation of 'magnetic islands' between the reconnection points, as shown in fig. 1.7. These magnetic islands, which are isolated from the background magnetic field, have a tendency to collapse into smaller islands under field line tension, enhancing the energy dissipation rate. The original formulation of this tearing mode was addressed by Furth et al. (1963) with an application to solar flares by Spicer (1976, 1977). Spicer (1976, 1977) also showed that the reconnecting regions can overlap resulting in a large increase in the number of X-type neutral points, a corresponding increase in the volume of reconnecting regions and very rapid energy dissipation. This is called the *multiple tearing mode.*

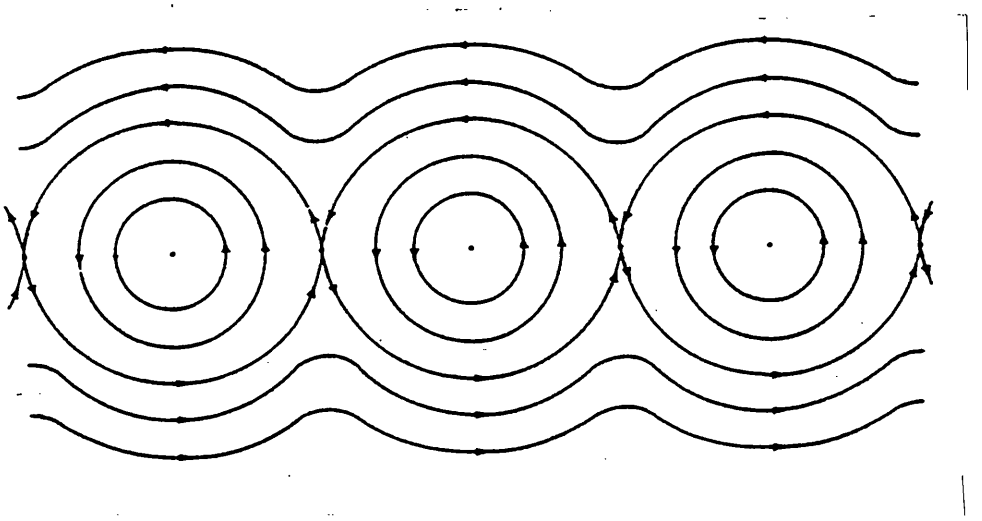

Figure 1.7: Formation of magnetic islands between X-type neutral points, as a result of a rippling disturbance in a neutral sheet geometry. The tension in the closed field lines acts to increase the outflow velocity at the neutral points and as a result enhances the rate of magnetic energy dissipation. (from Tandberg-Hanssen and Emslie, 1988)

1.3.1 Energy dissipation rates

The rate of energy release for these reconnection models is given by

$$\frac{d\epsilon}{dt} = (\frac{B^2}{8\pi})V\tau_R^{-1} \tag{1.15}$$

where B is the pre-flare magnetic field strength, V the volume of the reconnecting region or regions and τ_R the reconnection timescale. Then if we consider a pre-flare loop with length $L = 10^9$ cm, $B = 300$ G, $n = 10^{10}$ cm^{-3} and $T = 2 \times 10^6$ K the Alfvén speed, $v_A = 6 \times 10^8$ cms^{-1} and the classical resistivity $\eta = 5 \times 10^{17}$ s. From these the magnetic Reynolds number, R_m can be calculated for the large scale field from eqn. 1.11. The reconnection timescale, τ_R can then be calculated from the equation, $\tau_R = 1/2R_m^{1/4}\sqrt{(\tau_A\tau_D)}$. Using equation 1.15 we can then calculate energy dissipation rates for the various models:

- $\frac{d\epsilon}{dt}|_{neutral\ sheet} \simeq 2 \times 10^{23} ergs^{-1}$
- $\frac{d\epsilon}{dt}|_{single\ region\ Petschek} \simeq 7 \times 10^{24} ergs^{-1}$
- $\frac{d\epsilon}{dt}|_{tearing\ mode} \simeq 7 \times 10^{25} ergs^{-1}$
- $\frac{d\epsilon}{dt}|_{multiple\ tearing\ mode} \simeq 3 \times 10^{31} ergs^{-1}$

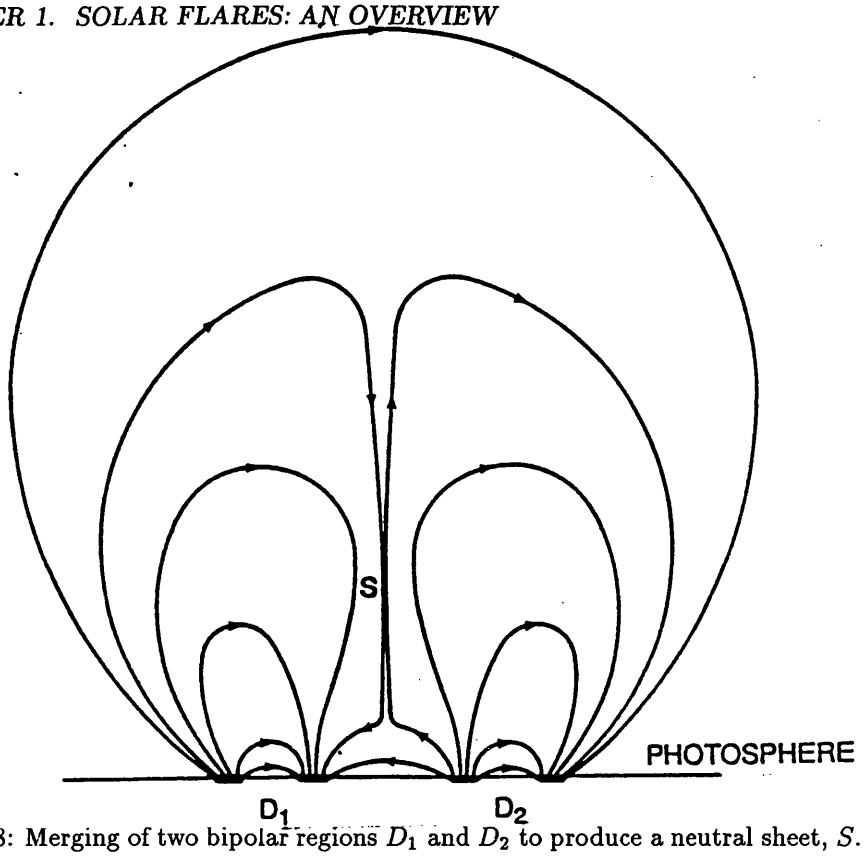

Figure 1.8: Merging of two bipolar regions D_1 and D_2 to produce a neutral sheet, S. (After Sweet, 1958)

From this it appears that only the multiple tearing mode is capable of accounting for the energy release, although it is likely that in practice the resistivity in the region will be enhanced anomalously as a result of waves e.g. ion-acoustic waves, generated by a plasma instability.

1.4 Flare models

Having identified the physical process responsible for the energy release (i.e. magnetic reconnection) the question remains as to how conditions appropriate for reconnection to occur, arise. This topic is what is usually known as flare modelling, a complete and comprehensive review of which can be found in Sturrock (1980). The only real difference between the models described below is in the magnetic geometry and the causes of it.

It is the topology of the reconnection region which characterizes the model. A variety of reconnection models have been proposed over the years, beginning with Sweet's (1958) model. This proposed the formation of a neutral sheet between two merging bipolar flux regions, fig. 1.8. A similar model was also proposed by Syrovatskii (1966, 1969). In 1960 Gold and Hoyle postulated the merging of two flux tubes (fig. 1.9). The toroidal currents in this model are parallel causing the two flux tubes to attract one another, whilst the poloidal fields are oppositely directed, giving rise to a neutral sheet configuration.

A helmet streamer configuration was proposed by Sturrock in 1968, (see fig. 1.10) with a

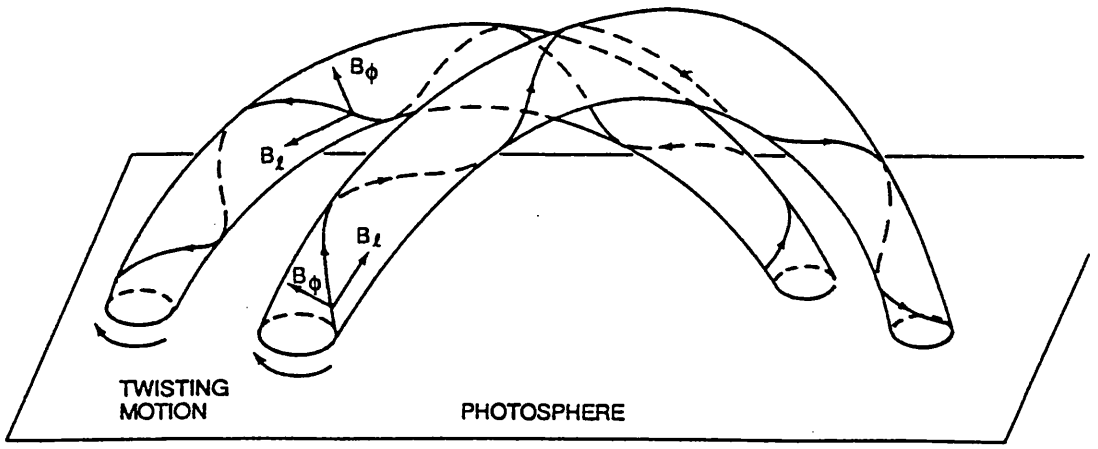

Figure 1.9: Gold and Hoyle's model of a solar flare. Two flux tubes carry similar currents and so attract each other. The longitudinal fields are anti-parallel, and therefore so are the poloidal fields at the boundary. This creates a neutral sheet configuration at the surface where the tubes meet. (After Gold and Hoyle, 1960)

neutral sheet forming above a Y-type neutral point. Streamer-like structures are often observed with coronagraphs, making this a popular scenario.

Heyvaerts et al. (1977) suggested that flares occur when new flux emerges from below the photosphere as a result of its magnetic buoyancy, and collides with existing flux tubes creating a neutral sheet at the common boundary of the tubes (see fig. 1.11). Since emerging flux is often associated with flares, and the characteristic quadrupole field of this configuration has been observed (Velusamy and Kundu, 1982), this model has also met with some favour.

Finally, Spicer (1976, 1977) proposed that magnetic kink instabilities in a toroidal arch might produce overlapping field lines similar to the tearing mode instability. This model could provide a good explanation for compact flares which does not involve a lot of global field restructuring.

1.5 Energy transport

There are several different possible mechanisms for the transport of energy from the corona to the energy dissipation regions in the lower corona and chromosphere.

1. energy transport by thermal conduction in a thermal plasma with $T \geq 10^8$ K; hard X-rays produced by thermal bremsstrahlung

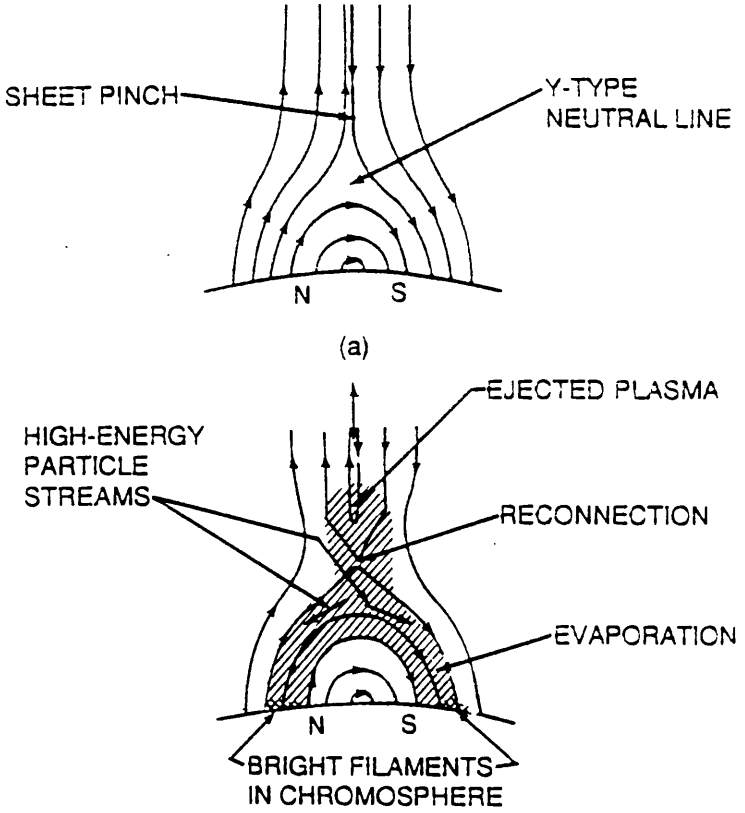

Figure 1.10: The central helmet streamer configuration creates a neutral sheet ending in a Y-type neutral point, which is the region of initial reconnection. The field lines below the Y-point are closed, and produce the hard X-ray and H_α emissions, etc. The field lines above the Y-point are open and are responsible for particle ejecta. (After Sturrock, 1968)

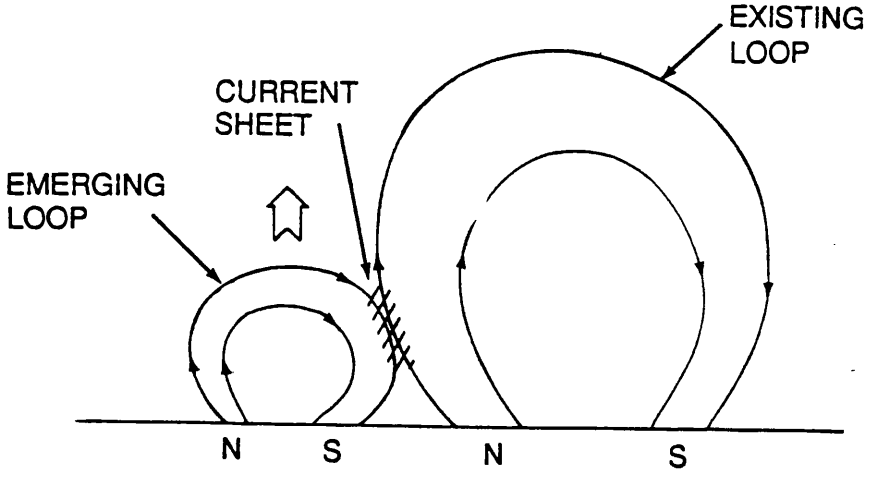

Figure 1.11: Emerging flux model. A new flux tube rises and collides with an existing flux tube, creating a current sheet. During the impulsive phase the reconnection is 'driven', but relaxes to a steady state during the main phase. (After Heyvaerts et al., 1977)

2. fast electrons with energies $\geq$ 20 keV; hard X-rays produced by thick- target bremsstrahlung

3. relativistic electrons; hard X-rays produced by inverse Compton interactions

4. protons with energies $\leq$ 1 MeV: fast electrons produced at the footpoints by some undefined mechanism then produce bremsstrahlung X-rays

5. protons with energies $>$ 1 MeV; hard X-rays produced by inverse bremsstrahlung

The first mechanism is the familiar thermal model (Brown, Melrose and Spicer, 1979; Smith and Lilliequist, 1979; Batchelor et al., 1985). In this model the energy released impulsively heats the plasma close to the release site to $T \geq 10^8$ K and the hot plasma is confined by ion-acoustic conduction fronts that move at the ion-sound speed ($10^8 - 10^9 cms^{-1}$) down the loop legs to the footpoints. This takes $\sim$ 20 seconds for typical loop parameters of $L \sim 3 \times 10^9$ cm and $n = 10^{10} cm^{-3}$.

(2) describes the thick target model (e.g. Brown, 1971) in which electrons are accelerated high in the loop and propagate along the field lines producing heating and X-ray bremsstrahlung as they go. The highest energy electrons lose most of their energy in the higher density regions of the lower corona and upper chromosphere. This is the model which has been most successful at explaining the observations, e.g. hard X-ray emission at the loop footpoints.

Models involving relativistic electrons (3) are appealing in that they have much smaller total energy requirements than the other models (Brown, 1976). However, the hard X-ray emission from relativistic elecrons is produced via synchrotron or inverse Compton processes and for this there is a need for $>$ 1 GeV electrons for synchrotron and $>$ 1 MeV electrons for inverse Compton processes. Sufficient numbers of these high energy electrons to produce the observed HXR burst are inconsistent with the observed microwave burst intensities and are not observed in interplanetary space (Brown, Smith and Spicer, 1981), making this an unlikely scenario.

Simnett (1986) proposed that most of the flare energy in the impulsive phase is first transferred to protons with energies between 100 keV - 1 MeV. Recent models have included that of Martens (1988) in which protons are generated in two ribbon flares. Hénoux et al. (1990) suggested that H_α impact polarization was evidence of atmospheric bombardment by deka-keV protons. The best hope of detecting protons has been through the predicted red shifted component of the L_α line ($1216 \AA$) from the decay of excited hydrogen atoms in charge exchange interactions between protons and the ambient plasma (Orrall and Zirker, 1976). Measurements of H_α impact polarization (e.g. Hénoux et al., 1990, Fletcher and Brown, 1992) are another possible way of identifying the presence of protons. However, more diagnostics for low energy protons are required before this model can be either proven or disproven.

Heristchi (1986) claimed that bremsstrahlung by fast protons ($\gg$ 1 MeV) on stationary electrons could be the origin of the HXR emission in flares. However, Emslie and Brown (1985) pointed out

that despite being feasible on energetic grounds, the number of protons required is three orders of magnitude greater than that required to produce the observed γ-ray fluxes (e.g. Ramaty and Murphy, 1987). Also, large numbers of pions and neutrons should be produced in this model and the electron/positron and γ-ray decay products of the pions should give far more γ-rays than are observed with *SMM* GRS (Dennis and Schwartz, 1989). The neutron flux should also be higher than observed.

Since in terms of the rest of this thesis the electron heated thick target model is important, we consider it in somewhat greater detail.

Nonthermal electron bremsstrahlung in a cold target is a relatively inefficient way of producing hard X-rays. Here the efficiency is the ratio of the bremsstrahlung production rate to the collisional energy loss rate, i.e.

$$\eta \simeq \frac{4\alpha}{3\pi\Lambda}[\frac{E}{m_e c^2}] \tag{1.16}$$

where η is the efficiency, Λ is the Coulomb logarithm, α is the fine structure constant and E the electron energy.

Typically for $E \simeq 30$ keV and $\Lambda = 20$, $\eta = 10^{-5}$. In order to maximise the bremsstrahlung production the target is made thick, i.e. we require that the electrons decay to the threshold energy, ϵ in the source (ϵ is the energy of the photon produced by the electron).

Because of this low efficiency a considerable fraction of the flare energy release has to go into the acceleration of nonthermal electrons. These electrons then propagate down the field lines and are then ultimately stopped in the dense lower loop, this then constitutes the thick target (Brown, 1971).

Apart from the problem of how to accelerate these electrons in the first place there are other issues associated with the thick target model. Firstly, the total number of electrons in a loop is $\sim 10^{37}$ (density $10^{10} cm^{-3}$ x volume $10^{27} cm^3$), implying that all the electrons would be depleted in a few seconds unless there were some constant supply of new electrons. Secondly, the current associated with such a beam is greatly in excess of the Alfvén-Lawson limit (the maximum current attainable before the beam breaks up, see Chap. 4) and has a self-magnetic field associated with it of $\sim 10^8$ G. Apart from the fact that magnetic field strengths of that size are not observed on the Sun, the energy associated with a field of this size is orders of magnitude greater than the total flare energy itself.

These problems are resolved in part by the existence of a return current co-spatial with the beam flows (e.g. Knight and Sturrock, 1977; van den Oord, 1990). The return current neutralizes the beam current and cancels the charge separation electric field. However, since it must exist outside the acceleration region- otherwise electrons would be moving in an opposite direction to the applied force- it cannot replenish it. This problem (Holman, 1985) remains. The return current

will be discussed in greater depth in Chapter 5.

An alternative to the cospatial return current is external current closure which replenishes the acceleration region and solves the charge separation problem but cannot neutralize the beam current locally unless there are lots of oppositely directed beams, requiring a highly structured energy release mechanism. Holman (1985) estimated that at least 10,000 separate energy release regions would be necessary.

Stochastic acceleration produces no preferred beam direction and as such obviates the need for a return current in the acceleration region at all, although one is still needed in the propagation region. However, by its nature stochastic acceleration produces more heating than lower energy fast particles.

1.6 Optical emission

The first recorded solar flare observation was in white-light (Carrington, Hodgson, 1859). White-light flare observations, although now becoming much more frequent (Hudson et al., 1994) have previously been rare and most optical observations are carried out in chromospheric spectral lines such as the helium D3 and 10830 Ålines; Ca II H and K and, most often, the first Balmer line of Hydrogen, H_α. In the quiet Sun H_α is a strong absorption line which is formed in the chromosphere, but in flares it is seen in emission. Flare patrol telescopes routinely observe in H_α using narrow band ($\sim$ 0.5 nm) filters.

Since H_α emission originates in the chromosphere, flares were first thought to be an exclusively chromospheric phenomenon, but observations in X-rays and microwaves have shown that the base of the corona attains temperatures $> 10^7$ K during flares and a large fraction of the flare energy resides in this hot plasma, leading to the conclusion that the chromospheric flare is a secondary feature.

Despite this, H_α observations have provided estimates of the densities and temperatures of the flaring chromosphere ($T \sim 10^4 - 10^5 K$, $n \sim 10^{16} m^{-3}$) and a wealth of information about flare morphology and its relationship to the magnetic field. Indeed, the first flare classification schemes, as described above, were based on H_α observations.

Most H_α flares are relatively small and compact, $\leq$ 30". They occur close to the neutral line, particularly favouring regions with strong gradients in either the magnetic field strength or direction. The larger flares show a variety of different morphologies, the most common of which is the two ribbon flare, as shown in fig. 1.12. The ribbons show the footpoints of an arcade of magnetic loops and are observed to move apart as the flare progresses with higher and higher loops bridging them.

The smallest flares observed in H_α show unresolved 'blobs'. In all probability these also have

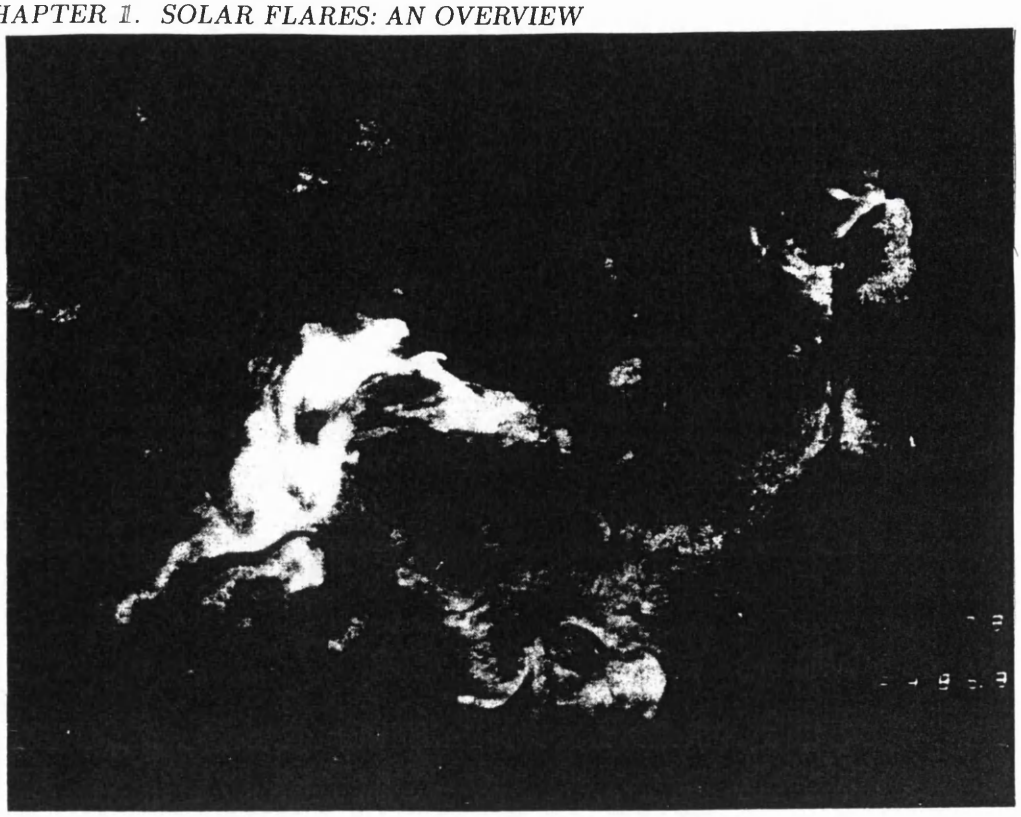

Figure 1.12: An H_α photograph of a two ribbon flare (Big Bear Solar Observatory).

footpoints or ribbons but occur in loops which are too small to be resolved. Tang (1985) has observed footpoints in very small flares of this nature in the wings of H_α. In the wings the absorption coefficient is small and we see down to cooler chromospheric parts of the loop than the hotter more disturbed overlying parts that we see when we observe in the line centre.

1.6.1 White-light flares

White-light flares are characterized by an increase in emission in the visible range and in integrated light. These enhancements can be seen as patches, waves or ribbons, often with < 3" kernels (Neidig and Cliver, 1983; Canfield et al.,1986). They are associated with sudden ionospheric disturbances; interplanetary proton events and strong emission in X-rays, microwaves and H_α (e.g. Neidig and Cliver, 1983a). White-light flares are important because their huge radiative losses ($> 10^{28}$ erg s^{-1} in the continuum) place strong constraints on energy transport mechanisms. In 1989, small aperture patrol telescopes, observing in the range $\lambda < 4000\mathring{A}$, were reporting about 15 white-light flares a year near solar maximum. The observations indicate that the origin of this emission is in the low chromosphere and upper photosphere, implying that these layers are being heated during the flare. One of the most important questions that white-light emission in solar flares raises is whether this temperature increase can be explained in terms of the transport of energy from the corona, or whether it requires either partial or total in situ energy release.

Up until now only > 90 white-light flares have been reported. In all probability white-light flares are no different from 'ordinary' flares, and the low number of observations is due to a detection

threshold effect and a dearth of dedicated white-light flare patrols. Indeed, *Yohkoh* has observed M class flares which exhibit white-light emission (van Driel-Gesztelyi et al., 1994), contrary to the popular notion that white-light emission is associated with only the largest events. Detection has been made difficult by several factors: white-light flares often occur in regions of large image contrast (sunspots and faculae); the nonlinear response of film recording and general seeing effects.

Important progress in the study of white-light flares has been in the concept of two types of white-light flare, as proposed by Machado et al. (1986).

- Type I - these flares show a Balmer jump and continuum emission which is produced predominantly by hydrogen free-bound, H_{bf}, transitions.
- Type II - these flares do not exhibit a Balmer jump and the continuum emission is mostly due to H^-.

Combinations of these two types have also been observed (Fang and Ding, 1995).

1.7 EUV and UV emission

UV and EUV emission cover the wavelength range from $\sim 10 - 300$ nm. The division between the two is around 150 nm. Above this wavelength emission is primarily from the photosphere and below it from the chromosphere and transition region.

UV emission in solar flares is not particularly conspicuous except in white-light flares, for which there has previously been little data. The principal mechanism for enhanced UV emission is the shift of the temperature minimum region to lower altitudes, higher densities and higher temperatures with the wavelength of minimum brightness shifting from $\sim$ 165 nm to $\sim$ 175 nm. This is caused by heating of the temperature minimum region by X-ray illumination from the coronal flare plasma (e.g. Canfield et al., 1980).

EUV radiation originates from layers in the solar atmosphere with $T < 10^6$ K, i.e. the transition region and upper chromosphere. The transport of flare energy through the atmosphere produces sufficient impulsive heating of these dense and relatively cool layers to produce EUV radiation. Enhanced densities in these heated regions result in an increase in the EUV emission measure, producing a burst of EUV radiation.

Some early EUV observations were made by studying the ionospheric response to incident EUV radiation from the Sun (Donnelly, 1976). The incoming EUV flux can be determined from the study of sudden frequency deviations (SFDs) in radio waves - radio waves reflected from the ionosphere are subject to sudden impulsive Doppler shifts as the ionosphere responds to the EUV flux (Kane and Donnelly, 1971). This method can show relative flux variations at the 1% level in the band $10 - 1030\mathring{A}$ (Tandberg-Hanssen and Emslie, 1988), corresponding to continua and lines formed in the upper chromosphere.

The broadband , $10-1030\mathring{A}$ EUV flux has been shown (Kane and Donnelly, 1971; Donnelly and Kane, 1978; Emslie et al., 1978) to peak simultaneously with the hard X-ray burst. Also, Donnelly and Kane (1978) showed that the rise phase of the EUV bursts corresponds closely with the rise of the hard X-rays around 30 keV. From this they concluded that energetic electrons of this energy were responsible for the excitation of the EUV burst. A centre to limb study of EUV to HXR ratios led them to suggest that the EUV source consisted of a 'trench' dug out of the atmosphere by an electron beam, surrounded by a shallower well of soft X-ray irradiation (Machado et al., 1978; Somov, 1981).

The EUV burst has also been observed in narrow emission lines formed at transition region temperatures. Emission in the O V line at $1371\mathring{A}$ (corresponding to a temperature of formation, $T \sim 2 \times 10^5$ K) has also been observed to peak with the hard X-ray burst (Cheng et al., 1985; Orwig and Woodgate, 1986), as have parts of the EUV continuum formed near the temperature minimum region in the deep chromosphere, suggesting that radiation transport is significant for the heating of the lower atmosphere in flares.

This observed synchronism between the broadband EUV and HXR bursts suggests a very fast energy transport mechanism between the site of the energy release and the chromosphere, e.g. high energy electrons. This is further supported by the rise time studies by Donnelly and Kane (1978). However, Emslie et al. (1978) found that the ratio of EUV/HXR burst intensities is inconsistent with the thick target electron heating model (e.g. Brown, 1971). Such a model should produce more broadband EUV emission than is actually observed.

This anomaly can be resolved if the model is modified to include either electron trapping or a very small injection area, $\sim 10^{16} cm^2$. In the latter case the high beam fluxes required to produce the observed HXR emission would result in a high degree of chromospheric evaporation and a relatively small fraction of the beam energy being deposited in the cool EUV emitting plasma (Emslie et al., 1978). This model, with a simple form for the optically thin radiative losses in the chromosphere, gives a power law dependence between the HXR and EUV which is consistent with Kane and Donnelly's (1971) observations.

Line emission synchronism with the HXR burst is rather more difficult to explain since although the beam energy input lowers the level of the EUV emitting layer and thus increases the density, it also steepens the temperature gradients (resulting in a larger conductive flux). What this means is that the differential emission measure need not necessarily increase. Poland et al. (1984), Emslie and Nagai (1985) and Mariska and Poland (1985) showed that only relatively short bursts of electron heating can produce the observed behaviour of the line fluxes.

1.8 Soft X-ray Emission

Soft X-ray emission extends over a wavelength range of $1-100\mathring{A}$. The amount of energy contained in this wavelength range from solar flares contains a significant fraction of the total radiated energy of the flare (Canfield et al., 1978). The soft X-ray emission comprises a mixture of continuum including bremsstrahlung (free-free)and bound-free continua, and spectral lines, usually due to highly ionized metals such as Fe XXV and Ca XIX. The electron population responsible for exciting this emission is typically thermal with a characteristic temperature of between 10^6 and 10^7 K. This kind of temperature is commensurate with that of the flaring corona, and as such, soft X-ray emission provides the most direct means available to us of investigating the flaring corona, particularly in determing temperatures, densities and velocities of the coronal plasma.

The field of soft X-ray observations is now entering its fifth decade, a period of time during which the instrumentation has steadily improved, providing better observations and a greater level of understanding of the soft X-ray emitting plasma. Observations in this area have been provided by the *OSO*, *Solrad*, *Skylab*, *GOES*, P78-1, *SMM*, *Hinotori* satellite missions; their latest successor being the *Yohkoh* mission which incorporates the Soft X-ray Telescope (SXT), an imaging telescope, and the Bragg Crystal Spectrometer (BCS), a bent crystal spectrometer which observes the resonance line complexes of S XV, Ca XIX, Fe XXV and Fe XXVI.

The major results from *SMM* and *Hinotori* were: observations of enhancements in the nonthermal line broadening observed in soft X-ray lines early in the flare which could be directly related to the primary energy release (Antonucci, 1989); convective upflows which were observed during the impulsive phase and could be associated with chromospheric evaporation (Antonucci et al., 1982); observation in Fe XXV and Fe XXVI from *Hinotori* which indicated the presence of a super-hot component, and density measurements which indicated that the flare region was probably highly filamented (e.g. Linford and Wolfson, 1989; Wolfson et al, 1983).

Flare densities measured from He-like O VII, Ne IX and Mg XI by McKenzie at al. (1980) and Doschek at al. (1981) indicated a range between $n_e \sim 3 \times 10^{11} - 3 \times 10^{12} cm^{-3}$ which are, in general, much higher than those measured indirectly from emission measures and geometry information. This could suggest that density sensitive ions emit from a lower temperature soft X-ray source (Antonucci, 1989), or that that the plasma is confined in very thin loops (e.g. Linford and Wolfson, 1989). Linford and Wolfson (1989) and Wolfson et al. (1983) derived filling factors of between $3 \times 10^{-4} - 10^{-2}$. These are consistent with the values found for soft X-ray loops in non-flaring conditions on the basis of scaling law considerations (Martens et al., 1985) and for active regions in the pre-flare phase (Antonucci et al., 1986).

The two distinctive characteristics of soft X-ray lines in the impulsive phase are large nonthermal broadenings (see Chapter 3 for a more detailed discussion) and significant blue shifted emission (Antonucci et al., 1982). Nonthermal broadenings are normally interpreted as evidence

for random motions within the flaring plasma, with blue shifts as the hydrodynamic response of the chromosphere to the impulsive energy release. The radiative instability caused by heating results in an expansion of chromospheric material into the lower density corona with high velocity upflows being observed. This is known as chromospheric evaporation and the onset of these blue shifts is seen to be roughly coincident with the onset of the hard X-ray emission. The blue shifts are not observed in limb flares as would be expected since line-of-sight effects would make it impossible to see plasma upflows here. The fact that they are observed in disk flares lends support to the idea of chromospheric evaporation. Nonthermal line broadenings are usually observed before the blue shifts (Antonucci, 1989), suggesting that these occur as a direct consequence of the initial energy release rather than as an indirect response to secondary heating. However, *Yohkoh* results have shown some events which have blue shifts prior to the HXR emission (e.g. Cheng et al., 1994).

1.8.1 New Discoveries from *Yohkoh*

Data from *Yohkoh* has provided confirmation of many of the observations made with *SMM* and *Hinotori*, as well as making some new discoveries in the realm of the soft X-ray flare and non-flare related phenomena. The main advances brought about by *Yohkoh* have been reviewed by Hudson (1995).

Outer corona - SXT has observed the outer corona out to a height greater than one solar radius above the photosphere, seeing a quasi-spherical component away from the coronal holes, and large scale loop configurations, most often over the polar crown region. Cusped coronal structures, indicative of continuing magnetic reconnection in a neutral sheet configuration (Priest et al., 1991) have also been observed (e.g. Tsuneta et al., 1992a). A particularly spectacular event of this nature was Tsuneta et al.'s (1992a) 'candle flame' event of February 21 1992.

Expanding active region loops - Frequent slow eruption of active region loops (Uchida et al., 1992) has been observed, with velocities in the range $10 - 100 kms^{-1}$, thus discriminating these events from the area of coronal mass ejections (CMEs).

Filament activations - Structures associated with H_α filaments have frequently been observed with SXT on *Yohkoh* (Khan et al., 1994; Alexander et al., 1994). There seems to be little difference between these events observed at active region latitudes and those observed in the polar crown region. Tsuneta et al. (1992) have observed polar crown structures developing on a vast scale, commensurate with the streamer blow out phenomenon (Kahler, 1992). The geometry of these filament activations appears to be complex and their development appears unlikely to be just two-dimensional.

Coronal mass ejections (CMEs) - SXT has observed many mass ejections, which were identified

during a routine data survey (Klimchuk et al., 1994) biased away from flare associations. The mean projected speed of these ejections has been found to be $48 kms^{-1}$, faster than the active region expansions studied by Uchida et al. (1992).

X-ray jets - Several kinds of X-ray jets have been identified by SXT (Shibata et al., 1992; Strong et al., 1992; Shibata et al., 1994). These are a new discovery with a likely connection to the small scale nonthermal phenomena which are observed in UV (Brueckner and Bartoe, 1983). However, such a connection is unconfirmed due to a lack of simultaneous UV and X-ray observations. In general, the jets tend to be tightly collimated and their evolution suggestive of reconnection geometries.

Microflares - *Yohkoh* has observed many 'active region transient brightenings' (Shimizu et al., 1994), although most of them are not temporally and spatially resolved by SXT. SXT has seen events of this kind with energies down below 10^{24} ergs; from the microflare range to below the nanoflare range (Parker, 1988). These observations indicate that there is no tendency for a preferred scale. Watanabe et al. (1994) have also shown that these microflares still have flare-like temperatures.

Impulsive footpoints - Often SXT observes impulsive footpoint brightenings which seem to see the evaporating chromospheric plasma as it flows upwards in the flare loop (Hudson et al., 1994a). The BCS instrument also often observes blue shifts in the profiles of soft X-ray lines, synchronous with impulsive flare emissions (Mariska et al., 1993) and with timing that is consistent with evaporation scenarios (Bentley at al., 1993). These footpoints seem relatively cool (McTiernan et al., 1993; Hudson et al., 1994a) and so incapable of accounting for the 'superhot' component.

Loop top sources - Loop top kernels and condensations have been observed with SXT (Acton et al., 1992; Feldman et al., 1994). Compact loop top sources were first identified by Skylab (Widing and Cheng, 1974; Cheng and Widing, 1975) but the data limits at that time did not allow the possibility of simple conductive-radiative loop equilibrium (Rosner et al., 1978) to be discounted. *Yohkoh* may have observed anomalous brightenings which are consistent with high pressure, high density regions. Other possible explanations for these sources involve projection effects of curved flux tubes. A curved and twisted flux tube could also have the appearance of a cusp.

Superhot sources - These were first identified by Lin et al. (1981) using balloon-borne instruments, and were then identified by Tanaka (1987) in the *Hinotori* data. Indeed, Tanaka's (1987) classification scheme includes Type A sources which consist of a nearly isothermal plasma at a temperature above the normal flare range, i.e. up to $\sim 2 \times 10^7$ K. The Fe XXV and Fe XXVI

channels of the BCS and the lower energy channels of HXT provide the means to study this component of the flare plasma. Pike et al. (1996) have compiled a considerable list of flares observed by *Yohkoh* which show Fe XXVI emission.

Cusps - the observation of cusps, e.g. the February 21 1992 event (Tsuneta et al., 1992a) has been cited as evidence for the presence of neutral sheet geometry in some flares (Hudson, 1994). In the February 21 event a rapidly rising structure is observed just at the onset of the soft and hard X-ray bursts.

SXT has discovered some new phenomena, e.g. X-ray jets, but has also confirmed some long standing ideas such as the neutral sheet configuration for large flares (Carmichael, 1964) and the general scenario of chromospheric evaporation (Antonucci et al., 1982).

Microflares and nanoflares as a source of coronal heating, however, has not been confirmed. It has been sugegsted by Hudson (1991) that this implies different physics for these small events if they are to explain coronal heating (Parker, 1988). Loop-loop interactions have not been strongly supported by *Yohkoh* observations either (but see Akioka et al., 1993; Hanaoka, 1994). Despite observations of multiple loops it has not been possible to prove any interaction.

1.9 Hard X-ray Emission

The first hard X-rays from the Sun were detected by Peterson and Winckler (1959) with a balloon-borne experiment in the energy range 20-500 keV. The photon energy spectrum was estimated from only two data points to be a power law. They attributed the observed HXR emission to bremsstrahlung emission of 0.05-1.0 MeV electrons stopping in the photosphere. Chubb et al. (1966) claimed that this data could be equally well fitted by a thermal bremsstrahlung spectrum from an isothermal plasma with temperature in excess of 10^8 K, (e.g. Crannell et al., 1978) viz.

$$I(\epsilon) = 1.3 \times 10^{-42}(n^2V)\epsilon^{-1.4}(k_BT)^{-0.1}e^{-\epsilon/k_BT} \tag{1.17}$$

where ϵ is the photon energy, (n^2V) is the emission measure; k_B is Boltzmann's constant and T the temperature of the plasma.

Since then many missions have measured spatially averaged hard X-ray spectra from solar flares. In general these energy spectra are roughly consistent with a power law of the form

$$I(\epsilon) = A\epsilon^{-\gamma} \ photons\ cm^{-2}\ s^{-1}\ keV^{-1} \tag{1.18}$$

(Kane, 1969; Frost, 1969) with spectral index generally in the range $3 \lesssim \gamma \lesssim 8$.

A spectral break in the 60-100 keV range (Frost, 1969; Kane and Anderson, 1970; Frost and Dennis, 1971) is often observed. This can be expressed as

$$I(\epsilon) = \begin{cases} A\epsilon^{-\gamma_1} & \epsilon \leq \epsilon_0 \\ A\epsilon_0^{\gamma_2-\gamma_1}\epsilon^{-\gamma_2} & \epsilon > \epsilon_0 \end{cases} \tag{1.19}$$

where ϵ_0 is the break energy and A is a constant.

Elcan (1978) found that 28 out of 38 events studied from the Orbiting Solar Observatory-7 (OSO-7) were better characterized by either the double power law fit or the exponential fit than a single power law at the peak of the impulsive emission. He suggested that a single temperature thermal source at $T \simeq 5.4 \times 10^7 - 3.6 \times 10^8$ K was responsible for the impulsive solar hard X-ray emission (c.f. Piana, et al., 1995).

Equations 1.17, 1.18 and 1.19 are really only useful for describing the observed hard X-ray spectra because of uncertainties in deconvolving the energy response of detectors (e.g. Dennis, 1982). Derivation of the original electron spectrum in a meaningful manner is even more difficult due to the broad nature of the electron-ion bremsstrahlung cross-section which results in a smoothing of fine details in the recovered electron spectrum (Craig and Brown, 1976).

However, Lin et al. (1981) and Lin and Schwartz (1987) observed X-rays in the range 15-200 KeV with very high resolution and high purity germanium detectors. The spectral response of these detectors was essentially considered to be a δ-function so that the incident X-ray spectra could be recovered directly. Work has also been done by Johns and Lin (1992) Thompson et al. (1992) and Piana (1994) on recovering the parent electron spectrum assuming a bremsstrahlung interaction.

Generally the spectrum of the hard X-ray emission displays a soft-hard-soft behaviour typical of type B (see below) impulsive flares as recognized by Kane and Anderson (1970). However, there are some events which display soft-hard-harder behaviour, characteristic of type C (see below) gradual flares (Tsuneta, 1984a; Cliver et al., 1986).

Kane (1969) found that hard X-ray flares consist of an impulsive and a gradual component, with the energy spectrum of the impulsive component consistent with a power law and a steeper spectrum characterizing the gradual component. He concluded that this was consistent with the suggestion (Acton, 1968; Takakura 1969) that the hard X-ray emission consists of both a nonthermal and a thermal component.

The thermal component (Kane, 1969) is commonly seen in flares with $T_e \sim 1 - 2 \times 10^7$ K and is probably due to evaporated chromospheric material (e.g. Antonucci et al., 1982). There are also some observations (e.g. Takakura et al., 1982) indicating the presence of a very high temperature plasma with $T_e \geq 3 \times 10^7$ K. This component has a very steep spectrum which would be equivalent to a spectral index $\gamma \sim 11$ if it were fitted with a power law spectrum at 35 keV. Lin et al. (1981) observed this component in the flare of June 27 1980 and found that before its appearance the hard X-ray spectrum was best fitted by a double power law which breaks down at high energies. They argued that this spectral form was consistent with electrons being accelerated by a DC electric

field along magnetic field lines (Syrovatskii, 1966).

Hard X-ray emission is produced in the energy range from $\sim 10 - 300$ keV. In principle X-rays in this energy range can be produced by electron-ion bremsstrahlung, magnetobremsstrahlung and inverse Compton scattering of ambient thermal protons. However, Korchak (1967,1971) showed that emission via the magnetobremsstrahlung process was unlikely to contribute to the observed hard X-rays since it would require an extension of the electron distribution to high energies which would involve high energy loss rates. He also showed that the although inverse Compton scattering could contribute significantly this was only possible at low densities. As a result, it is generally accepted that the hard X-ray emission in solar flares is produced by electron-ion bremsstrahlung.

Models of hard X-ray emission essentially fall into two categories; nonthermal and thermal. The nonthermal models have as their energy source a beam of high energy electrons, whilst thermal models invoke emission from a high temperature plasma with $T_e \gtrsim 10^8$ K.

1.9.1 Nonthermal models

This category of theories again subdivides into the thick and thin target models and combinations of the two. In the thick target scenario (e.g. Brown, 1971) the electrons immediately lose their energy via Coulomb collisions with the ambient plasma as they precipitate down the loop legs; whilst in the thin target model the electrons continue to emit hard X-rays while travelling in a low density plasma along the field lines. This could occur when electrons are injected low in the corona and emit X-rays as they travel up, or if they are trapped in a coronal magnetic bottle and continue to emit X-rays.

In some events the peak time of the higher energy hard X-ray emission is delayed with respect to the lower energy emission (Bai and Ramaty, 1979). This type of behaviour is consistent with the trap plus precipitation model (e.g. Takakura and Kai, 1966; Brown, 1974; Brown and Melrose, 1976; Bai and Ramaty, 1979). In this model both thick and thin target hard X-ray emission is produced when a proportion of the electrons are trapped by magnetic mirroring in the coronal part of the loop and produce thin target emission, whilst the rest precipitate down the loop legs producing thick target emission.

1.9.2 Thermal model

The thermal model is an alternative bremsstrahlung source for hard X-ray emission involving a very high energy plasma with $T_e \gtrsim 10^8$ K. Thermal bremsstrahlung was in fact the first proposed mechanism for solar flare hard X-ray production (Chubb, 1966). Its advantage over the nonthermal models is that in principle it is much more efficient than nonthermal bremsstrahlung processes.

However, Kahler (1971a, b) pointed out that 10 keV ($k_B T_e \sim 10$ keV) electrons can easily escape from the hot plasma because of their very long collisional mean free path. Also, the conductive

cooling rate of such a hot plasma can be shorter than the actual burst time. Brown et al. (1979) countered that strong return currents would be set up when the electrons started to escape from the plasma which would be unstable to the generation of ion-acoustic waves. Ion-acoustic conduction fronts would be set up which would help confine the plasma.

1.9.3 Other models- ion beams

Simnett (1986) proposed that the bulk of the energy released in the impulsive phase in fact goes into 100 keV-1 MeV protons, rather than electron beams, which then stream down the field lines producing high temperature plasma at the loop footpoints ($T_e \sim 10^8 - 10^9$ K) from which hard X-ray emission is produced by thermal bremmstrahlung. Simnett and Haines (1991) and Simnett (1991) also recently suggested that instead the hard X-rays are emitted by electrons which are accelerated in a runaway process caused by the proton beam near the footpoints. The proton beam carries with it neutralizing electrons at the same speed and when this neutral beam reaches the chromosphere the electrons are scattered and the protons carry on precipitating deeper into the atmosphere. This produces an electric field which causes runaway acceleration of electrons near the footpoints and nonthermal hard X-ray emission from the interaction of these electrons with the ambient chromosphere.

However, as Brown (1991) has pointed out, the neutralizing electron current is in fact a return current which propagates in the same manner as for an electron beam but in the opposite direction. These electrons are not moving at the same speed as the protons. The electric field generated by the proton beam drags denser plasma electrons to form a slow moving return drift current.

1.9.4 *SMM* and *Hinotori* Observations

One of the most important findings from these missions was that hard X-ray emission from flares can be classified into three categories with respect to its temporal, spectral and spatial characteristics, viz. type A, type B and type C (Tanaka, 1983).

Type A - Super-hot flares

These flares show a gradual ($\sim$ 1 minute) rise and fall in the energy range below about 40 keV (Tanaka et al., 1982; Tsuneta et al., 1984b). Impulsive emission is seen at higher energies but it is much weaker than that observed in type B impulsive flares. The energy spectra can be fitted with a thermal component of characteristic temperature $T_e = 3 - 4 \times 10^7$ K, below 40 keV, and with a power law of $\gamma \gtrsim 7$ above 40 keV. They show weak radio emission and the sources are compact ($\lesssim$ 5000 km) and low altitude ($<$ 6000 km) (Tsuneta et al., 1984b).

Type B -Impulsive flares

Most flares are of this type. Their spectra show soft-hard-soft behaviour and can be fitted by a double power law which breaks down at high energies or an exponential during the rise phase and

at the peak of the emission; becoming a single or double power law during the decay phase (e.g. Winglee et al., 1992).

These flares have low altitude sources evolving to more compact higher sources as the flare progresses. Some impulsive flares observed with HXIS on *SMM* showed double source structure (e.g. Duijveman et al., 1982). However, MacKinnon et al. (1985) studied the same events using Maximum Entropy deconvolution and found that these footpoints were much less visble above the noise level in the higher channels. They also argued that incorporating Poisson noise statistics rendered the footpoint synchronism highly uncertain. They concluded that a thermal model at $T_e \gtrsim 10^8$ K was equally good at accounting for the observations.

Type C - Gradual hard flares

These flares were only observed with the Solar X-Ray Telescope (SXT) on *Hinotori* (Tsuneta et al., 1984a). They show gradually varying hard X-ray emission on timescales of a few minutes and last up to 30 minutes. Sources are high in the corona ($\sim 2 \times 10^4 - 9 \times 10^4$ km) and have a larger size than type A and type B sources, sometimes as big as 70" x 30" (Takakura et al., 1984b).

Sakurai (1983, 1985) showed through a photospheric potential field extrapolation that these sources are located at the top of either a single loop or an arcade where the magnetic field strength is about 50 G.

These event show strong microwave emission (Kai et al., 1985; Bai and Dennis, 1985) with a relatively low peak frequency compared to type B events. This is consistent with emission higher in the corona where the magnetic field strength is lower. They also show continuous and gradual spectral hardening throughout the flare (Kosugi et al., 1988), with spectra better described by a power law than a single temperature source.

Kosugi et al. (1988) studied about 400 flares observed with HXRBS on *SMM* and found 3 type A events, 13 type C, 62 microwave gradual rise and fall events and the rest all type B impulsive.

1.9.5 *Yohkoh* observations

The Hard X-ray Telescope (HXT) on board *Yohkoh* has observed over 800 flares and the main features of the results of analyses of some of these flares have been summarized by Kosugi (1994). These results can be summarized as follows.

- The hard X-ray flares that have been observed in the low channel of HXT (13.7 - 22.7 keV) appear to have structures which trace the flare loop; the hard X-ray images in this channel clearly resemble the corresponding soft X-ray images.

- In the higher energy channels of HXT the sources are seen to be more compact and patchy. We **do** typically see two separate sources corresponding to the ends of the long thin structure observed in the low channel (Sakao, 1994). This is fairly convincing evidence for the thick

target bremsstrahlung model in which electrons are accelerated at or near the apex of the flaring loop and precipitate down the loop legs. This is quite different from what we saw with *Hinotori*, where single high sources were observed more often than double footpoint sources. However, *Hinotori* was incapable of imaging above $\sim$ 30 keV and also had poorer temporal and spatial resolution than *Yohkoh*.

- The average height of hard X-ray sources decreases with increasing energy (Matsushita et al., 1992)
- Sometimes we observe a sudden shift in the location of the hard X-ray sources during the impulsive peaks; suggesting the successive flaring of adjacent loops.

New results

Sakao et al. (1992) showed that for the flare of November 15 1991 the two sources are located on either side of the magnetic neutral line. The higher energy ($>$ 30 keV) X-rays from this event at the impulsive peaks show the most pronounced double source structure. The $\lesssim$ 30 keV X-rays at the valleys between these impulsive peaks originate from near the loop apex. Kosugi (1994) suggests that this could be interpreted as evidence for the DC electric field runaway model (Benka and Holman, 1992), in which electron acceleration and direct heating occur. This could be the case for the November 15 flare but with enhanced electron acceleration occurring at the peaks in the impulsive phase. However, the observation of white-light emission from this flare (Hudson et al., 1992) provides rather more compelling evidence for the trap plus precipitation model of Melrose and Brown (1976).

An analysis of 33 impulsive flares was carried out by Sakao (1994), in which he reported several general trends.

1. The double source structure, with the two sources located on either side of the magnetic neutral line, separated by $\sim 10 - 30$ arc seconds, are found in 40% cases of those examined.
2. The double sources show an intensity variation with a time lag consistent with 0.0 s within the 1σ level (Sakao, 1994).
3. The brighter source tends to correspond to a footpoint where the photospheric magnetic field is weaker.
4. The brighter source tends to exhibit a harder spectrum.

These results are all strongly suggestive of the idea that electrons are accelerated at or near the apex of the loop and precipitate down the loop legs. One might also expect that the footpoint with the larger photospheric magnetic field would be fainter, since electrons are likely to be mirrored by this stronger field.

Loop top sources

For several limb flares one or more sources in addition to the double footpoints, have been observed in the range $\gtrsim 20$ keV at a height of $> 10^4$ km above the photosphere (Masuda, 1994). In some cases this source occurs **above** the apex of the corresponding soft X-ray loop. The loop top sources are generally fainter than the footpoint sources but the variation in intensity is very similar and their spectrum relatively hard. Assuming that the emission is thermal in nature results in a temperature determination of $T \sim 2 \times 10^8$ K and an emission measure, EM $\sim 10^{44} - 10^{45} cm^{-3}$. There is then little doubt that the source is impulsive in nature.

The presence of this source above the apex of the soft X-ray loop is important. It tells us that something energetic is happening outside the soft X-ray loop and that whatever that is is connected with particle acceleration. Kosugi (1994) speculates that what we are actually seeing in this loop top source *is* the particle acceleration site.

For most of the observed flares during the impulsive phase the emission in the low channel of HXT appears to consist of a gradually varying component with superimposed impulsive spikes. Images of these sources place it between the footpoint sources and with a structure closely resembling that of the soft X-ray emission. Emission from this type of source continues after the impulsive phase and has a steep high energy spectrum typical of a thermal source of temperature $T \simeq 2 - 4 \times 10^8$ K and emission measure $EM \simeq 10^{46} - 10^{49} cm^{-3}$ (Masuda, 1994a,b).

The problem of how this thermal plasma is created has been addressed by a number of authors, including Culhane et al. (1994), Inda-Koide et al. (1994) and Wülser et al. (1994), using a combination of HXT, SXT and BCS observations. However, its origin is still not clear. For example, nonthermal electrons can create the high observed temperatures; evaporation can create high emission measures but not temperatures and heat conduction is incapable of producing temperatures of $4 \times 10^8 K$ unless the heat source is even hotter than this.

Some flares have been observed in which a hard X-ray source ($\gtrsim 25$ keV) has been observed as much as 40 arc seconds distant from the brightest loop seen by the HXT L-band or by SXT. The 24 October 1991 event observed by Masuda et al. (1994a) is such an event. In this case the remote source is located south west of the double source and is a unipolar region with the same polarity as that of the western footpoint of the double source structure. Masuda (1994a) has concluded that 2 loops are involved, the outer loop more efficient at electron acceleration and the inner loop mainly producing high temperature plasma with gradual hard X-ray emission. This may be evidence for loop-loop interactions. Similar events have been seen by Yaji et al. (1994)

Superhot sources

Superhot thermal flares are those characterized by predominantly thermal emission from a plasma of temperature $T \gtrsim 3 \times 10^7$ K in hard X-rays (Tanaka et al., 1982). By implication these events are much less efficient at particle acceleration and imaging of them might provide clues as

to where the primary energy release site is, how the hot plasma is created and what determines the particle acceleration efficiency. These sources could also be important for understanding the loop-top gradual sources.

Gradual hard sources (type C)

These flares are characterized by high altitude ($\sim 5\times10^4$ km) hard X-ray sources which produce gradually varying X-ray and microwave fluxes; spectral hardening in the X-ray spectrum and a large microwave to HXR flux ratio. All these characteristics are indicative of trapped nonthermal electrons and/or continuous acceleration (Tanaka, 1983; Tsuneta et al., 1984; Dennis, 1985; Kosugi et al., 1988).

Yohkoh observations have identified for us the existence of several different types of source in the hard X-ray range, i.e. double footpoint; loop-top impulsive; loop-top gradual; remote-site impulsive and superhot thermal sources (Kosugi, 1994). All of these sources appear to display different characteristics and may in fact represent different aspects of the flare energetics.

1.10 Radio and microwave emission

The principal types of emission mechanism in this wavelength range include plasma radiation, free-free bremsstrahlung, gyroresonance and thermal and nonthermal gyrosynchrotron.

1.10.1 Observations

Most solar observations in the radio wavelength, particularly from flares, are in the form of dynamic spectra which are named in terms of their historical classification, viz. Type I, II, III, IV (Wild et al., 1963).

Type I - Type I events last between hours and days and are not necessarily flare associated. The emission is spread quite uniformly over a large frequency range and does not display the coherent time drifts that are observed in Type II and III events. Type I bursts are shorter duration more intense versions of Type I events. These are not yet well understood, but are thought to be caused by energetic electrons trapped in coronal loops.

Type II - These events have a duration of many minutes and are characterized by a slow drift down in frequency. Often Type II emission is observed following the impulsive phase in solar flares, when it is frequently seen at two frequencies, separated by about a factor of 2. The frequency drift is suggestive of a rising source with a velocity in the range $400 - 2000 kms^{-1}$. Type II emission is inferred to be caused by a flare-generated shock wave propagating out through the solar corona (Wild, 1950).

Type III - This emission is often but not always seen accompanying flares. Sometimes these events

occur in groups of 10 -100 seconds and show a similar frequency drift to the Type II events. Their duration is a few seconds and the corresponding frequency drift rate is much higher, corresponding to a velocity of $\sim 10^{10} cms^{-1}$. These events are interpreted as a burst initiated by a beam of mildly relativistic electrons. The emission possesses a coherent time structure over one order of magnitude in frequency, which is equivalent to about four coronal scale heights (since $n \sim \omega_p^2$ and $n \propto e^{-z/H}$) The stability of the electron beams that this implies provides stringent modelling constraints for theoreticians.

Type IV - Type IV events are always associated with flares and last between a few minutes and a few hours after the optical flare has decayed. Often they follow an associated Type II burst and their source moves through the solar atmosphere at velocities of $\sim 10^3$ kms^{-1}. The emission has the character of a smooth continuum and has been explained by Boischot and Denisse (1957) in terms of synchrotron radiation from electrons with energies of afew MeV.

Type V - Type V bursts are broadband continuum radiation which sometimes follow Type III bursts. These are rare.

Flare associated radio emission occurs in both the decimetre and metre wavelength ranges in a variety of different forms of the types listed above. Possibly the most complex and least well understood are the decimetre bursts, of which there are several categories.

Microwave spike bursts- These actually occur in the range $\sim 0.5 - 3$ GHz, i.e. covering a lot of the decimetre wavelength range. They are characterized by rapidly varying spikes with rise times $\lesssim 10$ ms, durations $\lesssim 40$ ms, flux densities of up to 10^{-18}Wm^{-2}Hz^{-1} and up to 100% circular polarization. Detailed descriptions of these bursts have been given by Dröge (1977) and Slottje (1978). They have a very high brightness temperature which implies that the radiation must be coherent. The most plausible emission process is the electron-cyclotron maser (Melrose and Dulk, 1982b).

Impulsive phase bursts- Often fast drift bursts are seen at decimetre wavelengths during the impulsive phase (Dulk and McLean, 1986). They occur together with impulsive microwave bursts at higher frequencies and type III bursts at lower frequencies.

Extended phase bursts - these are type IV bursts with an opposite sense of polarization to the accompanying microwave burst. They are much less regular in appearance than bursts at higher and lower frequencies.

Metrewave bursts

These originate high in the corona outside the confines of the active region. The earliest

and fastest bursts occur during the impulsive phase and are related to sub-relativistic electrons streaming through the corona. A second, slower, group of bursts follows a few minutes after the impulsive phase and can last for up to an hour. These are associated with shock waves and mass motions in the corona.

Finally there is a period of enhanced activity which begins tens of minutes to an hour after the impulsive phase and can last anything from hours to days. This storm phase could be caused by a gradual rearrangement of the coronal field after a mass ejection (Dulk et al., 1986).

Impulsive phase bursts- these are bursts of type III, V and FCE (flare continuum early) plus inverted U and J bursts which are variations of the type III emission. They all occur within a few seconds to a few minutes of the impulsive phase. The energy is transported through the corona at $\gtrsim 0.1c$, suggesting energetic electrons (Dulk et al., 1986).

Groups of type III bursts are the most common flare associated bursts- sometimes they are the only radio emission. Types V and FCE are better correlated with the microwave burst, and the combination of microwave and FCE burst is thought to indicate that protons and nuclei are being accelerated to $\gtrsim 10$ MeV.

Slower bursts - Type II bursts, due to shock waves in the corona, FCII (flare continuum associated with type II) and moving type IV bursts fall into this category. Radiation similar to the FCII can occur without the accompanying type II burst; this is called slow drift continuum. Type II and type IV bursts may occur either separately or together; when they occur together the type II burst occurs first. All of these are rare and liable only to be observed during sunspot maximum.

Like emission in all other wavelengths from flares metrewave emission varies greatly from one flare to another, the larger and more intense the flare the more likely that all of these bursts will be observed. The top portion of fig. 1.1 shows the the types of bursts which may occur and at which stages during the flare.

1.10.2 Microwave bursts

Radio observations are capable of resolving fine scale structure with sub arc second resolution and considerable detail has been observed in microwave images, especially with the Very large Array (VLA) which can provide images and spectra simultaneously (Marsh and Hurford, 1982).

Overlays of VLA maps of flares onto H_α images show that the microwave emission at 6cm typically comes from a region situated between the two footpoints, which is presumably near the loop top (Kundu, 1983b), i.e. near the site of primary energy release.

Observations of bursts at 2cm (Marsh and Hurford, 1980) show that in the impulsive phase the emission is dominated by a compact source between the two H_α kernels. Later, the microwave

source becomes larger and elongated along the field lines, presumably connecting the H_α kernels. Further observations at this wavelength (Marsh et al., 1981) showed two components of emission, one on either side of the neutral line with opposite senses of circular polarization. Shevgaonkar and Kundu (1985) noted that the 2cm radiation often comes from the footpoint sources at the bottom of the loop. These observations are highly suggestive of electron acceleration and propagation down the loop legs. The different sense of polarization can be attributed to the different sense of the longitudinal magnetic field component when measured from the top of the loop down.

Observations at 20cm (e.g. Melozzi et al., 1985) usually show extended sources separated from the shorter wavelength emission. This is believed to be gyrosynchrotron emission from a hot thermal plasma confined in a loop. Since the intensity of gyrosynchrotron emission is dependent on the magnetic field strength we might expect that emission should be stronger at the footpoints. However, gyrosynchrotron emissivity is strongly peaked in a direction perpendicular to the magnetic field lines, so when observing at right angles to the field at the top of the loop a greater fraction of emission is seen than when observing along the field lines at the footpoints.

Early analyses (e.g. Takakura, 1969, 1975) estimated the total number of electrons required to produce the microwave burst to be some 3-4 orders of magnitude lower than that required to produce the hard X-ray burst. Since the similar time structure of these bursts indicates that they are produced by the same electron population, this was a serious anomaly. However, Gary (1985) pointed out that these analyses had all assumed a thin target hard X-ray production mechanism, the inefficiency of which leads to an over-estimate of the number of electrons required. The use of the thick target model removes this discrepancy.

Microwave observations at 22 and 44 GHz by Kaufmann et al. (1984) showed very rapid fluctuations down to a few tens of milliseconds, similar to those observed in the HXR burst. This type of very rapid fluctuation is evidence for the scenario that the impulsive phase is composed of a series of separate energy releases, consistent with some of the magnetic reconnection flare models.

1.10.3 Production mechanisms

Microwave emission in flares arises from three different processes: thermal bremsstrahlung, gyrosynchrotron and collective plasma processes.

Thermal bremsstrahlung - this is free-free continuum emission, the low frequency end of the blackbody radiation curve for a hot gas at temperature, T. It is optically thick and unpolarized.

Gyrosynchrotron - low energy electrons gyrating around the magnetic field lines emit circularly polarized radiation at the gyrofrequency, $\nu_e = eB/2\pi m_e c$.

For mildly relativistic electrons the radiation is beamed, resulting in a spiky radiation signal.

The degree of beaming is a function of the energy of the emitting electron and so Fourier decomposition results in a complicated spectrum. At low frequencies the source is optically thick and has a positive spectral slope in the range ν^2 for thermal distributions and ν^3 for nonthermal distributions.

At higher frequencies the source becomes optically thin and the spectrum changes to a negative slope; ν^{-8} for a thermal population and between $\nu^{-1} - \nu^{-4}$ for a nonthermal population, depending on the spectral index of the electron distribution. The maximum power is emitted at frequencies which correspond to an optical depth of one. Measurement of this turnover frequency can provide information on either the column density, temperature or magnetic field strength, provided one has an independent estimate of the others.

Coherent plasma emission - the passage of a beam of high energy electrons through a plasma can cause Langmuir waves to grow which can couple nonlinearly to produce an electromagnetic wave at $\omega = \omega_{pe} = (4\pi ne^2/m_e)^{1/2}$ (Tsytovich, 1970). If these are not strongly gyroresonance absorbed they can propagate out and be observed. Emslie and Smith (1984) and McClements (1987b) calculated that the microwave contribution from this process could exceed the gyrosynchrotron contribution.

Another collective process which could contribute to the microwave emission is the maser (Microwave Amplification by the Stimulated Emission of Radiation) process.

1.11 γ-ray emission

Gamma-ray emission is entirely absent in quiet Sun observations. During a flare we observe both continuum ($< 1MeV$) and line emission,as shown in fig. 1.13. The most commonly observed lines in flares are: positron annihilation at 0.511 keV; neutron capture at 2.223 MeV; and the nuclear de-excitation lines from carbon, 4.438 MeV and oxygen, 6.129 MeV. Prior to *SMM* only a few flares with emission above 100 keV had been observed and all our understanding of high energy phenomena on the Sun was largely inferred from lower energy X-ray observations and measurements of interplanetary particles. As a result of this the general view was that energetic ion and relativistic electron acceleration in flares was a rare occurrence.

SMM and *Hinotori* showed that high energy radiation was in fact a common characteristic of flares which could provide us with information on the composition, energy spectrum, angular distribution and production history of energetic particles at the flare site. One of *SMM*'s most important discoveries was to show that often hard X-ray and γ-ray time profiles were essentially coincident, contrary to the popular two-step acceleration theory (see Chupp, 1984)

Other important results from *SMM* included the identification of a centre-to-limb variation in the bremsstrahlung continuum. When spectra in the range 300 keV - 1 MeV were fit by power laws events near the limb had a mean spectral index that was harder than that of disk events by

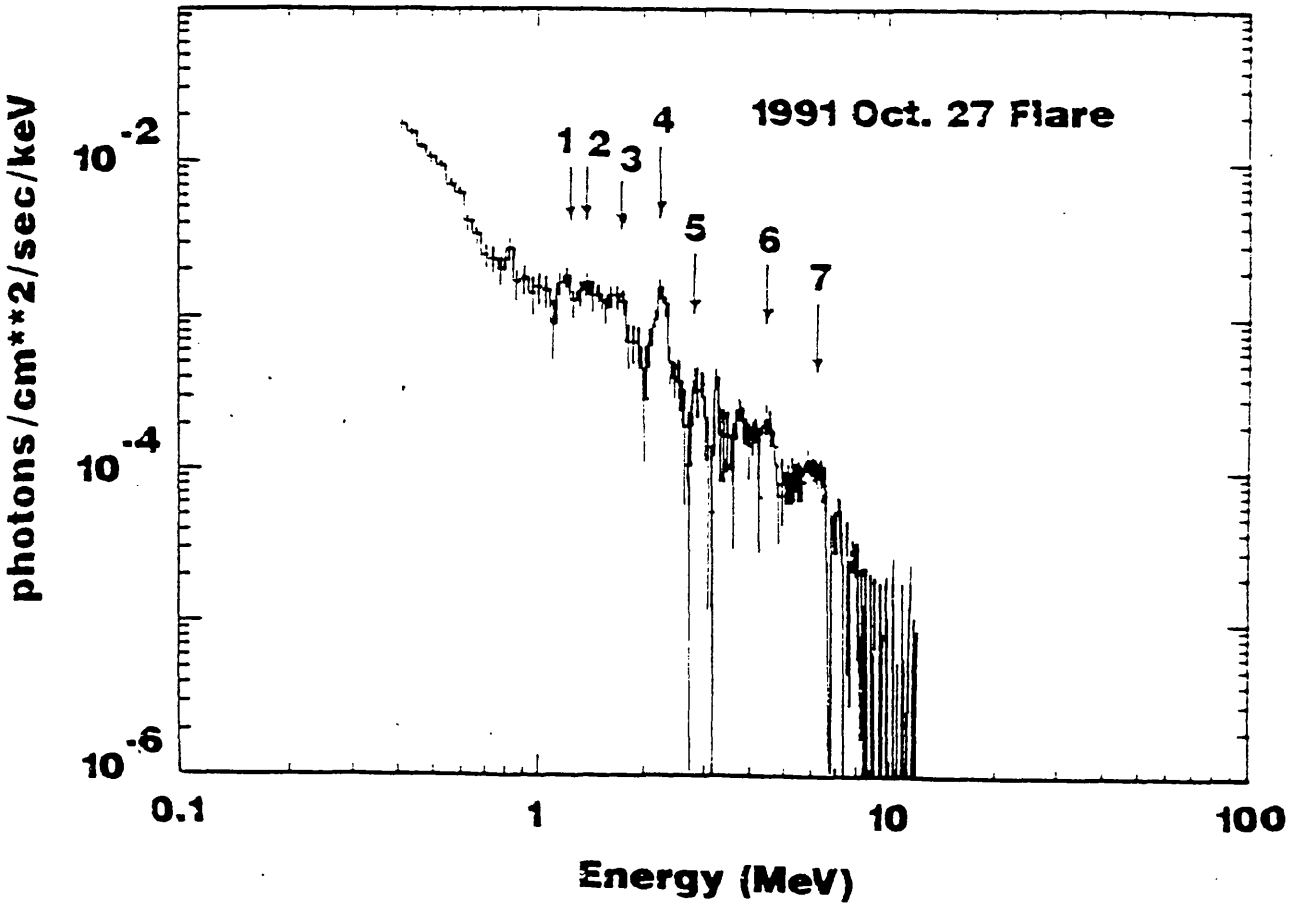

Figure 1.13: Gamma-ray spectrum for the event of October 27 1991, indicating the γ-ray lines - 1. Fe at 1.25 MeV; 2. Mg at 1.37 MeV; 3. Ne at 1.63 MeV +Si at 1.78 MeV; 4. neutron capture at 2.223 MeV; 5. O + Ne + Mg lines around 2.7 MeV; 6. C at 4.44 MeV; 7. O at 6.13 MeV. (after Yoshimori et al., 1994)

$\Delta s = 0.37 \pm 0.11$ (Vestrand et al., 1987). Compton backscatter is small at energies > 300 keV implying that the spectral hardening must be caused by an anisotropic angular distribution.

The first serious attempts at deriving solar abundance information from γ-ray spectroscopy were made possible with measurements from *SMM* GRS. Murphy et al. (1985) derived best fit target abundances for the event of April 27 1981. When these were compared with local galactic abundances, believed to be similar to photospheric abundances, they showed significant enhancements of Ne, Mg, Si and Fe relative to C and O. Since γ-ray nuclear line production probably occurs in the chromosphere this suggests a fractionation of abundances between the photosphere and the chromosphere. A possible mechanism could be charge dependent mass transport (Meyer, 1985), since C and O have higher first ionization potentials than Si, Mg and Fe. However, this cannot explain the enhancement in Ne which has a very high first ionization potential.

The neutron capture line at 2.223 MeV is the strongest observed line in solar flare spectra and indicates recent neutron production. A comparison of the neutron half-life, $\tau_{1/2} \sim 900$ seconds with the typical neutron capture time, $\sim 10^{19}/n_H$, implies that for efficient production of the 2.223 MeV line the density has to be greater than $10^{16} cm^{-3}$ which puts the production region in the photosphere. Wang and Ramaty (1974) pointed out that Compton scattering would attenuate this capture line emission for limb events. Chupp (1982) has observed this phenomenon with the *SMM* GRS.

The number and energy spectrum of the accelerated particles can be determined from a comparison of the neutron capture line fluence (integrated flux) with the fluence in the 4 - 7 MeV band. Since the time histories of the emission in these bands is quite different one cannot just compare the flux. The 4 - 7 MeV emission is generated in the chromosphere by ions with slightly lower energies than those whose interactions produce the neutrons. So, the ratio of the two fluences is a measure of the spectral hardness. Theoretical calculations (e.g. Hua and Lingenfelter, 1987b) have led to the conclusion that the spectral variation from flare to flare is very small (Ramaty and Murphy, 1987), see fig. 1.14.

Successful measurements from *SMM* have also allowed an upper limit on the $^3He/^1H$ ratio to be determined as 3.8×10^{-5} (Prince et al., 1983). A more detailed analysis for the June 3 1982 flare implied a photospheric $^3He/^1H = 2.3 \pm 1.2 \times 10^{-5}$ at the 90% confidence level (Hua and Lingenfelter, 1987b), consistent with the value expected from primordial nucleosynthesis. This rules out the idea of coronal enhancements caused by turbulent diffusion from the solar interior to the photosphere.

Nearly 70 flares with γ-ray line emission were detected during *SMM*'s lifetime, in contrast to only 2 detected by OSO - 7, the very large events of August 1972. Forrest (1983) used > 300 keV fluence of GRS flares as a measure of flare size and studied the correlation with nuclear line fluence in the 4 - 7 MeV band. He found a good correlation and concluded that, within the sensitivity of

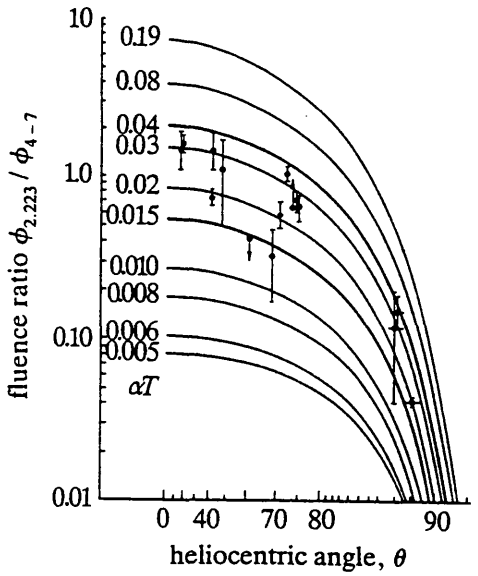

Figure 1.14: Measured fluence ratios plotted against the heliocentric angle of the flare. The smooth curves show predictions for Bessel function ion energy spectra with a horizontal fan beam angular distribution. (After Hua and Lingenfelter, 1987a)

the detector, ions are always accelerated in flares. A similar study using the 40 -140 keV flux also found no evidence for a threshold in the neutron capture line production.

Extended phase emission was first observed by *SMM* GRS from the June 3 1982 flare (Forrest et al., 1986). The extended phase occurred about a minute after the impulsive phase and had a much harder spectrum than that measured in the impulsive phase, consistent with the hypothesis that the high energy emission is generated by pion decay. Also discovered was the failure of the good correlation between electron and ion acceleration that is observed in the impulsive phase.

Murphy et al. (1987) argued that this extended emission was produced by a second phase of acceleration. Their model postulates a first phase which stochastically accelerates energetic ions and relativistic electrons that are trapped in the solar atmosphere. In the second phase a very hard ion spectrum is created by delayed shock acceleration on open field lines. In support of this theory they noted that the proton spectrum required to generate the pion decay spectrum had the same shape as the interplanetary proton spectrum associated with this event (McDonald and Van Hollebecke, 1985).

The first energetic neutrons from the Sun were observed by *SMM* from the event of June 21 1980. After the impulsive γ-ray burst *SMM* GRS recorded a significant high energy excess counting rate with a time dependence similar to that predicted for impulsively generated neutrons arriving at the earth (Lingenfelter et al., 1965; Lingenfelter and Ramaty, 1967). A consideration of the instrumental background and the energy loss spectrum (Chupp et al., 1982) indicated that they

had to be neutrons.

1.11.1 *Yohkoh* γ-ray observations

Since its launch in August 1991 *Yohkoh* has recorded several X class flares with emission above 1 MeV between October and December 1991. Unfortunately, there appear to have been no further γ-ray events since January 1992 (Kosugi, 1994).

Yoshimori et al. (1994) have reported on three particular events: October 27 1991, November 15 1991 and December 3 1991. The event of October 27 showed significant bremsstrahlung emission below 1 MeV and γ-ray lines in the 1-7 MeV band. This event is typical of those observed by *SMM* and implies that protons and ions are being efficiently accelerated to $>$ 10 MeV per nucleon. However, the temporal evolution of the ratio of the counting rate in the 4-7 Mev band to the counting rate in the 0.4 - 0.7 MeV band varies with time, indicating either that electrons and protons were not accelerated simultaneously, or that the proton acceleration becomes more efficient with time.

The December 3 event showed a strong bremsstrahlung component up to 10 MeV but no significant line emission., implying that electrons were preferentially accelerated during this event. Rieger and Marschhäuser (1990) observed a small number of these electron dominated events. Yoshimori et al. (1994) found that the ratio of the count rate in the 4-7 MeV band to that in the 0.4-0.7 MeV band was constant for this event, indicating that both low and high energy electrons were accelerated simultaneously.

The Be and Li lines at 429 keV and 478 keV respectively, were observed in the November 15 event. Usually, these are not observed, probably because at the peak of the flare the electron bremsstrahlung continuum masks them. These lines are strongly dependent on the angular distribution of the interacting nuclei (Murphy et al.,1988; Murphy et al., 1990). Yoshimori et al. (1994) compared the observed count spectra in these lines with calculated spectra for three different angular distributions, strong pitch angle scattering, no pitch angle scattering and isotropic. Whilst the spectra calculated from the strong pitch angle scattering distribution provided a good fit to the data, they concluded that the spectra derived from the isotropic distribution were probably also consistent with the data. The high resolution spectra from HESI are eagerly awaited!

Also observed in the November 15 flare was the positron annihilation line at 0.511 keV, during the decay phase. Detailed analysis by Kawabata et al. (1993) suggested these possible mechanisms for its production:

1. the main source of positrons is de-excitation of $^{16}O^{*}$ by electron -positron pair emission
2. β^{+} emitting nuclei of ^{31}S, ^{29}P, ^{27}Si, ^{26m}Al, ^{25}Al, ^{23}Mg, ^{19}Ne and ^{21}Na are also important positron sources in the decay phase

Gamma-ray lines are the most direct probe of nuclear processes in the solar atmosphere. They can give unique information on the beaming of energetic particles through measurements of the shifts in the energies of narrow lines; and on the timing of the nucleonic component in flares, through measurements of the light curves of prompt lines. Other information available from γ-ray observations includes details of the nucleonic energy spectrum, including number and energy content of the particles, from line ratios and line fluences (Ramaty, 1986); details of the site of the nuclear interactions through selective attenuation affects in limb flares and the spectrum and time dependence of the positron annihilation line (Ramaty and Murphy, 1987); the geometry of particle beams, through line shapes and Doppler shifts (Ramaty, 1986); estimates of the ^3He abundance, through the time dependence and fluence of the neutron capture line, and information on the chemical composition of both the ambient medium and the energetic particles, through line ratios (Ramaty, 1986).

1.12 Future satellite missions

Since satellite data will feature heavily in succeeding chapters of this thesis and since high quality data is pivotal in increasing our understanding of the Sun, this section will provide a brief introduction to some of the upcoming solar missions and what advances we hope we can make with them.

1.12.1 *SoHO*

SoHO was launched on December 2nd 1995 and has been designed to observe the Sun and the earth's environment for an expected lifetime of 2 years. It has been launched as we approach solar minimum and as such will provide us with mainly quiet sun observations. The primary objectives scientifically are the study of the internal structure of the sun, its outer atmosphere and the origins of the solar wind, especially coronal heating. It is hoped that *SoHO* will provide scientists with the first opportunity for an extended, uninterrupted view of the sun. Unlike most previous solar observatories which orbited the earth, *SoHO* will orbit the sun in a halo orbit around the L1 lagrangian point, i.e. where the sun and earth's gravitational fields are balanced.

The project is a joint venture between ESA and NASA as part of the framework of the Solar Terrestrial Science Program (STSP), comprising *SoHO* and *CLUSTER*, and the International Solar-Terrestrial Physics Program (ISTP) with *Geotail*, *Wind* and *Polar*.

Three instruments are dedicated to the study of the solar interior and helioseismology. These are VIRGO (Variability of solar IRradiance and Gravity Oscillations), GOLF (Global Oscillations at Low frequencies) and SOI/MDI (Solar Oscillation Investigation/Michelson Doppler Imager). GOLF and VIRGO will perform measurements of oscillations of the full solar disk in the velocity

and irradiance domains respectively. SOI/MDI will measure oscillations on the solar surface with high angular resolution. It is hoped that these experiments will provide precise information about the convection zone on the Sun.

SUMER (Solar Ultraviolet Measurements of Emitted Radiation), CDS (Coronal Diagnostic Spectrometer) , EIT (Extreme ultraviolet Imaging Telescope), UVCS (Ultraviolet Coronagraph Spectrometer) and LASCO (Large Angle Spectrometric COronagraph Experiment) make up a combination of telescopes, spectrometers and coronagraphs designed to observe the corona. SUMER, CDS and EIT will observe the inner corona, whilst UVCS and LASCO will observe both the inner and outer corona. All of these experiments will provide measurements of the temperature, density composition and velocity in the corona, also following the evolution of coronal structures with high resolution.

CELIAS (Charge, Element and Isotope Analysis System) and ERNE (Energetic and Relativistic Nuclei and Electrons experiment) will provide in situ measurements of the charge state and isotopic composition of the solar wind, as well as that of the energetic particles generated by the Sun. SWAN (Solar Wind ANisotropies) will make maps of the hydrogen density in the heliosphere from 10 solar diameters, allowing the large scale structure of the solar wind streams to be measured.

1.12.2 *Solar-B*

The *Solar-B* mission is an international collaboration based on the highly successful Japanese/U.S. venture *Solar-A* (*Yohkoh*). Still to be approved by the Japanese, it will carry a coordinated set of optical, UV and X-ray instruments dedicated to understanding the dynamic Sun and is due for launch around the year 2003; around the time of the next solar maximum. Observationally, the major advances of *Solar-B* will be to reveal the photospheric roots of the Sun's magnetic field and the way in which it links to the corona; to provide unprecedented spatial resolution and the first complete high resolution time coverage.

Its scientific objectives are to study the following questions:

1. The creation and destruction of the Sun's magnetic field
2. Modulation of the Sun's luminosity
3. Generation of UV and X-ray emission
4. Origin of the solar wind and eruptions

1.12.3 *TRACE*

TRACE is the Transition Region And Coronal Explorer. This will be the first purely U.S. solar research satellite since *SMM*. It will also be the first satellite to pursue continuous solar observations

without suffering from earth occultation during its orbit. It is due for launch in 1997 and will complement the data taken by *SoHO* during the rise phase of the solar cycle to sunspot maximum; no transition region or coronal imager has observed the rise of the solar cycle. The two missions provide a unique opportunity to obtain simultaneous measurements of all temperatures in the solar atmosphere with high-resolution images (*TRACE*) and spectroscopy (*SoHO*). Magnetograms produced by MDI on *SoHO* will provide the necessary record of the eruption and distribution of photospheric magnetic fields vital for understanding *TRACE* observations of coronal hole formation and CME's. Ideally we hope with *TRACE* to be able to study magnetic flux emergence in detail, from its origins at the base of the convection zone, through the photosphere, chromosphere and transition region to the corona. *TRACE* is designed to provide answers to the problem of modelling the connection between the magnetic fields and plasma structures on the sun. In the photosphere the magnetic fields and plasma are in approximate equipartition, but in the corona the magnetic fields are the dominant feature. *TRACE* will use multiple UV and normal incidence EUV channels to collect images of the solar plasma over a temperature range of 10^4 to 10^7 K. It's spatial resolution will be one arc second, a factor of 3 better than that achieved by the SXT on *Yohkoh*.

1.12.4 The High Energy Solar Imager (*HESI*)

The *HESI* mission, which is due to be launched in the year 2000, will consist of a single spin-stabilized spacecraft in a low altitude equatorial orbit with just one instrument on board: the High Energy Imaging SPECtrometer (HEISPEC). HEISPEC will have the capability to produce high resolution colour movies of solar flares in X-rays and γ-rays. Its launch is timed to take full advantage of the next solar maximum with up to three years of flight operations.

HEISPEC will use fine tungsten grids to modulate the solar X-ray flux as the spacecraft rotates and produce up to 20 images per second in the range from $\sim$ 2 keV to $\sim$ 1 MeV. This kind of time resolution should be adequate to track electrons from the acceleration site in the corona down into the lower solar atmosphere where they lose most of their energy.

Germanium detector X-ray and γ-ray spectroscopy will be performed over an energy range of 10 keV to 20 MeV with an energy resolution of about 1 keV which should be sufficient to provide new insights into the processes of electron and ion acceleration. The instrument will have the finest angular and spectral resolution up to γ-ray energies that has ever been flown in space and also has the capability to perform spatially resolved spectroscopy so that small scale features with in flares may be examined in detail.

The primary scientific objectives of the *HESI* mission will be to increase current understanding of the processes of impulsive energy release, particle acceleration and particle and energy transport. In particular it is hoped that it will provide new insights into the rapid release of energy stored in unstable configurations; the rapid conversion of this energy into the kinetic energy of the hot

plasma and accelerated particles; the transport of these particles through the solar atmosphere and into interplanetary space and the subsequent heating of the ambient solar atmosphere.

To gain the most from *HESI* observations other ground and space-based context images will be required. Specifically, soft X-ray, EUV and UV images and spectroscopic measurements with similar spatial and temporal resolution, and from the ground, radio and optical images and spectroscopic measurements and vector magnetograph data will be required.

As well as higher resolution hard X-ray images and hard X-ray and γ-ray spectra, *HESI* will for the first time provide spectrally resolved hard X-ray images, i.e. high resolution spectoscopic measurements will be available at each point in a hard X-ray image with subsecond time resolution allowing spectral changes to be measured as electrons propagate along the magnetic field in the flaring loop. This should provide important new constraints on the mechanisms of particle acceleration and energy loss.

Also possible with *HESI* will be imaging in certain γ-ray lines or energy ranges. The comparison of images in e.g. the positron annihilation line at 0.511 keV and the proton-alpha particle induced lines around 450 keV with hard X-ray images should be an important source of information on the effect of differences in charge and mass on the acceleration and propagation processes that has not previously been available.

More detailed discussions, including theory, of some of the aspects considered here can be found in later chapters.

Chapter 2

Yohkoh: Instrumentation

2.1 Introduction

The aim of this chapter is to give a basic overview of the instrumentation payload carried by the satellite *Yohkoh*. As much of the work carried out during my PhD. involved work on the analysis of data obtained by *Yohkoh* - although some of the attempts are not mentioned in this thesis - a familiarization with basic capabilities of its instruments is necessary to get a feel for the data. There is a (fairly) extensive literature describing *Yohkoh*'s payload in much greater detail than is given here, and most of it is referenced throughout this chapter.

2.2 The satellite and its scientific objectives

Yohkoh is the second satellite of the Institute of Space and Astronautical Science (hereafter ISAS) of Japan dedicated to the study of solar flares. The first, Hinotori, was launched during the last solar maximum, in February 1981. Hinotori had essentially the same scientific objectives as the Solar Maximum Mission (SMM), which had at that time been in operation for a year. Both of these satellites provided observations in the X- and γ-ray ranges and diagnosed high energy particles and high temperature plasmas involved in the flare process. SMM also had EUV and optical capabilities. These missions also provided us with the first hard X-ray images of solar flares, although they were not capable of imaging above around 30 keV.

Yohkoh was launched at 11.30 a.m. on August 30th 1991 from the Kagoshima Space Center (KSC) in Japan by an M-3SII-6 launcher. Its orbit has eccentricity, $e \sim 0.02$ and semi-major axis $\sim 7500km$. Its apogee and perigee are at about 792km and 517km respectively. The orbital inclination of the satellite is, $i \sim 31.3°$ and the period ~ 97 minutes. Typically, *Yohkoh* completes about 15 revolutions of the earth in one day.

Although the Sun is not observed during spacecraft night, the WBS is able to make non-solar

γ-ray observations. Also, during its passage over Brazil and the nearby South Atlantic Rgeion the spacecraft enters the earth's radiation belt. Normally the orbit of *Yohkoh* is below the equatorial level of the Earth's radiation belt, but over this area the altitude of the radiation belt is anomalously low; this is called the South Atlantic Anomaly. During this radiation belt passage the high voltage supplies of the BCS are switched off to protect the instruments from damage. Consequently, only quiet rate data is available at this time.

2.2.1 The spacecraft

The satellite itself has a rectangular box shape with dimensions $\sim 100 \times 100 \times 200$ cm, with two external solar panels on the outside of dimensions 150×200cm each which provide about 570 Watts of power during spacecraft day. *Yohkoh* weighs about 400 Kg and consists of seven panels; one central and six side panels, which provide the mechanical backbone. The HXT, SXT and BCS instruments are mounted on the central panel, while the WBS is mounted on the top panel which faces the Sun. Figure 2.1 shows the satellite and the positioning of the scientific instruments.

The scientific payload of *Yohkoh* consists of four instruments: the Bent Crystal Spectrometer (BCS), Soft X-ray Telescope (SXT), Hard X-ray Telescope (HXT) and the Wide Band Spectrometer (WBS). Each of these is described in detail below. The scientific objectives of the mission included the co-ordinated observations of high energy phenomena in solar flares by all four instruments.

2.2.2 Attitude control

Yohkoh is a three axis stabilized spacecraft with its z-axis pointing towards the Sun's centre. The y-axis is directed parallel to the solar north pole. Because both the SXT and the HXT take high resolution images of the Sun (with 2" and 5" resolution respectively) it is crucial that the attitude of the spacecraft is precisely controlled. In order to do this the following attitude sensors send signals to the Attitude Control Electronics (ACE): the Inertial Reference Unit (IRU), Two-dimensional Fine Sun Sensor (TFSS), Non-spin Type Solar Aspect Sensor (NSAS), Star Tracker (STT) and Geomagnetic Aspect Sensor (GAS). Once these signals have been received they are processed by the attitude control processor (ACP) and then sent to the actuators: the momentum wheels, the magnetic torquers and the control momentum gyros.

The TFSS and NSAS sensors monitor the position of the Sun and provide information about the x- and y-axes of the spacecraft. The NSAS provides the signals used to trigger the day-to-night transition of the spacecraft, the STT monitors Canopus, providing z-axis information and the IRU (high precision gyros) and GAS (monitors the Earth's magnetic fields) provide information about all three axes.

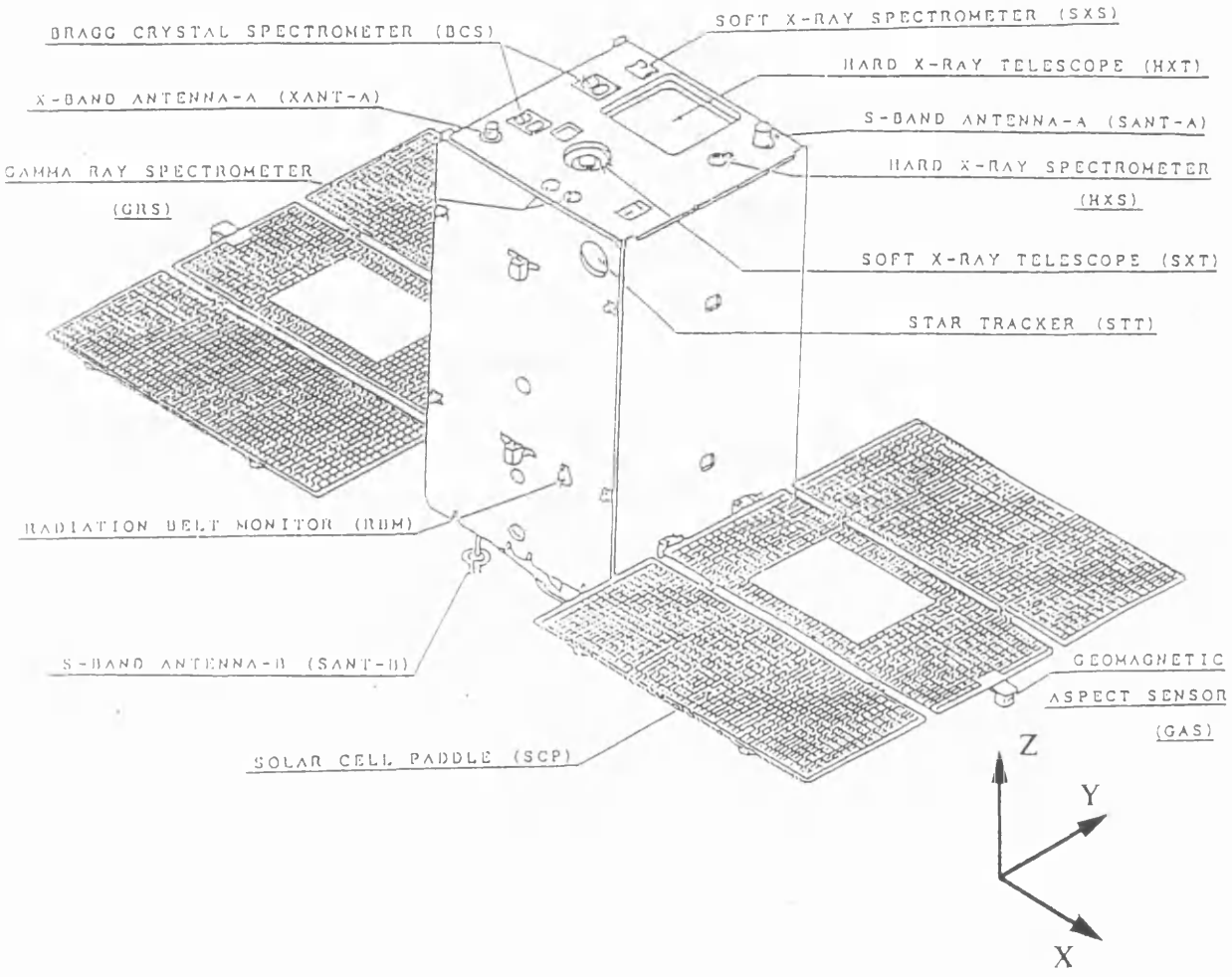

Figure 2.1: A schematic view of the *Yohkoh* satellite (from Ogawara et al., 1991).

2.2.3 Operation, Telemetry and Data Processing

The data processor (DP) on board *Yohkoh* automatically controls the observing mode and the operation of the instruments, as well as collecting the data from all the on-board instruments and editing it. The data are then either recorded onto the bubble data recorder (BDR) or telemetred directly to the ground. Out of the fifteen Earth revolutions there are five contacts a day with KSC during which time commands can be transmitted to the spacecraft and data downloaded. These contacts last about 12-16 minutes. Apart from these there are ten other contacts with NASA's Deep Space Network (DSN) stations at Madrid, Canberra and Goldstone and Santiago.

Communications between *Yohkoh* and the ground stations are conducted at two frequencies: S-band (2.2 GHz) and X-band (8.4 Ghz). At KSC the S-band is used for the transmission of commands to the spacecraft and the downloading of the real-time data at 32 kbps. The X-band is used to download the recorded data from the BDR at 262 kbps. Only KSC receives real-time data. The NASA DSN stations use only S-band telemetry to download recorded data at 262 kbps.

2.2.4 Observing Modes

Yohkoh has four observing modes and three telemetry or bit-rates. The four observing modes are: flare, quiet, night and BCS out-mode; and the bit-rates are: high (32kbps), medium (4kbps) and low (1kbps). High bit-rate corresponds to one major frame every 2 seconds; medium bit-rate to one major frame every 16 seconds. *Yohkoh* uses the HXS and SXS instruments of the WBS to monitor solar activity and when a threshold is passed the spacecraft enters flare mode. The combination of the observing mode and the bit-rate is known as the DP mode. For example, flare data can only be recorded in high and medium bit-rates and the DP mode for flare mode data with high bit-rate is flare-high. After ten minutes at high bit-rate the data processor (DP) goes into medium rate provided that the intensity of the flare has subsided but still remains above a certain threshold.

2.2.5 Bubble data recorder

The Bubble Data Recorder (BDR) onboard *Yohkoh* is used to store data between downlink stations, and is capable of storing $\sim$ 10 Mbytes or about 42 minutes worth of data in high bit-rate.

When the BDR is filled then new data will begin to overwrite the stored data. In order to prevent flare data being overwritten a data importance level is set for new data whilst a write protection level is set for data that has already been recorded. Only new data with a data importance level greater than the write protection level can overwrite existing data. Flare data has both a data importance level and a write protection level of 2, whilst quiet sun data has data importance level 1 and write protection level 0. Therefore, quiet Sun data is constantly overwritten whilst the flare data is protected. Since flare mode is generally triggered after the flare begins in order to

preserve the very important pre-flare data when a flare occurs the BDR block just prior to the flare observations has its write protection level set to the level of the flare data, thus ensuring we have pre-flare observations.

2.3 Scientific objectives

The primary scientific objective of *Yohkoh* is the study of high energy phenomena from solar flares; particularly X- and γ-rays. SMM and Hinotori revealed many new aspects of solar flares (eg. Kundu and Woodgate, 1986; Tanaka, 1987) and also provided the first opportunity of imaging hard X-rays above a few keV. Some of the more important aspects revealed by SMM and Hinotori are listed below:

1. Impulsive flares (type B; Tanaka, 1987) were shown to have two or more separate sources which brightened almost simultaneously in hard X-rays.

2. Type C (Tanaka, 1987) gradual flares appeared to have extended sources high in the corona.

3. Soft X-ray observations indicated that there was violent heating occurring in the transition region and chromosphere due to the precipitation of high energy electrons resulting in turbulent motions and chromospheric evaporation (Doschek et al., 1980; Antonucci et al., 1982). A group of type A flares (Tanaka, 1987) also showed H-like emission from 'superhot' ($> 3 \times 10^7 K$) thermal plasmas.

4. γ-ray flares were detected which showed that ions were accelerated to a few MeV in a few seconds simultaneously with electrons. These flares were preferentially observed near the solar limb, indicating possible anisotropy of γ-ray radiation.

The hard X-ray images obtained from these missions, although a great breakthrough, had several drawbacks. Firstly, they had relatively low spatial resolution, and secondly, they could only image at energies below 30 keV. At this upper energy limit there is still a significant possibility of soft X-ray emission contaminating the images. Also, although both SMM and Hinotori carried soft X-ray spectrometers, neither of these missions had a soft X-ray imaging telescope as SKYLAB had previously done. Soft X-ray images provide us with the most direct means of observing the coronal magnetic structures in which flares occur and are also useful in determining the location of hard X-ray sources.

Yohkoh improves on both SMM and Hinotori in a number of areas. Firstly, the Hard X-ray Telescope (HXT) produces high time resolution (0.5s) observations in four energy bands from $\sim$ 14 to 93 keV. Simultaneous images from the Soft X-ray Telescope (SXT) allow the location of these hard X-ray sources to be identified and provide the opportunity of a unique insight into the energy release and particle acceleration processes in solar flares. As both of these instruments have whole

Sun fields of view, most flares should have these simultaneous observations. The combination of the Bragg Crystal Spectrometer (BCS) and SXT open up the possibility of establishing the true motion of the flaring plasma, as distinct from other neighbouring active region which may also be emitting, and the high sensitivity and dynamic range of SXT makes it ideal for the study of quiet coronal structures and active region evolution.

Before the launch in August 1991, Ogawara et al. (1991) outlined the primary scientific objectives it was hoped that *Yohkoh* would study and shed new perspectives on:

Flares

1. active region evolution, especially pre-flare evolution in terms of coronal loops
2. flare onset
3. the formation of high temperature loops and arcades
4. particle acceleration processes
5. particle acceleration in γ-ray flares
6. chromospheric evaporation and mass ejections
7. flare ejecta, shocks and plasmoids
8. multi-wavelength relationships
9. whitelight flares

Dynamical Phenomena

1. Surges and Brueckner's jets in X-rays
2. quiescent filament evolution
3. CME's and related phenomena

Other Activity

1. X-ray bright points and possible solar cycle variations
2. micro- and nano-flares
3. formation and evolution of active region loops

Global Coronal Structure

1. formation and evolution of quiet coronal loops

2. behaviour of coronal holes

3. solar oscillations (SXT aspect sensor)

4. photospheric imaging

Yohkoh has now been in operation for four years providing high quality data from all of its instruments throughout this time. Many of these scientific questions have been addressed and many are still actively under investigation. In this chapter I will not even begin to discuss the wealth of literature that exists as a result of the analysis of *Yohkoh* data; although some of this has been discussed in Chapter 1. Amongst some of the more comprehensive collections of papers are the Proceedings of the International Symposium on the *Yohkoh* Scientific Results: X-ray Solar Physics from *Yohkoh* (Uchida Y.,Watanabe T., Shibata K., and Hudson H.S.; 1993) and the Proceedings of Kofu Symposium (Enome and Hirayama ; 1994). Further information about SXT can be found on the SXT homepage at http://pore1.space.lockheed.com/SXT/homepage.html

We now move on to discuss in more detail the scientific payload of *Yohkoh*; the Hard X-ray Telescope (HXT), Bragg Crystal Spectrometer (BCS), Soft X-ray Telescope (SXT) and Wide Band Spectrometer (WBS).

2.4 Hard X-ray Telescope (HXT)

The hard X-ray Telescope on board *Yohkoh* is a Fourier-type synthesis imager, consisting of 64 subcollimators. Each modulation subcollimator has a small NaI(Tl) scintillator and photomultiplier tube, which measure a modulated photon count. A set of the 64 spatially modulated photon count data may then be converted into an image by using image synthesis methods. In principle this can be achieved using Fourier transform methods, in practice it has been achieved using Maximum Entropy Methods (Sakao, 1994; McTiernan, 1994) and zeroth order regularization with pixon methods (Metcalf, 1995).

Count rate data is provided simultaneously in four channels: L(13.9-22.7 keV); M1 (22.7-32.7 keV); M2 (32.7-52.7 keV) and H (52.7-92.8 keV), with an angular resolution of 2.5" and a time resolution of 0.5 seconds. Each subcollimator has a field of view wider than the solar disc, and the total effective area of the collimator/detector system is $\sim 70cm^2$, twice that of the hard X-ray imager on Hinotori.

HXT provides the first opportunity to image hard X-rays at energies above 30 keV providing vital information on nonthermal processes occurring in solar flares. Coincident observations with SXT give us the first possibility of identifying the acceleration site with respect to the magnetic field configuration. Hard X-rays are primarily produced by collisions between high energy electrons and ions (i.e. bremsstrahlung) and since hard X-ray propagation is mostly unaffected by the

solar atmosphere they provide the most direct information available on the generation, transport and confinement of high energy electrons on the Sun. HXT is unique in its ability to produce observations in the energy range $\sim 30 - 100$keV where previous imagers, HXIS on SMM and the imager on Hinotori, were unable to produce images above 30 keV, where the likelihood of soft x-ray contamination is still high.

The instrument itself has three major sections, as shown in figure 2.2. These sections are as follows.

2.4.1 The Collimator - HXT-C

This is the X-ray optics part of the telescope, consisting of a metering tube with X-ray grid plates at both ends. Each grid plate consists of 64 subcollimator grids made of tungsten 0.5mm thick. At the centre are the aspect system optics (HXA), which have lenses and filters to provide white-light images of the sun, enabling positional determination of sources on the sun.

The front and rear grids of each subcollimator have identical slit spacing and a single discrete detector measures the resultant flux passing through these two grids. By using a pair of such collimators, differing by 90° in phase, and comparing their output with a measurement of unmodulated flux a measurement of a single Fourier component is obtained. With 64 such subcollimators you then get the equivalent of 32 Fourier components simultaneously.

Grid Assemblies

Each grid assembly consists of a base plate, four fanbeam element units and six Fourier element units. The base plate is a single sheet of molybdenum, 1.5 mm thick with 64 square holes with rounded corners, in which the X-ray optics fit. The holes are tapered, 37 mm at the front and 23 mm at the back. The rear hole determines the effective area of the subcollimator whilst the front is larger to ensure full efficiency.

A fanbeam element unit consists of a 0.5 mm thick tungsten plate with four fanbeam grids of one position angle. These are at the corners of the base plate. The six Fourier element units have eight Fourier grids of one position angle.

The aspect optics (HXA)

The determination of the position of hard X-ray sources with respect to soft X-ray and visible light features is achieved using the aspect system. The HXA optics consist of two identical systems, each comprising an achromatic doublet imaging lens with filters on the front grid assembly, fiducial marks on the rear and a one-dimensional CCD. The lens centre and the fiducial marks define the optical axis.

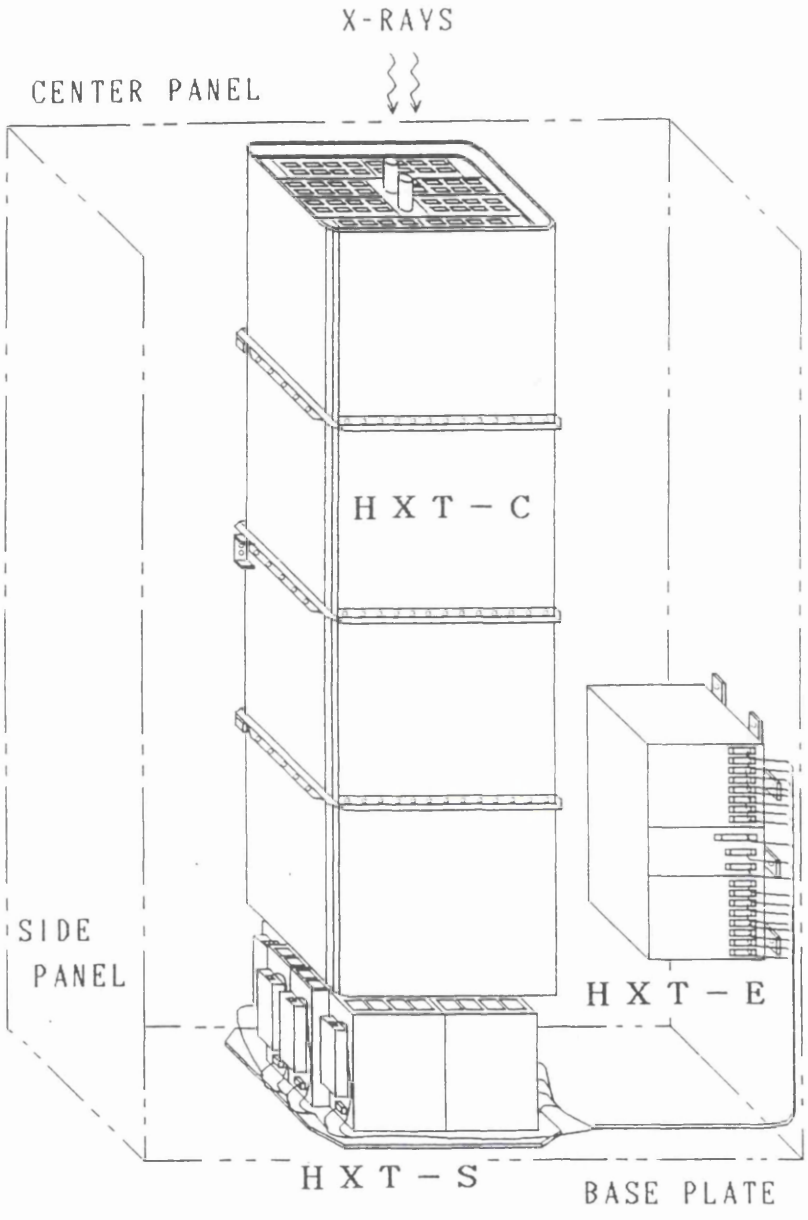

Figure 2.2: Schematic drawing of the HXT instrument, showing the 3 major sections: HXT-C, HXT-S and HXT-E (from Kosugi et al., 1991).

2.4.2 The Detector Assembly - HXT-S

This is a package of 64 detector modules, each of which consists of a NaI(Tl) scintillation crystal, a photomultiplier tube, with dynode bleeder string, and a pre-amplifier assembled as one unit. Eight high voltage power supply units are attached to the detector assembly. It also includes two 1-D CCD's at the centre to detect the HXA visible light signals. When an X-ray enters the detector electrons are knocked out of the atoms in the scintillation crystal. These free electrons produce photons inside the crystal which then hit a photocathode wihich releases photoelectrons. These electrons are then accelerated and focussed onto the dynode. The dynode multiplies the number of electrons and as a result a large pulse arrives at the anode, the energy of which is proportional to the total energy liberated inthe scintillation crystal.

2.4.3 The Electronics Unit - HXT-E

This processes the signals from HXT-S, converting pulse-height analogue signals to digital signals and counting incident photon number after energy discrimination. Signals from each individual subcollimator are processed separately and simultaneously. The photon count data is then sent to the data processor every 0.5 seconds.

Below is a table of HXT characteristics compared to the capabilities of previous hard X-ray imaging telescopes, from Kosugi et al. (1991). We can see that the main advantages that *Yohkoh* has over its predecessors are as follows:

1. higher energy range to $\sim$ 93 keV
2. higher sensitivity
3. better angular and temporal resolution
4. a wide field of view covering the whole Sun
5. simultaneous observations with SXT

HXT is the first X-ray telescope to employ the Fourier synthesis principle. This kind of telescope was initially discussed by Makishima et al. (1978) as a multi-pitch modulation collimator, and Prince et al. (1988) proposed a Fourier transform telescope using position sensitive detectors, each having one subcollimator and measuring one complex Fourier component. HXT differs frm these in that each subcollimator has a normal non-position sensitive detector and measures only one Fourier component pair.

The design of HXT is based on the fact that a single modulation collimator, with two identical grids having pitch (slit spacing) twice the slit width give a transmission pattern which is triangular. The mutual shadowing effect modulates the beam in one direction, with a period $\lambda = p/D$, where p is the pitch spacing and D is the separation of the grids. This principle is illustrated in figure 2.3.

	HXT	HINOTORI imager	HXIS (SMM)
Collimator type	Multi element bigrid MC	Rotating bigrid MC	Multi element IC
No. of elements	64 SC's	2 (orthogonal)	(F)304; (C)128
Size of elements	$23mm$ *square*	$120mm$◯	$7.5mm$◯
Image acquisition	2D Fourier synthesis	1D scans →2D image	1el./1 pixel
Angular resolution	~ 5"	~ 10"	8" (32")
Field of view	whole Sun	whole Sun	2'40" (6'24")
Synthesis aperture	2'06"	2'12"	2'40" (6'24")
Time resolution	0.5 s	~ 10 s	1.5-9 s
Energy Bands	4 channels	1 channel	6 channels
(keV)	Ch. L: 13.9-22.7		3.5-5.5-8.0
	Ch. M1: 22.7-32.7	5(17)-40	8.0-11.5-16
	Ch. M2: 32.7-52.7		16-22-30
	Ch. H: 52.7-92.8		
Detector	NaI(Tl) scint.	NaI(Tl) scint.	Gas proportional counter
	($25mm$ *square* × 64)	($120mm$ ◯ ×2)	($7.5mm$ ◯ ×900)
Effective area	~ $70cm^2$	~ $8cm^2$ × 2	$0.07cm^2pixel^{-1}$

Table 2.1: Main Characteristics of HXT. Note: MC=modulation collimator; IC=imaging collimator; SC=subcollimator; (F)=fine field of view; (C)=coarse field of view

If parallel radiation is incident on the first grid, then depending on the angle of incidence, the parts of the beam which are transmitted by the first grid can fall either solely on the wires of the second grid, or solely on the spaces or on both the wires and the spaces.The transmission of the grid system in the first two cases is 0% and 50% respectively, whilst in the latter case the transmission varies with the incident angle. So, the net angular response of a bigrid collimator is triangular with a peak transmission rate of 50%, as illustrated in figure 2.4. This triangular transmission pattern is similar to a cosine function if the DC component is disregarded. The transmission function of a pair of subcollimators can then be represented by $F_c(kr)$, where $r = Xcos\theta + Ysin\theta$, with k the wavenumber; kr the modulation phase; θ the position angle of the grid pattern; and X and Y the spatial coordinates normalized to the fundamental ($k = 1$) period of repetition. There is always a second subcollimator whose position angle and pich are the same as those of the first but whose relative slit positions are shifted by a quarter pitch. The transmission function of this subcollimator is then $F_s = F_c(kr - \pi/2)$.

One pair of subcollimators then gives the photon count data which form one generalized complex Fourier component if $B(X,Y)$ is the brightness distribution on the sky, viz.,

$$\begin{aligned} b_c(k,\theta) &= A \int B(X,Y) F_c(kr) dX dY \\ b_s(k,\theta) &= A \int B(X,Y) F_s(kr) dX dY \end{aligned} \tag{2.1}$$

where A is the effective area of the subcollimator.

So observing a distribution $B(X,Y)$ through a pair of cosine and sine collimators having the same k and θ uniquely determines a spatial Fourier component of this distribution corresponding to k and θ. A choice of (U,V) coordinates for the Fourier plane which is conjugate to (X,Y) means

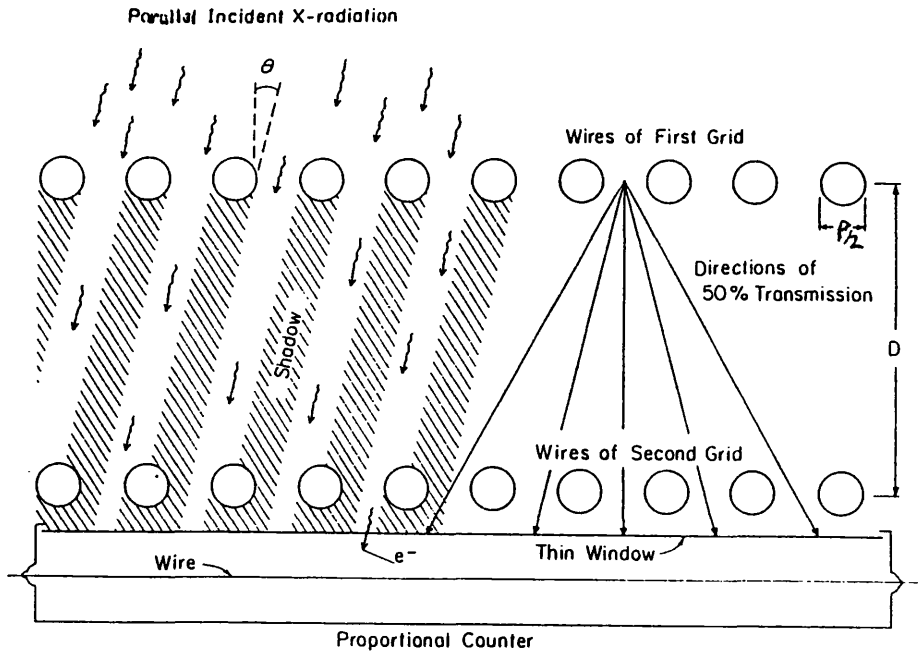

Figure 2.3: Geometry of a bigrid modulation collimator, for parallel incident radiation, taken from Bradt et al. (1968)

that a pair of cosine and sine collimators measure the complex Fourier component $b(U,V) = b_c + ib_s$, where $U = kcos\theta$ and $V = ksin\theta$. If there are a sufficient number of these cosine and sine pairs with different values of k and θ then the image, or the original distribution, can be reconstructed by inverse Fourier transform. In practice, 64 subcollimators do not provide sufficient (U,V) coverage to make this a practical option. Also, the modulation patterns, while close to being trigonometric, are triangular which also makes this an impractical solution. As a result of this the initial image synthesis procedures adopted by the HXT team were based on procedures developed by radio astronomers, e.g. CLEAN (Högbom, 1974) which is used for image reconstruction from an incomplete set of measurements; and MEM (e.g. Frieden, 1972; Gull and Daniell, 1978; Willingdale, 1981) which is used for image reconstruction with no specific requirement made on the transmission or modulation patterns. Initial procedures employed a modified version of CLEAN to synthesize dirty maps for source location, combined with MEM for the image reconstruction.

These initial simulations determined the optimum configuration of UV coverage. This was found to be $\sim$ 50 complex Fourier components. A reduction in the number of collimators reduces the quality of the synthesized images. For extended sources there is a general deterioration anyway. HXT compensates for this by replacing some of the Fourier elements at low k with fanbeam elements, whose wire width is three times the slit width. These suppress spurious sources whilst the Fourier elements give higher angular resolution.

HXT's increased performance over the hard X-ray imager on Hinotori is a result of both the precision of its grids and the increased length of the metering tube. However, the factors governing

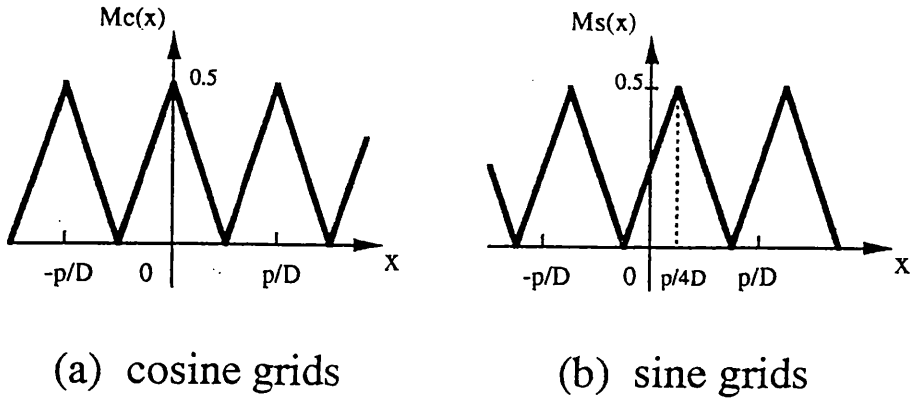

(a) cosine grids (b) sine grids

Figure 2.4: Modulation patterns for (a) cosine and (b) sine grids of HXT subcollimators, from Sakao (1994)

Energy Band	BGD count rate (cts/s/SC)
L	~ 1
M1	~ 2
M2	~ 1
H	~ 9

Table 2.2: Typical background count rates for each channel of HXT.

the image quality are rather more complicated. The most important factors are:

- the precision of the grids
- coalignment between the individual subcollimators to within 1"
- accurate modulation pattern evaluation
- 1% accuracy of the calibration and adjustment of the individual pulse height gain.

Two other important points are the arc second coalignment of the X-ray and HXA optics, and for the image synthesis itself, an appropriate choice of the background, especially for less intense flares since an inappropriate choice can result in the production of spurious sources. The typical background count rates in the four channels are, table 2.2:

It should also be noted that the above background count rates have an orbital dependence. For example, the NaI scintillators are activated during SAA passages and still have some counts even after exit. The most reliable background data is usually that taken just before or after a flare. These and other image synthesis matters are discussed further in Chapter 5.

2.5 The Bragg Crystal Spectrometer (BCS)

The BCS instrument on board *Yohkoh* provides observations at X-ray wavelengths to enable the study of plasma heating and dynamics; especially during the impulsive phase of solar flares. The

instrument itself consists of four bent germanium crystals to cover the wavelength range of the resonance line complexes of H-like FeXXVI and He-like FeXXV, CaXIX and SXV. It has a whole sun field of view and almost ten times better sensitivity than previous instruments of its kind. This increased sensitivity allows time resolution of better than 1 second to be achieved.

2.5.1 Scientific objectives

The BCS provides us with information on the high temperature ($T_e \simeq 10 - 40 \times 10^6 K$) plasma created following the impulsive energy release in solar flares. In particular BCS provides important information on plasma dynamics and heating, the 'superhot' component observed in some flares, and on the decay phase of solar flares.

Dynamics

Significant nonthermal broadening has been observed during the impulsive phase of flares, indicating mass motions with velocities up to $\sim 200 kms^{-1}$ (eg. Antonucci et al., 1992). A blue shifted component is also observed in disc flares (Doschek et al., 1980; Antonucci et al., 1982) indicating plasma upflow velocities of $> 300 kms^{-1}$. The details of the process of chromospheric evaporation may be clarified with BCS observations. There is also the suggestion of a possible hard X-ray flux nonthermal line broadening association, which can be investigated with BCS (e.g. Khan et al., 1995).

Heating and Dynamics

Significant evidence has been obtained from SMM and Hinotori that heating and turbulence occur before the impulsive phase. The increased sensitivity of BCS means that earlier reliable temperature measurements can be made to investigate this. In conjunction with SXT, much better estimates of temperature and emission measure are also available.

'Superhot' Component

Some flares have been observed where there is apparently plasma with temperatures in excess of $30 \times 10^6 K$ (Lin et al., 1981; Tanaka et al., 1982). H-like FeXXVI observations are very useful for studying plasma of this temperature and the enhanced spectral resolution of the BCS allows better time evolution of these line profiles.

Decay Phase

There is evidence for the continued energy injection during the decay phase of some flares. BCS can be used to observe the increase in height of the emitting plasma since spatial displacement translates to spectral displacement in the North-South direction, although this would not apply to limb flares. Also, line to continuum ratios taken during the flare decay phase can be used for solar elemental abundance studies.

2.5.2 Instrument design

The BCS consists of two bent crystal spectrometers, the BCS-A and BCS-B. For each spectrometer, a pair of germanium crystals diffract incoming X-rays into a single detector. These spectrometers are mounted at the front of the spacecraft on either side of the central panel, with a thermal filter in front of each. The crystal dispersion axes are oriented north-south. Rather than employing the standard method of a rotating flat crystal to provide scans in wavelength the BCS on *Yohkoh* employs four bent crystals at fixed radius so that a parallel beam of X-rays are incident at a range of Bragg angles, θ_1 to θ_2. Then the diffracted radiation at corresponding wavelengths, λ_1 to λ_2, is recorded in a 1-dimensional position sensitive proportioanl counter. Figure 2.5 illustrates the difference between the rotating flat crystal and bent crystal methods, and figure 2.6 shows how the four crystals are mounted.

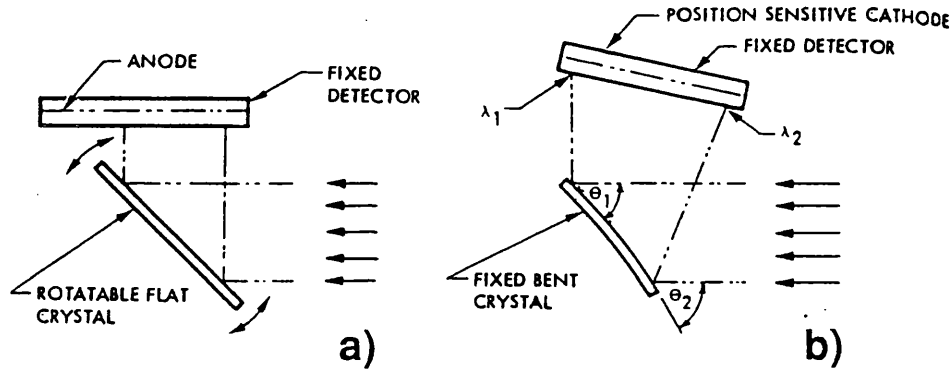

Figure 2.5: Diagram of a) a flat scanning crystal spectrometer and b) a fixed bent crystal spectrometer (from Culhane et al., 1991).

The wavelength ranges covered by the channels of the BCS are as follows:

Channel	Designed Wavelength Range (Å)	Bin Range	Lab. Measured Wavelength Range (Å)
1	1.7636 - 1.8044	212 - 28	1.7597 - 1.8121
2	1.8298 - 1.8942	224 - 36	2.8284 - 1.8957
3	3.1631 - 3.1912	27 - 229	3.1633 - 3.1933
4	5.0160 - 5.1143	40 - 234	5.0163 - 5.1143

Spectral resolution ($\lambda/\Delta\lambda$): 3000 - 8000

Angular resolution: full disc

Best time resolution: 0.125 s

Typical time resolution: 3.0 s in FLARE/HI

These wavelength ranges are only valid at the designed BCS boresight. With bent crystal

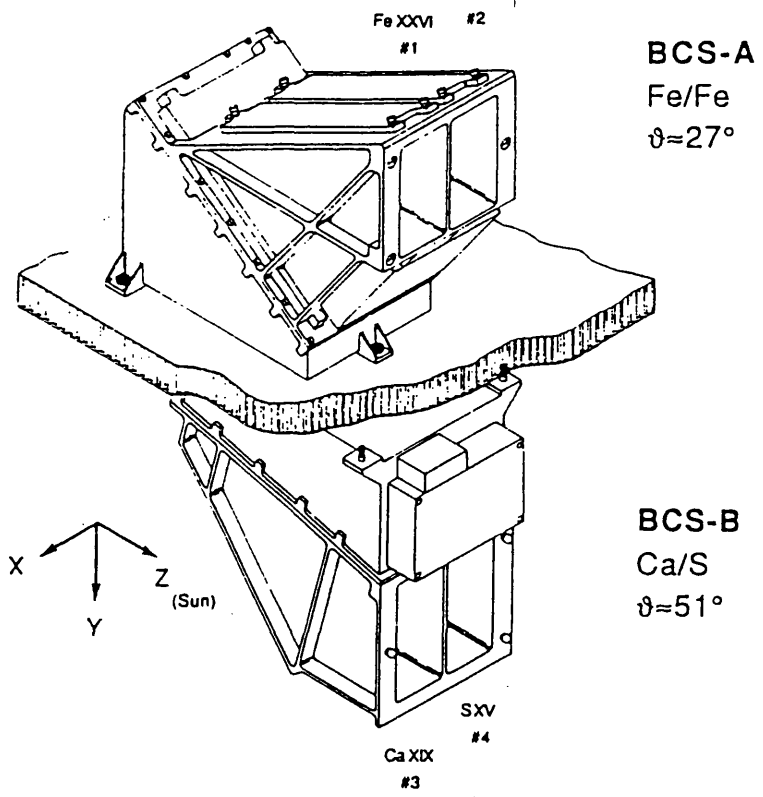

Figure 2.6: BCS detectors. Each of BCS-A and B consist of two spectrometers. BCS-A obtains Fe XXV and Fe XXVI line profiles, while BCS-B takes Ca XIX and S XV line profiles (from Culhane et al. 1991)

spectrometers observations at other than the boresight result in a shift of the observed wavelength range. Since *Yohkoh* is normally pointed several arc minutes north of its designed pointing to allow SXT better coverage of the north polar corona, channels 1 and 2 of BCS usually see wavelengths slightly shorter than intended, while channels 3 and 4 see slightly longer wavelengths. During October to January when the north pole of the Sun is tilted towards the Earth, BCS has severe problems in observing the blue wing of CaXIX for events in the southern solar hemisphere. The bin shifts caused by this pointing offset are listed in the *Yohkoh* Analysis Guide.

The resonance line complexes and the corresponding wavelength range covered by BCS are chosen to provide specific types of information. Channel 1 provides temperature and velocity information about the 'superhot' component while Channel 3 is essentially restricted to the Ca XIX resonance transition to provide velocity measurements at maximum sensitivity. However, some temperature information is available from the $n = 3$ satellite lines close to the long wavelength side of the resonance and x and y lines. Channels 2 and 4 provide a more complete coverage giving both velocity and temperature measurements.

2.5.3 Instrumental effects

The response of a particular spectrometer channel depends on several features: the transmission of the detector window, the detector linearity, the crystal curvature and the transmission of the

thermal filter. The details of the response functions for each channel of the BCS are available with the *Yohkoh* software or in Lang et al. (1993). The wavelength resolution of each channel depends on the rocking curve of that channel but also on the angle of incidence of the photons on the detector window. This effect is particularly important for the higher energy photons associated with channels 1 and 2 since these photons penetrate further into the detector volume. Photons which do not enter the window perpendicularly result in a broader positional distribution.

The dynamic range of the proportional counter used on the BCS is biased towards smaller flares so that observations can be made as early as possible during the flare. Because of this limited dynamic range large flares will cause the BCS to saturate. When this happens all positional information is lost, although the total event count may still be valid.

The analogue signals produced by the detector take a significant time to process when the count rate is high. The signal processing times of the anode and cathode, plus the time required to allow the signal to settle back down to zero amount to about $35\mu s$. During this 'deadtime' no new signals can be processed. As the count rate increases this effect becomes more important. If photon arrival times were evenly spaced then a pair of channels in one detector could see a maximum of $\sim 2.8 \times 10^5 counts/s$. In reality the number is about half this because of the random nature of the events and saturation effects.

The BCS has three counters per channel: the total event counter; the limited (in-window) event counter and the encoded event counter. The gate for the limited event counter only accepts events that fall into that energy window and also stops any event that arrived less than $35\mu s$ from the previous one. Knowledge of these event counters allows the 'correct' count rate to be reconstructed. In practice this is done using either of the analysis procedures, MK_BSC or MKBSD, within the *Yohkoh* software package.

2.5.4 Line Narrowing

In a number of large events an effect called 'line narrowing' has been observed with the BCS. When a large number of counts are put into a small length of the detector volume, a space charge effect develops which attracts the electron cloud towards that part of the detector. This results in a line that is taller and narrower than it should be, and distorts the linearity of the detector. In some cases it results in lines with widths smaller than the thermal width. Channel 4 (SXV) is particularly susceptible to this effect but it has also been observed in channels 2 (Fe XXV) and 3 (CaXIX). As a result of this effect when analyzing large events with the BCS one must consider all derived quantities, such as nonthermal velocity, to be lower limits. However, the total counts are unaffected and so temperature measurements are valid.

More detailed information on the BCS can be found in the *Yohkoh* Analysis Guide (YAG); BCS Experiment Users Guide; Culhane et al. (1991); Lang et al. (1992); Lang et al. (1993); Trow et

al. (1989) and Trow et al. (1993).

2.6 The Wide Band Spectrometer

The Wide Band Spectrometer (WBS) on board *Yohkoh* provides the opportunity for observing solar flare radiation over a range of 2 keV to 100 MeV using three spectrometers: the soft X-ray spectrometer (SXS); hard X-ray spectrometer (HXS) and gamma-ray spectrometer (GRS). In addition to these three spectrometers a radiation belt monitor (RBM) is also mounted and provides the alarm for the radiation belt passage. Cross-sectional views of the SXS, HXS and GRS instruments are shown in figure 2.7.

2.6.1 Soft X-ray spectrometer

The SXS consists of two gas filled proportional counters, SXS-1 and SXS-2, filled with Xe and CO_2 at a pressure of 1.16 atmospheres, which provide 128-channel pulse height data over the energy range 2- 30 keV every 2 seconds and 2-channel pulse count data every 0.25 seconds. The field of view of the spectrometers is about twenty times the diameter of the Sun, which means all flares on the visible hemisphere are observed. The background is controlled by an Al slit collimator. The SXS-1 counter has a large effective area making it most suitable for detecting small flares, whilt SXS-2 has a smaller effective area for the detection of large flares.

The primary output data from SXS is 128-channel pulse height data every 2 seconds in SXS-PH1 and SXS-PH2, and 2-channel pulse count data every 0.25 seconds in SXS-PC11 and 12 from SXS-1, and SXS-PC21 and 22 from SXS-2. The pulse count data from these spectrometers is used to monitor flare activity on the Sun and trigger flare mode.

2.6.2 Hard X-ray spectrometer

The HXS comprises a NaI scintillation detector optically coupled to a photomultiplier tube. This arrangement is covered with two stainless steel absorbers to suppress low energy X-ray counts. Output data is 32-channel pulse height data in the 2 - 400 keV range every 1 second (HXS-PH), and 2 channel pulse count data every 0.125 seconds (HXS-PC1 (20 - 50 keV) and HXS-PC2 (50 - 600 keV)).

The incident X-ray spectrum can be found from deconvolving the observed 32-channel energy loss spectrum using the HXS response matrix. The HXS-PC1 is also used in flare monitoring similarly to SXS.

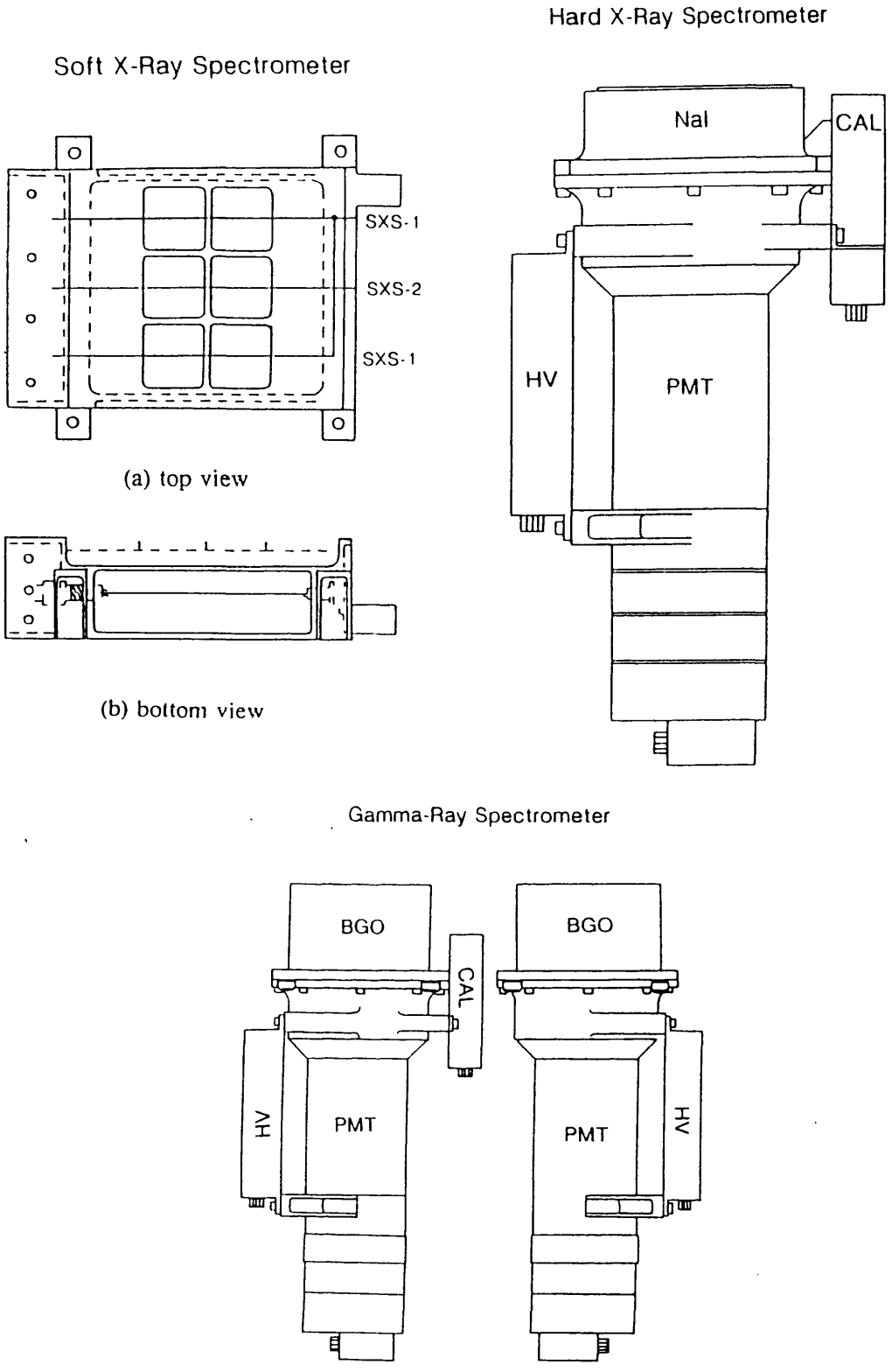

Figure 2.7: Cross-sectional view of SXS (left), HXS (centre) and GRS (right) detectors (from Yoshimori et al. 1991)

2.6.3 Gamma-ray spectrometer

The GRS consists of two identical BGO ($Bi_4Ge_3O_{12}$) scintillators optically coupled to a photomultiplier tube. Since BGO has both a high density and a high effective atomic number, the γ-ray detection sensitivity is greatly improved over previous detectors of this kind. Each scintillator is covered with thick lead to suppress low energy γ-ray events.

The primary output of GRS-L is 128-channel quadratic spaced pulse height data every 4 seconds (GRS-PHL1 and GRS-PHL2) and 4-channel pulse count data every 0.25 seconds for energies in the range 0.2 - 4 MeV and every 0.5 seconds for the range 4 -10 MeV. GRS-H produces 16-channel pulse height data every 4 seconds (GRS-PHH1 and GRS-PHH2) and 2-channel pulse count data every 0.5 seconds (GRS-PC15 and 25 for the range 8-30 MeV and GRS-PC16 and 26 for the range 30-100 MeV).

GRS also has neutron detection capabilities although it is difficult to determine the incident neutron energy from the GRS pulse height spectrum.

2.6.4 Radiation belt monitor

The radiation belt monitor comprises both an NaI scintillation detector and a Si detector, both of which are directed perpendicular to the Sun and are insensitive to both solar flare X-rays and γ-rays.

The NaI detector has an output which consists of 32-channel quadratic spaced pulse height data in the 5-300 keV range every 1 second, and 2-channel pulse count data (5-60 and 60-300 keV) every 0.25 seconds. The Si detector produces single channel pulse count data in energies above 20 keV every 0.25 seconds. When the pulse count of either of the NaI or Si detectors exceeds a certain threshold value then the alarm for the SAA radiation belt passage is sounded. Many of the high voltage supplies on the spacecraft are then switched off to prevent radiation damage.

2.6.5 γ-ray burst detection

Both HXS and the RBM NaI detectors are capable of monitoring non-solar X-ray and γ-ray bursts during solar quiet times and satellite night. When the HXS pulse count rate in the 50-600 keV range or the NaI pulse count rate in the 60-300 keV range exceed a threshold value then 32-channel pulse height data is recorded every 1 second and pulse count data every 0.25 seconds for a total of 256 seconds.

Table 2.3 below gives the relevant channel-energy relations for all of the WBS instruments.

2.7 The Soft X-ray Telescope

The soft X-ray telescope (SXT) provides a unique opportunity to image the Sun in X-rays over long time periods with high temporal and spatial resolution. The instrument itself is a glancing incidence telescope of 1.54m focal length which forms X-ray images in the 0.25-4.0 keV range on a 1024×1024 virtual phase charge coupled device (CCD). A series of thin metal filters mounted near the focal plane provide the means for gaining plasma temperature diagnostics. In addition to the X-ray telescope there is also a coaxially mounted visible light telescope to facillitate the determination of the X-ray source locations. This is called the aspect telescope. However, after just over a year of operation this ceased to function.

2.7.1 Scientific objectives

Soft X-ray images enable us to view almost directly the distribution of high temperature coronal plasma and the structure of its confining magnetic field. Studies of the evolution of coronal structures are potentially useful diagnostics of the appearance, migration and reconnection of magnetic flux. In particular they can be used to examine the following aspects:

1. the geometry of x-ray sources and the inferred magnetic topology
2. the temperature and density of the emitting plasma
3. spatial and temporal characteristics of flare energy deposition
4. the transport of high energy particles, as well as conduction fronts
5. the presence of waves or other disturbances associated with sprays, filament eruptions and coronal transients
6. location of energy release and particle acceleration

2.7.2 Instrumental properties

SXT has a dynamic range of $> 10^7$ and a time resolution of $\sim$ 2s to provide information covering the evolution of the impulsive phase. Its field of view is the whole solar disc and it is capable of angular resolution of $\sim$ 3 arc seconds, making it capable of locating flare footpoints as well as observing loop filling. Spectral diagnostic information for temperature derivations is available through the use of a series of filters mounted for the X-ray telescope, whilst the aspect telescope makes whitelight observations which are used for image alignment.

The telescope has a fixed focus and comprises a sensor, shutter, dual filter wheels and two co-aligned imaging elements: a mirror for X-rays and a lens for visible light. The position of the filter wheels determines whether an X-ray or visible light picture is taken. The same CCD detector

is used for both the optical and X-ray images. In order that the x-ray images are not contaminated by visible light, metallic filters are used to block the light from the aspect telescope.

The angular pixel size of the CCD is 2.45", which is approximately equal to the angular resolution of the X-ray and aspect telescope. The CCD subtends 42x42 minutes of arc resulting in full disk and coronal coverage in a single image.

Figure 2.8 and figure 2.9 show the optical arrangement of SXT (Tsuneta et al., 1991).

2.7.3 The X-ray telescope

X-rays are focussed by a glancing incidence mirror which uses hyperboloids of revolution for both optical surfaces to get better wide field angular resolution on a flat focal plane. The mirror employed is very short at 4.5cm, further enhancing wide field performance.

The five X-ray analysis filters are located in the rear filter wheel and are designed to produce attenuation which increases the dynamic range, and also to provide a means for temperature determination. These filters and their wavelength ranges are described below.

Instrument: Glancing incidence mirror/CCD sensor
Co-aligned optical telescope using same CCD

Wavelength range:	2.5-46 Å	no analysis filter (Noback)
	2.5-36 Å	1265 Å Al
	2.4-32 Å	2930 Å Al, 2070 Å Mg, 562 Å Mn, 190 Å C
	2.4-23 Å	2.52 micron Mg
	2.4-13 Å	11.6 micron Al
	2.3-10 Å	119 micron Be
	4600-4800 Å	Wide band optical filter
	4290-4320 Å	Narrow band optical filter

Spectral discrimination: Filters
Angular resolution: 3 arcsec
Field of view: 42x42 arcmin
Best time resolution: 0.5 sec.
Typical time resolution: 2.0 sec in FLARE, 8.0 sec in QUIET

Following the failure of an entrance filter in November 1992, the narrow band, wide band optical filters and the Noback X-ray filter became unusable.

2.7.4 The aspect telescope

The objective lens of the aspect telescope forms an image of the same scale as the X-ray image and is coaligned to $\sim$ 1 pixel. The SXT filter wheel has two optical band pass filters: a 30 Å filter

centred on the CN band at 4308 $\AA$ to observe magnetic plage and active regions, and a 140 $\AA$ filter centred at 4580 $\AA$ to give continuum images.

The primary uses for the aspect camera are as follows:

1. to obtain sunspot and limb images for SXT pointing determination to one arc second or better, and to help with image registration of ground based data.
2. to observe magnetic plage, sunspot and pore motions and also the development of active regions
3. the observation of whitelight flares
4. helioseismology
5. flat field illumination for the CCD gain calibration
6. to provide a source of blue light for photon flood of the CCD to anneal the soft X-ray degradation

2.7.5 The CCD

The CCD itself is a 1024x1024 virtual phase CCD with 18.3 μm pixels. The principal of virtual phase CCD operation is given by Hynecek (1979) and Janesick et al. (1981). The SXT camera is operated in charge collection rather than photon counting mode, and solar features can typically produce almost full well images with exposures of less than 1 second. Dark current control and gain stability are achieved by cooling the CCD to $-18°$ C. The CCD read noise is $\sim$ 85 electrons/pixel r.m.s., and at $-18°$ C the average dark current is $\sim$ 9 electrons/pixel/second. The charge transfer efficiency is 0.999989 for signals of greater than 10^4 electrons. The full well capacity of the CCD is around 250000 electrons, and at the conversion constant of 3.65 eV per electron for Si, this translates to $\sim 10^3$ 1 keV photons.

2.7.6 Response

SXT can in principle image over a temperature range of < 1 to > 50 MK. Because the solar soft X-ray spectrum is predominantly a line spectrum, the well defined absorption edges of the SXT analysis filters emphasize the detection of certain spectral lines or groups of spectral lines. This property gives basic spectral, and thus temperature, discrimination.

The dominant error in SXT photometry arises from photon statistics. A signal of 100 electrons produces an increment of one digital number from the analogue-to-digital converter (ADC), which corresponds to detecting a single photon of 34$\AA$. The 1σ readout and detector noise on a typical image is about 1 digital number. Other sources of error that should be considered when analysing

soft X-ray images from SXT are detailed in Tsuneta et al. (1991) and in the *Yohkoh* Analysis Guide.

2.7.7 Image Formats

Three types of images are transferred from the CCD to the image buffers of the data processor on *Yohkoh*. These are full frame images (FFI), partial frame images (PFI) and patrol images. A PFI is a subimage usually detailing the flaring active region. The patrol images are used by the data processor for automatic observing region selection and are not normally telemetered to the ground.

2.8 Further information

This chapter has just given a brief introduction to the *Yohkoh* satellite and data. Much more extensive information is available from Solar Physics, Volume 136, No. 1, 1991, where detailed instrument descriptions are given; and also from the *Yohkoh* Analysis Guide. The latter provides an invaluable introduction to the analysis software available.

In later chapters some of the more involved details the analysis of data from the BCS, HXT and WBS/GRS instruments are described, including the synthesis of hard X-ray images and spectral fitting over a broad wavelength range.

WBS Data	EnergyRange	High Bit Rate	Medium Bit Rate
SXS-1 PC11	(3-15keV)	0.25s	2s
PC12	(15-40keV)	0.25s	2s
SXS-PH1	128ch (3-30keV)	2s	16s
SXS-2 PC21	(3-15keV)	0.25s	2s
PC22	(15-40keV)	0.25s	2s
SXS-PH2	128 ch (3-30keV)	2s	16s
(Oct 1 1991 - June 9 1992)			
HXS-PC1	(20-65keV)	0.125s	1s
HXS-PC2	(65-657keV)	0.125s	1s
HXS-PH	32ch (20-657keV)	1s	8s
(June 9 1992 - present)			
HXS-PC1	(25-75keV)	0.125s	1s
HXS-PC2	(75-830keV)	0.125s	1s
HXS-PH	32ch (25-830keV)	1s	8s
GRS-1 PC11	(0.27-1.04MeV)	0.25s	2s
PC12	(1.04-5.47MeV)	0.25s	2s
PC13	(5.47-9.3MeV)	0.5s	4s
PC14	(9.3-13.1MeV)	0.5s	4s
PC15	(8-30MeV)	0.5s	4s
PC16	(30-100MeV)	0.5s	4s
GRS-PHL1	128ch (0.3-13.1MeV)	4s	32s
GRS-PHH1	16ch (8-100MeV)	4s	32s
GRS-2 PC21	(0.3-1.24MeV)	0.25s	2s
PC22	(1.24-5.66MeV)	0.25s	2s
PC23	(5.66-9.37MeV)	0.5s	4s
PC24	(9.37-13.68MeV)	0.5s	4s
PC25	(8-30MeV)	0.5s	4s
	PC26 (30-100MeV)	0.5	4s
GRS-PHL2	128ch (0.3-13.6MeV)	4s	32s
GRS-PHH2	16ch (8-100MeV)	4s	32s
RBM-SC-PC1	(5-50keV)	0.25s	2s
RBM-SC-PC2	(50-300keV)	0.25s	2s
RBM-PH	32ch (5-300keV)	1s	8s
RBM-SSD	(> 20keV)	0.25s	2s

Table 2.3: Channel-energy relationships for the WBS

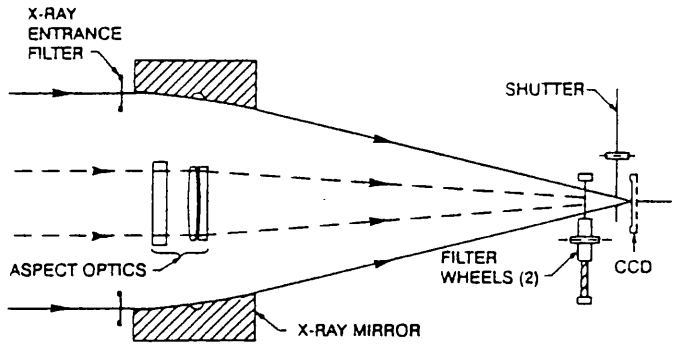

Figure 2.8: Schematic illustration of the optical concept and key elements of SXT (from Tsuneta et al., 1991).

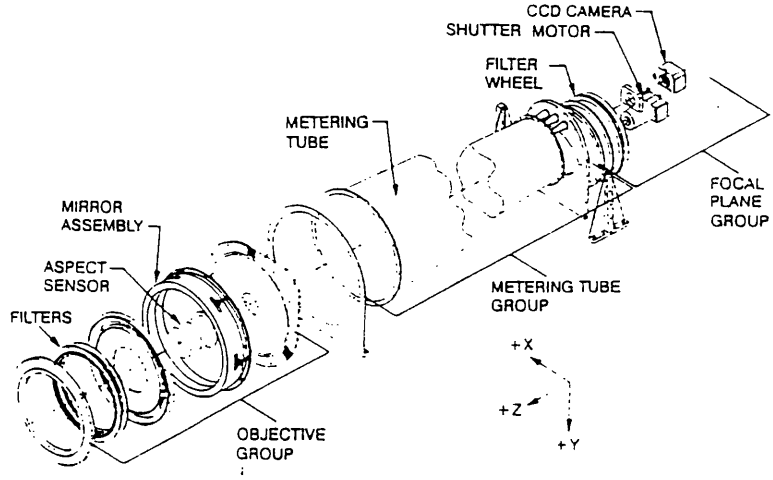

Figure 2.9: Diagram showing the design of SXT.

Chapter 3

Nonthermal Line Broadening in γ-ray Flares

3.1 Introduction

In this chapter we discuss the hypothesis that stochastic acceleration by Alfvén wave turbulence is responsible both for the acceleration of γ-ray producing protons, and for the observed nonthermal line broadening in coronal soft X-ray lines.

We begin with a general background to the subjects of nonthermal line broadening, particle acceleration and γ-ray production and move on to examine in detail, in terms of our hypothesis, the behaviour of four flares observed by SMM and one by *Yohkoh*.

3.2 Nonthermal line broadening in soft X-ray lines

The onset of soft X-ray emission during a solar flare is evidence for the formation of the high temperature thermal plasma, and it usually characterizes the gradual and decay phases of the flare. However, there is observational evidence to suggest that soft X-ray line profiles also carry impulsive phase signatures in the form of nonthermal broadenings enhanced above active region values, and significant blue-shifted emission (Antonucci et al. 1982).

Nonthermal broadenings are normally interpreted as evidence for isotropic flows or random motions within the flaring plasma, with blue shifts as the hydrodynamic response of the chromosphere to the impulsive energy release. The radiative instability caused by heating results in an expansion of chromospheric material into the lower density corona with high velocity upflows being observed. This is known as chromospheric evaporation (Antonucci et al., 1982) and the onset of these blue shifts is seen to be roughly coincident with the onset of the hard X-ray emission. However, in many

cases, the nonthermal line broadenings are observed before the blue shifts, suggesting that these occur as an immediate consequence of the initial energy release rather than as a time integrated response to secondary heating (e.g. Gabriel et al., 1981; Antonucci, 1984).

Many plausible explanations for nonthermal line broadening have been given. It has been explained by the presence of convective flows associated with the chromospheric evaporation; as the result of the superposition of emissions from convective flows observed in an arcade, where the loops have different projection angles (Doschek et al, 1986) or from an asymetrically heated loop (Cheng et al, 1984). They have also been attributed to the inherent spread of velocities in the distribution of an evaporating plasma which is not accounted for by simply fitting a two component spectrum (Emslie and Alexander, 1987). Other theories have included fluid turbulence (Bornmann, 1987), where the kinetic energy of the upflows transforms to thermal energy, and the temperature difference at sites where the evaporation occurs (De Jager, 1985).

The point to note about all of these explanations is their inability to explain the fact that the line width enhancements are often seen before the blue shifts. They are also unable to account for evidence that no further significant enhancement in broadening is observed when the convective flows are first seen.

The implication then seems to be that nonthermal line broadening is evidence for random or turbulent mass motions which seem to be related to the initial energy release. The initial enhancement is seen to be temporally correlated with the low intensity hard X-ray emission which precedes the main burst. This indicates that there may be an initial phase of particle acceleration occurring which is associated with an initial temperature increase in the soft X-ray source. At this time v_{nt} is already high and does not change appreciably when the energy release becomes impulsive, so it does not seem to be directly related to the amount of energy released.

Random plasma flows can be interpreted as a dynamic effect related to magnetic reconnection. This would particularly be the case for reconnection occurring in localized regions throughout the loop, such a picture being consistent with loops containing twisted magnetic fields caused by photospheric footpoint motions. Plasma is ejected from the reconnection regions at about the Alfvén velocity and an isotropic flow would result from the superposition of individual flows, giving rise to symmetric broadenings of soft X-ray lines. In this scenario broadening occurs simultaneously with the onset of magnetic energy dissipation in the flare region and persists for as long as the reconnection; this would make it a useful diagnostic for the reconnection process.

Usually these line widths may be characterized in terms of a nonthermal velocity, given by:

$$v_{nt} = \left[\frac{2k(T_D - T_e)}{m_i}\right]^{1/2} \tag{3.1}$$

where T_D is the doppler temperature, k is Boltzmann's constant, T_e the electron temperature and m_i the mass of the ion in question.

The presence of wave activity in the solar atmosphere is one possible cause of nonthermal line broadening, and in this chapter we consider the possible effect of the presence of Alfvén wave turbulence on observed soft X-ray line profiles.

3.3 Nonthermal line broadening by Alfvén waves

The possibility of detecting wave activity in the solar atmosphere, and particularly the presence of Alfvén waves, has been discussed by McClements et al (1991). Whilst with instruments of sufficient spatial and temporal resolution it might be possible to resolve one wavelength or one wave period of the wave, e.g. standing hydromagnetic waves in coronal loops should be observable by an instrument with spatial resolution of around one arc second, in practice the situation is complicated by the presence of a large number of normal modes. However, in principle any wave activity should have some effect on ion motions and therefore on the emission characteristics of these ions. This is true of Alfvén waves.

If the length of a coronal loop is much larger than its radius it is then reasonable to assume that the magnetic field in such a loop is predominantly toroidal, i.e. it is directed along the loop's axis. If we then consider a loop on the solar limb, lying in a plane perpendicular to the line of sight, then it is also reasonable to assume that the magnetic field in this loop is also perpendicular to the line of sight (even moderate loop twists are unstable, e.g. Spicer and Brown, 1980).

The magnetic field perturbation, $\delta\mathbf{B}$, is caused by the passage of an Alfvén wave, propagates along the magnetic field with the wave. The particle motions generated by this are hence in a direction transverse to the wave propagation, and the resultant bulk fluid velocity (Chen, 1974), is given by:

$$\mathbf{v} = \frac{\delta\mathbf{E} \times \mathbf{B}}{B^2} c \tag{3.2}$$

where $\delta\mathbf{E}$ is the electric field caused by the wave and c is the speed of light.

If the wave polarization is assumed to be random then the mean square velocity component directed towards the observer is

$$< v_{\|}^2 >= 1/2 < v^2 >= \frac{c^2}{2B^2} < \delta\mathbf{E}^2 > \tag{3.3}$$

and using the result that $< \delta\mathbf{B}^2 >= c^2/v_A^2 < \delta\mathbf{E}^2 > \gg < \delta\mathbf{E}^2 >$, we can write the energy flux associated with an Alfvén wave, Φ, as

$$\Phi = n m_p < v_{\|}^2 > v_A \tag{3.4}$$

since $c \gg v_A$ in the solar atmosphere.

The Doppler temperature, which is defined by the total width of the line, depends only on the component of of velocity towards or away from the observer. So when considering a thermally broadened line produced by an ion of mass m_i, we can write T_D as

$$kT_D = kT + m_i < v_{\|}^2 > \tag{3.5}$$

where T is the kinetic temperature. The observed line width due to this nonthermal broadening is then given by (McClements et al, 1991):

$$\frac{\Delta\lambda}{\lambda} = \frac{2}{c}\left(\frac{kT}{m_i} + \frac{2\pi^{1/2}}{(nm_p)^{1/2}B}\Phi\right)^{1/2} \tag{3.6}$$

when B is perpendicular to the line of sight. This reduces to $\frac{\Delta\lambda}{\lambda} = 2\left(\frac{kT}{m_i}\right)^{1/2}/c$ when the magnetic field is directed towards the observer, as would be the case for a loop perpendicular to the solar disk.

We should note here the assumptions made by McClements et al (1991). This analysis is only valid if the Alfvén wave is linear, which implies that the ambient magnetic field should not be significantly altered by the passage of the wave ($\delta\mathbf{B} \ll \mathbf{B}$). For the solar case this is equivalent to

$$\Phi \ll 9 \times 10^{10} \frac{B_2^3}{n_{10}^2}\ erg\ cm^{-2}\ s^{-1}$$

where $B_2 = B/100G$ and $n_{10} = n/10^{10}cm^{-3}$. Accelerating ions to the required energies in the required timescales needs fluxes of the order of $10^9\ erg\ cm^{-2}\ s^{-1}$ (Smith and Brecht, 1989; Miller et al, 1990). This value satisfies the criterion and therefore the linear assumption is valid. Also, the dispersion relation has been assumed to be linear. Given a relatively short wavelength and a uniform flaring loop this should not be a problem.

3.4 γ-ray production

The sudden release of energy in a solar flare results in the acceleration of charged particles, electrons, protons and ions. These particles then interact with the ambient solar atmosphere to produce a variety of electromagnetic radiations. Gamma rays can be produced directly by relativistic electron bremsstrahlung, or indirectly from secondary products such as neutrons, excited nuclei and π-mesons. At energies below $\sim$ 1MeV the emission is predominantly electron bremsstrahlung which has the form of a relatively featureless near power-law continuum (Ramaty and Murphy, 1987). Bremsstrahlung emission may well continue to higher energies as well, but above 1MeV the contribution from nuclear processes dominates. This emission takes the form of a nuclear continuum with weak structure and narrow lines superimposed on it (Murphy et al., 1990).

3.4.1 Observations

The first observations of γ-rays from solar flares were recorded by Chupp et al (1973, 1975) and Suri et al (1975) from the two large flares observed by OSO-7 in August 1972. From the August 4th flare γ-ray lines were detected at 0.511 MeV, 2.223 MeV, 4.439 MeV and 6.129 MeV and from the August 7th flare the positron annihilation (0.511 MeV) and neutron capture lines were recorded. These observations confirmed the theoretical predictions of the strongest observable lines from solar flares. Since then observations of π -meson decay, escaping neutrons and protons from neutron decay in interplanetary space have also been recorded.

Ramaty and Murphy (1987) summarized the conclusions of γ-ray observations to date:

1. we see γ-ray emission $\sim$ 0.3 MeV due to electron bremsstrahlung from many flares
2. nuclear line emission is well correlated with this emission
3. flares have been observed for which the γ-ray line emission and hard X-ray emission are coincident within the temporal resolution of the SMM detector ($\sim$ 2 secs)
4. broad-band γ-ray emitting sites are located predominantly near the limb
5. the observed emission is a complex spectrum with nuclear lines consistent with the energies expected from the de-excitation of the most abundant elements in the solar atmosphere

All of these facts imply that proton and relativistic electron acceleration is a common property of the impulsive energy release process in solar flares. Also, the apparent preponderance of γ-ray limb flares strongly suggests that the angular distribution of electrons in the interaction region is anisotropic (e.g. Dermer and Ramaty, 1986, Reiger et al., 1983, Reiger, 1989).

There are three dominant mechanisms responsible for the production of γ- ray line emission in the flare environment. These are nuclear de-excitation, neutron capture and positron annihilation.

Detailed studies of γ-ray production from nuclear de-excitation have been carried out by Ramaty et al. (1979), and of neutron production by Ramaty et al (1983a), Kocharov (1983), Efimov and Kocharov (1985), Murphy et al. (1987) and Hua and Lingenfelter (1987a). Such studies, together with the use of SMM, ground-based and interplanetary neutron decay proton data were used by Murphy and Ramaty (1984) to determine the energy spectrum of protons at the Sun. This study has shown that this cannot be an unbroken power law over an extended range from about 10 MeV to 1 GeV since the power law spectrum which would provide the correct normalization generally implies a time profile for neutrons which is inconsistent with the data and vice versa.

Additional constraints on the proton spectrum have been obtained through studies of neutron transport in the solar atmosphere and the production of the 2.223 MeV neutron capture line; this information has helped set limits on proton beaming and the ^3He abundance in the photosphere.

Also the variation of the ratio of the observed and calculated fluences of the de- excitation and neutron capture lines have confirmed the predicted limb darkening of the 2.223MeV line (Wang and Ramaty, 1974).

3.4.2 Interaction Models

The accelerated particles leave the acceleration region and γ-rays are produced in the interaction region. Models for the interaction region fall into two basic categories: thick and thin target.

Thick Target - In this case nuclear reactions are produced by particles as they slow down in the collisionally thick solar atmosphere. These charged particles and their spallation products thermalize and are effectively mixed back into the ambient atmosphere. The thick target interaction region is, however, optically thin to γ-rays and neutrons.

Thin Target - Here nuclear reactions are produced by escaping particles. These particles can be detected in interplanetary space. If enough of these thin target interactions occur to produce the observed γ-rays then there should also be detectable fluxes of the spallation products, ^2H, ^3H, Li, Be and B.

Thick target interactions are the most probable from several points of view (e.g. Ramaty, 1986).

1. most γ-ray producing ions remain trapped. The inferred total number of interacting protons far exceeds the number of escaping protons observed in interplanetary space (e.g. Murphy and Ramaty, 1984).

2. the escaping particles do not produce many nuclear reactions, as can be inferred from the upper limit on the ^2H in the escaping particles (McGuire et al., 1986) which in turn gives an upper limit of $\sim 0.1 gcm^{-2}$ for the amount of matter traversed by escaping particles. The nuclear line emission which would result from the estimated number of escaping particles covering $\sim 0.1 gcm^{-2}$ is very much less than that which we observe (Ramaty, 1986).

3. the bulk of secondary positrons produced remain trapped at the Sun, suggesting that all charged particles remain trapped.

The interaction region is probably the chromosphere. We can show this by considering how we might place limits on the density of the interaction region. Lower limits on the density can be set by the following methods:

- the inferred slowing down and annihilation times of positrons require that $n \geq 10^{12} cm^{-3}$ (Ramaty and Murphy, 1984)

- the inferred slowing down time of GeV protons inferred from the observed time profile of pion decay emission in the event of June 3 1982, implies that $n \geq 10^{14} cm^{-3}$

$\Rightarrow$ interaction region lies below the chromosphere-corona transition region

An upper limit on the density can also be inferred from observations of escaping neutrons, (Ramaty et al, 1983b) and is found to be $\sim 5 \times 10^{15} cm^{-3}$, corresponding to the top of the photosphere. The lack of significant attenuation of the observed neutron flux implies this density (Ramaty et al., 1983b). This limit requires that the accelerated protons and nuclei are stopped in the solar atmosphere by magnetic scattering or mirroring at column densities much smaller than their Coulomb interaction ranges in matter. The absence of a spectral break in the relativistic electron spectrum also helps constrain the density, since this limits synchrotron energy losses (Ramaty et al., 1983b).The acceleration region is probably much higher in the atmosphere since effective acceleration requires much lower ambient densities. It would be possible through γ-ray observations to differentiate between acceleration in closed loops and open magnetic structures. The former scenario would produce strong γ-ray emission with few escaping particles, whilst the latter would produce a strong interplanetary observation but weaker γ-ray emission (Ramaty and Murphy, 1987).

3.4.3 What happens in the interaction region

Accelerated protons and heavier nuclei suffer Coulomb energy losses and elastic nuclear collisions, while accelerated electrons suffer Coulomb, bremsstrahlung and synchrotron losses. The chromosphere is only partially ionized so that Coulomb losses are essentially ionization losses in a neutral medium (Ramaty and Murphy, 1987). Nuclear collisions produce secondary products such as protons, neutrons and heavier nuclei, which are also capable of producing γ-rays.

Acceleration and transport between the acceleration and interaction regions can potentially lead to significant anisotropies, viz. flares near the limb emit γ-rays more than disc flares, (e.g. Rieger et al., 1983) suggesting that the electron distribution in the interaction region is anisotropic. No such evidence for protons has been found, however, so generally the simplifying assumption that protons and nuclei are isotropic in the interaction region is applied. This would be quite plausible if they were confined by magnetic fields or isotropized by wave-particle interactions.

For most accelerated particle energy spectra, assuming photospheric abundances, the dominant neutron-producing reactions are $p-p$, $p-\alpha$ and $\alpha-\alpha$ reactions (Ramaty and Murphy, 1987). However, neutrons are also produced in α and p reactions with ^{12}C and heavier nuclei.

If we consider a stochastic acceleration spectrum, such as might be produced through turbulent acceleration, then below $\sim$ 10 MeV most of the neutrons are produced via $p-\alpha$ reactions, while at higher energies the bulk of production is due to accelerated α particles, via $\alpha-p$ and $\alpha-\alpha$ reactions (Ramaty and Murphy, 1987). For this kind of spectrum the neutron production yield is highly sensitive to the composition of the accelerated particle spectrum. A reduction in the α particle abundance relative to the proton abundance will result in a significant decrease in neutron

production (Ramaty and Murphy, 1987). For shock acceleration we find that most neutrons are produced by protons, via $p - \alpha$ at lower energies and p - p at high energies. This spectrum is not nearly as sensitive to the α/p ratio.

3.4.4 Neutron Capture

Neutrons which remain at the sun either decay or are captured through reactions such as $^1H(n,\gamma)^2H$ and $^3He(n,p)^3H$. These reactions occur in the photosphere and as a result the line produced by capture on ^1H at 2.223 MeV is strongly attenuated at the limb. Capture on ^3He is radiationless, but it does affect the time dependent flux of the 2.223 MeV line, enabling constraints to be placed on the photospheric $^3He/H$ ratio. The 2.223MeV line is very narrow ($FWHM < 100$ keV), the width being due to thermal broadening in the photosphere.

3.4.5 Positrons

Positrons are produced on the Sun mainly through the decay of radioactive β^+ emitting nuclei (eg. ^{11}C, ^{13}N, ^{15}O, ^{19}Ne), de-excitation of nuclei (^{16}O, ^{40}Ca) and the decay of π^+, all produced in interactions of accelerated protons and heavier nuclei with the ambient solar atmosphere. Pair production, although possible, is relatively unimportant in solar flares. The range of lifetimes of the β^+ emitters is very broad and consequently we find that the time dependence of the positron annihilation line at 0.511MeV is very complex. We also find that typically positrons from β^+ emitting nuclei have energies $\sim$ 1MeV, while those from π^+ decay have energies $\sim$ 30 MeV.

In the thick target scenario essentially all positrons emitted by β^+ nucei and 80% of those from π^+ decay are slowed to energies where they will either form positronium or annihilate directly after thermalization (Crannell et al, 1976). The other 20% from π^+ decay annihilate in flight at relativistic energies producing broad band emission.

Direct annihilation produces two 0.511MeV γ-rays per positron. Positronium annihilation via the singlet state (formed 25% of the time, electron spins anti-parallel) also produces two 0.511 MeV γ-ray photons. Positronium annihilation via the triplet state (formed 75% of the time, electron spins parallel) produces three photons of energies $<$ 0.511 MeV. Triplet positronium can also annihilate before it is broken up by collisions if the ambient density is less than $10^{15} cm^{-3}$. The three photon continuum can in theory be observed from solar flares. Angular distributions of both the line and the continuum radiation are essentially isotropic since they are produced after the positrons have lost most of their energy.

The number of escaping photons is characterized by a quantity called $f_{0.511}$, which we later use to determine the energy spectra of the interacting protons. If all positrons annihilate at the Sun and the 0.511 MeV line is not attenuated, then $f_{0.511}$ depends only on the fraction annihilating via positronium. $f_{0.511} = 0.5$ if they all annihilate via positronium and $f_{0.511} = 2$ if all the positrons

annihilate directly.

Laboratory measurements of positron annihilation (Brown et al, 1986) in neutral H give $f_{0.511} = 0.65$. This is particularly relevant for the solar flare case since the 0.511 MeV line is formed in the chromosphere. The width of the positron annihilation line is dependent on temperature, degree of ionization and density. The FWHM should be < 3.5 keV for $T < 10^5$K. At higher temperatures the width varies as $T^{1/2}$ with $FWHM \simeq 11$ keV at $T = 10^6$ K.

3.4.6 Nuclear De-excitation Lines

The observed narrow nuclear lines result from the interaction of accelerated protons and α particles with ambient He and heavier particles, whilst the underlying emission - very broad lines forming a continuum with weak structure - is due to accelerated C and heavier nuclei interacting with H and He. Li and Be are essentially absent from the solar atmosphere, but are produced by α particle reactions with ^4He. The line we observe at ~ 0.454MeV has an unusually large width of 100keV. This line is the result of the blending of the 0.478MeV ^7Li and 0.429MeV ^7Be lines. However, if the distribution of α particles is anisotropic then these lines are separated.

Emission in the 4-7 MeV band has been shown by Ramaty et al (1977) and Ibragimov and Kocharov (1977) to be also due primarily to nuclear de-excitation rather than primary electron bremsstrahlung. This was first demonstrated for the August 4th 1972 flare, but has been shown to be true for most flares by SMM. The fluence in this band together with that of the neutron capture line at 2.223MeV are used primarily for the calculation of the spectral shape of the initial accelerated proton distribution, as will be discussed later on. In practice, this 4-7MeV emission is nearly isotropic and therefore independent of the angular distribution of the accelerated particles.

3.5 Determination of accelerated particle spectra

Gamma-ray and neutron observations of solar flares provide us with information about the accelerated particle energy spectra in flares, as do measurements of charged particles in the interplanetary medium. Most of the neutrons and γ-rays produced in solar flares are the result of particles slowing down and thermalizing in the solar atmosphere. These then provide us with information about those particles that remain trapped at the Sun, whilst interplanetary observations give us information about the energy spectra of escaping particles.

Proton spectra can be obtained from γ-ray and neutron observations primarily by the three following methods.

1. $\frac{\Phi_{2.223}}{\Phi_{4-7}}$ fluence ratios

2. neutron energy spectra

3. $\frac{\Phi(100MeV)}{\Phi_{4.1-6.4MeV}}$ fluence ratios

We will consider each of these methods in turn.

(1) - This ratio is most sensitive to the spectrum in the 10-100 MeV range. If one considers a thick target model with a stochastic acceleration process and a photospheric α-particle/proton ratio, then αT, which characterizes the hardness of Bessel function shaped spectra arising from such an acceleration process, where α is the acceleration efficiency and T is the escape time from the region, falls in the range 0.01-0.04 (Murphy and Ramaty, 1984, Hua and Lingenfelter 1987a). Observations have shown that the variation between αT values obtained for different events is not very large. The implication of this result is that the escape time, T, from the acceleration region is probably not controlled by the spatial diffusion due to pitch angle scattering.

Now α, the acceleration efficiency, is controlled by diffusion in momentum space for a stochastic process with small energy increments, so if T were also diffusive then an increase in α would result in a corresponding increase in T, and we would see much larger variations in αT from flare to flare. If instead T were the time to damp the turbulence which accelerated the particles and if this damping was due to the particle acceleration itself, then this would imply a decrease in T resulting from an increase in α. We would then expect not much variation in αT.

(2) - Neutron energy spectra are ideally suited to probing the 50 MeV to several GeV range. Observations of the time dependence of the flux of neutrons arriving at the Earth plus measurements of the energy spectrum of protons produced as the result of neutron decay in interplanetary space provides us with information on the spectrum of neutrons at the Sun. For flares whose duration is short compared to the Sun - Earth transit time of neutrons, neutron energies may be determined from their observed arrival times.

(3) - The fluence ratio $\frac{\Phi(100MeV)}{\Phi_{4.1-6.4MeV}}$ is strongly dependent on the shape of the accelerated particle spectrum. It also describes the ratio of the number of particles in the 10-100 MeV range to the number above the pion production threshold (a few tens of MeV). Observations of the June 3rd 1982 (Ramaty et al., 1987) flare showed that the time dependences of these two fluxes are very different. Therefore, a single accelerated particle population with a time dependent energy spectrum will not fit the data. Murphy et al. (1987) proposed a model incorporating two particle populations with different interaction time histories and different, but time independent energy spectra. The first population is identified with the so-called first phase acceleration, which accelerates ions and electrons to between 10-100 keV; and the second population with the second phase acceleration, (Wild et al, 1963) where the acceleration is probably due to shocks in the corona andelectrons are accelerated to $\sim$ 1 MeV, ions to $\sim$ 1 Gev per nucleon.

3.6 Acceleration Mechanisms

The acceleration mechanisms which have received the most attention in relation to the solar flare process are stochastic and shock acceleration (see e.g. Forman et al, 1986). Acceleration in DC electric fields has also been considered (Holman, 1985; Tsuneta, 1985; Benka and Holman, 1992) and has recently been applied to the analysis of data from *Yohkoh* and *CGRO* (e.g. Zarro et al., 1995, Kosugi et al., 1994, Dennis et al., 1994).

The main requirements of any acceleration mechanism should be the ability to account for: the accelerated particle energy spectra and total numbers, the electron to proton ratios and the acceleration timescales. It should also be capable of accounting for observations such as the observed ^3He abundance and heavy element enrichment. This is a pretty tall order and as yet no completely satisfactory theory of the acceleration mechanism in solar flares exists.

The first point to realise about particle acceleration is that particles must be accelerated by electric fields. Magnetic fields do no work. The most straightforward acceleration mechanism we can consider is acceleration in an electric field parallel to the magnetic field, since a perpendicular field would just cause a drift of the particles across the magnetic field lines.

3.6.1 DC Field Acceleration

The DC electric field model has received a lot of attention recently (e.g. Holman, 1985; Tsuneta, 1985; Benka and Holman 1992: Benka and Holam, 1994). This model assumes the presence of one or more discrete current channels, consistent with the observation that flares generally occur in regions of high magnetic shear (Benka, 1994). These channels can be either sheets or filaments and are constrained in one direction - perpendicular to the magnetic field - by Ampère's law. Since the corona has a low but nevertheless non-zero resisitivity the presence of currents means that a macroscopic electric field must be present. These current channels are hotter than the ambient plasma in which they reside and dissipate energy at a rate $Q = \mathbf{J}.\mathbf{E}$ ergs cm^{-3} s^{-1}. The heated plasma then emits thermal X-rays, which can, if the temperature is high enough, extend to hard X-ray energies. At the same time electrons in the current channels which have velocities in excess of the critical velocity, $v_c = (E_D/E)^{1/2}$ (where E_D is the Dreicer field), are freely accelerated by the electric field. These runaway electrons either then emit hard X-rays in the chromosphere via thick target interactions or escape into interplanetary space along open field lines.

This model is particularly attractive in its potential for simultaneously explaining thermal and nonthermal processes in solar flares. The most important parameter in assessing the relative importance of thermal and nonthermal processes is the ratio $\epsilon = E_D/E$. An electric field with $\epsilon = 1.0$ (i.e. equal to the Dreicer field) would subject the entire thermal distribution to runaway acceleration and the model breaks down for fields of this strength (Benka, 1994). Data interpretation

suggests that $\epsilon < 0.25$ (Benka, 1994).

Benka and Holman (1994) applied this model to the flare of June 27 1980 and confirmed the hypothesis of Lin and Schwartz (1987) that the HXR emission consists of a gradual component with a series of short duration spikes superimposed on it. They showed that this gradual component was well described by using both thermal and nonthermal bremsstrahlung, coupled by the common temperature of the current channels. The thermal emission contributes most at energies $< 20 - 40$ keV and falls off exponentially at higher energies. The remaining hard X-rays are nonthermal thick target bremsstrahlung produced by runaway electrons. The spectrum of the nonthermal emission is very hard, softening at high photon energies due to the finite potential drop along the acceleration region (Benka and Holman, 1994). This softening should be observable with high spectral resolution provided that it is not obscured by some later mechanism e.g. stochastic acceleration.

This model can also make predictions about the spatial distribution of the hard X-rays with respect to energy and spectrum. If the current channels are aligned with closed magnetic structures in the corona then the heated plasma is also in the corona resulting in an extended coronal X-ray source. This source, being thermal, will be apparent only at lower photon energies and will have a soft spectrum. Runaway electrons being accelerated along the current channels will produce compact sources of nonthermal HXR emission located at the loop footpoints. If the runaway flux is too small to produce detectable thick target emission and if the thermal emission measure is large enough then we will only see the thermal emission. We see only the nonthermal footpoint emission when ϵ is high enough, or when the temperature in the current channels is too low for significant thermal HXR emission, or heat transport out of the current channels is too slow to build up a high enough emission measure (e.g. short, impulsive events).

Benka and Holman (1994) also found that the spikes superimposed on the gradual component have a spectrum consistent with simple runaway thick target emission. Isolating this emission from the gradual component shows that the spikes have a very hard spectrum with almost no evidence of thermal emission even at low energies, entirely consistent with runaway acceleration. This implies that during the brief HXR spikes additional nonthermal footpoint emission should be observed with no coincident change in the coronal thermal emission.

3.6.2 Shock Acceleration

There are basically two kinds of shock acceleration:

1. Scatter-free: In this case particles gain energy by reflection in a single shock encounter (Sonnerup, 1973)

2. Diffusive: Here particles gain energy by repeated scattering between the plasmas on either side of the shock (e.g. Axford et al, 1977)

The first method of scatter-free acceleration can increase the particle energy by around an order of magnitude if **B** is almost perpendicular to the shock normal (Ramaty and Murphy, 1987). However, only particles with speeds $\gg$ shock speed can be reflected in this case. Further acceleration requires multiple reflections, which would be possible if, say, the particles were trapped between converging shocks in a loop.

For calculations of γ-ray and neutron production the most common mechanism to be considered is diffusive acceleration at a planar quasi-parallel shock, Murphy et al (1977). The most straightforward example of this kind takes into account only losses due to convection of the particles away from the shock downstream. Then the particle density in phase space $\propto p^{-s}$, where p is the particle momentum and $s = \frac{3V}{\Delta V}$, with V the shock speed and ΔV the discontinuity in the plasma speed at the shock. s can also be described in terms of the shock compression ratio, r, viz. $s = 3r/r - 1$.

However, at the site of the impulsive energy release the magnetic field is high and the Alfvén speed is expected to exceed the velocity of mass motions and, hence, magnetoshocks will not develop (Ramaty and Mandzhavidze, 1994). On the other hand, turbulence in the region is very likely to develop.

We now turn to consider stochastic acceleration.

3.6.3 Stochastic Acceleration

Processes in turbulent plasmas which cause particles to change their energy in some random manner, with both increases and decreases in energy, lead to stochastic acceleration. It can occur as the result of resonant pitch angle scattering from Alfvén waves with wavelengths of the order of a particle gyroradius and also from interactions with magnetosonic waves whose wavelength is much greater than the particle gyroradius.

Fermi (1949) was the first person to consider stochastic acceleration as a method of accelerating cosmic rays through collisions with massive moving magnetic clouds or scattering centres. He took into account only the systematic gain in energy. Davis (1956) and Parker and Tidman (1958) went further in demonstrating the diffusive nature of the acceleration; when the random energy increments are small compared with the initial particle energy, then the acceleration process can be described in terms of a diffusion in momentum space. Davis derived the diffusion coefficient for the process considering a simplification in which the probability of gaining a fixed amount of energy was greater than losing it. Parker and Tidman (1958) instead considered the scattering centres to be randomly moving hard spheres so that a collision produced a distribution of energy changes.

Davis (1956), Tverskoi (1967) and Kulsrud and Ferrari (1971) then considered the acceleration

in the context of plasma turbulence. Here particles are accelerated by adiabatic collisions with waves of $\lambda \gg$ particle gyroradius as well as a distribution of amplitudes. To see that this process would result in a net energy gain of the particles we think about the process in thermodynamic terms. Then the energy of the particles will tend towards the mean energy density of the turbulence, and the temperature associated with hydromagnetic turbulence turns out to be quite large. Thus, on average particles will gain energy in such a process.

For turbulent interactions, then, mirroring by magnetic fluctuations is analogous to elastic scattering, but since the collisions are adiabatic $p_\perp^2/B$ is conserved. This also implies that there is a systematic gain of parallel momentum during the acceleration process. However, the result of this gain is a loss in acceleration efficiency since mirroring does not occur as the pitch angle decreases (more particles will escape through the loss cone and interact with the solar atmosphere to produce γ-rays). To offset this problem the above authors invoked rapid pitch angle scattering from short wavelength waves of unspecified origin to maintain the isotropy of the particle distribution. Melrose (1974) demonstrated that the anisotropic proton distribution resulting from acceleration by adiabatic collisions can themselves generate an isotropising level of Alfvén waves, circumventing the need for externally added waves.

3.6.4 The accelerated proton spectrum

Assuming that the turbulence is present in the flare region as a direct consequence of the primary energy release, the acceleration process in a such a model results from the interaction of the particles with the turbulent plasma waves and can essentially be regarded as a second order Fermi process, and the solution of the diffusion equation, for the case where the acceleration efficiency and the escape time, T, are independent of energy, results in a fast particle energy distribution given by a modified second order Bessel function for particle energies less than about 100MeV or so. This is characteristic of stochastic acceleration processes.

Miller at al. (1990) numerically solved the Fokker-Planck equation to obtain the accelerated proton spectrum due to stochastic acceleration. In general all stochastic acceleration can be characterized in terms of a diffusion in momentum space. For Fermi acceleration the diffusion coefficient for this process is $D(p) = \alpha p^2/3\beta$, where α is the acceleration efficiency (Ramaty, 1979, Achterberg, 1981), $\beta = v/c$ and p is the particle momentum. The Fokker-Planck and diffusion equations are equivalent descriptions of the process, but the Fokker-Planck equation more readily displays both the diffusive and convective nature of stochastic acceleration. With this approach the convection and the diffusion of the particles can be characterized by coefficients which can be directly related to the general form of the diffusion coefficient for Fermi acceleration, $D(p)$. However, these coefficients have a time independent form and by adopting these Miller at al (1990) neglect the fact that energy is lost from the turbulence in accelerating the particles, and hence that the turbulence

evolves.

MacKinnon (1991) considered the production of fast particles via Alfvén mode turbulence in which the turbulent energy density is allowed to decline as the particle energy increases, i.e. time dependence of the momentum diffusion coefficient is included. In his analysis he assumed that the proton distribution is isotropic, that the acceleration region is homogeneous and that spatial variations and escape may be neglected. The first of these assumptions is commonly made and is justifiable since rapid pitch angle scattering is required for effective acceleration by fast mode turbulence, and it automatically accompanies turbulence in the Alfvén mode. Secondly, if this isotropising pitch angle scattering is very rapid, then transport is likely to be in the form of spatial diffusion and escape would then be relatively unimportant. Smith (1990) demonstrated that this was the case for solar flares.

However, the diffusion equation alone represents only half the picture, in the sense that it does not take into account wave evolution. Livshits and Tsytovich (1970), Tsytovich (1972) and Smith and Brecht (1989) have shown that the statistical properties of the turbulence will alter in time due to both particle acceleration and nonlinear effects, such as scattering on the polarization clouds of ions. By allowing the magnitude of the diffusion coefficient to decline with time, MacKinnon (1991) was able to include the evolution of the turbulence.

While it is assumed that the turbulence loses energy only to particle acceleration, it is necessary to appeal to the domination of such nonlinear effects as described above over particle acceleration in order to separate the time and wavenumber dependences of D. The scattering of waves on the polarization clouds of ions has the following effects (Livshits and Tsytovich, 1970, Smith and Brecht, 1989): energy in a particular wave mode is transferred from one part of the wavenumber spectrum to another, and energy is transferred between the Alfvén and fast modes (Alfvén turbulence is rapidly isotropised). Energy is ultimately transferred to parts of the wavenumber spectrum where damping is effective. Despite this, the energy lost is at most comparable with the energy lost due to particle acceleration (Smith and Brecht, 1989), and even if these losses are neglected we do not obtain order of magnitude errors in the acceleration region parameters. Hence, nonlinear effects dominate in the determination of the form of the turbulence but do not introduce large additional energy losses. So, the form of the wavenumber spectrum stays fairly constant in time while the total turbulent energy density changes, and $D(p,t)$ is separable in momentum and time. An analytic solution for the fast particle distribution function, $f(p,\tau)$ and subsequently the energy density is then possible (MaKinnon, 1991) viz.,

$$f(p,\tau) = \frac{n_0}{(3-\delta)p_0^3\tau}\bar{p}^{-\delta/2}exp\left[-\frac{\bar{p}^{(3-\delta)}-1}{(3-\delta)^2\tau}\right]I_m\left(\frac{2}{(3-\delta)^2\tau}\bar{p}^{(3-\delta)/2}\right) \tag{3.7}$$

3.7 Particle acceleration and nonthermal line broadening

MacKinnon (1991) and Alexander and MacKinnon (1993), in conjunction with the results of McClements et al (1991), have both considered the possible association of the temporal development of the MHD wave energy density, governed by the particle acceleration process, with the behaviour of the observed nonthermal component in soft X-ray line profiles. Soft X-ray line profiles observed during the impulsive phase of solar flares are found to have widths far in excess of the thermal widths expected from the measured electron temperatures (cf. Grineva et al., 1973; Doschek et al., 1979; Antonucci et al., 1982; Tanaka et al., 1982). In fact, maximum nonthermal velocities of order 100-200kms^{-1} are typical at the flare onset. For many flares there is evidence that the nonthermal line broadening is associated with the initial energy release and the initial appearance of energetic particles (Gabriel et al., 1981; Antonucci, 1984). For this type of events, we find that the degree of nonthermal broadening remains fairly constant from the onset phase to the impulsive phase, suggesting that the process responsible for the nonthermal component is a direct consequence of the flare initialisation rather than an indirect response to subsequent flare heating or dynamics.

As discussed above, McClements et al (1991) demonstrated that the presence of a significant flux of Alfvén waves is capable of producing significant Doppler velocities in coronal soft X-ray line profiles. Here we consider the possibility that this flux of Alfvén waves is responsible both for the acceleration of γ-ray producing protons and the observed nonthermal line broadening in soft X-rays. If this were the case then as the wave flux diminishes through losses to particle acceleration we should observe a corresponding decay of the measured nonthermal velocities in soft X-rays. This was demonstrated qualitatively by Alexander and MacKinnon (1993) for the flare of June 29 1980, and in this chapter we analyse in detail four flares which exhibited nuclear line spectra detected by SMM/GRS and also showed coincident soft X-ray spectra. The number of these events is restricted both by the small number of relevant γ-ray analyses that have been published, and also because of the failure of the SMM pointing between late 1980 and early 1984. Consequently, we found only four flares recorded by SMM which had well studied γ-ray emission and significant emission in soft X-rays. However, in the section 3.11 we will look at some similar events observed by Yohkoh, performing both the γ-ray and soft X-ray analysis prior to model testing.

The events considered first though are the Cycle 21 events of June 21 and July 1 1980, and the Cycle 22 events of December 16 1988 and March 6 1989.

3.7.1 Gamma-ray flare analysis

Murphy and Ramaty (1985) and Hua and Lingenfelter (1987a), demonstrated that the spectral form of the incident protons can be determined from the ratios of the fluences in various γ-ray lines, and the total number of interacting protons may be inferred from the fluence in any particular

nuclear line. Typically, we find that $\sim 10^{32}$ protons are accelerated to energies as high as 1GeV during a solar flare (Ramaty and Murphy, 1987).

The spectral shape of the proton spectrum inferred from line ratios is model dependent, i.e. it depends heavily on the model of particle acceleration assumed. Here, we use γ-ray analyses based on the assumption of stochastic acceleration models. These spectra then have the characteristic Bessel function shape viz.,

$$N_p(E) \propto K_2 \left[2(3p/m_p c\alpha T)^{1/2}\right] \tag{3.8}$$

with corresponding 'hardness' parameter αT (Ramaty and Murphy, 1987). The ratio of the observed fluences, $F_{2.223}/F_{4-7}$ and $F_{0.511}/F_{4-7}$, for a specific event, can then be used to infer a value for αT, and once the spectral shape is determined the individual γ-ray line intensities can be used to obtain the total number of interacting protons, N_p.

In some of these analyses the ratio F_{π^o}/F_{4-7} was used to determine the spectral form. In this case the data came from the GRS High Energy matrix of the GRS. The High Energy Matrix covers an energy loss range of about 10-100 MeV, compared to the 0.3 to 9 MeV range covered by the γ-ray detector.

Neutral pion emission has the form of a strongly Doppler broadened feature which is sensitive to accelerated protons above $\sim$ 300 MeV. The nuclear de-excitation lines and the π^o decay emission are prompt, production being essentially instantaneous from interactions of the energetic ions with the solar atmosphere. However, the neutron capture line at 2.223 MeV is delayed. This line is produced after thermalization and capture, with a timescale of $\sim$ 100 s (Prince et al, 1983, Hua and Lingenfelter, 1987b) and so the time behaviour of the 2.223MeV line must be modelled in order to find the fluence of 2.223 MeV γ-rays that is to be associated with a given burst of nuclear de-excitation radiation. Dunphy and Chupp (1992) have modelled this time behaviour with a single time constant (cf. Prince et al., 1983) and consequently the inferred αT from the $F_{2.223}/F_{4-7}$ ratio properly accounts for the neutron capture time delay.

Of the γ-ray events for which there are published results only four displayed significant soft X-ray emission detectable by the BCS. This is primarily due to the failure of the satellite pointing between November 1980 and April 1984. The events we use in the present analysis are the Cycle 21 flares of June 21 1980 and July 1 1980 and the Cycle 22 flares of December 16 1988 and March 6 1989. Analyses for these events have been carried out by several authors. Since the inferred spectral parameters, αT and N_p, where N_p denotes $N_p(> 30MeV)$, are model dependent we find that different values have been obtained by different authors for the same event depending on the model assumptions made. For example, different compositions of the accelerated and ambient particles (Ramaty et al, 1993) or different angular distributions of the injected protons (Hua and Lingenfelter, 1987a) can result in order of magnitude differences in the inferred values of N_p. We

consider all the inferred values of αT and N_p in our analysis.

3.7.2 The events

June 21 1980

The flare of June 21 1980 occurred on the solar limb, W90 N20 - heliocentric angle 89°, with γ-ray emission beginning at ~0118UT. This was an X3/1B class flare associated with active region 2502. The γ-ray emission lasted for over 60s and exhibited >10MeV emission as well as nuclear lines.

July 1 1980

The flare of July 1 1980 was produced by active region 2544 at W38 S12 on the solar disk, heliocentric angle 41°. The γ-ray emission, both lines and >10MeV, began at ~1627UT and lasted 66s with overlapping soft X-ray observations with a peak CaXIX count rate of 2603 c/s in the BCS. This was an X2/1B flare.

December 16 1988

The X4.7/1B flare of December 16 1988 began at ~0830UT in the GRS. It was produced by active region 5278 located at E33 N27 on the solar disk, corresponding to a heliocentric angle of 43°. This flare was one of the most intense above 10MeV seen by the GRS with >10MeV emission lasting some 24 minutes. The peak CaXIX count rate in the BCS was 8210 c/s.

March 6 1989

Active region 5395 was visible on the solar disk between March 6 and March 19 1989 during which time it produced 11 GOES X-class flares and numerous smaller flares. The first of these X-class events was an X15/3B flare on March 6 at ~1350UT located at E69 N35 on the solar disk (heliocentric angle 77°). The γ-ray emission from this event lasted almost two hours and was in the form of several distinct phases of emission (see Rieger and Marschhäuser, 1990). The BCS emission covering the main phases of emission showed a peak CaXIX count rate of 7989 c/s.

The Cycle 22 events discussed above displayed very long duration γ-ray emission with significant time structure in the emission. In fact, seven distinct periods of emission have been identified (Rieger and Marschhäuser, 1990) for the event of March 6 1989. In this study we wish only to consider a potential correspondence between particle acceleration and soft X-ray line widths during the short period (<1 min) after the initial energy release. After this time the nonthermal line broadening is strongly affected, if not in fact dominated, by the hydrodynamic motions of the flaring plasma induced by the deposition of energy released in the flare initialisation. This makes it difficult to isolate the effects due to the presence of Alfvén waves and consequently we confine ouselves to considering only the initial impulsive phases of these flares (cf. Alexander, Dunphy and MacKinnon, 1994).

The values of the spectral parameters for each of these events are shown in Table 3.1 where we use the calculations of several authors. For the events of June 21 1980 and July 1 1980 we have used the results of Murphy and Ramaty (1985) and those of Ramaty et al. (1993). In the latter work the authors determined the γ-ray parameters under the assumption of two different particle compositions. Composition 1 assumes that both the ambient (target) particles and the accelerated (incident) particles have a photospheric composition derived by Anders and Grevesse (1989). Composition 2 assumes the elemental abundances derived for the flare of April 27 1981 by Murphy et al. (1991). This analysis gave different ambient and accelerated compositions. For the events of December 16 1988 and March 6 1989, we have taken the $F_{2.223}/F_{4-7}$ ratios for the relevant time periods correcting for the production time of the 2.223MeV line (P. Dunphy - private communication), and used the results of Hua and Lingenfelter (1987a) and Murphy and Ramaty (1985) to derive αT and N_p values. These are shown in Table 3.1. Hua and Lingenfelter (1987a) considered distinct cases of proton injection; downward ($\theta = 0^o$), horizontal ($\theta = 89^o$) and isotropic. The downward injection results did not differ significantly for the values of interest relevant here and so we only consider the two cases of horizontal and isotropic injection (see also Alexander, Dunphy and MacKinnon, 1994). The published values of αT and N_p for these events (Ramaty et al.,1993) are not appropriate here since these results are based on the calculations of Dunphy and Chupp (1991, 1992), who concentrated on the times of peak π^o production in the SMM/GRS High Energy Matrix in each of these events. Neither of these time periods coincided with the initial impulsive phase in the respective events. The derived numbers for each event will be used in succeeding sections to derive the temporal behaviour of the Alfvén turbulence, assumed in this analysis to be responsible for the acceleration of the γ-ray producing protons.

3.8 Decay of wave energy density

As discussed above, McClements et al (1991) showed that the presence of Alfvén waves in the solar atmosphere can be inferred from their effect on soft X-ray lines. The passage of an Alfvén wave causes a magnetic field perturbation which in turn generates a bulk fluid velocity of the ambient plasma particles. The line-of-sight component of this velocity manifests itself as an excess Doppler width in the soft X-ray emission lines and the nonthermal energy in these lines due to the wave turbulence is found to be directly proportional to the Alfvén wave flux, Φ, viz.

$$v_{nt}^2 = \frac{4\pi^{1/2}}{(nm_p)^{1/2}B}\Phi = \frac{2}{nm_p}W \tag{3.9}$$

where v_{nt} is the non-thermal velocity, n is the ambient solar plasma density and B its magnetic field, $\Phi = W \times v_A$ is the total wave flux with W the wave energy density and v_A the Alfvén speed

Using observations obtained by the Bent Crystal Spectrometer (BCS) on board SMM we can examine the temporal behaviour of the nonthermal velocity component of these lines (cf. Antonucci,

Event	αT	N_p	Reference	Spectrum #
Jun 21 1980	0.022 ± 0.007	$6.1 \pm 1.2 \times 10^{32}$	1	1
	$\sim$0.025	$\sim 7.2 \times 10^{32}$	2	2
	0.012	2.5×10^{32}	3[a]	3
	0.013	4.2×10^{31}	3[b]	4
Jul 1 1980	0.032 ± 0.007	$2.2 \pm 0.8 \times 10^{31}$	1	5
	0.025 ± 0.006	$\sim 2.8 \times 10^{31}$	2	6
	0.019	10^{31}	3[a]	7
	0.021	1.6×10^{30}	3[b]	8
Dec 16 1988	0.020	1.1×10^{32}	4[a]	9
	0.035	5.7×10^{31}	4[b]	10
Mar 6 1989	0.011	3.73×10^{32}	4[a]	11
	0.015	3.5×10^{32}	4[b]	12

Table 3.1: Spectral parameters inferred from γ-ray emission for the solar flare events discussed in the text. The references used are (1) Hua and Lingenfelter, 1987a (2) Murphy and Ramaty, 1985 (3) Ramaty et al., 1993, a:-composition 1, b:-composition 2 (4) The present work, a: isotropic injection, b: horizontal injection (see text)

1989; Saba and Strong, 1991). The BCS instrument on SMM had eight channels which are each sensitive to emission from a different soft X-ray line sequence, measurements being made with a time resolution of 0.128s (Acton et al, 1980). For this analysis we are particularly interested in Channels 1 and 4 which cover the CaXIX (3.165-3.226Å) and FeXXV (1.843-1.896Å) line sequences, respectively. The temperature over any integration time (normally >6s for reasonable photon statistics) is determined from the ratio of the flux in a dielectronic recombination satellite line to that in the resonance line (Gabriel et al., 1972). This temperature is the electron temperature which is then implicitly set equal to the ion temperature. Typically, the BCS samples plasma at temperatures $> 10^7$K. Having determined the temperature, in principle it is a simple matter to obtain the non-thermal component in the line profiles, i.e. the excess width remaining after subtracting the thermal component, $(kT/m)^{1/2}$, where m is the mass of the ion. However, The BCS instrument on *SMM* had a very wide collimator which means that if the flare size is large in the crystal dispersion direction there will be additional line width due to this factor. This is almost certainly important for those flares considered in this analysis, since inevitably those flares which produce substantial γ-ray emission are large. Since the effect of the flare size has not been calculated here, we must assume the nonthermal velocities calculated here to be upper limits. These observations show that the nonthermal velocity is already close to its maximum when the soft X-ray emission is first detected with statistically significant count rates (Antonucci, 1989). Although the BCS requires the plasma to be heated to $\sim 10^7$K in order to emit in the appropriate soft X-ray lines and this heating takes a certain amount of time, these observations suggest that the source of the nonthermal line broadening is present at, or soon after, flare onset. There is also some

evidence that the nonthermal line broadening is associated with the initial appearance of energetic particles (Gabriel et al., 1981). One possible source of the nonthermal line broadening could be the bulk velocity associated with a flux of Alfvén waves as discussed above. Since we might expect a degree of MHD wave turbulence at the onset of a solar flare (Mandzhavidze and Ramaty, 1993), it is worth investigating the contention that the energetic protons and nonthermally broadened soft X-ray lines are caused by the same physical phenomenon, namely Alfvén wave propagation.

The stochastic acceleration of particles in the presence of Alfvén wave turbulence can be described as a diffusion of the particles in momentum space, i.e.

$$\frac{\partial f}{\partial t} = \frac{1}{p^2}\frac{\partial}{\partial p}\left(Dp^2\frac{\partial f}{\partial p}\right) \tag{3.10}$$

where p is the particle momentum, f(p,t) is the particle distribution function (particles per unit volume in phase space) and D(p,t) is the diffusion coefficient obtained from the statistical properties of the turbulence via quasi-linear theory (Melrose, 1974). The form of D(p,t) is model dependent and usually taken to be time independent. For Alfvén wave turbulence, which may be regarded as a second order Fermi process, we find that D(p) = $\alpha p^2/3\beta$ where v=βc is the particle velocity and the acceleration efficiency $\alpha = \frac{3\pi}{64}\frac{v_A^2}{c}(k_{min})E_A$, where E_A is the total wave energy density in units of the energy density of the ambient magnetic field ($E_A = 8\pi W/B^2$) and k_{min} is the minimum wavenumber associated with the turbulent acceleration (cf. Miller, Guessoum and Ramaty, 1990).

In obtaining the diffusion equation $f(p,t)$ has been assumed to be isotropic, the acceleration region to be homogeneous and escape from the region has been neglected. The validity of these assumptions was discussed above.

MacKinnon (1991) considered the consequences of injecting the turbulent energy density impulsively at $t = 0$ and allowing the magnitude of the diffusion coefficient to decline with time as energy is lost to particle acceleration. Now, we have shown that we may separate the diffusion coefficient in momentum and time by appealing to nonlinear effects, and if we also assume that all of the turbulence is in the Alfvén mode and has an isotropic wavenumber spectrum of the form $k^{-\delta}$, then the diffusion coefficient is given by (cf. Miller and Ramaty, 1989b),

$$D(p,t) = D_0 W(t) p^{n-1} \tag{3.11}$$

where D_0 is a numerical constant involving the ambient solar parameters, $D_0 = 2.65 \times 10^{-9} B/n$, and k_{min}, and W(t) is the total wave energy density of the turbulence. Although MacKinnon (1991) considered arbitrary values of δ we consider only the case $\delta = 2$, for Fermi acceleration. The problem is then tractable analytically.

We follow MacKinnon's (1991) analysis in allowing the turbulent energy density, W, to decline monotonically from some initial value, W_0, at time $t = 0$, until the pitch angle scattering time equals the loop transit time and the particles precipitate to the chromosphere producing significant

γ-ray emission. The particle acceleration is then described by the diffusion equation, the equation for the diffusion coefficient, and the initial condition,

$$f(p, t = 0) = \frac{n_0}{p^2}\delta(p - p_0) \tag{3.12}$$

where n_0 is the fast proton density and δ is the Dirac delta function, p_0 is the initial proton momentum (note that $p_0 \geq m_p v_A$ is necessary for a proton to interact with the turbulence).

MacKinnon (1991) solved the diffusion equation to obtain the particle distribution function

$$f(p, \tau) = \frac{n_0}{(3-\delta)p_0^3\tau}\bar{p}^{-\delta/2}exp\left[-\frac{\bar{p}^{(3-\delta)}-1}{(3-\delta)^2\tau}\right]I_m\left(\frac{2}{(3-\delta)^2\tau}\bar{p}^{(3-\delta)/2}\right) \tag{3.13}$$

where $\bar{p} = p/p_0$, p_0 is the initial proton momentum, n_0 is the fast proton density, I_m is the Bessel function of imaginary argument of order m [here m=δ/(3-δ)] and τ is a dimensionless quantity which characterises the hardness of the proton spectrum;

$$\tau = \frac{1}{W_0}\int_0^{\frac{D_0 W_0}{p_0}t} W(t')dt' \tag{3.14}$$

Then the value of τ attained when effective acceleration ceases must be capable of accounting for the observed γ-ray emission.

3.8.1 Turbulent Energy Density

To determine the evolution of the total turbulent energy density, W(t), we appeal to energy conservation. Since we assume that losses are dominated by particle acceleration we have

$$W + T = W_0 + T_0 \tag{3.15}$$

where

$$T(\tau) = \int \frac{p^2}{2m_p}f(p, \tau)p^2dp \tag{3.16}$$

is the fast proton energy density and $T_0 = n_0 p_0^2/2m_p$ is the initial fast proton energy density. Note that this is only appropriate if we assume that there are no further additional sources of wave generation after the time $t = 0$. We are therefore, in effect, ignoring the details of the wave generation as the event evolves. We justify this from the point of view that we are only interested in the decay of the nonthermal line broadening and observations typically show that as soon as photon statistics are good enough to obtain spectra, v_{nt} is already very high. Since the observations are not sensitive enough to provide information on the rise phase of the flare we assume that all the waves have been produced by the time the observations start, and that energy conservation is valid. Then substituting for $f(p, \tau)$ in equation 3.13, after a little reduction we find that

$$T(\tau) = T_0[12\tau^2 + 8\tau + 1] \tag{3.17}$$

Now, to find the hardest spectrum available - i.e. the value of τ when effective acceleration ceases- we put $W = 0$ into our equation of energy conservation (eqn. 3.15), and introduce the quantity $R_0 = W_0/T_0$ which, with the definition of T_0, results in an expression for the wave energy density at t=0, namely

$$W_0 = \frac{\nu B^2}{8\pi} R_0 \tag{3.18}$$

where we have assumed that $p_0 = m_p v_A$ (i.e. the minimum possible) and $\nu = n_0/n$ is the fraction of all protons in the volume with energies high enough to be accelerated by the Alfvén waves. Gamma ray line observations yield the total number of protons accelerated, N_p, see section 3.7.1, and so we have $n_0 = N_p/V$ where V is the volume of the acceleration region, and consequently

$$\nu = N_p/Vn \tag{3.19}$$

The value τ_∞ denotes the value of τ corresponding to the hardest spectrum available, i.e when effective acceleration has ceased.

$$\tau_\infty = \frac{1}{3}\left[(1 + \frac{3R_0}{4})^{1/2} - 1\right] \tag{3.20}$$

We also have that $W/W_0 \propto d\tau/dt$ and consequently we find

$$\frac{\tau}{\tau_\infty} = \frac{(\tau_\infty + 2/3)(e^x - 1)}{\tau_\infty + (\tau_\infty + 2/3)e^x} \tag{3.21}$$

where $x = 24(\tau_\infty + 1/3)D_0 W_0 t/p_0 R_0$. Thus, knowing τ_∞, we can determine the time dependence of the wave energy density through equation 3.17 and the conservation of energy. Knowledge of the number of particles required to give the observed γ-ray line fluences then normalises the wave energy density to the volume of the acceleration region via equation 3.18. Wave energy densities in excess of $\simeq 2$ ergs cm^{-3} are necessary for sufficient acceleration to take place (Miller and Ramaty, 1987).

When we obtained the proton spectral parameters given by the γ-ray line fluence ratios we used the calculations of several authors (Murphy, Dermer and Ramaty, 1987; Hua and Lingenfelter, 1987a; Ramaty et al., 1993), all of whom assumed an injected proton spectrum of the form

$$N_p(E) \propto K_2\left[2(3p/m_p c\alpha T)^{1/2}\right] \tag{3.22}$$

where α is the acceleration efficiency, T is the particle escape time and K_2 is the modified second order Bessel function. This model assumes that the particle scatterers are hard spheres and is a steady state calculation; the calculation performed by MacKinnon (1991) is time-dependent and this explains the difference in the resultant spectral form. However, the γ-ray line fluence ratios give a value for the 'hardness' parameter of the spectrum, αT, which characterizes the slope of the proton energy distribution. If we then calculate the slope of this spectrum over the energy range from 10-100 MeV and also calculate the spectrum obtained from the scattering of Alfvén

waves over the same energy range for a particular value of αT then we can obtain a value for τ_∞ which produces the same average slope. It is then a straightforward matter to interpolate for any new value of αT. We should note here that the τ_∞-αT relationship is sensitive to the ambient magnetic field and plasma density through the dependence of f(p,τ) on the initial proton momentum, $p_0 = m_p v_A$. Once we have inferred a value for τ_∞ from the γ-ray observations the time dependence of the wave energy density can be calculated from eqn. 3.17, eqn. 3.18 and eqn. 3.20, where W_0 is given by the number of accelerated protons, which we also get from the observations, and the assumed volume of the acceleration region.

Figure 3.1 shows the wave energy density decays derived from the γ-ray observations for the event of June 21 1980. Here each curve represents the wave energy density decay for each set of spectral parameters, αT and N_p inferred by the different authors (Hua and Lingenfelter, 1987a; Murphy and Ramaty, 1984; Ramaty et al., 1993); these are detailed in Table 3.1. In all of these cases we have assumed $B = 100G$, $n = 10^{10} cm^{-3}$ and $V = 10^{27} cm^3$ for the ambient flare parameters. We can see clearly from this figure the differences in the details of the decay for differing spectral parameters. Typically, it appears that the larger the number of energetic protons required to account for the observed γ-ray emission, the faster the decay of the wave energy density. Also, from this graph we see that the wave decay profiles for parameter sets of $(\alpha T, N_p)$ do not differ significantly for small differences in these values. Spectra 3 and 4, however, give very different decays. This is not too surprising since Ramaty et al. (1993) obtain significantly lower values for αT and N_p than previous studies. These authors use more updated nuclear de-excitation cross-sections (Murphy et al., 1991) than the other works quoted and consider different ambient and accelerated elemental abundances. This yields softer Bessel function spectra, and higher theoretical intensities for any given αT yielding much lower values for N_p.

We see that high values of N_p give high initial values of the wave energy density, W_0, as well as steep decays. It appears that the lower the value of N_p the longer the e-folding time. This result is mainly due to the dependence of W_0 on N_p, as we can see in equation 3.18. There is also an αT dependence in W_0 through R_0 but we can see from figure 3.1 that the dependence on N_p is much stronger. Given the similarity of the results obtained for references 1 and 2 in Table 3.1 for the June 21 1980 event, from now on we will take the results of Murphy and Ramaty (1985) (reference 2 in Table 3.1), as being typical of these decays.

3.9 Comparison with soft X-ray emission

The γ-ray events that we have considered here all displayed significant soft X-ray line emission in the BCS. The soft X-ray data for these events was analysed by Alexander (Alexander and Matthews, 1994) using the software provided by the SMM Data Analysis Center at Goddard

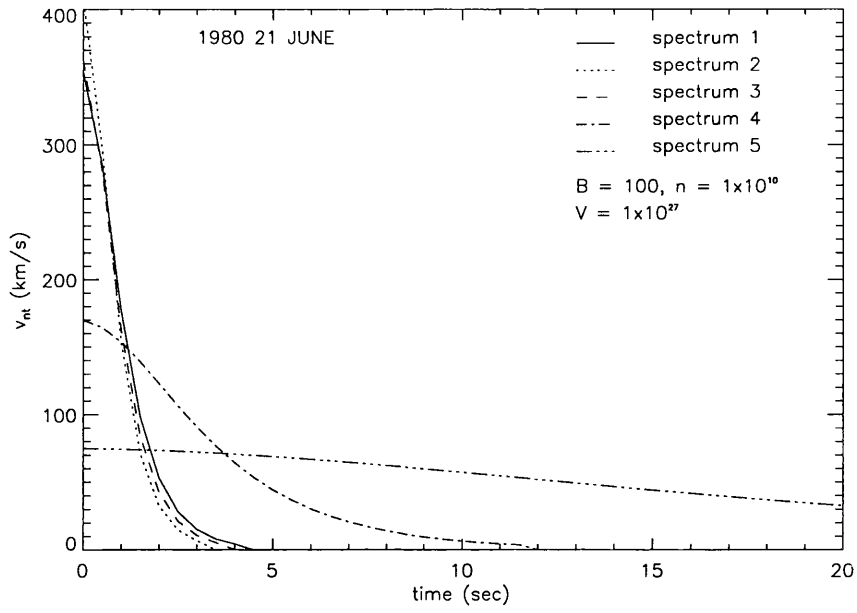

Figure 3.1: The temporal behaviour of the Alfvén wave energy density, in terms of v_{nt}, for the event of June 21 1980. All of the decays illustrated have been calculated for an ambient magnetic field of 100G, density $10^{10} cm^{-3}$, and acceleration region volume of $10^{27} cm^{-3}$. The spectrum numbers are those given in Table 3.1.

Space Flight Center. The evolution of the nonthermal velocity recorded in the Ca XIX and FeXXV channels are shown for each event we have considered in figures 3.2 - fig. 3.8. The integration times used to produce these figures were minimized to 6s at the expense of photon statistics in order that we could see clearly the initial decline in the nonthermal broadening. It is quite clear from these figures that there is a slight ion dependence in the nonthermal width, indicating a possible temperature dependency of the broadening process. This is not what you would expect to see from the simple Alfvén wave broadening mechanism we are considering. However, to determine v_{nt} from the soft X-ray line profiles we must first subtract the thermal contribution $(kT/m)^{1/2}$. Now, temperatures derived from line ratios are ion dependent, since these ions sample on average different temperature plasmas, and are also subject to uncertainties which depend on several factors, including inaccuracies in our understanding of the atomic physics (cf. Doschek et al, 1986). So, we cannot definitely say that the derived nonthermal velocities show a clear and systematic physical ion dependence. When we look at data from the Yohkoh BCS instrument, which has a wider ion coverage, in section 3.11 we will be able to clarify this point a little further.

To compare the soft X-ray decays with the decay of the wave energy density we assume that the peak of the nonthermal velocity corresponds to $t = 0$ in the γ-ray decays. From eqn. 3.13, eqn. 3.14, eqn. 3.17 and eqn. 3.18 we see that there are three intrinsic flare parameters which determine the details of the nonthermal velocity decay, viz., the magnetic field, B, the plasma density, n, and the volume of the acceleration region, V. The magnetic field and plasma density determine the initial

momentum, p_0, which determines the shape of the fast proton energy distribution, while V acts as a scaling parameter via the fast particle number density (see equation 3.19). In the analysis which follows we allow all three of these parameters to vary and compare the nonthermal velocity decays obtained with the SMM/BCS velocity data. We perform a χ^2 fit to the data minimising with respect to the parameter set (B, n, V),

$$\chi^2_{min} = min \sum_i \frac{\left(v_{nt}^{ji} - v_{nt}^{0i}\right)^2}{\sigma_i^2} \tag{3.23}$$

where j runs over all the calculated velocities with varying (B, n, V), i=1,i_{max} corresponds to the data times of interest, v_{nt}^{ji} are the calculated decay curves, v_{nt}^{0i} are the observed non-thermal velocities and σ_i represents the errors in these values. Here we have allowed i_{max} to vary between each event, which explains the large event-to-event variation in the quoted χ^2-values (see figures 3.2-3.8). By performing such a χ^2 fit we have assumed that the decay of the Alfvén wave energy density inferred from the γ-ray observations is the sole cause of the development of the nonthermal line broadening in the soft X-ray lines. From this point of view how effective the model is at explaining the observations is then determined by the values of B, n and V needed to relate the two emissions within the assumptions of the model.

Allowing i_{max} to vary from event to event is necessary because after the first 30s or so following the initial energy release hydrodynamic effects will dominate over other mechanisms in determining the excess line widths (Emslie and Alexander, 1987) and we can then no longer claim that the temporal evolution we see is a result of the wave energy density decay. In fact in all the events that we have considered there is an initial steep decay of the nonthermal broadening over a period of about 30-40 seconds followed by a rise to a roughly steady value. Our model cannot explain this observed increase in v_{nt}, and so our attention is restricted to the initial steep decay and we assume that it is the emergence of these predominant hydrodynamic effects which are responsible for the details of the v_{nt} evolution after this time.

Separating the relative effects of the magnetic field and plasma density on the development of the wave decays is complicated by the fact that both are required to define the initial proton momentum, $p_0 = m_p v_A$ and the initial momentum affects the time behaviour in a rather complicated manner as shown by equation 3.13 for the particle distribution function. Variations in the volume of the acceleration region also make a complicated contribution through equation 3.21. It is straightforward to see how these three parameters would affect the initial wave energy density, W_0. From equation 3.9 and eqn. 3.18 we see that

$$v_{nt,0} \propto B\sqrt{\frac{N_p R_0}{V n^3}} \tag{3.24}$$

Now, N_p is just the total number of accelerated particles which is independent of B, n and V. R_0, however, is proportional to τ_∞^2 (for large R_0) and τ_∞ is determined from a comparison between

equation 3.13 and eqn. 3.22 at different energies, i.e. the slope of the accelerated proton spectrum. Because of the form of the proton energy distribution in this work (equation 3.13) we note that approximately $\tau_\infty \propto p_0^{-1} \propto n^{1/2}B^{-1}$ (the exponential term dominates the distribution since the momenta considered in the ratios are much greater than p_0). That is, if p_0 increases, the value of τ_∞ implied by the value of αT, for a particular event, should decrease proportionately. Thus, we find that, for $\tau_\infty >> 1$,

$$v_{nt,0} \propto \frac{1}{n\sqrt{V}} \tag{3.25}$$

and consequently the peak value of the nonthermal velocity does not depend too critically on the magnetic field. Thus the peak nonthermal velocity is inversely proportional to both the ambient plasma density and the square root of the volume of the acceleration region. We can get a feel for the time dependence by considering equation 3.21 with a constant volume and assuming that $\tau_\infty >> 1$. Applying a similar approach to that above we determine

$$\tau \simeq \frac{(e^{at}-1)}{(e^{at}+1)\tau_\infty} \propto \frac{\sqrt{n}}{B} \tag{3.26}$$

where a is a constant in which we have applied $\tau_\infty \propto n^{1/2}B^{-1}$. Thus, from equation 3.26 we see that increasing the plasma density will tend to increase τ and consequently increase the decay rate (equation 3.17) while an increase in the magnetic field tends to produce slower decays.

We have solved equations 3.13-eqn. 3.22 using the γ-ray data detailed in Table 3.1 and determined the best fit values to the data using eqn. 3.23. The resulting nonthermal velocity decays for the different γ-ray spectra are shown superimposed upon the data in Figures 3.2 - fig. 3.8 with the best-fit parameter values quoted. Our results are summarised in Table 3.2.

We can see from Figures 3.2 -fig. 3.8 that the initial decays of the non-thermal line broadening can be reproduced by a suitable choice of parameters. In all cases the best fit decays were obtained with the plasma density, n$\leq 10^{10}cm^{-3}$, suggesting that our model is only valid when the flaring plasma is relatively diffuse, $\sim$ few $\times 10^9 cm^{-3}$. If any acceleration process is to be efficient enough to produce the large numbers of energetic ions required by the observed γ-ray emission on fast enough timescales, the coronal plasma density must be reasonably low (Forman, Ramaty and Zweibel, 1986). The low densities would also be consistent with our assumption of neglecting hydrodynamic effects during the initial decline of the nonthermal velocity, which would tend to produce a more dense coronal volume due to the upflow of large quantities of plasma.

We can see that the flare of June 21 1980 requires large volumes implying that the whole coronal loop would have to be involved in the acceleration process, if this model is to provide the observed nonthermal line broadening and its decay. For efficient acceleration to take place throughout such large volumes would be difficult to justify. The CaXIX data for this event are, however, quite noisy and this may be the cause of the unreasonably large volumes attained. In addition, the γ-ray

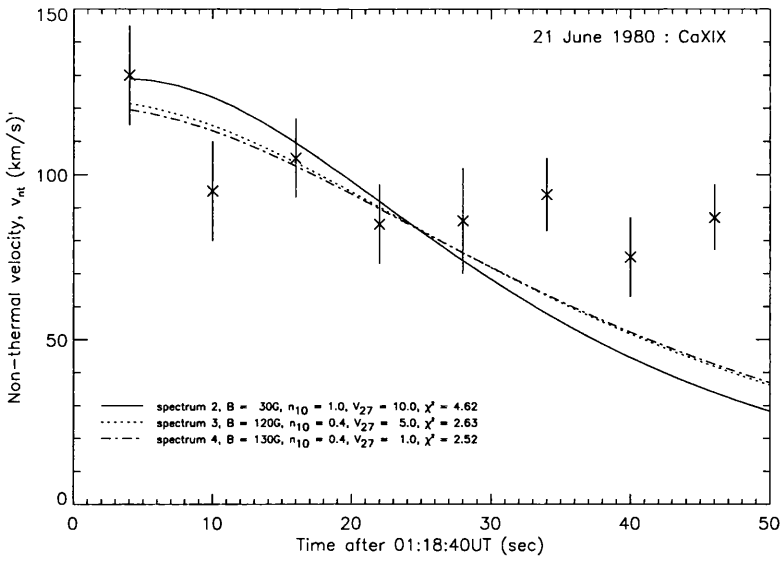

Figure 3.2: Nonthermal line broadening observed in the Ca XIX line for the event of June 21 1980. The best-fit calculated temporal behaviour for each γ-ray parameter set is superimposed on the data and the derived ambient parameters are quoted together with the χ^2 value of the fit. Again the spectrum numbers correspond to those in Table 3.1.

parameters inferred for this flare by Murphy and Ramaty (1985) yield a best fit magnetic field of $30G$ which is somewhat lower than what would be expected for the flaring solar corona. The more recent γ-ray analysis of Ramaty et al. (1993) produce physically reasonable magnetic fields and plasma densities and it should be noted that there is little to differentiate between the results obtained for composition 1 and composition 2 models.

In contrast to the June event, the other Cycle 21 flare, that of July 1 1980, yields best fit acceleration region volumes significantly lower than the typical flare volume assumed ($10^{27}cm^3$). There is a degree of discrepancy between the CaXIX results and those of FeXXV but this may be due to the rather noisy CaXIX decay, presumably caused by errors in the temperature determination, see Figure 3.3. For this flare we again see that the values of αT and N_p determined by Murphy and Ramaty (1985) result in the requirement of too low a magnetic field. In the case of the nonthermal decays observed in FeXXV we note that there is a distinct difference between the different compositions discussed by Ramaty et al. (1993). The composition 1 model yields a magnetic field of $35G$ coupled to an acceleration region volume of $10^{26}cm^3$. On the other hand, the composition 2 model yields a more reasonable magnetic field, $100G$, coupled to an extremely low acceleration region volume of $3 \times 10^{25}cm^3$. Such a low volume would require the ratio of fast particles to ambient particles, $\nu = N_p/nV = 10^{-5}$, where we have used the inferred values of N_p, n and V from Tables 3.1 and 3.2. This is a fairly typical value for γ-ray flares (MacKinnon, 1991) and in this particular case the small volume is compensated for by the fact that only some 10^{30} protons are required to produce the γ-ray emission for the assumed ambient and accelerated

Event	Spectrum #	CaXIX			FeXXV		
		$< B >$	$< n >$	$< V >$	$< B >$	$< n >$	$< V >$
Jun 21 1980	2	30	10^{10}	10^{28}	-	-	-
	3	120	4×10^{9}	5×10^{27}	-	-	-
	4	130	4×10^{9}	10^{27}	-	-	-
Jul 1 1980	6	30	10^{10}	6×10^{26}	75	5×10^{9}	5×10^{26}
	7	130	4×10^{9}	3×10^{26}	35	7×10^{9}	10^{26}
	8	160	4×10^{9}	10^{26}	100	4×10^{9}	3×10^{25}
Dec 16 1988	9	30	6×10^{9}	9×10^{26}	30	7×10^{9}	10^{27}
	10	35	6×10^{9}	8×10^{26}	50	6×10^{9}	10^{27}
Mar 6 1989	11	25	4×10^{9}	2×10^{27}	10	5×10^{9}	8×10^{26}
	12	60	3×10^{9}	3×10^{27}	60	2×10^{9}	2×10^{27}

Table 3.2: Best fit parameters in cgs units for each of the events discussed in the text. The spectrum # corresponds to those designated in Table 3.1.

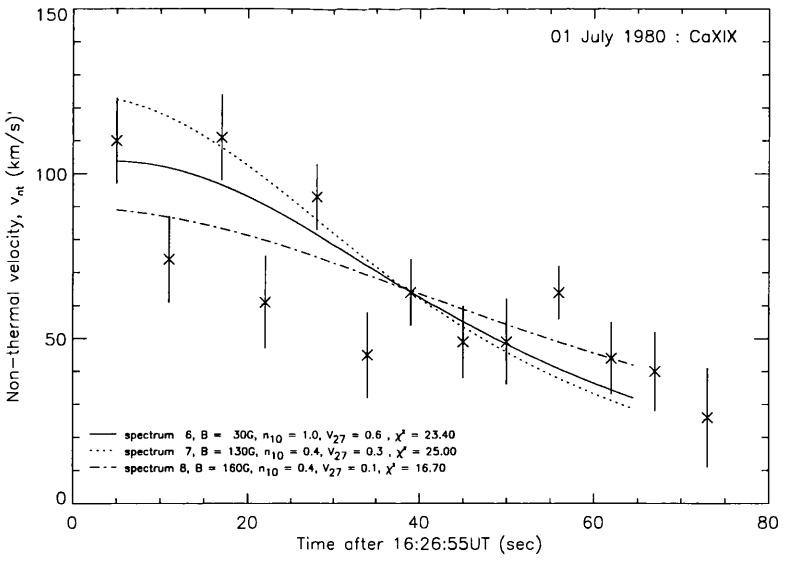

Figure 3.3: As Figure 3.2 for the nonthermal line broadening observed in Ca XIX for the event of July 1 1980.

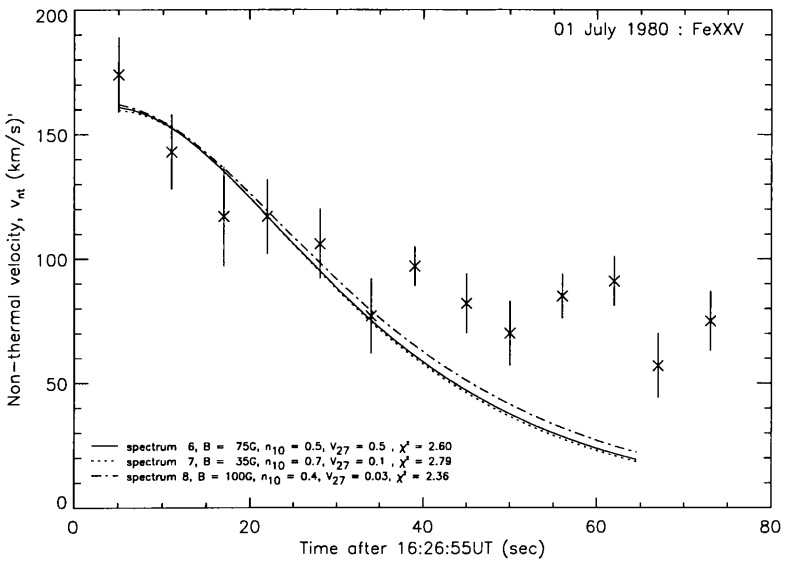

Figure 3.4: As Figure 3.2 for the nonthermal line broadening observed in Fe XXV for the event of July 1 1980.

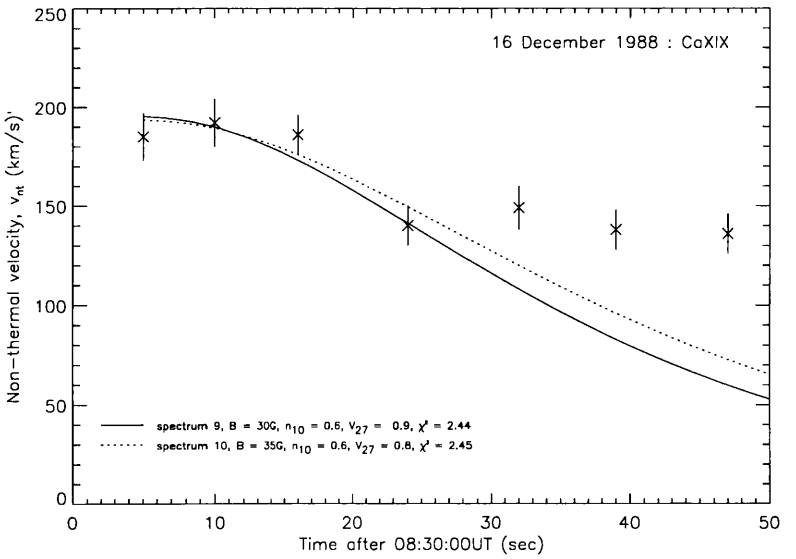

Figure 3.5: As Figure 3.2 for the nonthermal line broadening observed in Ca XIX for the event of December 16 1988.

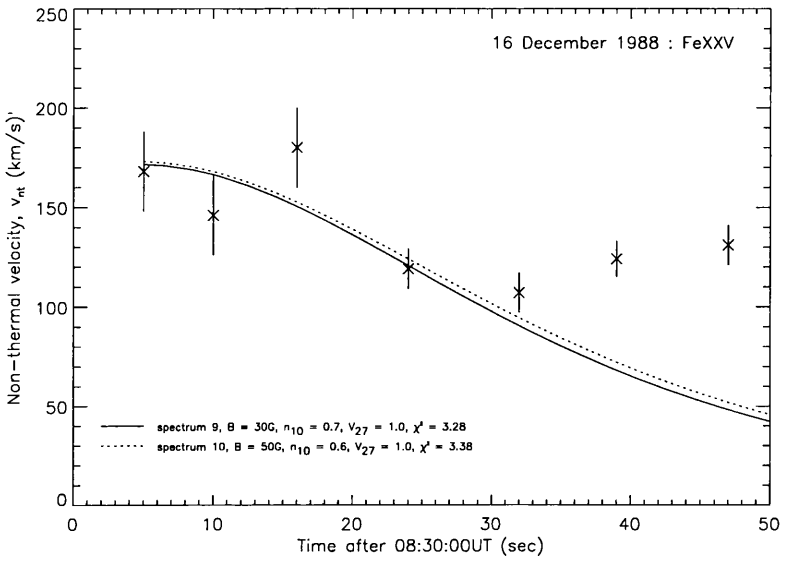

Figure 3.6: As Figure 3.2 for the nonthermal line broadening observed in Fe XXV for the event of December 16 1988.

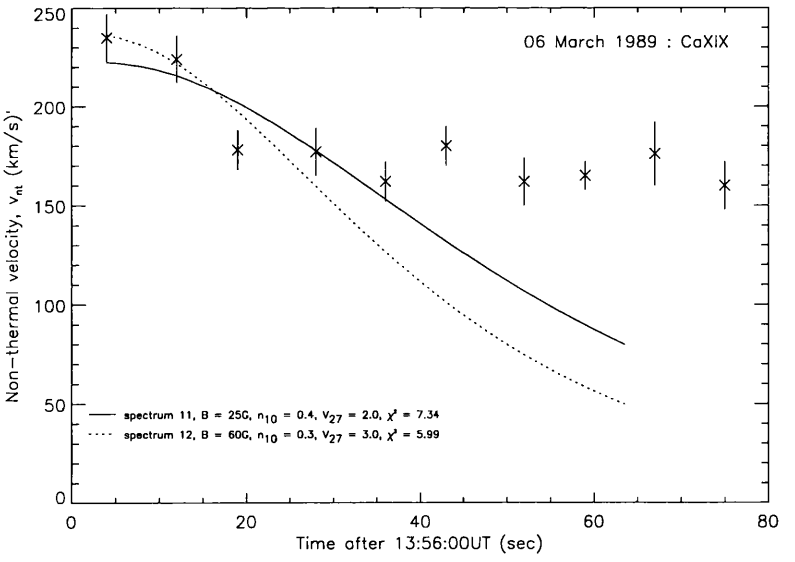

Figure 3.7: As Figure 3.2 for the nonthermal line broadening observed in Ca XIX for the first impulsive phase of the event of March 6 1989 (see Rieger and Marschhäuser, 1990).

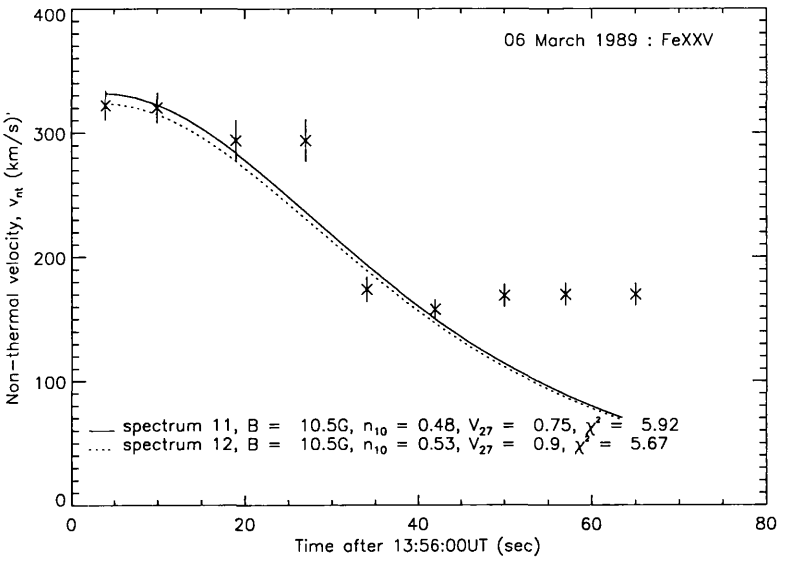

Figure 3.8: As Figure 3.2 for the nonthermal line broadening observed in Fe XXV for the first impulsive phase of the event of March 6 1989 (see Rieger and Marschhäuser, 1990).

particle compositions.

The Cycle 22 events of December 16 1988 and March 6 1989, show no significant Ca-Fe variation in the best fit parameters in contrast with the event of July 1 1980 discussed above. In addition, the horizontal and isotropic injection models adopted, which are used to provide αT and N_p, give similar results. In the case of March 6 1989, this is due to the fact that the γ-ray line ratios for either of the assumed injection models yield roughly the same αT and N_p. In all cases the inferred magnetic field values are very much lower than what might be expected in the flaring corona. However, **B** is lower near currents sheets, which also occupy a small volume. This would be fairly consistent with the results from the composition 1 model of Ramaty et al. (1993).

3.10 Summary of SMM Results

The idea that a direct correlation exists between the onset of solar flares and the observed nonthermal line broadening is interesting in that it would imply a relationship between the production of energetic particles and the details of the thermal emission. In this chapter we have looked at a number of γ-ray flares in order to examine this possibility. In particular we have looked at the possibility that the popularly invoked model of particle acceleration due to the presence of MHD turbulence (Miller, Guessoum and Ramaty, 1990; MacKinnon, 1991) might also be responsible for the nonthermal line broadening that we observe in soft X-ray lines. To enable us to compare the evolution of the wave turbulence with nonthermal velocity decays we appealed to the conservation of energy, assuming that losses were due only to particle acceleration. This treatment is described

in detail by Alexander and MacKinnon (1993), and they obtained analytic results relating the temporal development of the wave flux with the decay of the nonthermal line broadening observed in the soft X-ray profiles. McClements, Harrison and Alexander (1991) demonstrated that the presence of a significant energy density of Alfvén waves can produce Doppler velocities in the emitting ions which would be detectable as excess line widths in the soft X-ray observations. Here we have considered four flare events which were observed by both the SMM/GRS and BCS instruments. The small number of such events limits our conclusions but does allow a reasonable test of our assumed model.

We used the results of several authors to determine the relevant γ-ray parameters; N_p - the total number of protons accelerated to energies greater than 30MeV, αT - a measure of the proton energy distribution. The proton spectrum, resulting from the Alfvén wave acceleration model used here is significantly different from that used by other authors and so we had to find some way of obtaining the 'equivalent' spectral shape appropriate for the stochastic acceleration by wave turbulence rather than from hard spheres. We did this by choosing the spectral parameter, τ (equation 3.14), to yield the same average slope over the proton energy range 10-100MeV as the distribution functions adopted by Ramaty and collaborators (equation (3.19)). Once the appropriate γ-ray parameters were determined, (τ_∞, N_p), the wave energy density decays could be calculated. The temporal development of the turbulence then determined the decay of the nonthermal line broadening to be compared with the soft X-ray observations. To compare the calculated decays with the decay of the observed soft X-ray nonthermal velocities, we let three parameters vary, namely, the coronal magnetic field, the coronal plasma density and the volume of the acceleration region. When we did this we found that it was possible to obtain reasonable fits to the data for the short time period that we were interested in, so the possibility that there is a correlation between the physical processes responsible for energetic γ-ray emission and those responsible for the considerably less energetic thermal processes indeed exists. In all cases considered, low coronal plasma densities were required and in the more acceptable cases, low acceleration region volumes were obtained. Both of these conditions would be favourable for the rapid and efficient acceleration of a significant number of protons to γ-ray emitting energies. Also, the small volumes, compared to the total flare volume could explain the rather low **B** values we find as being those near a neutral sheet. However, when calculating the nonthermal velocity we have implicitly set the ion temperature equal to the electron tempertaure. While at higher densities (e.g. $n \sim 10^{11}$ cm^{-3}) this would be quite reasonable since the ion-electron equilibrium time is of the order of a second (Spitzer, 1962), densities as low as those implied by this model (a few $\times 10^9$ cm^{-3}) suggest equilibrium times on the order of a few hundred seconds. This is difficult to reconcile.

Many possible mechanisms for broadening soft X-ray line profiles in excess of the thermal widths have been proposed and we discussed some of these briefly at the beginning of the chapter. In

particular, the superposition of directed flow velocities along the line of sight, e.g. chromospheric evaporation (Antonucci, 1989), would produce lines with substantial widths (Emslie and Alexander, 1987). However, it is clear that in such events there is a strong stationary component in the line profiles (McClements and Alexander, 1989; Doschek et al., 1992) suggesting that a significant proportion of the plasma is at a velocity below 100 kms^{-1}. A typical hydrodynamical timescale for the loops considered here is of the order of 30s or so and it is reasonable, therefore, to suggest that hydrodynamical effects will not be important on timescales much shorter than this. Indeed, it is apparent for all of the events considered that the initial steep decline of the non-thermal broadening, lasting some 20-30s, is followed by an enhancement in the excess widths (Figure 3.2-fig. 3.8). This cannot be explained by the simple model proposed here -i.e. impulsive creation of waves only at the event onset- since it would require an additional generation of wave turbulence. We, therefore, appeal to the emerging dominance of hydrodynamic effects on these timescales to explain the development of excess line widths.

While the simplified model that we have considered here has shown us that it is possible for a self-consistent model of MHD turbulence to explain the very diverse phenomena of γ-ray production and soft X-ray line broadening, it is important to realise its limitations. The application of energy conservation to determine the transfer of energy from waves to particles, while a basic physical tenet, is important to emphasise in this context. In most particle acceleration models involving MHD turbulence an infinite reservoir of waves is assumed with a time-independent diffusion coefficient (e.g. Miller and Ramaty, 1989; Miller, Guessoum and Ramaty, 1990) and this ignores the fact that the turbulence will evolve.

3.11 *Yohkoh* Observations

Potentially, observations from the *Yohkoh* mission provide a much larger data set for testing our model as well as a wider ion coverage enabling the temperature dependence of the nonthermal velocity component to be studied. Indeed, *Yohkoh* has observed several γ-ray flares for which there is coincident soft X-ray data from the BCS instrument. However, there appear to have been no γ-ray events recorded since January 1992 (Kosugi, 1994), and to date published analyses of only three events: October 27 1991; November 15 1991 and December 3 1991, exist (Yoshimori et al., 1994; Kawabate et al., 1994). In the case of the October 27 1991 the BCS had not yet been switched on and so there is no coincident soft X-ray data for this event; and for December 3 1991 the analysis shows (Yoshimori et al., 1994) this event to be electron dominated with no significant nuclear line emission. So, without embarking on extensive analysis of further γ-ray events observed by *Yohkoh* (see Chap. 6) we are left with the event of November 15 1991.

November 15 1991

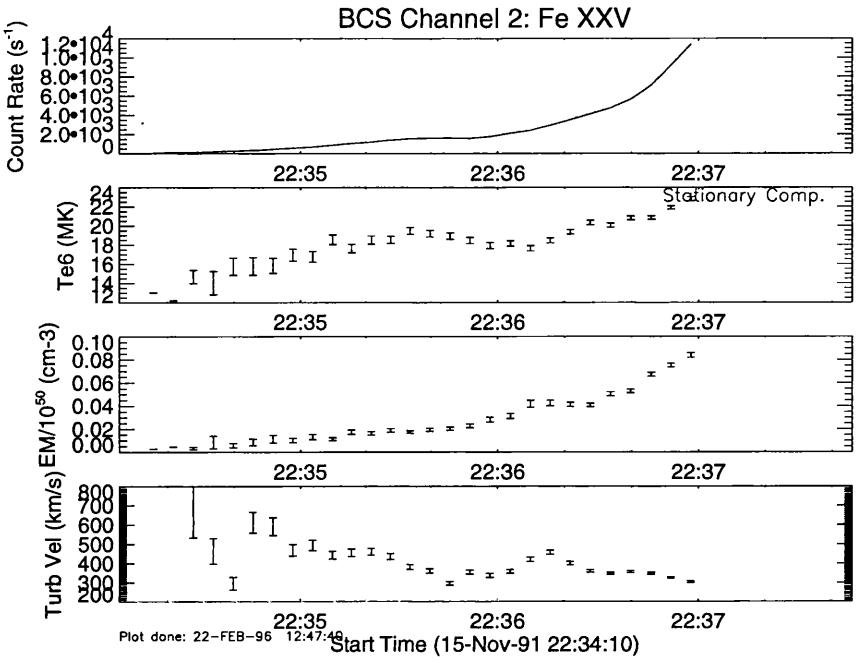

Figure 3.9: Count rate, temperature, emission measure and nonthermal velocity evolution in Fe XXV for the event of November 15 1991.

This event was a *GOES* class X1.5 event which occurred in NOAA active region 6919 (S14W19). The event began $\sim$ 22 : 34 : 50 UT, and the BCS saturated after 22:37 UT, when the main hard X-ray burst began (Culhane et al., 1993). The *Yohkoh* hard X-ray and γ-ray spectrometers first detected this flare at 22:37 UT. Gamma-ray emission in the 4-7 MeV band started to become enhanced at 22:37:32 UT, attained a maximum at 22:37:52 UT, and lasted until 22:38:00 UT. The emission in the 418-472 keV band showed similar temporal variations (Kawabata et al., 1994). The positron annihilation line at 0.511 MeV was also detected from this flare (Kawabata et al., 1994). It showed similar characteristics to the 4-7 MeV and 413-478 keV bands before the peak time ($\sim$ 22 : 37 : 50 UT) but more gradual behaviour after this.

Soft X-ray data for this event from channels 2 (Fe XXV), 3 (Ca XIX) and 4 (S XV) of the BCS were analysed from $\sim$ 22 : 34 UT until $\sim$ 22 : 37 UT using software from the *Yohkoh* data analysis package (Morrison, 1994). The integration times were 6s in the case of Fe XXV and S XV and 7s for Ca XIX. In doing this we trade off the ability to examine closely the initial decline of the nonthermal velocity against better photon statistics. Fig. 3.9, fig. 3.10 and fig. 3.11 show plots of the total count rate, temperature, emission measure and nonthermal velocities derived from Fe XXV, Ca XIX and S XV spectra respectively.

We can see from these figures that it appears that the peak of the nonthermal velocity occurs at around 22:34:30 UT in the Ca XIX and Fe XXV channels, and significantly before that in S XV. This is significantly before the first enhancement in the γ-ray emission is seen at $\sim$ 22 : 37 : 30 UT. In our previous analyses of SMM data we assumed that the peak of the nonthermal velocity

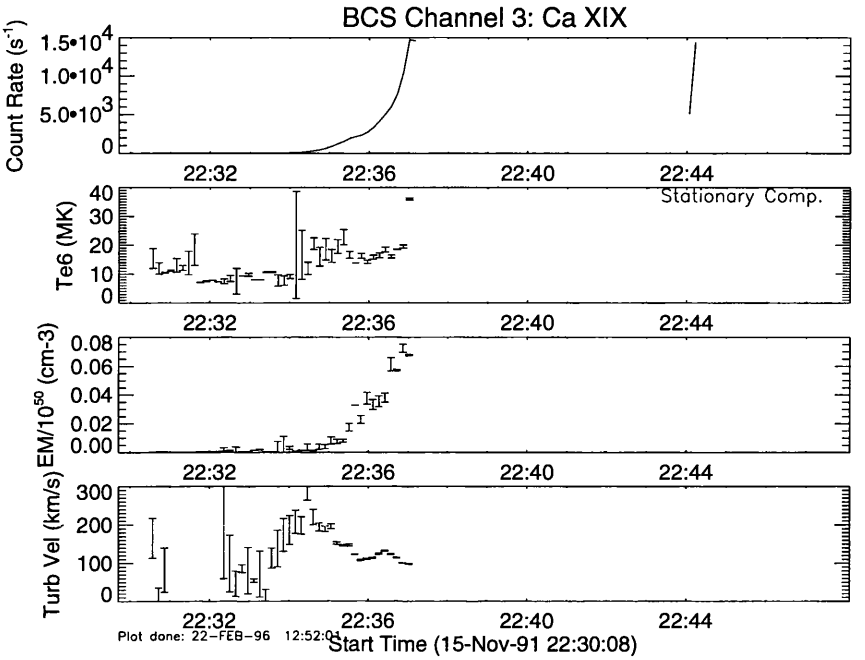

Figure 3.10: As fig. 3.9 for Ca XIX.

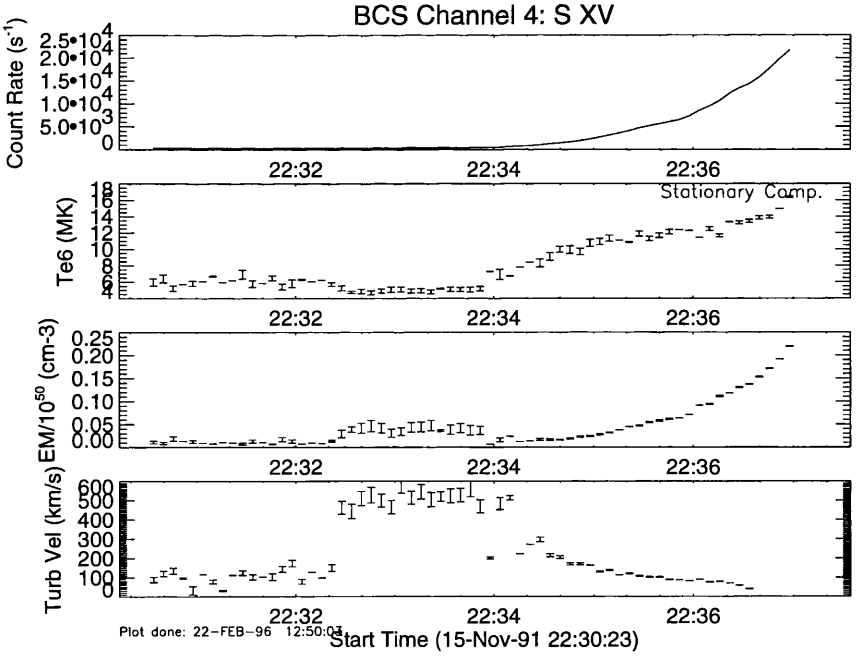

Figure 3.11: As fig. 3.11 for S XV.

CaXIX			FeXXV			S XV		
$< B >$	$< n >$	$< V >$	$< B >$	$< n >$	$< V >$	$< B >$	$< n >$	$< V >$
37	2.9×10^9	10^{27}	50	9.0×10^8	5.5×10^{26}	65	1.7×10^9	10^{27}

Table 3.3: Best fit parameters in c.g.s. units for the event of November 15 1991. The γ-ray parameters are $\alpha T = 0.01$ and $N_p = 1.1 \times 10^{32}$ (Yoshimori et al., 1994)

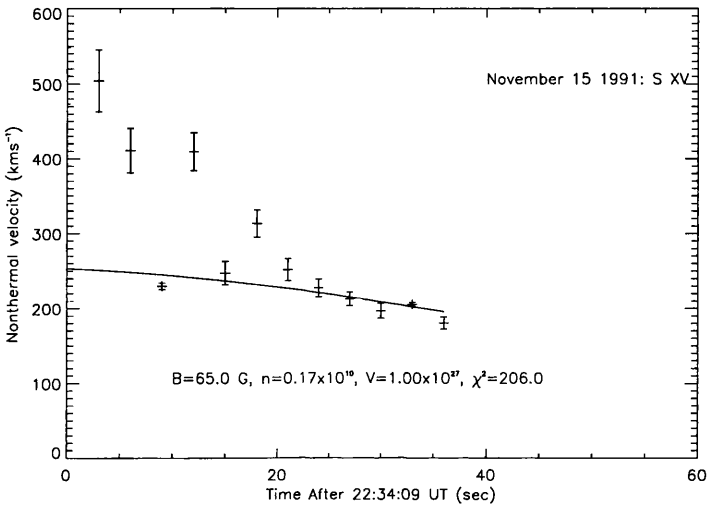

Figure 3.12: Nonthermal line broadening observed in the S XV channel for the event of November 15 1991. The best fit calculated temporal behaviour for the γ-ray parameter set is superimposed on the data set and the derived ambient parameters are quoted together with the χ^2 value of the fit.

corresponded to the time t=0 in the γ-ray decays. It is difficult in this case, given that some three minutes elapse between the peak of the nonthermal line broadening in soft X-rays and the beginning of γ-ray emission, to associate these two emissions. However, since no soft X-ray data is available from 22:37 UT due to saturation of the BCS, it is not inconceivable that the nonthermal velocity did in fact increase again during the period between about 22:37 - 22:40 UT.

Strictly, given this soft X-ray data gap during the period of γ-ray emission, this event is unsuitable for comparison with our model. However, since this is the only data available at present from *Yohkoh*, in a suitable form, the decay of the wave energy density derived from the γ-ray parameters given by Yoshimori et al. (1994) has been calculated and overlaid on the v_{nt} decays. Table 3.3 gives the values of αT and N_p for the γ-ray emission (Yoshimori et al., 1994) as well as the best fit parameters for the magnetic field strength, density and volume for each channel of the BCS. Figure 3.12, fig. 3.13 and fig. 3.14 show the best fit calculated temporal behaviour for the γ-ray data superimposed on the soft X-ray data. Also indicated are the best fit parameters and the χ^2 value of the fit.

From figure 3.12 - fig. 3.14 there still appears to be an ion dependence; the fit to Fe XXV is

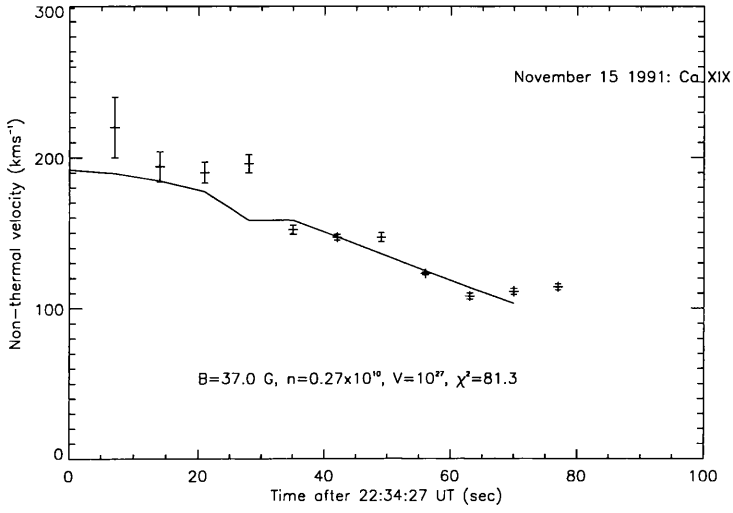

Figure 3.13: As fig. 3.12 for Ca XIX.

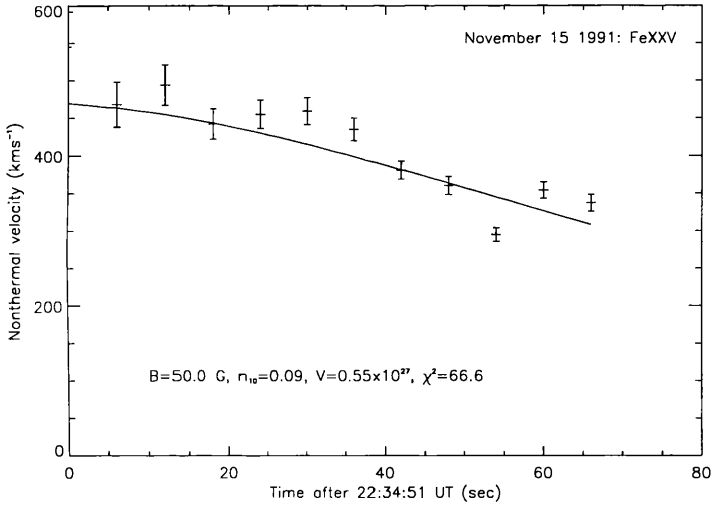

Figure 3.14: As fig. 3.12 for Fe XXV.

better than that to Ca XIX and both of these are considerably better than that of S XV. However, all of these fits have rather larger values of χ^2 than are consistent with this hypothesis being true for the number of degrees of freedom in each event by at least one order of magnitude. Part of the reason for this is that the errors on the derived nonthermal velocities are rather small, and probably artificially so, but the most likely reason is the discrepancy in the timing between the soft X-ray and γ-ray data.

The best fit parameters again indicate a relatively diffuse flaring plasma, few x $10^9 cm^{-3}$. For Fe XXV this value is even lower at $9 \times 10^8 cm^{-3}$. The magnetic fields for all channels are rather lower than might be expected from the the flaring corona and we find that for Ca XIX and S XV the best fit volumes imply that the whole coronal loop must be involved to reproduce the observed decay. Even higher volumes are implied by the low derived densities if we examine the emission measures obtained by BCS, see figs. 3.9-3.11. Typically we see that the emission measure is of the order of 10^{48} cm^{-3} for this event, which coupled with the derived densities implies a volume of $\sim 10^{30}$ cm^{-3}. This would be extremely difficult to justify and is irreconcilable with observations of the volumes of flaring loops. This coupled with the problem of ion-electron equilibrium times at these densities (see section 3.10) would appear to render this model unlikely. However, given the gap in the BCS data available for this flare it is perhaps unfair to draw conclusions based on these results. The problem of ion-electron equilibrium times is apparent in all the SMM flares analysed though, and must be addressed.

It is difficult to conclude anything at all from this particular event for a number of reasons. Firstly, and undoubtedly most importantly, the peak of the available soft X-ray nonthermal velocity data occurs 3 minutes *before* the onset of the γ-ray emission. There was soft X-ray emission at the time of the γ-ray emission however, and this was clearly significant since the BCS saturated at this time. Because of this we cannot say that there is no link between the soft X-ray line broadening and the proton acceleration. What is still interesting about this event is the apparent temperature dependence of the nonthermal velocity, which is at odds with the hypothesis of broadening by Alfvén waves.

In fact, Mariska (1992) and Antonucci and Dodero (1995) have shown that the nonthermal velocities derived from soft X-ray lines in the flaring corona depend on the temperature of line formation, and that nonthermal velocities derived from lines with higher temperatures of formation are systematically higher than those with lower formation temperatures. This is at odds with the hypothesis that Alfén wave turbulence is capable of accounting for the entire nonthermal velocity. However, as we have seen already, this model cannot account for the observed rise in v_{nt} after about 30 seconds (in its present form), but the agreement in the first 30 seconds is still good, particularly for the SMM events. It is possible then that a combination of processes, which may include Alfvén wave turbulence, may be producing the observed velocities.

Chapter 4

Beam Driven Return Current Instabilities

4.1 Introduction

Much of the electromagnetic emission that we observe from solar flares must originate from a plasma regime where the densities are consistent with those found in the chromosphere rather than the corona (Knight and Sturrock, 1977). Emissions of this kind include hard X-rays, microwaves and γ-rays. However, the corona provides a much greater volume in which magnetic energy can be stored, a plasma β regime where magnetic pressure dominates and also its lower density makes for efficient particle acceleration. Because of this apparent disparity between the site of primary energy release in solar flares and the location of the observed emission many flare models have been formulated in which free magnetic energy is released in the corona and then propagates to the chromosphere in the form of high energy particle beams (Sweet, 1969; Sturrock, 1974).

The question of how such beams propagate through the solar atmosphere is a non-trivial problem. For example, if we consider that a typical hard X-ray producing electron beam has a flux, F, of $10^{36}s^{-1}$, then this constitutes a current of $\sim 10^{17}A$. The energy in the self magnetic field of such a beam is $[\sim (eF/c)^2 \times \textit{beam length}]$, (where the typical beam length is 10^9 cm, e.g. Porter and Klimchuk, 1995) which is orders of magnitude greater than the total beam kinetic energy and also the total flare energy (a beam of this size would have a self-magnetic field of $\sim 10^5 G$ where the average magnetic field in the corona is $\sim 100G$, this implies that the energy contained in the self magnetic field of this beam is about 6 orders of magnitude greater than the pre-flare energy content of the coronal field). Another problem associated with the self-magnetic field of a beam of charged particles was discovered by Alfvén (1939) and Lawson (1957). They noted that there is a maximum possible current allowable for beam propagation; currents in excess of this limit prevent

the beam from propagating.

Since it is generally accepted that electron beams do exist in solar flares and are responsible for many of the observed radiations, then the resolution of these problems requires that a return current is induced in the ambient plasma to provide current neutralization (Knight and Sturrock, 1977; Spicer and Sudan, 1984 ; Brown and Bingham, 1984). In this chapter we investigate the possibility of the return current-beam system becoming unstable in the deep chromosphere of solar flares as a result of the low ionization in this region.

4.1.1 Particle Beams

Before discussing the return current itself it may be useful to look first at what distinguishes the behaviour of a particle beam from the behaviour of a single charged particle, and the observations which lead us to believe that high energy particle beams play such a ubiquitous rôle in solar flares.

Following Melrose (1980) we define a particle beam to be a collection of particles with a non-zero mean velocity which exhibits some property that cannot be explained in terms of single particle dynamics, i.e. exhibits some kind of collective behaviour. Given this definition there are then three types of particle beam which we might encounter: electron beams, ion beams and neutral beams.

In solar physics the most widely studied beams are non-relativistic electron beams in connection with hard X-ray bursts, type III radio bursts but also with several other kinds of radio burst, types I and II, as well as microwave emission. These beams have characteristic energies in the range from a few keV to hundreds of keV. We see evidence for ion beams on the Sun in the form of γ-ray line emission. The energy of these beams corresponds to $\geq$ 30 MeV per nucleon (Ramaty, 1986) and at present there is no direct evidence for ion beams with energies less than this, although the possibility of indirect detection via observations of H_α impact polarization exists (Hénoux, 1990; Fletcher and Brown, 1992). We also do not see evidence for neutral beams; the mass flows that we observe in spicules and CME's are not generally classified as beams.

There are four main properties of beams which are of interest,

1. beam energization or acceleration
2. escape from the acceleration region to form a beam
3. beam propagation
4. dissipation or destruction of the beam

Point (1) is essentially a problem of particle acceleration following the primary energy release in a solar flare and is not addressed in this chapter. We simply assume that for our purposes the particles have been accelerated by some 'black box' mechanism and have escaped from the acceleration region to form the beam. We will, however, consider the final two points and in particular, the problem of beam dissipation.

4.2 Electron Beams

A plasma has a tendency to preserve neutrality. If an electron beam is suddenly introduced into a plasma then the resultant sudden change in the magnetic field and charge structure will induce electric fields opposing the primary current. It is then not unreasonable to ask whether a return current develops in the corona, balancing, or almost balancing, the primary current of an electron beam propagating from the corona to the chromosphere and producing current neutralization.

Consider a symmetrical flux tube rooted in the photosphere and extending into the corona. We then assume that electrons are accelerated at the top of the loop by the development of stochastic electric fields or some other 'black box' process. When the electrons start to stream down the legs of the flux tube a charge and current imbalance are induced which in turn cause the development of electric fields which tend to restore the charge balance. If there is no net change in the charge density in the loop then whatever current flows must be constant. If the flux tube is symmetrical then this current must be zero. So, the tendency of a plasma to remain neutral implies that if a current is generated in a plasma which would violate $\frac{\partial J}{\partial t} = 0$ on timescales $\gg$ a plasma period (i.e. a non-MHD current), then this current will generate a self-neutralizing return current (Knight and Sturrock, 1977).

There are then three interesting types of beams in the solar atmosphere: electric current-carrying beams, current neutralized beams and ion beams.

4.2.1 Electric currents

The idea that a beam of charged particles constitutes a current was first acknowledged by Alfvén (1939) when he considered galactic cosmic rays propagating towards the Earth. He considered the beam to be a cylinder of radius r_0 and the self magnetic field of such a beam is then just that of a current carrying wire, viz.

$$B_0 = \frac{\mu_0 I}{2\pi r_0} \tag{4.1}$$

The radius of the particle orbits in the beam magnetic field is then,

$$R = \frac{\gamma m v}{qB} \tag{4.2}$$

where γ is the Lorentz factor, m is the mass of the charged particle, v the speed, q the charge and B_0 the magnetic field strength. For $R \simeq r_0$ the particles have figure-of-eight type orbits and for $R \leq r_0$ the particle orbit in the self-magnetic field prevents propagation in the direction of the beam and hence the beam cannot exist. This relation $R \leq r_0$ implies that there is a maximum current allowable for the beam to propagate. Lawson (1957) also noted this effect and associated it with the self pinching of currents (Bennett, 1934). The Alfvén-Lawson limit then defines the

maximum current for electrons that allows a beam to propagate,

$$I_A = \frac{2\pi m_e \gamma v}{e\mu_0} = 1.7 \times 10^4 \beta\gamma A \tag{4.3}$$

where $\beta = v/c$.

All the currents of interest in the solar atmosphere exceed the Alfvén-Lawson limit. Even ambient drift currents producing $B \simeq 100G$ far exceed the Alfvén-Lawson limit but these Ohmic drift currents are collision dominated and the Alfvén-Lawson collisionless beam argument does not apply. For example, the ≥ 20 keV beam electrons which produce hard X-ray bursts precipitate at a rate which can exceed $10^{36}s^{-1}$. This constitutes a current in excess of 10^{17} A, whilst for this case $I_A = 10^3$A. Despite this, there are ways in which currents larger than I_A can flow.

1. If there is an ambient magnetic field larger than the self-magnetic field of the beam then the particle orbits remain roughly spiral as opposed to having a figure-of-eight shape in the self field.

2. If there is a medium present then the ambient particles can set up a return current so that the net local current density is always small. This is current neutralization.

A second limitation is that for a current I to flow in a cylinder of radius r_0 we must have an ambient magnetic field, B, such that

$$B \geq \frac{\mu_0 I}{2\pi r_0} \tag{4.4}$$

For typical active region values of $r_0 = 2 \times 10^8 cm$, $B = 1500G$ this implies that $I \leq 2 \times 10^{12}$A, and for coronal values we find that I cannot exceed 10^{12}A, which places a strong constraint on solar flare models. In particular, Spicer's (1981) loop model with only Joule dissipation and Kane et al's (1983) photospheric dynamo model cannot meet this constraint.

This limit on the current which may flow in the corona applies to **all** currents, including those which flow in filaments or sheets. Since it is widely believed that in order to account for the energy release in flares a large scale current must flow in filaments or sheets, equation (4.4) then implies a limit on the thickness of a filament or sheet which is carrying such a current. For example the ion acoustic instability has a limiting current density $\sim J = n_e e v_{is}$ which implies that the radius of a filament, $r_0 \leq B/(\mu_0 n_e e v_{is})$. That is, the radius of the filament is inversely proportional to the electron density which in dense regions such as the chromosphere restricts r_0 to around a metre and in the less dense corona to about a kilometre before the ion-acoustic instability sets in. The need for anomalous resistivity to dissipate the energy in flares is then clear. This and the current limitation imply that the energy in solar flares is released in very thin layers of the atmosphere.

4.2.2 Evidence for electron beams in the corona

The first evidence for electron beams came from metre-wave radio burst observations with a dynamic spectrograph. Wild (1950) suggested that type III radio bursts were due to a disturbance

propagating out through the corona at between $2 \times 10^4 - 10^5 kms^{-1}$. Type III radio bursts are intense bursts of unpolarized radiation that show a rapid decrease in frequency with time (Kundu, 1965). These are interpreted as plasma radiation either at the fundamental or the second harmonic of the plasma frequency, where $\omega_p^2 = n_e e^2/\epsilon_0 m_e$ is the plasma frequency, produced when Langmuir waves scatter off ion-acoustic waves or other Langmuir waves, respectively. The frequency decrease is just due to the decrease in the density of the excited plasma as the disturbance moves higher in the corona. Conventionally, type III radio bursts are thought to be high energy electron beams propagating at a significant fraction of the speed of light out from the flare site into the ever less dense coronal regions. That the disturbance is an electron beam was confirmed by in situ measurements in the solar wind (Lin, 1985).

Other bursts which indicate the presence of electron beams are

1. Type II radio bursts. These are very high intensity bursts following large flares. They exhibit a slow drift to lower frequencies indicating a propagation speed of $\sim 1000 - 1500 kms^{-1}$ outwards. This emission is thought to be produced by plasma waves excited by the Moreton wave as it travels outward, where the Moreton wave is a weak MHD shock wave propagating spherically from the flare site. About half of type II bursts show harmonic structure with two parallel bursts, at the fundamental and second harmonic. Often these harmonics themselves show two closely parallel bands of emission on the frequency-time diagram. This has been explained as mixing with the gyrofrequency, Doppler shifts or parallel streams. (Krüger, 1979). Sometimes, a complex 'herringbone' structure of type III bursts is excited by the passage of a type II front.

2. Drift-pair bursts (Roberts, 1958) and S-bursts (Ellis, 1969)

3. Type I bursts are also believed to be due to electron beams. These consist of circularly polarized narrow band ($\sim$ 5 MHz) bursts lasting a second or less with complex spectral properties. When superposed on a continuous background, they make up the type I noise storm. They are due to coherent plasma radiation at frequencies in the range of the electron plasma frequency.

4.2.3 Hard X-rays

The first hard X-ray data came from balloon observations in the early 1960's and later from spacecraft (Kane, 1974). This data led to a picture of the energy release in solar flares involving two phases of acceleration, eg. Wild et al (1963). This is an over-simplification, but the first phase was thought to involve acceleration of $\geq$ 20 keV electrons to produce type III bursts and hard X-rays, with type III bursts being caused by electron beams propagating upwards and hard X-ray bursts by downward propagating beams. However, interplanetary data suggests that lower

energy (2-20 keV) electrons are important in type III emission (eg. Lin, 1985) and as these could not escape throught the denser coronal regions they must be accelerated higher in the atmosphere than the site of the primary energy release, in a second phase of acceleration. It is also widely accepted that H_α, UV and soft X-ray emissions in flares are due to secondary effects resulting from the impact of hard X-ray emitting electrons on the denser regions of the solar atmosphere.

The first detailed observations of solar hard X-ray bursts (Frost, 1969) provided evidence on the energy spectra of the precipitating electrons (Brown, 1971). The high quality spacecraft data now available on hard X-ray bursts (eg, Hinotori, SMM, Yohkoh), both images and Ge detector spectra have led to the acceptance that there are some events which display a quasi-thermal nature, others that are clearly nonthermal, and that most hard X-rays are produced by thick target bremsstrahlung - the evolution of an electron distribution in a source is described by the continuity equation in energy (Lin, 1974) viz.,

$$\frac{\partial N(E,t)}{\partial t} = Q(E,t) - \frac{N(E,t)}{\tau_e(E)} - \frac{\partial}{\partial E}\left[N(E,t)\frac{dE}{dt}\right] \tag{4.5}$$

where $N(E,t)dE$ is the number of electrons with energies in the range E to $E+dE$, $Q(E,t)$ is the source function (i.e. the number of electrons produced per unit time per unit energy), $\tau_e(E)$ is the characteristic electron escape time and $\frac{dE}{dt}$ is the rate of change of energy of the electron in ambient plasma interactions. For Coulomb collisions,

$$\frac{dE}{dt} = -4.9 \times 10^{-9} n E^{-1/2}\ keV s^{-1} \tag{4.6}$$

where n is the ambient proton density (Trubnikov, 1965). Approximating $\frac{\partial N}{\partial E}$ by N/E and considering only the decay phase so that $Q(E,t) = 0$, we have

$$\frac{\partial N}{\partial t} = -\left(\frac{1}{\tau_e} - \frac{1}{\tau_d}\right) N \tag{4.7}$$

where $\tau_d = 4.8 \times 10^8 E^{3/2} n^{-1}$ is the characteristic energy loss time for an electron of energy E. There are the two cases to consider: thin target and thick target, viz.,

Thin target- $\tau_e \ll \tau_d$. The electron escapes from the source with its energy essentially intact and the evolution of N is governed entirely be electron escape. In this case the total hard X-ray emission is proportional to the column density traversed by an electron before it escapes. Thus it depends on the density, volume and geometry of the source (e.g. Lin, 1974).

Thick target - $\tau_d \ll \tau_e$. The electron loses all its energy in the source through collisions with the ambient electrons, and the evolution of N is governed by the temporal evolution of this energy decay. In this case the total (time integrated) HXR emission is independent of the density because the density dependences in the bremsstrahlung rate and the energy loss rate cancel (Brown, 1971).

The energy in the electrons that produce the hard X-ray emission is also thought to provide the energy for the H_α, EUV, optical and soft X-ray emission. Most of the energy in these electrons goes

into the ablation of chromospheric material which produces the soft X-ray emission; the so-called chromospheric evaporation (e.g. Antonucci et al., 1982). De Jager and Svéstka (1985) compared the energy in a $>$ 20keV electron beam (obtained from hard X-ray observations) with the energy in the upward moving material and found the two to be approximately equal, lending credence to this argument.

Downward propagating electron beams carry momentum as well as energy to the chromosphere (Brown and Craig, 1983). The required momentum balance is then provided by the chromospheric gas having both red-shifted and blue-shifted components (eg, Zarro et al., 1988). Evidence for both momentum and energy balance then supports the idea of chromospheric evaporation and in turn the idea that much of the flare energy is released in the form of $\geq$ 20keV electrons.

4.3 Return current generation

Both upwardly moving type III emitting electron beams and downward propagating hard X-ray producing electron beams require return currents, and the return current must be very nearly co-spatial with the beam current to ensure that I does not exceed I_A.

Once the need for a return current has been established, the two main questions one might wish to ask are: 1) what observational evidence might we see for such a return current, and 2) how is it actually set up?

A return current is formed by thermal electrons drifting in the opposite direction to the primary electron beam such that the drift speed, v_D is

$$v_D = \frac{n_b}{n_p} v_b \tag{4.8}$$

where n_b is the beam density, n_p is the ambient plasma density and v_b is the speed of the beam associated with the mean energy of the particles in the beam.

If this drift speed exceeds the threshold for a current driven instability then waves appropriate to this instability are generated. The ion-acoustic instability is most often considered. Possible consequences of the generation of ion-acoustic waves are the following:

1. enhanced plasma emission in type III bursts (Melrose, 1970). Here the ion- acoustic waves coalesce with Langmuir waves and scatter the Langmuir waves into the background direction to produce enhanced forms of the fundamental and second harmonic emission.

2. ion-acoustic turbulence causes anomalous thermal conductivity in a thermal conduction front that limits the escape of energetic electrons from the region of primary energy release in a flare (Brown, Melrose and Spicer, 1979).

3. ion-acoustic turbulence causes anomalous electric conductivity leading to an enhanced form

of thermal dissipation for hard X-ray generating beams (Hoyng et al. ,1976; Brown and Melrose, 1977; Knight and Sturrock, 1977).

4. the onset of anomalous conductivity and the resulting pulse of enhanced Ohmic heating may lead to burst-like enhancements in X-ray, EUV and optical emissions.

The question of how the return current is set up has been somewhat controversial. The charge displacement caused by the propagation of an electron beam produces an electric field which acts in such a way as to redistribute the ambient plasma electrons in order to neutralize the local charge build up. Since this electric field is caused by charge effects it is usually referred to as electrostatic. In a plasma the magnetic field does not vary much over times shorter than the magnetic diffusion time. The reason for this is that the introduction of a varying current into a plasma will induce an electric field which drives a current of plasma electrons in such a way as to prevent magnetic field variations. Essentially both of these processes, electrostatic and inductive, drive a return current of plasma electrons, as pointed out by van den Oord (1990). Following much controversy-e.g. Brown and Bingham (1984), Spicer and Sudan (1985) - van den Oord (1990) showed that the question of the relative importance of electrostatic and inductive effects is irrelevant for a full electrodynamic treatment. Electrostatic effects permit the plasma to redistribute the excess charge imposed by the beam and inductive effects prevent the magnetic field from changing on a timescale less than the diffusion time.

However, the problem is still not resolved. As we have seen already, a hard X-ray producing beam with a flux of $10^{36}s^{-1}$ constitutes a current of $\sim 10^{17}$ A. The Alfvén-Lawson limit for this situation implies that $I_A = 10^3$A. We are then faced with the problem of ensuring current neutralization to one part in 10^{14} at all places at all times. What this means is that we have to consider how the return current is driven both on the scale size of the beam and also on the scale size of the smallest current that has to be neutralized.

If we are to discover exactly how the return current is set up a model of the acceleration of the electrons and of their escape from the acceleration region is required. Winglee et al. (1988a, b) proposed a simple model and found that the direct and return currents were not co-spatial on a microscopic scale. The implications of this for the overall generation of the return current are, however, unclear (van den Oord, 1994).

4.3.1 Current driven instabilities

Downward propagating electron beams are susceptible to various plasma instabilities. For example one particular instability involves Langmuir-type waves generated by the anomalous Doppler effect in a region where the electron cyclotron frequency exceeds the plasma frequency (eg, Lifshitz and Tomozov, 1974). Similarly to the case of Langmuir waves in type III bursts Vlahos and

Papadopoulos (1979) have argued that marginal stability (i.e. steady state with $\omega = 0$) can be achieved in this case. Then there can be an interaction between the streaming instability and the anomalous Doppler instability (Vlahos and Rowland, 1984). These and other instabilities generate waves which cannot escape directly from the plasma and are loosely described as longitudinal waves. Plasma emission due to these longitudinal waves is one possible direct signature of such instabilities, probably in the form of a spike in the microwave emission.

Radio spikes (eg, Benz, 1986) are generally regarded as signatures of precipitating electrons. The favoured emission process for these is electron cyclotron maser emission (Holman et al., 1980; Melrose and Dulk, 1982).

So, downward propagating electron beams may be subject to both electrostatic and electromagnetic instabilities. Radio spikes due to plasma emission are an example of an electrostatic instability, whilst electron cyclotron maser emission is an example of the electromagnetic case.

In a magnetized plasma ion-cyclotron waves have a lower threshold for instability than ion-acoustic waves, but provided that $T_e < 8T_i$, where T_e is the electron temperature and T_i is th ion temperature, they do not contribute greatly to the anomalous resistivity (Papadopoulos, 1977). One of the results of the onset of electrostatic waves in a plasma is an increase in the Ohmic heating rate, due to the increase in the plasma resistivity. This enhanced resistivity is known as anomalous resistivity.

The determinant factor in assessing which type of instability dominates in a particular situation is largely the ratio of T_e to T_i. Here we consider the circumstances and effects of three types of current instability

1. the ion-cyclotron instability
2. the Buneman instability
3. the ion-acoustic instability

The ion-cyclotron instability

This instability has the lowest threshold for the case $T_i = T_e$. It is driven by moving electrons in anomalous Doppler resonance with the left-hand mode.

Gyromagnetic emission and gyromagnetic absorption result from a resonant interaction between a wave and a helically moving charge. The gyro-resonance condition is the Doppler conditon, viz.,

$$\omega - s\Omega - k_z v_z = 0 \tag{4.9}$$

where k_z is the wavenumber in the z direction, v_z is the velocity in the z direction, and Ω is the cyclotron frequency. Then resonances which occur at $s < 0$ happen via the normal Doppler effect, whilst those with $s > 0$ are via the anomalous Doppler effect.

The threshold for the growth of electrostatic ion-cyclotron waves for a Maxwellian distribution is

$$v_D \gtrsim 15\frac{T_e}{T_i}v_{ti} \tag{4.10}$$

This is the ideal case; in practice the electron distribution is somewhat skewed by the electric field and the threshold is actually higher. How this instability saturates is not yet well determined, but it is thought that the wave energy level at saturation is low. These waves preferentially heat ions over electrons.

Buneman instability

If the drift velocity v_D increases and the ion and electron distributions get displaced from one another by more than the thermal velocity, i.e. if $v_D \gg v_{te}$ then they behave like two cold streams. The waves generated by this instability are of the beam mode, i.e. the frequency of the oscillations is less than the plasma frequency, and they are purely electrostatic. The threshold is

$$v_D \gtrsim 1.7(v_{te} + v_{ti}) \tag{4.11}$$

The evolution of this instability is non-linear and saturates because the presence of these waves causes the resonant electrons to diffuse, forming a plateau between the peaks of the ion and electron distributions, that is, the system approaches marginal stability.

With this instability electrons are preferentially heated over ions to the point where $v_{Te} \simeq v_D$. Because of this at some point the electron temperature will greatly exceed the ion temperature, at which point the onset of the ion acoustic instability is likely.

Ion-acoustic instability

Ion-acoustic waves are ion oscillations modified by the Debye shielding effect of the electrons. Plain acoustic waves are the result of an interaction between the pressure as the restoring force and inertia. At high frequencies (i.e. higher than MHD frequencies) pressure disturbances are carried by the electric fields rather than collisions. The ion-acoustic waves are an electrostatic mode and are important in plasmas with $T_e \gg T_i$; they are heavily damped in plasmas where $T_e \simeq T_i$. For $T_e \gg T_i$ the phase velocity=the group velocity, where

$$v_{ph} = \sqrt{k_B T_e/m_i} \tag{4.12}$$

This reflects the fact that mobile electrons carry the pressure disturbance and the ions provide the inertia. When $T_e \gg T_i$ the mean thermal speed of the electrons is so high that they immediately shield the ion density fluctuations and maintain neutrality. The electric field that holds the electrons against their own pressure also acts back on the ions and provides the restoring force. So density disturbances propagate like sound waves except that the electric field takes the rôle of collisions. Provided that $(k\lambda_{De})^2 \ll 1^2$, where k is the wavenumber and λ_{De} is the Debye radius, then the frequency of the waves is well below the plasma frequency.

The threshold for this instability is

$$v_D \gtrsim \frac{\omega}{k}\left(1+\left(\frac{T_e^3 m_i}{T_i^3 m_e}\right)^{1/2} exp\left[-1/2\left(\frac{\omega}{k v_{Ti}}\right)^2\right]\right) \tag{4.13}$$

For $T_e \gtrsim 15T_i$, the second term in this equation is negligible and ion-acoustic waves will grow if $v_D \gtrsim v_{is}$. This is important for strong electric currents. The waves grow because the instability feeds energy from the current into the waves, as a result of which the resistivity is increased above the collisional value.

Both ions and electrons are heated by the ion-acoustic instability in parallel directions. For $v_D \gtrsim 2v_{is}$ and $T_e > T_i$ electrons get a larger fraction of the energy and T_e/T_i rises. Saturation of this instability occurs when unstable waves are scattered on ions into different waves that are not driven by the current and are damped; this is called non-linear Landau damping. At saturation $T_e \simeq 10T_i$. This instability is capable of producing an equilibrium between the driving current and the wave turbulence resulting in the onset of anomalous resistivity which limits v_D.

4.3.2 Resistivity

As magnetic field lines move through a plasma, resistive damping of the induced currents occurs. The Ohmic heating produced by this damping removes energy from the field which then appears as heat in the plasma. Since this ohmic heating can be expressed as $P = \eta J^2$, where η is the electrical resistivit, the magnetic energy dissipation time, τ_L, is given by

$$\tau_L = \frac{B^2}{8\pi\eta J^2} s \tag{4.14}$$

where the energy per unit volume lost in a time τ_L is $\eta J^2 \tau_L$. It acts in a similar way to radiation in that provides a mechanism for transforming magnetic energy into heat.

The equation of motion along the magnetic field of an electron drifting with a velocity v_D relative to a stationary background of ions is

$$m_e \frac{dv_D}{dt} = -eE - m_e v_D \nu(v) \tag{4.15}$$

where E is the constant macroscopic electric field and $\nu(v)$ is the collision frequency, given by Spitzer (1962) for Coulomb collisions as

$$\nu(v) = \frac{4\pi n_e e^4 ln\Lambda}{m_e^2 v^3} \tag{4.16}$$

where n_e is the electron density and $ln\Lambda = ln(4\pi n_e \lambda_{De}^3)$ and λ_{De} is the Debye radius.

In the absence of collisions the electrons are freely accelerated relative to the ions, and v_D is given by,

$$v_D = \frac{-eEt}{m_e} \tag{4.17}$$

However, when electrons undergo collisions with ions or slower electrons it is possible for a steady state to be reached, characterized by the drift velocity, v_D,

$$v_D = \frac{-eE}{m_e \nu(v)} \tag{4.18}$$

The effect of these collisions is to produce random velocities so that the free energy associated with the drift velocity is converted to heat energy. The current density, J, is connected to the drift velocity via the relationship $J = -n_e e v_D$, so that a simple local relationship between the electric field and the current density is given by Ohm's Law

$$E = \eta J \tag{4.19}$$

where η is the classical resistivity given by Spitzer (1962),

$$\eta = \frac{m_e \nu(v)}{n_e e^2} \tag{4.20}$$

For electron with drift velocities smaller than the electron thermal speed, v_{Te}, then $v = \sqrt{v_D^2 + v_{Te}^2} \simeq v_{Te}$, and

$$\nu = \frac{4\pi n_e e^4 ln\Lambda}{m_e^2 (k_B T_e)^{3/2}} \tag{4.21}$$

When $v_D < v_{Te}$ then the drag force on the electrons $\sim v_D / v_{Te}^3$ and it is possible to achieve a steady state. However, if $v_D > v_{Te}$ then the drag force $\sim v_D^{-2}$, which decreases as v_D increases. So, for the case of $v_D < v_{Te}$ the drag force dominates over the electric field, the electron velocities are random and a steady drift is possible. For the other case, $v_D > v_{Te}$, a critical velocity is reached beyond which electrons are accelerated by the electric field faster than they can be decelerated by collisions. Eventually, they are freely accelerated by the magnetic field until some other loss mechanism becomes dominant. This might be radiation or an instability. These electrons are called 'runaway' electrons and the critical electric field strength at which an electron gains energy equivalent to the thermal energy in one collision is called the Dreicer field, E_D, where $E_D = e \ln \Lambda / \lambda_{De}^2$.

More realistically we should consider the effect of an externally applied electric field on an electron distribution rather than a single particle. In the collision dominated part of the velocity distribution, the electron distribution will look like a skewed Maxwellian drifting relative to the ion background. The whole electron distribution will consist of this skewed and drifting Maxwellian, which has most of the electrons, plus a very long anisotropic high energy tail antiparallel to the electric field. This distribution is a source of free energy which is capable of exciting plasma micro-instabilities which could then act to inhibit the acceleration of the electrons in the tail of the distribution, i.e to prevent the electron 'runaway'. By a micro-instability we mean that for distributions which are not Maxwellian there is a possibility that waves can grow at the expense of the particle kinetic energy. This type of instability depends on the microscopic details of the

velocity distribution, hence the term micro-instability. They generally involve the growth of small scale waves so that they produce an enhanced level of fluctuations rather than actual bulk plasma motion.

If the drift velocity characterizing the skewed Maxwellian distribution is greater than both the ion-sound and ion thermal speeds, but less than the electron thermal speed, then the bulk of the current carrying electrons are capable of exciting current driven instabilities. If the tail of the distribution has a bump in it then this too is capable of exciting micro-instabilities; this happens because there is a portion of the velocity distribution where $\frac{\partial f}{\partial v} > 0$, see fig. 4.1, which allows waves to grow (Benz, 1993). Electrostatic waves are particularly likely in this case since they can be fuelled by the excess free energy associated with the drift energy of the electrons. The scattering of these drifting electrons by turbulent wave fields causes enhanced momentum and energy loss leading to the onset of anomalous resistivity. What happens is that the electrostatic waves modulate the ion density in the sense that the colliding electrons see bunches of ions with an effective charge-to-mass ratio $> q_i/m_i$, where q_i and m_i are the charge and the mass of the ion respectively. As a result of this the diffusion constant is enhanced and the collisional stopping time of the electrons is reduced.

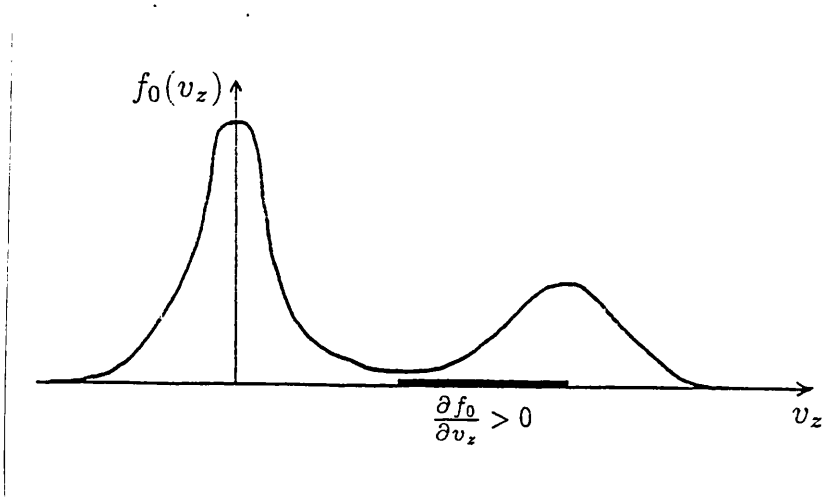

Figure 4.1: One-dimensional velocity distribution of a particle beam indicating the region of positive gradient where instability may develop

Current instabilities tend to heat electrons and develop ion acoustic turbulence. The wave energy density at saturation in these waves depends only on the ratios T_e/T_i and v_{is}/v_D, where v_{is} is the ion-sound speed, and the effective collision frequency at saturation was calculated by Sagdeev,

$$\nu_{eff} = \frac{\omega_p^e T_e v_D}{32\pi T_i v_{Te}} \tag{4.22}$$

where ω_p^e is the electron plasma frequency. From this the effective conductivity, σ_{eff}, and hence the effective resistivity, η_{eff}, may be found, viz.,

$$\sigma_{eff} = \frac{8T_i v_{Te}\omega_p^e}{T_e v_D} \tag{4.23}$$

$$\eta_{eff} = \frac{T_e v_D}{8T_i v_{Te}\omega_p^e} \tag{4.24}$$

Laboratory experiments and numerical simulations have confirmed that the v_D of currents at saturation is around $(1-3)v_{is}$ and the minimum anomalous resistivity is

$$\eta_{eff} \simeq \frac{1}{20\omega_p^e} \tag{4.25}$$

4.3.3 Ohmic heating

The existence of a finite resistivity, be it classical or anomalous, results in the dissipation of heat at the rate **J.E**. This energy heats the current-carrying region on a timescale

$$\tau_j = \frac{n_e k_B T_e}{\mathbf{J}.\mathbf{E}} = \frac{2}{9\pi}\left(\frac{E_D}{E}\right)^2 \frac{1}{\nu} \tag{4.26}$$

assuming that the current is parallel to the magnetic field with $\mathbf{J} = \sigma\mathbf{E}$. For anomalous resistivity the effective collision rate, ν_{eff} should replace ν in this equation. Once the temperature of the region has risen sufficiently an equilibrium can be attained with radiative and conductive losses.

When current instabilities occur they generally grow on timescales shorter than the magnetic diffusion time. Ampére's law requires that the total current changes on the slow inductive timescale. If then the total current is constant, the current density must remain roughly constant through the initial increase of resistivity and so **E** has to rise by an amount η_{eff}/η. Consequently the Ohmic heating increases. Later there will be an expansion of the current-carrying region so that the heating rate per volume decreases and the total power released by Ohmic heating returns to the initial value. So, we see that this sudden increase in the resistivity leads to a burst of enhanced Ohmic heating.

4.4 Effects of Low Ionization

We consider here the possibility that the return current driven by a thick target flare beam may be unstable to ion-acoustic wave generation in the deep chromosphere, particularly for intense hard beams and early in the flare. This is likely despite the strong collisional attenuation of the beam and the high plasma density in the chromosphere because the low ionization there results in a high drift velocity of the few free electrons available to carry the return current. As discussed above the resulting ion-acoustic wave generation will lead to enhanced resistivity and consequently enhanced

local beam heating, which will affect diagnostics through the presence of enhanced microscopic and return current electric fields.

The potential importance for flare beam transport of the electric field set up to drive a beam-neutralising return current against the finite plasma resistivity was first noted by Hoyng (1975), Hoyng et al (1976), Brown and Melrose (1977) and Knight and Sturrock (1977) and discussed in greater detail by Emslie (1980,1981) and Brown and Hayward (1980) among others. An important limiting factor in beam propagation is that intense enough beams drive a return current faster than the critical drift speed for electrostatic wave generation. These waves enhance the resistivity and hence Ohmic energy losses of the beam to plasma heating and may even act to limit the maximum possible beam flux to the wave generation threshold value (e.g. Brown and Melrose (1977)). In these previous analyses it has been assumed that if the return current is subcritical at the injection site it will remain so thereafter because collisions reduce the beam flux with depth and the atmospheric density rises much faster than the thermal speed falls (apart from across the transition region) - cf. Emslie (1981). In this chapter we consider the possibility that this assumption can be invalid when allowance is made for the fall in the free electron density available to carry the return current in the weakly ionised low chromosphere.We consider only the case of an electron beam but essentially the same considerations apply to a proton beam.

4.5 Collisional beam propagation

As a first approximation we assume the beam distribution with depth to be collision dominated and use the resulting beam current variation with depth to assess the self-consistency of the assumption in terms of return current stability. We adopt a power law spectrum at injection of flux spectral index δ and total flux $F_1(cm^{-2}s^{-1})$ above cut-off energy E_1, and zero pitch angle. Allowing for Coulomb scattering and energy losses, following Brown's (1972) treatment gives for the beam current at column density $N(cm^{-2})$ from the injection site

$$j_b(N) = \begin{cases} F_1 e & N \leq N_1 \\ F_1 e \left(\frac{3KN}{E_1^2}\right)^{(1-\delta)/2} & N > N_1 \end{cases} \tag{4.27}$$

where $N_1 = E_1^2/3K$ and the constant $K = 2\pi e^4 ln\Lambda$ in the Coulomb cross-section K/E^2 has been assumed independent of N. In practice the Coulomb logarithm Λ will decline from its ionised hydrogen value Λ_{ee} of around 20 near the hot injection site to its neutral hydrogen value $\Lambda_{eH} = \Lambda_{ee}/2.6$ in the deep atmosphere (Brown 1973, Emslie 1978). For simplicity we will consider the limiting cases of $\Lambda = \Lambda_{ee}$ everywhere and $\Lambda = \Lambda_{eH}$ everywhere with the latter more relevant to the weakly ionised layers of interest here.

Beam current neutralization then requires a plasma electron drift current density $j_p = -n_e e v_D = j_b$ at speed v_D where n_e is the electron density given by $n_e = n(x + x_M)$ with n the total (neutral

and ionised) hydrogen density, x the degree of hydrogen ionization, and x_M the correction for metallic electrons which we take as 10^{-4}. In the sections above we have discussed several current driven instabilities and their thresholds. All of these thresholds are given for a fully ionized plasma. Mikhailovskii (1974) has discussed ion-acoustic waves and their generation by a drift current in a weakly ionised plasma with neutral collisions and the key parameter is the ratio of v_D to the ion sound speed $v_{is} = (kT_e/m_i)^{1/2}$. Equating j_p to j_b given by (4.27) yields for this ratio

$$R(N) = \frac{\frac{v_D}{v_{is}}}{\frac{F_1}{n(N)(x(N)+x_M)(kT_e(N))^{1/2}}} \times \begin{cases} 1 & N \leq N_1 \\ \left(\frac{3KN}{E_1^2}\right)^{(1-\delta)/2} & N > N_1 \end{cases} \tag{4.28}$$

Mikhailovskii (1974) gives the criterion $R \geq 1$ for ion sound wave growth for cold ions but not the dependence of the criterion on T_e/T_i. Since we are concerned here only with checking whether instability may arise because of the low free electron density we will take the criterion $R \geq 1$ as of the right order of magnitude. It is quite likely, however, that the threshold is actually somewhat higher than this.

4.6 Target atmosphere distribution

The importance of return current dissipation and possible instability depend on conditions in the target atmosphere, being greatest when the atmosphere is coolest and least dense, such as at the start of the flare. Here we consider the value of $R(N)$ for the values of $n(N)$, $T(N)$, $x(N)$ in a variety of atmospheres ranging from the quiet sun (QS) and active region (AR) models of Basri et al. (1979) to the flare models, 1, 2 and 3 of Machado and Linsky (1975).

Using L_α data from the first rocket flight of the NRL High Resolution Telescope and Spectrograph Basri et al. (1979) computed semi-empirical models for the quiet Sun chromosphere, bright and dark points in the quiet Sun and for bright regions in plages using a five level plus continuum non-LTE code for Hydrogen. Their data covered network and cell regions in the quiet Sun, umbral and penumbral regions of a sunspot, two plages and a quiescent prominence off the limb. They found that the quiet Sun model of Vernazza et al. (VAL, 1973) led to L_α profiles which were 35% too faint, exhibited too much self reversal near the line centre, showed flatter wings than the observed profile and showed limb darkening in the wings. They proposed a new model which was more consistent with the observed L_α integrated intensity, the Lyman continuum slope and the millimetre continuum.

Their approach to the modelling of the chromosphere was to assume an initial temperature distribution for the atmosphere and then compute a model chromosphere and theoretical L_α line profiles by solving the equations of statistical equilibrium and radiative transfer for the five level Hydrogen atom. The model is then adjusted until the computed line profiles match the observations

in shape and intensity. The physical parameters of the model atmosphere are then specified in terms of a quantity called the reduced mass, m_R, where $m_R = m - m_0$. Here m is the mass column density above a given layer and m_0 is the mass column density at the highest level in the atmosphere, corresponding to the base of the transition zone. The use of this quantity simplifies the solution of the equation of hydrostatic equilibrium. However, for our purposes we convert this mass column density back to the column density, N. This is simply done by computing $N = m/1.4m_H$, where a 10% Helium abundance by mass has been included.

The primary differences between the models C, BP and P that we consider here lies in the value of m_0. The result of this is to produce differences in the physical height of the transition region by up to 1600km. Model C in this case is the mean quiet Sun model, model BP is for bright points in the quiet Sun, and model P of plage regions.

The other model that we will consider here is a flare model atmosphere by Machado and Linsky (1975). Here homogeneous plane parallel model atmospheres of solar flares were computed by solving the equations of statistical equilibrium and radiative transfer for a three level Hydrogen atom and a five level Calcium atom. Machado and Linsky also give atmospheric parameters in terms of the reduced mass. Tables 4.1 - table 4.4 give the atmospheric parameters for models C, BP, P and flare model importance 1.

$n_H(cm^{-3})$	$n_e(cm^{-3})$	x (degree of ionization)	$T(K)$	$N\ (cm^{-2})$
1.654×10^{10}	8.5×10^{9}	0.5138	4.0×10^{4}	2.01×10^{18}
1.964×10^{10}	1.0×10^{10}	0.5091	3.12×10^{4}	2.013×10^{18}
2.535×10^{10}	1.3×10^{10}	0.5129	2.25×10^{4}	2.016×10^{18}
2.606×10^{10}	1.35×10^{10}	0.518	2.18×10^{4}	2.03×10^{18}
2.791×10^{10}	1.45×10^{10}	0.5195	2.09×10^{4}	2.08×10^{18}
3.198×10^{10}	1.73×10^{10}	0.541	2.0×10^{4}	2.34×10^{18}
4.469×10^{10}	2.3×10^{10}	0.5147	1.25×10^{4}	2.36×10^{18}
5.681×10^{10}	2.8×10^{20}	0.4928	9.9×10^{3}	2.48×10^{18}
7.27×10^{10}	3.55×10^{10}	0.4883	7.7×10^{3}	2.87×10^{18}
1.495×10^{11}	4.85×10^{10}	0.3244	6.8×10^{3}	4.15×10^{18}
3.352×10^{11}	4.1×10^{10}	0.1223	6.75×10^{3}	8.43×10^{18}
1.067×10^{12}	7.8×10^{10}	0.0731	6.7×10^{3}	2.13×10^{19}
2.124×10^{12}	4.8×10^{9}	2.26×10^{-3}	5.7×10^{3}	3.71×10^{19}
7.478×10^{12}	3.7×10^{10}	4.948×10^{-3}	5.35×10^{3}	1.089×10^{20}
3.014×10^{13}	7.5×10^{10}	2.488×10^{-3}	5.28×10^{3}	4.17×10^{20}
1.315×10^{14}	1.26×10^{11}	9.582×10^{-4}	5.2×10^{3}	1.63×10^{21}
5.323×10^{14}	1.3×10^{11}	2.444×10^{-4}	4.8×10^{3}	5.99×10^{21}
1.76×10^{15}	2.2×10^{11}	1.25×10^{-4}	4.46×10^{-3}	1.90×10^{22}
4.8×10^{15}	5.06×10^{11}	1.054×10^{-4}	4.5×10^{3}	5.13×10^{22}
1.713×10^{16}	2.0×10^{12}	1.168×10^{-4}	4.8×10^{3}	2.14×10^{23}
5.606×10^{16}	8.1×10^{12}	1.445×10^{-4}	5.3×10^{3}	7.27×10^{23}
1.209×10^{17}	2.6×10^{13}	2.15×10^{-4}	5.77×10^{3}	1.58×10^{24}

Table 4.1: Atmospheric parameters for the chromospheric quiet Sun model C of Basri et al. (1979)

$n_H(cm^{-3})$	$n_e(cm^{-3})$	x (degree of ionization)	$T(K)$	$N\ (cm^{-2})$
7.733×10^{10}	4.0×10^{10}	0.5173	4.0×10^{4}	7.72×10^{18}
9.838×10^{10}	5.0×10^{10}	0.5082	3.3×10^{4}	7.74×10^{18}
1.034×10^{11}	5.3×10^{10}	0.5125	2.7×10^{4}	7.78×10^{18}
1.285×10^{11}	6.7×10^{10}	0.5214	2.2×10^{4}	7.86×10^{18}
1.407×10^{11}	7.3×10^{10}	0.5189	2.09×10^{4}	8.045×10^{18}
1.682×10^{11}	8.7×10^{10}	0.5172	1.7×10^{4}	8.55×10^{18}
1.917×10^{11}	9.5×10^{10}	0.4956	1.25×10^{4}	8.68×10^{18}
2.248×10^{11}	1.0×10^{11}	0.4448	9.0×10^{3}	9.11×10^{18}
2.62×10^{11}	1.1×10^{11}	0.4199	7.7×10^{3}	9.92×10^{18}
2.91×10^{11}	9.8×10^{10}	0.3368	6.8×10^{3}	1.11×10^{19}
5.208×10^{11}	8.2×10^{10}	0.163	6.75×10^{3}	1.58×10^{19}
1.053×10^{12}	7.3×10^{10}	0.0693	6.7×10^{3}	2.69×10^{19}
2.6×10^{12}	3.4×10^{10}	0.0131	5.7×10^{3}	4.833×10^{19}
9.689×10^{12}	4.5×10^{10}	4.64×10^{-3}	5.35×10^{3}	1.45×10^{20}
3.01×10^{13}	5.2×10^{10}	1.73×10^{-3}	5.28×10^{3}	4.23×10^{20}
1.314×10^{14}	6.5×10^{10}	4.947×10^{-4}	5.2×10^{3}	1.63×10^{21}
5.331×10^{14}	9.4×10^{11}	1.763×10^{-3}	4.8×10^{3}	5.996×10^{21}
1.76×10^{15}	2.1×10^{11}	1.193×10^{-4}	4.46×10^{3}	1.904×10^{22}
4.8×10^{15}	4.9×10^{11}	1.021×10^{-4}	4.5×10^{3}	5.13×10^{22}
1.713×10^{16}	1.9×10^{12}	1.109×10^{-4}	4.8×10^{3}	2.14×10^{23}
5.606×10^{16}	7.3×10^{12}	1.302×10^{-4}	5.03×10^{3}	7.27×10^{23}
1.21×10^{17}	2.2×10^{13}	1.826×10^{-4}	5.77×10^{3}	1.58×10^{24}

Table 4.2: Atmospheric parameters for the chromospheric model BP of Basri et al. (1979)

For the coronal region we have followed the procedure of Emslie (1981) and extrapolated across a constant pressure transition zone to an isothermal corona, using $n(N) = \frac{P_c-(N-N_c)m_H g}{2kT_0}$, where P_c and N_c are the pressure and column density of the transition zone respectively, and T_0 is the temperature of our isothermal corona which we take to be 10^6K for the quiet sun, 3×10^6K for the active region plage, 2×10^6K for active region bright points and 1.5, 2 and 4×10^7K for flare models 1, 2 and 3 respectively. The assumption of an isothermal corona can be justified on the grounds that because of the very high temperatures present in the corona the temperature gradient length scale is $L \simeq (\kappa_0 T^{7/2} I_B)^{1/2}$, where κ_0 is the coefficient of thermal conductivity and I_B is the energy deposition rate. For the corona L is of the order of $5 \times 10^{10} cm$, which is much larger than typical flare dimensions, so for our purposes an isothermal corona is adequate. Figure 4.2 - fig. 4.6 show the run of R and $x + x_m$ with N, the column density, found from these published models by translating geometric height into column density N where necessary.

We have computed $R(N)$ from (2) for these models for electron fluxes $F_1 = 10^{17} cm^{-2} s^{-1}$ and $F_1 = 1.5 \times 10^{17} cm^{-2} s^{-1}$ above $E_c = 25$ keV based on the total injection rate required for a large hard x-ray burst (Hoyng et al 1976) spread over an area of $10^{18} cm^2$. Results are shown in figures 4.2-4.5 for spectral indices $\delta = 3, 4$. These flux values have been chosen in order that the ratio of v_D/v_{is} remains less than 1 throughout the corona. Because of the relatively low densities and high dgeree of ionization, which we take to be 1 in the corona, this is a fairly stringent limit to meet and

$n_H(cm^{-3})$	$n_e(cm^{-3})$	x (degree of ionization)	$T(K)$	$N\ (cm^{-2})$
3.788×10^{11}	1.6×10^{11}	0.4224	6.0×10^{4}	3.42×10^{19}
5.457×10^{11}	2.0×10^{11}	0.3665	5.0×10^{4}	3.46×10^{19}
7.014×10^{11}	2.4×10^{11}	0.3422	4.1×10^{4}	3.59×10^{19}
9.051×10^{11}	3.4×10^{11}	0.3756	3.2×10^{4}	3.68×10^{19}
1.151×10^{12}	4.2×10^{11}	0.365	2.3×10^{4}	3.81×10^{19}
1.428×10^{12}	5.3×10^{11}	0.371	1.77×10^{4}	3.98×10^{19}
1.54×10^{12}	5.9×10^{11}	0.3832	1.44×10^{4}	4.23×10^{19}
1.505×10^{12}	6.2×10^{11}	0.412	1.11×10^{4}	4.58×10^{19}
1.683×10^{12}	6.5×10^{11}	0.3863	9.17×10^{3}	4.96×10^{19}
1.887×10^{12}	5.5×10^{11}	0.2915	7.9×10^{3}	5.39×10^{19}
1.97×10^{12}	2.8×10^{11}	0.1421	7.0×10^{3}	5.86×10^{19}
2.309×10^{12}	1.5×10^{11}	0.065	6.2×10^{3}	6.42×10^{19}
4.139×10^{12}	9.5×10^{10}	0.023	5.8×10^{3}	8.98×10^{19}
9.387×10^{12}	5.4×10^{10}	5.753×10^{-3}	5.46×10^{3}	1.63×10^{20}
3.476×10^{13}	6.2×10^{10}	1.784×10^{-3}	5.35×10^{3}	5.004×10^{20}
1.35×10^{14}	7.9×10^{10}	5.852×10^{-4}	5.24×10^{3}	1.698×10^{21}
5.322×10^{14}	9.5×10^{10}	1.785×10^{-4}	4.8×10^{3}	6.02×10^{21}
1.74×10^{15}	2.0×10^{11}	1.149×10^{-4}	4.46×10^{3}	1.885×10^{22}
4.8×10^{15}	4.9×10^{11}	1.021×10^{-4}	4.5×10^{3}	5.14×10^{22}
1.713×10^{16}	1.9×10^{12}	1.109×10^{-4}	4.8×10^{3}	2.14×10^{23}
5.606×10^{16}	7.3×10^{12}	1.302×10^{-4}	5.3×10^{3}	7.27×10^{23}
1.209×10^{17}	2.1×10^{13}	1.736×10^{-4}	5.77×10^{3}	1.58×10^{24}

Table 4.3: Atmospheric parameters for the chromospheric model P of Basri et al. (1979)

severely limits the size of the beam flux. However, if we consider that is likely that the threshold for the onset of the ion-acoustic instability is somewhat higher than $R \geq 1$, then larger beam fluxes could be considered that will still maintain the stability of the beam throughout the corona. Another point to note is that the first instability to switch on is likely to be the ion-cyclotron instability; since this preferentially heats ions and saturates early, this could also mean that we may increase the beam flux again. This instability will tend to reduce the ratio T_e/T_i and as we have noted above, the ion-acoustic instability requires that $T_e \gg T_i$, so again an increased beam flux is likely to propagate through the corona intact. The drift velocity associated with a larger beam flux will obviously be higher as well so that the Buneman instability could provide the correct conditions for the onset of ion-acoustic turbulence deep in the chromosphere. Here, however, we consider the case of $R \geq 1$ to examine first the possibility of the generation of ion-acoustic waves.

4.7 Discussion and conclusions

We see from Figure 4.4 and fig. 4.5 that the best candidate for instability for the models, fluxes and spectral indices considered, is the Basri P model of the active region plage, i.e. for a relatively cool atmosphere relevant to flare onset, as anticipated above. For both limiting cases of Λ and F_1 considered we find that v_D is consistently less than v_{is} on injection but grows with decreasing

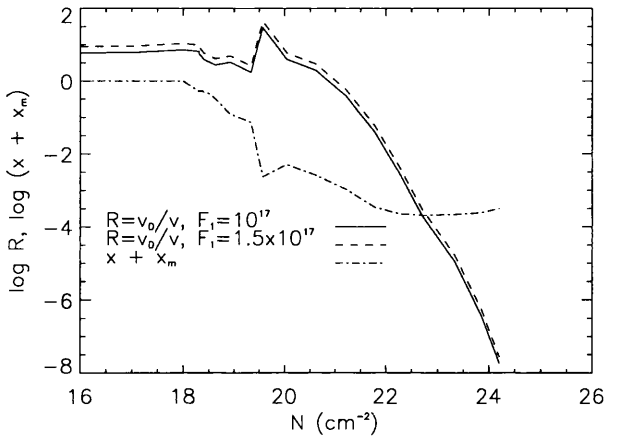

Figure 4.2: Variation of R and degree of total ionization with column density,N, for quiet sun model, Basri et al model C. $\Lambda = \Lambda_{eH}$ and $F_1 = 1.5 \times 10^{17}, 10^{17} cm^{-2} s^{-1}$, $\delta = 4$.

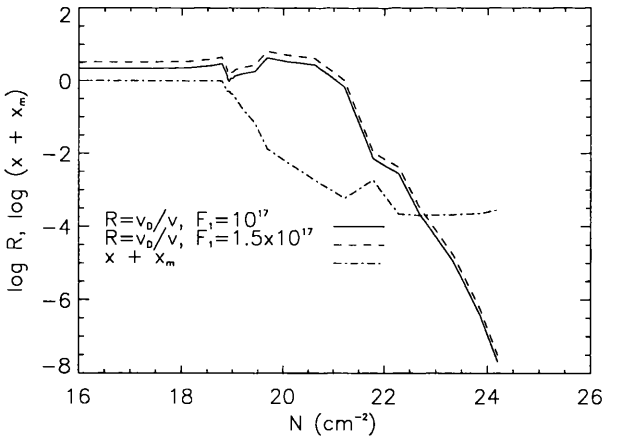

Figure 4.3: Variation of R and degree of total ionization with column density, N, for active region bright point model, Basri et al model BP. $\Lambda = \Lambda_{eH}$ and $F_1 = 1.5 \times 10^{17}, 10^{17} cm^{-2} s^{-1}$, $\delta = 4$.

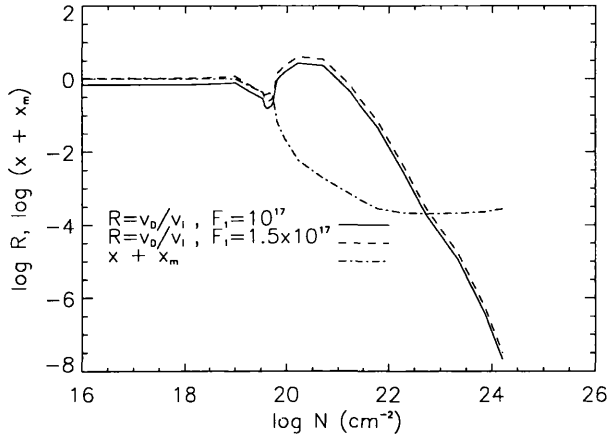

Figure 4.4: Variation of R and degree of total ionization with column density,N, for active region plage model, Basri et al model P. $\Lambda = \Lambda_{eH}$ and $F_1 = 1.5 \times 10^{17}, 10^{17} cm^{-2} s^{-1}$, $\delta = 4$.

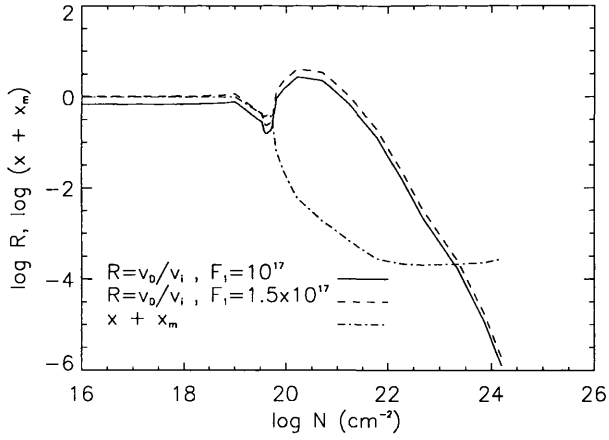

Figure 4.5: Variation of R and degree of total ionization with column density,N, for active region plage model, Basri et al model P. $\Lambda = \Lambda_{eH}$ and $F_1 = 1.5 \times 10^{17}, 10^{17} cm^{-2} s^{-1}$, $\delta = 3$.

$n_H(cm^{-3})$	$n_e(cm^{-3})$	x (degree of ionization)	$T(K)$	$N\ (cm^{-2})$
6.19×10^{12}	6.19×10^{12}	0.5	1.5×10^{4}	4.2×10^{20}
1.54×10^{13}	6.22×10^{12}	0.288	8.4×10^{3}	4.201×10^{20}
1.42×10^{13}	7.96×10^{12}	0.353	8.391×10^{3}	4.222×10^{20}
1.43×10^{13}	7.92×10^{12}	0.356	8.383×10^{3}	4.243×10^{20}
1.50×10^{13}	8.15×10^{12}	0.352	8.315×10^{3}	4.414×10^{20}
2.75×10^{13}	7.44×10^{12}	0.213	7.812×10^{3}	6.343×10^{20}
4.90×10^{13}	6.07×10^{12}	0.110	7.411×10^{3}	9.589×10^{20}
2.14×10^{14}	1.23×10^{12}	5.715×10^{-3}	6.107×10^{3}	3.119×10^{21}
7.14×10^{14}	3.26×10^{11}	4.564×10^{-4}	5.288×10^{3}	8.932×10^{21}
1.80×10^{15}	3.87×10^{11}	2.15×10^{-4}	5.116×10^{3}	2.185×10^{22}
4.60×10^{16}	6.16×10^{11}	1.339×10^{-5}	4.974×10^{3}	5.431×10^{22}
1.44×10^{16}	1.64×10^{12}	1.139×10^{-4}	5.008×10^{3}	1.707×10^{23}
5.55×10^{16}	6.67×10^{12}	1.20×10^{-4}	5.32×10^{3}	7.019×10^{23}
9.96×10^{16}	1.69×10^{13}	1.696×10^{-4}	5.72×10^{3}	1.352×10^{24}

Table 4.4: Atmospheric parameters for the chromospheric flare model, importance 1, of Machado and Linsky (1975)

ionization as N increases until the stability criterion is exceeded over a very substantial range of N. Here we show only the results for Λ_{eH}, the more relevant value in the deep chromosphere

A similar analysis applied to Basri et al. quiet sun model C, Figure 4.2, seems to indicate that the drift velocity even at the relatively low initial fluxes considered here, will always exceed the ion sound speed throughout the corona. This would lead to rapid disintegration of the beam, or coronal heating leading to stabilization.

From Figure 4.3 we can see that the results obtained for active region model BP seem to imply that beam stability through the corona in this model atmosphere would require a slightly lower initial flux than those considered here - for such a lower beam flux the stability criterion would be somewhat exceeded in the chromosphere.

Figure 4.6 shows the results obtained when considering beam propagation through Machado and Linsky's flare model atmosphere, importance 1. The coronal drift velocity is well below the ion sound speed for the conditions considered, since the corona is hot. We can see that after an initial decline, R begins to rise again to a small peak at $N \simeq 5 \times 10^{22} cm^{-2}$, but for the stability criterion to be exceeded at this level a very large initial electron flux is required to compensate for the reduction in chromospheric beam flux caused by the large densities in this model. This would produce a corresponding increase in R throughout the corona, leading to beam disintegration before such a level was reached. Results obtained using the same beam parameters for models of importances 2 and 3 are similar.

These results are summarized in Table 4.5, where the range of flux and column density for which the beam-return current system is unstable to ion-acoustic wave generation is indicated. In all of those cases shown the beam is stable throughout the corona for the threshold $R \geq 1$. In

the cases of the Basri C and BP models the fluxes shown are very low, but if we assume that the threshold for ion-acoustic wave generation is actually higher than that considered here then we see that there is a potential for the beam to become unstable in the chromosphere for all of the models considered here; including the flare model, importance 1. That is, if we could maintain the stability of a stronger beam throughout the corona.

It appears from this preliminary analysis that the low ionization in the chromosphere could provide a high enough drift velocity of those electrons free to carry the return current, sufficient to excite ion acoustic wave generation. This will, however, only occur for a limited set of conditions, particularly those in a 'cool' initial atmosphere affected by sudden beam onset. The onset of ion-acoustic waves will result in an increase in the effective collision frequency, ν_{eff}, and hence in the development of anomalous resistivity. When this occurs several effects are possible. Firstly, there may be rapid electron heating causing an increase of the value of v_{is} which will in turn reduce the value of $R(N)$. In this case the instability will switch off and the resistivity will return to a classical value. Secondly, the increased heating associated with anomalous resistivity may lead to increased collisional ionization of the ambient plasma. In this case $x(N) + x_m$ will increase, $R(N)$ will correspondingly decrease, and again the instability will switch off. However, if the resistivity remains anomalous on a sufficiently long timescale than we will find that the beam is strongly decelerated over a very short distance. The reason for this strong deceleration is that the electric field of the return current will increase, since $E = \eta J_p = \eta J_b$, and it is this increased electric field which decelerates the beam.

Anomalous resistivity increases the rate of Ohmic return current dissipation and the timescale on which the beam is stopped is given by $\tau_{stop} = (n_p/n_b)2/\nu_{eff}$ seconds (van den Oord, 1990). The beam is then stopped over a distance $v_b \tau_{stop} \simeq 30\beta(n_p/n_b)$ cm. At the point where this occurs there will be very significant anomalous Ohmic energy deposition in the atmosphere.

Abourdarham and Hénoux (1985) showed that whitelight flare continuum emission can be produced as a result of heating caused by electron bombardment in the chromosphere. For an electron flux with a low energy cut-off at 80 keV they calculated that an energy flux of $2.5 \times 10^{10} erg\ cm^{-2}\ s^{-1}$ is required to produce the observed emission. If we consider the model atmosphere P of Basri et al. (1979) then we can see that the a beam of 80 keV electrons would be stopped by the deceleration described above in a distance of $\sim 9 \times 10^6$ cm. For this model $R(N) > 1$ over a range of column depths $\sim 6 \times 10^{19} - 5 \times 10^{20} cm^{-2}$. Therefore, it is likely that there will then be very significant anomalous Ohmic energy deposition in the layers of the atmosphere where anomalous resistivity dominates, capable of producing whitelight continuum emission.

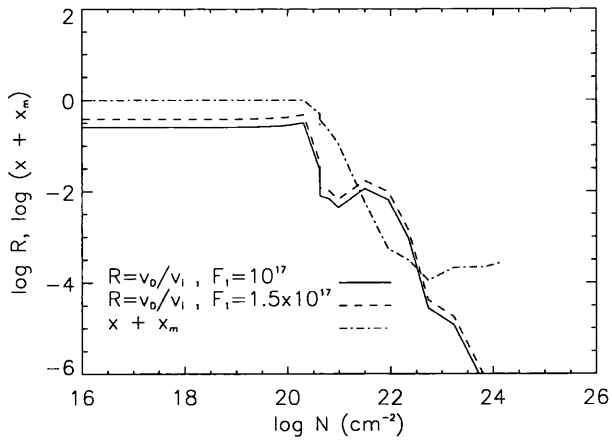

Figure 4.6: Variation of R and degree of total ionization with column density, N, for flare model importance 1, Machado and Linsky. $\Lambda = \Lambda_{eH}$ and $F_1 = 1.5 \times 10^{17}, 10^{17} cm^{-2} s^{-1}$, $\delta = 4$.

The ratio of return current to beam collisional heating rates at a depth N is given by

$$\frac{P_{RC}}{P_{coll}} = \alpha \times \frac{\left[\frac{7.26\times10^{-9}x}{T^{3/2}} ln\left[\frac{3}{2e^3}\left(\frac{k_B^3 T^3}{\pi n}\right)^{1/2}\right] + A\right] F_b^2 e^2}{\pi e^4 n\gamma(\delta-2)B(\delta/2, \frac{2}{4+\beta})\mathcal{F}_1\left[\frac{(2+\beta/2)\gamma KN}{E_1^2}\right]^{-\delta/2}} \tag{4.29}$$

where α is the factor by which the resistivity is enhanced over the collisional value, and for an electron beam:

$$A = \frac{7.6 \times 10^{-18}(1-x)T^{1/2}}{x} \tag{4.30}$$

$$\beta = \frac{2x\Lambda_{ee} + (1-x)(\Lambda" - \Lambda_{eH})}{\Lambda_{eH} + x(\Lambda_{ee} - \Lambda eH)} \tag{4.31}$$

$$\Lambda" = ln\left[\frac{1}{\alpha}\left(\frac{m}{m_e}\right)\left(\frac{v}{c}\right)\right] \tag{4.32}$$

(Emslie, 1978) and

$$\gamma = m/m_e[x\Lambda_{ee} + (1-x)\Lambda_{eH}] \tag{4.33}$$

For the fluxes used in Fig. 4.4 and at N values near the peak in R, this ratio is about $0.05 \times \alpha$. Thus, we see that if the resistivity is enhanced by wave generation by a factor $\alpha > 20$, then return current heating will dominate in this part of the chromosphere.

In the next chapter we consider a number of white-light flares observed by Yohkoh and examine the parameters of the hard X-ray producing electron beams in terms of this analysis. We will consider whether the values of F_1 and δ derived from the hard X-ray observations associated with the white-light flare are compatible with those values that we have shown to be susceptible to the ion-acoustic instability.

Model	Flux ($cm^{-2}s^{-1}$)	Range of N where $R(N) > 1$
BP	2.4×10^{16}	$4.833 - 4.93 \times 10^{19}$
	$2.5 - 2.6 \times 10^{16}$	$4.833 - 5.0 \times 10^{19}$
	$2.7 - 2.8 \times 10^{16}$	$4.833 - 5.5 \times 10^{19}$
	$2.9 - 3.0 \times 10^{16}$	$4.833 - 6.0 \times 10^{19}$
	3.1×10^{16}	$4.833 \times 10^{19} - 1.45 \times 10^{20}$
	$3.2 - 3.5 \times 10^{16}$	$4.833 \times 10^{19} - 1.6 \times 10^{20}$
	3.6×10^{16}	$4.833 \times 10^{19} - 1.8 \times 10^{20}$
	$3.7 - 4.4 \times 10^{16}$	$4.833 \times 10^{19} - 4.23 \times 10^{20}$
P	$3.7 - 1.3 \times 10^{16}$	$1.63 - 1.634 \times 10^{20}$
	3.8×10^{16}	$1.63 - 1.67 \times 10^{20}$
	$3.9 - 4.0 \times 10^{16}$	$1.62 - 1.7 \times 10^{20}$
	4.1×10^{16}	$1.60 - 1.8 \times 10^{20}$
	4.2×10^{16}	$1.59 - 1.8 \times 10^{20}$
	4.3×10^{16}	$1.58 - 1.8 \times 10^{20}$
	$4.4 - 6.6 \times 10^{16}$	$1.63 - 5.004 \times 10^{20}$
	$6.7 \times 10^{16} - 1.0 \times 10^{17}$	$8.98 \times 10^{19} - 5.004 \times 10^{20}$
	$1.1 - 1.3 \times 1017$	$6.42 \times 10^{19} - 5.004 \times 10^{20}$
C	$4 - 5 \times 10^{15}$	$3.2 - 3.71 \times 10^{19}$
	$6 \times 10^{15} - 1.3 \times 10^{16}$	$2.5 - 4 \times 10^{19}$
	$9 \times 10^{15} - 1.3 \times 10^{16}$	$2.5 - 6 \times 10^{19}$
	$1.2 - 1.3 \times 10^{16}$	$2.5 - 7 \times 10^{19}$

Table 4.5: The range of column densities over which $R(N) > 1$ for a variety of F_1 in the models Basri C, BP and P. All of these fluxes are stable throughout the corona. Since stability in the corona with instability in the chromosphere cannot be achieved for the flare model importance 1 this is not shown.

Chapter 5

Return Currents and the White-Light Flare Phenomenon

5.1 Introduction

Following the results of Chapter 4, we consider the possibility that anomalous resistivity generated by the onset of the ion-acoustic instability in the electron beam/return current system can produce a significant enough energy deposition in the deep chromosphere to account for the white-light emission that is observed in solar flares.

Firstly, we will review the observational data available on white-light emission and the existing theories for its production. We will then consider four white-light flares observed with the aspect camera of the SXT instrument on Yohkoh and investigate the correlation between the possible onset of anomalous resistivity, driven by ion-acoustic turbulence, and the white-light emission.

5.2 Observations

White-Light flares are characterized by an increase in emission in the visible range and in integrated light. These enhancements can be seen as patches, waves or ribbons, often with < 3" kernels (Neidig and Cliver, 1983; Canfield et al., 1986). In 1989, small aperture patrol telescopes, observing in the range $\lambda < 4000\mathring{A}$, were reporting about 15 white-light flares a year near solar maximum. The observations indicate that the origin of this emission is in the low chromosphere and upper photosphere, implying that these layers are being heated during the flare. One of the most important questions that white-light emission in solar flares raises is whether this temperature increase can be explained in terms of the transport of energy from the corona, or whether it requires either partial or total in situ energy release.

Traditionally white-light flares (hereafter WLFs) have always been thought of as rare events associated with very large and energetic flares. However, the advent of ground-based WLF patrols (Neidig, 1989) and space-based observations (Hudson et al., 1992) has shown that, in fact, probably all flares have some kind of enhanced continuum emission, the apparent rarity being a detection threshold effect. Indeed, M class flares have been detected by the SXT Aspect Camera on *Yohkoh* (Hudson et al., 1994).

There are several reasons for the difficulties in WLF detection. Firstly, as noted by van Driel-Gesztelyi et al. (1994), these events often occur in regions which already show large image contrast, e.g. sunspots and faculae, which makes WLF identification difficult. Other problems include the non-linear response of the film which is usually used to record these events and the effects of poor seeing, although space-based observations such as those from *Yohkoh* are obviously free from the effects of poor seeing.

WLFs can be divided into two types according to their spectral features (Machado et al., 1986). Type I events are usually the brightest events and show a Balmer jump at $3.64\mathring{A}$ and probably a Paschen discontinuity. The Balmer lines in this type of event are strong and very broad, generally with strong central reversals. Type II events show continuum enhancement with no Balmer jump and weak Balmer lines, with no lines above HII appearing.

The emission in WLFs has been attributed to either hydrogen free-bound transitions to the second and third levels, i.e. Balmer and Paschen continua, or to H^- emission processes (e.g. Svéstka, 1976). The first of these emission processes is linked with Type I events, the latter with Type II emission. The emission process relates directly to the location of the WLF source in the atmosphere, and, as a result, constrains the possible heating mechanisms. For Type I events where the emission is considered to be due to bound-free transitions in H, strong heating must occur up to temperatures $\sim 10^4$ K in deep chromospheric layers characterized by $m > 10^{-2}\mathrm{gcm}^{-2}$ and number densities $n_H > 10^{14}$ cm^{-3} (Machado et al., 1989). These conditions have to be satisfied in order for there to be sufficient opacity in the Paschen continuum region to produce the required brightness enhancement over the photospheric background. This hypothesis has received support from observations of Balmer and Paschen jumps in strong events (Neidig and Wiborg, 1984; Neidig, 1986). If the emission is due to H^- then the source of the WLF must be in the upper photosphere, below the temperature minimum at $m > 0.1$ g cm^{-2} and $n_H > 10^{16}cm^{-3}$. Again these conditions are necessary to provide sufficient opacity to produce the observed brightness enhancements with relatively small ($\sim$ 100 K) temperature enhancements.

It is widely believed that the energy release in solar flares occurs in the corona and the energy is then transported to the low chromosphere where the optical emission is produced. This transport mechanism, however, is still a matter for debate with investigations based on the comparison of modelled energy deposition rates with measurements of radiative losses as a function of height.

WLFs represent the largest fraction of the total flare radiative output (Neidig, 1989), so the study of WLFs is important from the point of view of establishing whether the heating of these low atmospheric layers is due to energy transport mechanisms or whether some in situ energy release is occurring at these layers. The huge radiative losses associated with the continuum emission ($> 10^{28}$ erg s^{-1}) place very strong constraints on any energy transport mechanism.

Ground-based WLF patrols generally take data in the broadband $10 - 100\mathring{A}$ range at several different wavelengths. These bands are usually chosen to avoid strong chromospheric flare lines, although it is still difficult to completely exclude the various narrow phtotospheric and low chromospheric absorption lines. As a result this data cannot be considered to be pure continuum. Neidig (1989) demonstrated that the spectra are relatively flat at $\lambda > 4000\mathring{A}$ but begin to show a marked increase at wavelengths below this. WLFs are much brighter at $\sim 3600\mathring{A}$ than at $5000\mathring{A}$, i.e. they are blue. This blueness has been attributed to (Neidig, 1989):

1. the presence of the Balmer continuum
2. the higher temperature of the flare relative to the quiet Sun
3. the merging of Balmer lines near the Balmer limit (Donati-Falciani et al., 1986)
4. emission in photospheric and low chromospheric lines which become more numerous at shorter wavelengths

5.2.1 Possible energy transport mechanisms

Various existing theories for plausible energy transport mechanisms capable of powering the WLF have been reviewed by Neidig (1989), these are as follows:

Heat conduction -Assuming that the conductivity is the classical value given by Spitzer (1962) and employing the constant density and pressure assumptions of Schmeleva and Syrovatskii (1973) it can be seen that the temperature gradient required to sustain the required fluxes results in an emission measure at $T < 10^5$ K that is too small to radiate the observed flux (Brown, 1973).

Electron beams - According to the thick target model of hard X-ray production (e.g. Brown, 1971), the total power in a beam of nonthermal electrons with energy $E \geq 50$ keV is sufficient to power the chromospheric WLF emission (Kane et al., 1986; Canfield et al., 1986). Electrons in this energy range are stopped at a depth in the atmosphere corresponding to $n_H > 10^{13.5} cm^{-3}$, appropriate for chromospheric WLFs. The observed simultaneity between the HXR and WLF emission time profiles also lends considerable support to this hypothesis. However, it is highly improbable that electron beams would be capable of producing photospheric WLF emission since this would require electron energies in excess of 900 keV, which carry too little power.

High energy protons - There is certainly sufficient energy associated with a beam of > 4 MeV protons, but analysis of γ-ray and WLF observations from the July 1 1980 flare by Ryan et al.

(1983) showed that thick target heating by energetic protons was insufficient at the time of peak WLF emission. Ryan et al. (1983) and Canfield et al. (1986) also concluded that during the impulsive phase, which occurred well before the WLF emission, the flare could equally well have been powered by protons or electrons. Generally, there is no observed correlation between the γ-ray and WLF emission.

Low energy protons - Simnett (1986) proposed that the bulk of the flare energy went into low energy protons. These are stopped at a relatively low chromospheric density, resulting in explosive heating and a downward propagating compression wave. In this model the HXR emission is thermally produced. This possibility can not at present actually be ruled out as it is difficult to distinguish between thermally and non-thermally produced HXR emission and there are few actual diagnostics for low energy protons. However, observations of H_α impact polarization (Hénoux and Chambe, 1990) may provide a key to establishing whether low energy protons do play a rôle.

Soft X-ray irradiation $(1 - 8\mathring{A})$ - At the peak of the WLF emission the power in the $1 - 8\mathring{A}$ range directed towards the solar surface is 10^{-1} of the observed power of the WLF. This makes this a very unlikely mechanism.

EUV irradiation $(10 - 1030\mathring{A})$ - WLFs are associated with a large EUV flux (McIntosh and Donnelly, 1972) of around $6 - 23 \times 10^{27}$ erg s^{-1}; and there is a correlation between the EUV and HXR fluxes. The problem is whether or not EUV photons have a sufficient range in an atmosphere that is normally opaque to EUV radiation. Poland et al. (1987) showed that EUV radiation $< 912\mathring{A}$ cannot be the sole energy source but can contribute.

Alfvén waves - Emslie and Sturrock (1982) proposed Alfvén wave dissipation in regions of high resistivity as a means of explaining the heating of the temperature minimum region in ordinary flares (Macahdo et al., 1978). However, they made no attempt to account for the 10^3 erg cm$^{-3}s^{-1}$ rates which apply in WLFs. Delays of several seconds would be expected between the HXR and WLF emission in this case because of the finite wave velocity.

We showed in the previous chapter that it is possible for the return current driven by a thick target electron beam to be unstable to the generation of ion-acoustic waves. The generation of such turbulence leads to an enhanced level of resistivity in the region and an enhanced level of Ohmic energy deposition. In this chapter we will consider that this enhanced level of energy deposition is sufficient to power the WLF.

5.3 The White-Light events

For the purposes of establishing whether there is indeed a connection worth pursuing between anomalous heating caused by a return current instability and white-light flare emission four events observed by *Yohkoh* which exhibited white-light emission were studied. These events (October

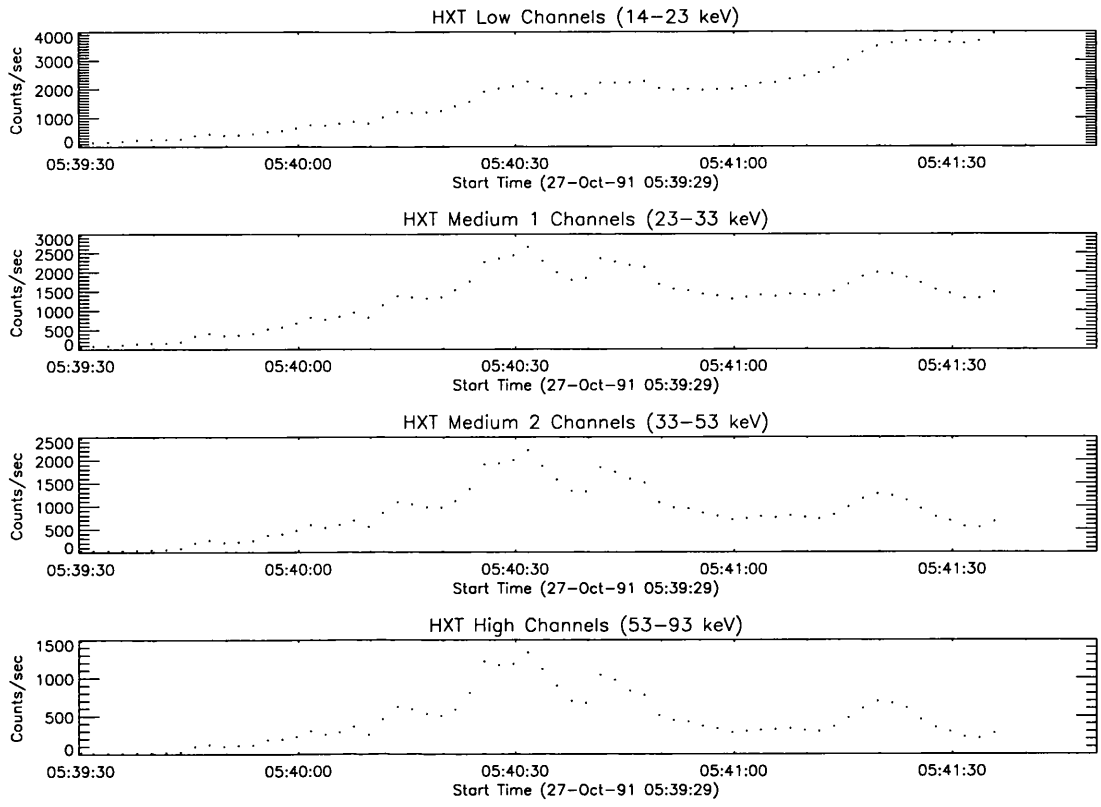

Figure 5.1: Light curves in the 4 channels of HXT for the event of October 27 1991.

27 1991; November 15 1991; January 26 1992 and February 14 1992) formed part of a white-light survey by Hudson et al. (1994) and van Driel-Gesztelyi et al. (1994). They have also been the subject of studies by other members of the *Yohkoh* team in different wavelength ranges (e.g. Culhane et al., 1993, Kawabata et al., 1994, Yoshimori et al., 1994, McTiernan, 1994).

October 27 1991

This event occurred at S13E15 in NOAA active region 6891. The GOES satellite records the start of the flare as 05:37 UT with emission continuing until 07:12 UT. The start of the hard X-ray emission recorded by HXT was 05:47. However, the flare began in a data gap preceding this time. The GOES class was X6.1 and the H_α importance 3B. This event was also observed by the Nobeyama radioheliograph. Hard X-ray light curves in all four channels of the HXT and the white-light light curve for the whole event are shown in fig. 5.1 and fig. 5.2, respectively. The evolution of the spectral index for each footpoint is also shown in fig. 5.3.

November 15 1991

The event of November 15 1991 occurred in NOAA active region 6919 at S14W19, commencing at 22:34 UT. The GOES class of this event was X1.5 and the H_α importance 2B. Flare mode was triggered at 24:34:38 UT. As well as white-light emission both γ-ray line and continuum emission

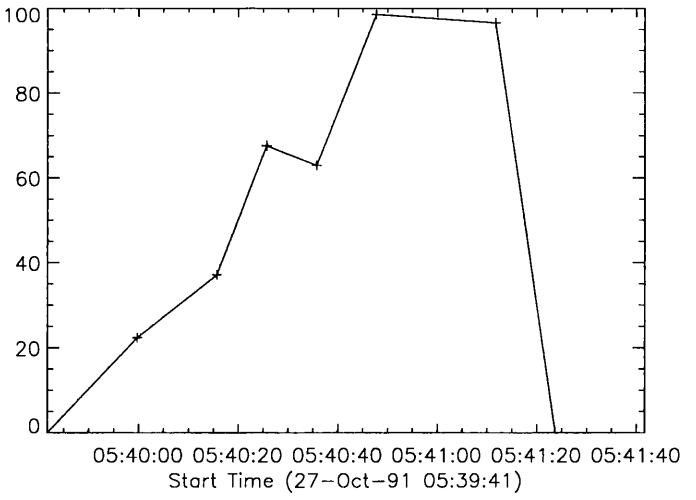

Figure 5.2: Light curve of the total white-light emission for October 27 1991.

were observed from this event. This event was also observed by the Solar X-ray/Cosmic Gamma-Ray Burst Experiment (Hurley et al., 1992) aboard Ulysses, the hard X-ray and γ-ray spectrometers on PVO, the Compton Gamma ray Observatory and the Nobeyama Radioheliograph. It has been extensively studied in the hard X-ray range by Sakao (1994) and before BCS saturation at 22:37 UT by Culhane et al. (1993). Again the hard X-ray light curves and light curve for the total white-light emission are shown in fig. 5.4 and fig. 5.5, respectively. Spectral index evolution for each hard X-ray footpoint is shown in fig. 5.6 and fig. 5.7.

January 26 1992

This flare occurred in NOAA active region 7012 at S16W66. It commenced at 15:21 UT and had GOES class X1.0 and H_α importance 3B. Flare mode was triggered at 15:24:53 UT. This event was a 'spotless' flare. Light curves for the 4 HXT channels and the white-light emission are shown in fig. 5.8 and fig. 5.9. Fig. 5.10 shows the evolution of the hard X-ray spectral index throughout the event for each footpoint.

February 14 1992

This flare commenced at 23:04 UT in NOAA active region 7056 at S13E02. It was a GOES class M7.0 event with H_α importance 2B. It was also observed by the Nobeyama Radioheliograph. Figure 5.11 shows light curves for all four HXT channels and for the total white-light emission from the event.

5.4 Data Analysis

The four events which were considered have been described briefly above. Since we are interested in the heating caused by a thick target electron beam and its relationship to the white-light flare

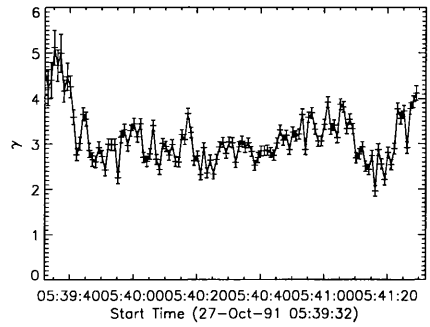

(a)

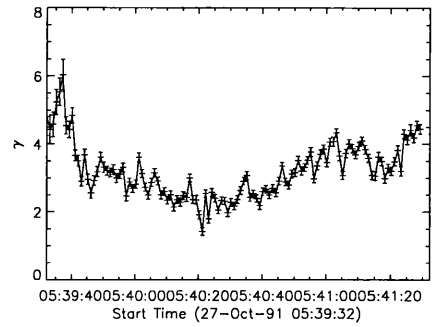

(b)

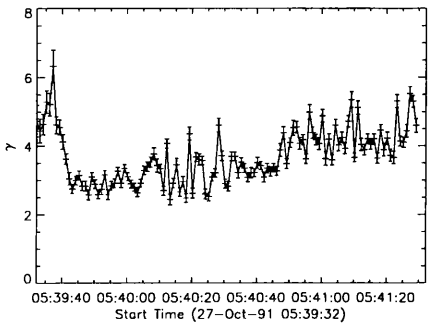

(c)

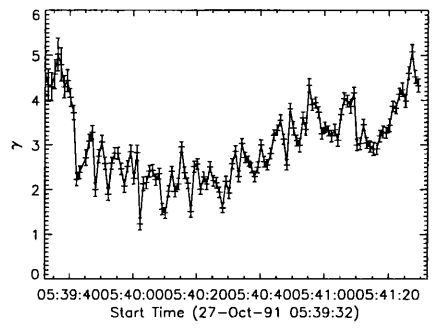

(d)

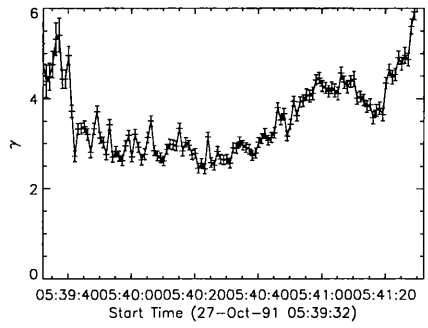

(e)

Figure 5.3: Evolution of the hard X-ray spectral index, γ, for the event of October 27 1991. Fig. a) shows footpoint A, fig. b) footpoint B and so on.

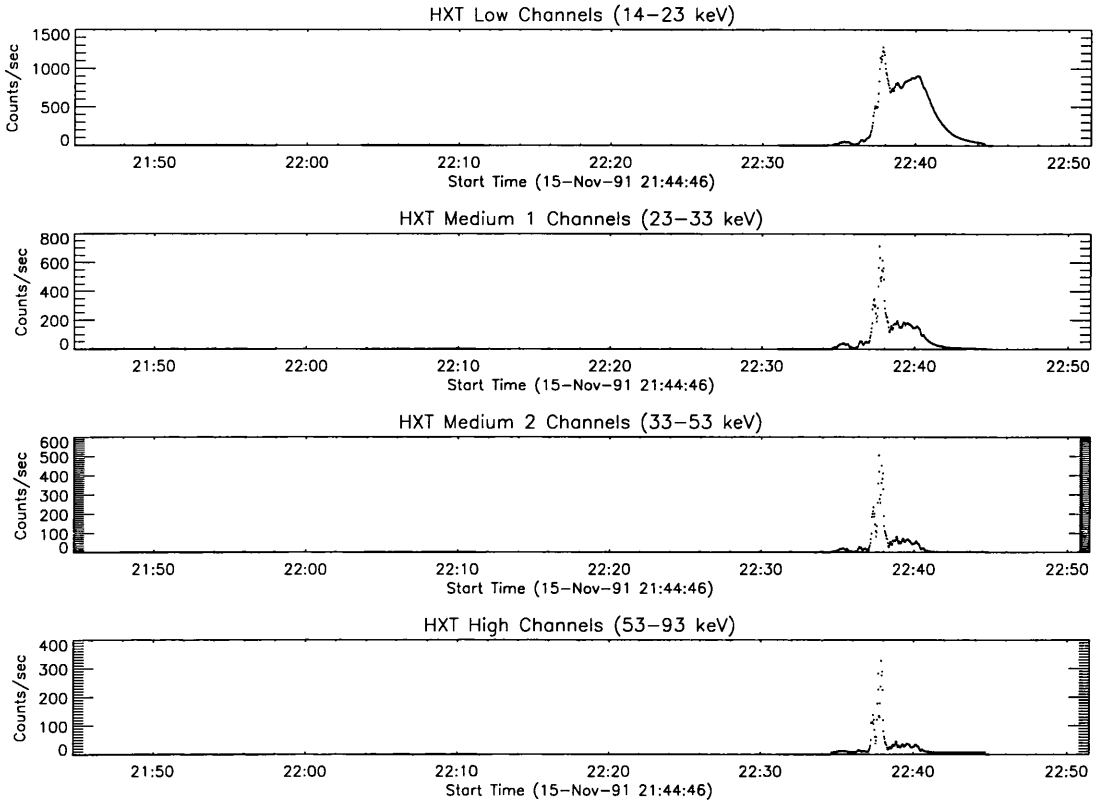

Figure 5.4: Light curves in the 4 channels of HXT for the event of November 15 1991.

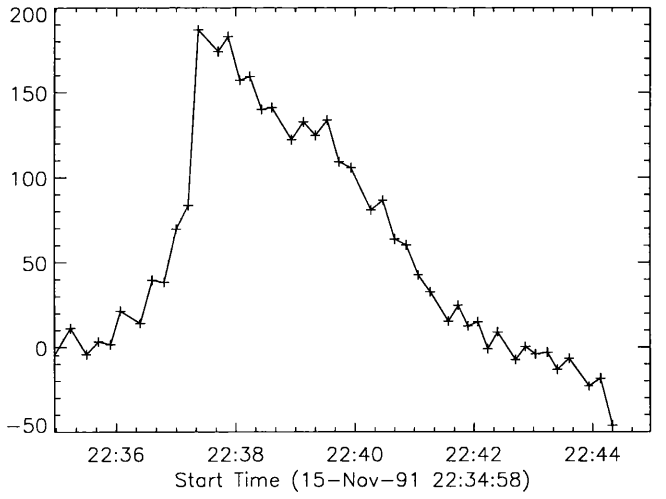

Figure 5.5: Light curve of the total white-light emission for November 15 1991.

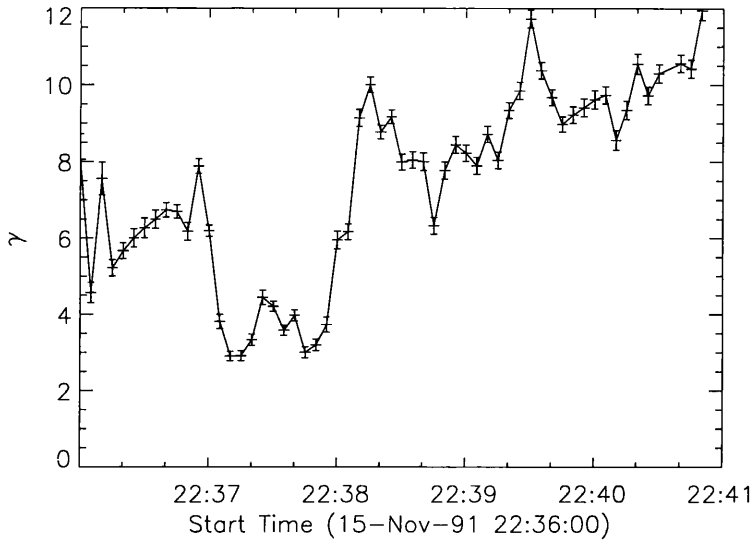

Figure 5.6: Evolution of the spectral index γ of the hard X-ray photon spectrum for footpoint B of November 15 1991.

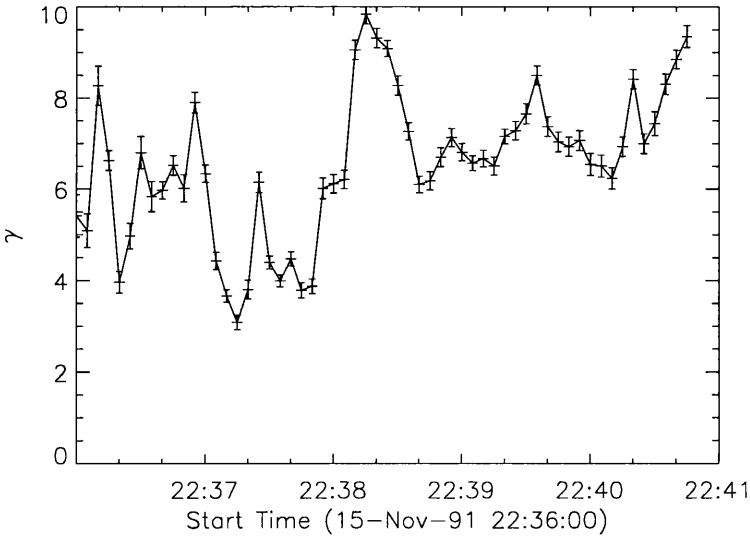

Figure 5.7: As fig. 5.6 for footpoint A.

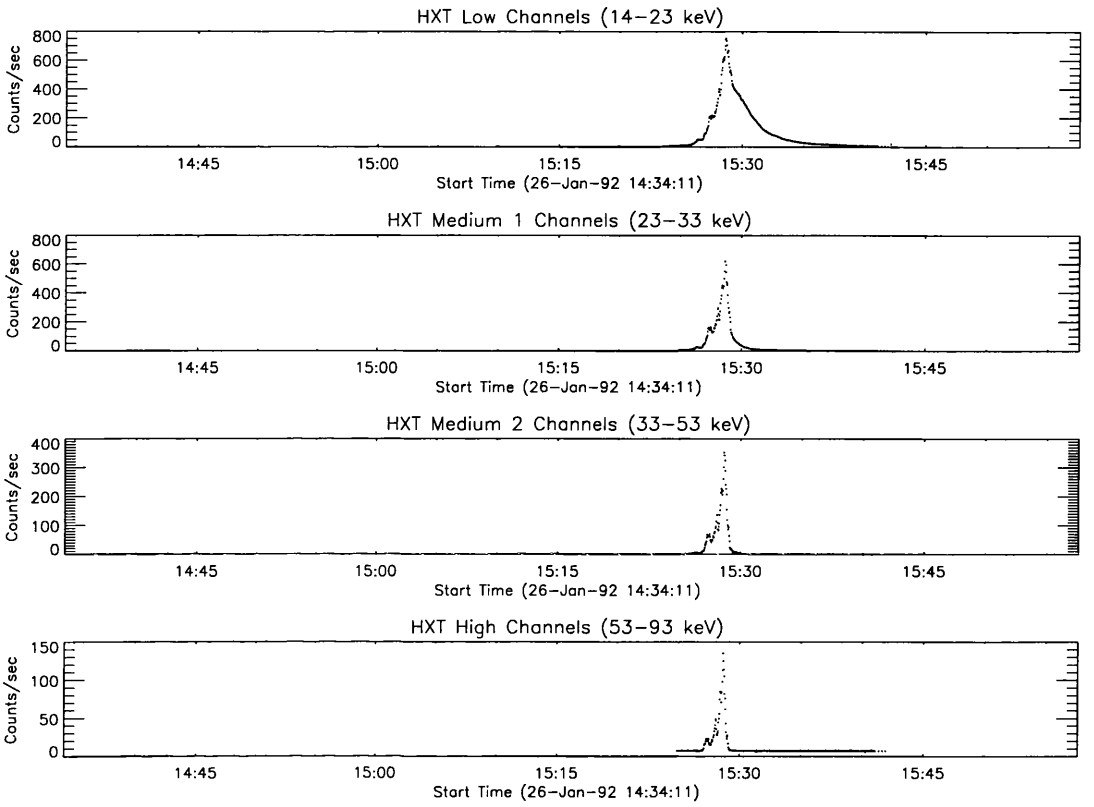

Figure 5.8: Light curves in the 4 channels of HXT for the event of January 26 1992.

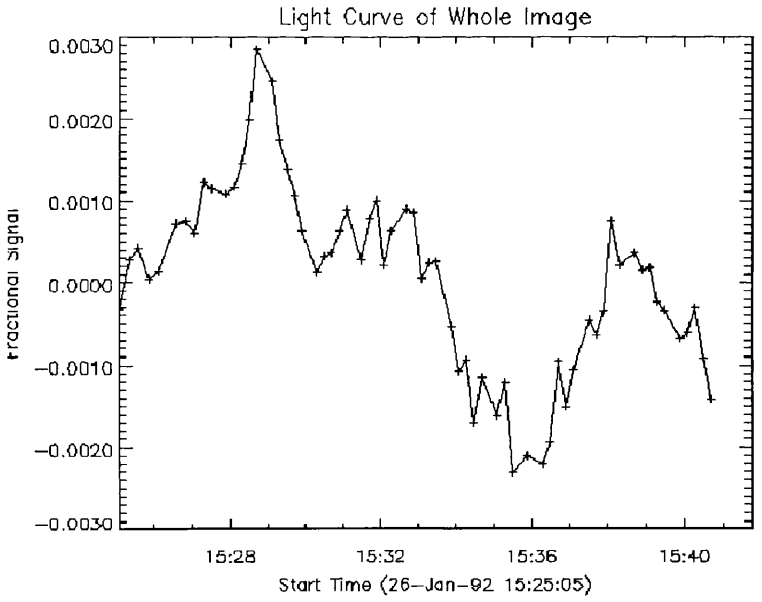

Figure 5.9: Light curve of the total white-light emission for the event of January 26 1992.

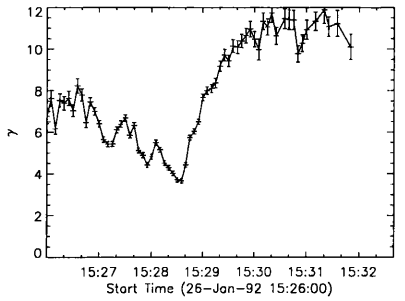

(a)

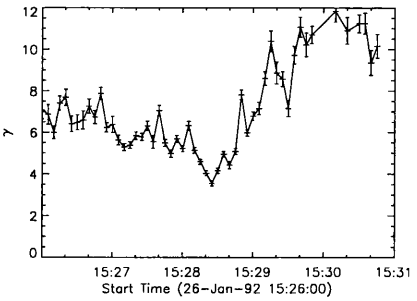

(b)

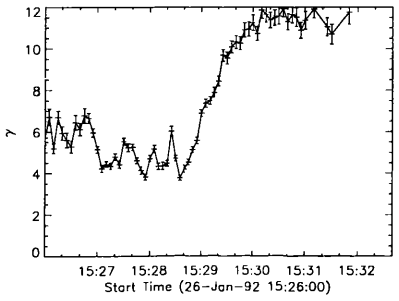

(c)

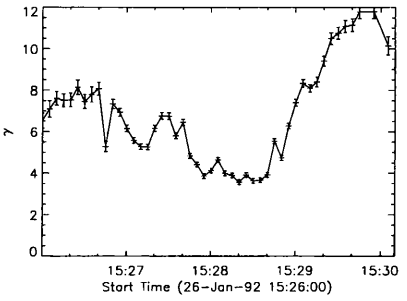

(d)

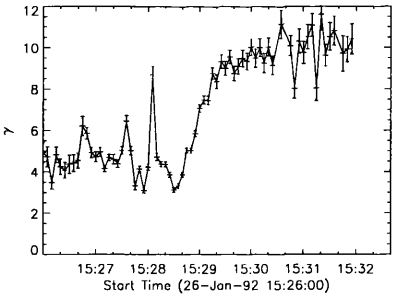

(e)

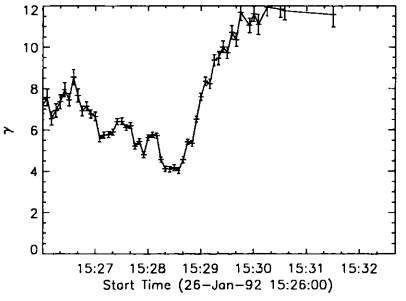

(f)

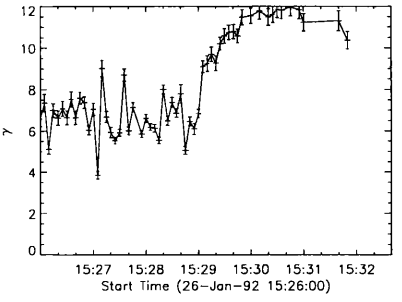

(g)

Figure 5.10: Evolution of the hard X-ray spectral index, γ, for the event of Janauary 26 1992. Fig. a) is footpoint A, fig. b) footpoint B and so on.

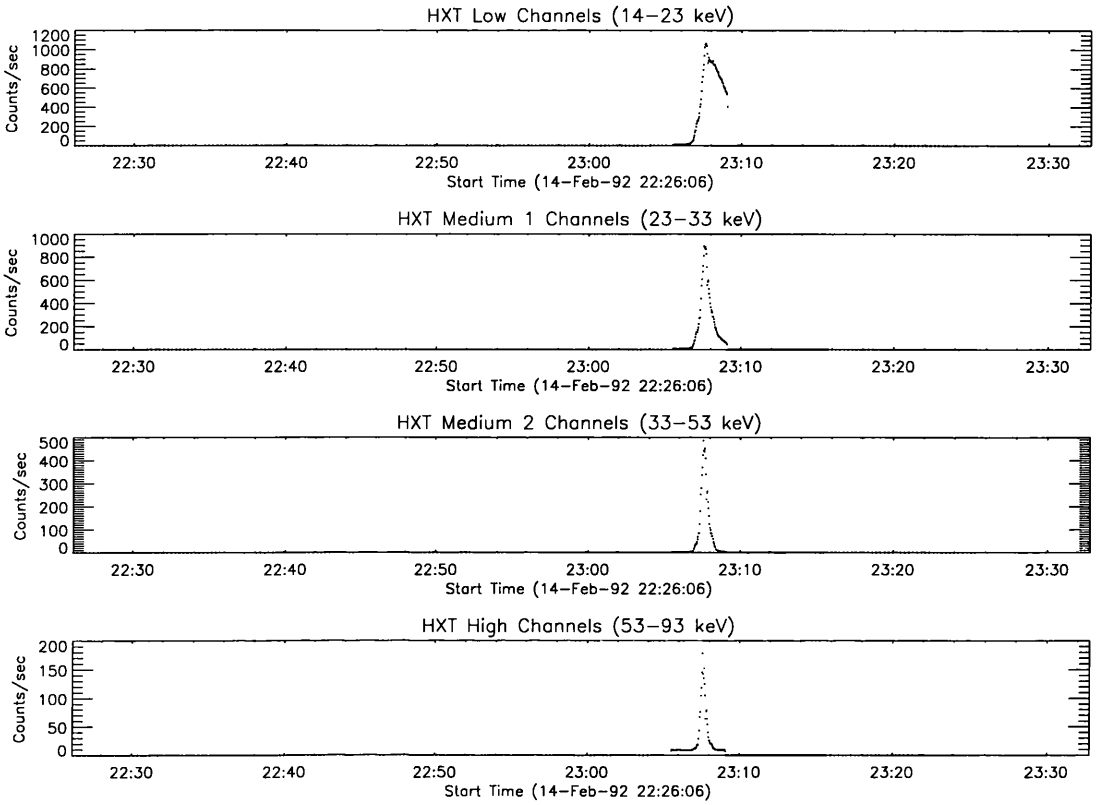

Figure 5.11: Light curves in the 4 channels of HXT for the event of February 14 1992.

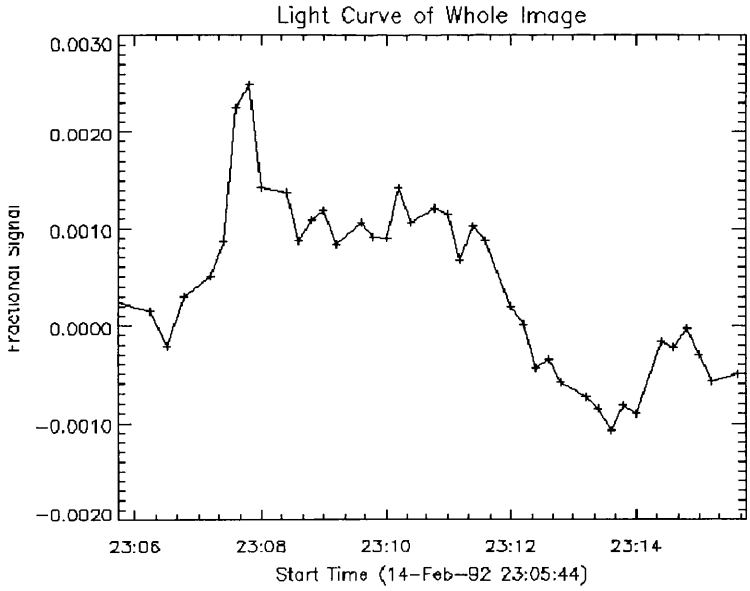

Figure 5.12: Light curve of the total white-light emission of February 14 1992.

we require both hard X-ray and white-light data.

5.4.1 White-light movies

The Soft X-ray Telescope on board *Yohkoh* has an aspect camera (no longer operational) which provides white-light images at 431 nm with a bandpass of 3 nm. The image interval is typically 10-12 seconds and this is the first white-light data which has been obtained from outside the Earth's atmosphere.

The preparation of the white-light data is based on the timewise application of photographic cancellation (Uchida and Hudson, 1972). This technique, first pioneered by Leighton (1960) for observing photospheric velocity fields, provides improved detection of time varying small features. It works by first making a positive copy of a time series of WLF images around the time of the flare and overlaying it on a negative series shifted by various time intervals or a number of frames. In this way time stationary features should cancel. By subtracting a pre-flare image of the active region the white-light emission is easier to detect. The routine used here to prepare the white-light movies was written by Hugh Hudson.

Once a series of white-light images has been obtained a light curve is prepared for each kernel of emission throughout the event. It is important when making light curves to ensure that the area selected around each kernel is the same size (van Driel-Gesztelyi - private communication) to ensure that comparisons between the intensities are meaningful. There is a significant amount of fluctuation in the light curves of the non-flaring regions surrounding the white-light patches and there is no reason to suspect that this is not the case for the areas of enhanced emission as well. For this reason the value of the average background fluctuation in each event is calculated and can be thought of as the error on the light curves for the white-light emission.

5.4.2 Hard X-ray Image Synthesis

Since we wish to consider the possibility that anomalous heating caused by an unstable return current accompanying a thick target electron beam is responsible for the WLF emission, we have to establish that there is spatial coincidence between the WLF emission and the hard X-ray emission. In fact, before even going that far we need to establish that there is a temporal relationship between the two emissions - if the WLF emission occurs *before* the hard X-ray emission then the same electron population cannot be responsible for producing both types of emission. Also, if there is a long delay between the hard X-ray emission and the white-light it is less likely that the two are connected by the same parent distribution. Figure 5.13, fig. 5.14, fig. 5.23, fig. 5.24, fig. 5.36, fig. 5.37, fig. 5.48, fig. 5.49, fig. 5.50 and fig. 5.51 show the hard X-ray light curves overlaid with the light curves of the white-light emission for the whole event.

Image synthesis was carried out in all four channels of HXT for all four events that were

studied. This was necessary in order to establish a spatial coincidence between the hard X-ray kernels and the white-light kernels. Without this spatial coincidence it is highly unlikely that the electron population responsible for the hard X-ray emission can be connected with the white-light emission.

The image synthesis itself was performed using an IDL version (McTiernan, 1994) of a fortran code written by Sakao (1994). This code employs a Maximum Entropy algorithm to reconstruct the images. Before discussing briefly how Maximum Entropy works there are several general points that should be addressed about image reconstruction.

Firstly, there is the issue of background subtraction. Inappropriate background subtraction can often lead to spurious sources and generally strange results. Typical background rates in the four channels are given in Table 2.2. It is usually safest to select the background accumulation time in the HI channel. The other important thing to make sure of is that the background data is all in the same mode, i.e. flare mode rather than a mixture of e.g. quiet and flare modes, and that this mode is the same as that of the image accumulation time. The frame where the mode switch occurs can be problematic.

Secondly, and most pertinent to the use of the Maximum Entropy algorithm, is the issue of the count rate in the individual channels. MEM will not produce statistically significant images for a count rate $\lesssim 100$ counts/subcollimator. This makes it difficult to observe the beginning of flares at high resolution in the higher energy channels of HXT. It is important also to be aware that unless the images are very well converged the non-linear nature of MEM makes the derivation of reliable quantitative results difficult.

In principle, since the data from HXT is a time series of sets of 64 two-dimensional Fourier components, a two-dimensional Fourier transform should be sufficient to reconstruct the original brightness distribution. In practice, however, because of the limited UV coverage and the fact that the modulation patterns are really triangular rather than sinusoidal, this proves ineffective.

The first step in performing the image reconstruction, after background subtraction, is to accurately determine the flare position on the solar disk in HXT co-ordinates. This enables the synthesis aperture to be defined and the reconstruction proceeds on the premise that no hard X-ray sources contribute to the count rate from outside this field of view. An accurate determination of the flare location is also useful for alignment with soft X-ray images from SXT.

Determining the flare location involves constructing a so-called 'dirty map'. When there are a limited number of 2-D Fourier components (i.e. limited UV coverage) for a particular brightness distribution then a simple reconstruction through inverse Fourier transform gives a 'dirty map' with spurious structure like side lobes and repetitive patterns. This map also has negative data points since the DC level is subtracted from every Fourier component. However, it is still possible to see a brightness enhancement in such a map at the source location, and this is used as a first

estimate of the source location.

The details of the dirty map construction can be found in Sakao (1994) but are essentially the following. Firstly, the DC count is determined from the background subtracted counts. This is just the expected incident count for each subcollimator from a flat brightness distribution. Using this information the actual observed DC level subtracted counts are determined for each subcollimator. From these values the Fourier components for both the fanbeam and Fourier grids are obtained (see Sakao, 1994) and the value of each pixel in the dirty map is estimated.

In order to reconstruct the original hard X-ray brightness distribution we have not only to invert the Fourier components, but also to consider that these measurements are convolved with the instrumental response function.

The observed X-ray count rate, b_k^0, for the kth modulation collimator due to a brightness distribution, B_{ij}, is given for the two-dimensional response matrix $P_{ij,k}$ by (Sakao, 1994)

$$b_k^0 = \sum_{i,j=1}^{N} P_{ij,k} B_{ij}^0 + n_k^0 \tag{5.1}$$

where n_k^0 are the uncertainties in the measured count due to Poisson statistics and systematic errors. A detailed discussion of the response matrix for each subcollimator is again given in Sakao (1994).

5.4.3 Maximum Entropy Method (MEM)

The Maximum Entropy Method (MEM) employed for HXT image synthesis is based on that of Gull and Daniell (1978) and Willingdale (1981). MEM works by maximizing a quantity called entropy within the constraints of the observations. The main advantages of MEM image reconstruction are that it chooses the smoothest solution consistent with the data; it reconstructs positive images and it handles Poisson errors well.

The maximum entropy solution correspondng to the equation 5.1 is

$$b_k = \sum_{i,j=1}^{N} P_{ij,k} B_{ij} \tag{5.2}$$

where B_{ij} is the MEM image of the source. The entropy term adopted by Sakao (1994) is that of Frieden (1972):

$$S = -\sum_{i,j=1}^{N} \left(\frac{B_{ij}}{\bar{B_0}}\right) ln \left(\frac{B_{ij}}{\bar{B_0}}\right) \tag{5.3}$$

where $\bar{B_0}$ is the average incident photon count per pixel,

$$\bar{B_0} = \frac{1}{N^2} B_0^{tot} \tag{5.4}$$

A larger value of S implies less information. What this means is that if the entropy is maximized with no observational constraints then the result is a flat brightness distribution. The basic idea then is to reconstruct a brightness distribution with the maximum entropy value that gives b_k consistent with the observations, b_k^0, i.e.

$$\chi^2 = \frac{1}{64}\sum_{k=1}^{64}\frac{(b_k - b_k^0)^2}{\sigma_k^{0\,2}} \sim 1.0 \tag{5.5}$$

where σ_k^0 is the standard deviation of the photon count error including Poisson and systematic errors and χ^2 is the normalized chi-squared distribution.

The problem is then equivalent to maximizing

$$\bar{S} = S - \frac{\lambda}{2}\chi^2 \tag{5.6}$$

where λ is a smoothing parameter which balances the relative weight between the observations and the entropy. Increasing λ gives more weight to the observations than the smoothness of the solution.

5.4.4 Fractal pixon image reconstruction

As mentioned above the MEM method really requires $\gtrsim$ 100 counts/SC to produce statistically significant images. This makes high time resolution studies of the beginning of the flare difficult to do using this method; especially in the higher energy channels, M2 and H. A new imaging method for HXT which copes much better with lower count rates is fractal pixon image reconstruction (Metcalf et al., 1995). This method is also an algorithm based on Bayesian methods like MEM. All Bayesian methods produce the most likely image subject to the data constraints. The likelihood of this image is defined by the goodness-of-fit (GOF) which describes how well the image predicts the data, and also by the image prior which characterizes how well the image fits the model. With Bayesian techniques the choice of image prior is important, especially when the data is poor. In MEM the image prior defines the flattest image as the most likely, while pixon methods define the image with the fewest degrees of freedom as the most likely.

The most important idea behind pixon-based image reconstruction is in utilizing the fact that not all parts of the image require the same degree of spatial resolution. With hard X-ray images most of the image is in fact blank and does not need the same resolution as the areas of the emission.

A pixon is a generalized image cell in the image representing one degree of freedom in the reconstruction (Pina and Puetter, 1993). The ideal case is to use the minimum number of pixons to describe the data, i.e. the goal of pixon algorithms is to find the fewest number of cells which have the most amount of information in each cell whilst satisfying the GOF criterion.

Pina and Puetter (1993) introduced the fractal pixon basis to solve the problem of computing the size and distribution of pixons. This is a 'fuzzy' basis in which the pixons do not have rigid edges and can share some of their signal with adjacent pixons. This is achieved by locally convolving a pixon shape function with a pseudo image to derive the reconstructed image (Metcalf et al., 1995). This reduces the problem to the calculation of the pixon map which is a map of the local pixon size at each pixel.

The maximum entropy reconstruction for HXT images is performed on a 64x64 grid which has 4096 degrees of freedom but only 64 data points. The result of this is the fairly regular appearance of spurious sources. Because pixons minimize the number of degrees of freedom this method should produce fewer spurious sources. Typically Metcalf et al. (1995) found that 100 degrees of freedom were sufficient for image reconstruction from HXT. Also, pixon based algorithms are much better at imaging with a limited count rate. The number of counts observed within the field of view is conserved; with MEM these counts are removed from the real sources and distributed to the spurious sources. With pixon methods there are fewer spurious sources and better photometry. Currently, there still remains some debate over the merits of MEM versus pixons, particularly with reference to weak sources.

The pixon map (Puetter, 1995) gives the local spatial scale of the image and hence determines the size and location of the pixons necessary to reconstruct the image. The spatial scale at each pixel can be found by investigating how the contribution to the GOF parameter from each pixel ($G_i(s)$) varies with pixon size, s, and pixel number, viz.,

$$\delta G_i(s) \equiv \delta s \frac{dG_i}{ds} \tag{5.7}$$

Metcalf et al. (1995). The pixon map is the set of local spatial scales given by $\delta_i \equiv max_s(\delta G_i(s))$, see Metcalf et al. (1995).

The computation of the pixon map in this way needs a residual image, however. With Fourier synthesis data there is no residual image. Metcalf et al. (1995) defined the variation with resolution of the contribution to the GOF parameter from each pixel to be

$$\delta G_i(s) \equiv \delta I_i \frac{dG}{dI_i} = \left(\delta s \frac{dI_i}{ds}\right) \frac{dG}{dI_i} \tag{5.8}$$

where $\frac{dG}{dI_i}$ is the derivative of the GOF parameter with respect to the count rate in the ith pixel, δI_i is the change in the count rate as the pixon size changes by δs and δs is the variation in the pixon size.

However, despite the fact that pixon methods offer an opportunity to produce much better reconstructed images with lower count rates, fuzzy pixons are very inefficient since the algorithm uses every pixel in the image. At the moment this method is very computationally intensive and time constraints have meant that only one of the events considered here, February 14 1992, has

been imaged using pixon methods. This event was also imaged using MEM and the results from the two methods will be compared later.

5.4.5 Hard X-ray spectral analysis

Once the image synthesis has been performed on the hard X-ray data the first step is to identify that the hard X-ray emission is co-spatial with the white-light emission. The temporal resolution of the white-light observations is somewhat lower than that of the hard X-ray observations; typically the white-light images are 10-12 seconds apart whilst the hard X-ray images are typically 5 second accumulations. Note that although the actual time resolution of HXT is 0.5 seconds it is rather impractical and difficult to accumulate enough counts to produce images at this resolution. Also, it would be computationally very intensive to produce a result with such poor photon statistics.

In Chapter 4 we showed that for the return current to become unstable to the generation of ion-acoustic waves the drift speed, v_D, must exceed the ion-sound speed, v_{is}. The calculation of the drift speed then necessarily involves a knowledge of the parameters of the electron spectrum, as well as of the atmospheric structure. The parameters of the electron spectrum can be derived from spatially resolved hard X-ray data.

It is possible to derive spatially resolved spectra for the hard X-ray footpoints corresponding to the kernels of white-light flare emission. In doing this the assumption was made that the photon spectrum could be well described by a single power law, and then the spectral parameters A and γ can be calculated or each image in the hard X-ray movie, usually at 5 second time intervals.

The photon spectrum is assumed to have the form:

$$I(\epsilon) = A\epsilon^{-\gamma}\ photons\ cm^{-2}\ s^{-1}\ keV^{-1} \tag{5.9}$$

Then, if the count rates in two adjacent channels are I_A and I_B and the upper and lower edges of channels A and B are ϵ_{A1} and ϵ_{A2} and ϵ_{B1} and ϵ_{B2} respectively, the spectral hardness of the photon spectrum is given by:

$$H = \frac{I_A}{I_B} = \frac{\epsilon_{A2}^{1-\gamma} - \epsilon_{A1}^{1-\gamma}}{\epsilon_{B2}^{1-\gamma} - \epsilon_{B1}^{1-\gamma}} \tag{5.10}$$

When these channels are adjacent the $\epsilon_{A2} = \epsilon_{B1}$ and

$$H = \frac{1 - \epsilon_1^{1-\gamma}}{\epsilon_2^{1-\gamma}} \tag{5.11}$$

where $\epsilon_1 = \epsilon_{A1}/\epsilon_{A2}$ and $\epsilon_2 = \epsilon_{B1}/\epsilon_{B2}$. In practice the routine used to derive the spectral paramters of the hard X-ray photon spectrum used all four channels of the HXT instrument, rather than just taking ratios between two adjacent channels.

If we then also assume that the parent electron spectrum is a power law, viz.,

$$F(E) = F_0 E^{-\delta} \; electrons \; s^{-1} \; keV^{-1} \tag{5.12}$$

then for thick target emission we can calculate the parameters of the electron spectrum, (F_0, δ) from the photon spectrum viz., (e.g. Hoyng et al., 1976)

$$\begin{aligned} \delta &= \gamma + 1 \\ F_0 &= 4.15 \times 10^{33} A(\gamma - 1)^2 B(\gamma - 1/2, \gamma) E_1^{-\gamma} \; s^{-1} \end{aligned} \tag{5.13}$$

where $B(\gamma - 1/2, \gamma)$ is the Beta function, E_1 is the cut-off energy of the spectrum and 4.15×10^{33} is a constant.

If we recall that

$$v_D = \frac{F_1 \left(\frac{3KN}{E_1^2}\right)^{1/2(1-\delta)}}{(x + x_M) n_H} \tag{5.14}$$

then $F_1 = F_0/area$ and δ can be derived from the measured photon spectrum. The area of the electron beam, assuming that the whole of this contributes to the area of the corresponding hard X-ray emission can be calculated from the hard X-ray movie, since we know that the pixel size is 2.46" and $S^{3/2} = N_{pix}^{3/2} V_P$. Here S is the area, N_{pix} the number of pixels in the region of interest, and $V_p = 5.7 \times 10^{24}$ is the pixel volume (McTiernan et al., 1994).

However, in order to calculate v_D and v_{is} we still require certain parameters of the atmospheric distribution, i.e., the column density, total hydrogen density, degree of ionization and tempertaure. We take these to be those parameters from the semi -empirical model atmospheres of Basri et al. (1979), model P in the range where we have calculated theoretically that $v_D > v_{is}$. The ratio $R = v_D/v_{is}$ can then be calculated for each time interval of the hard X-ray data and its evolution compared with that of the white-light emission.

5.5 November 15 1991 - Results

The hard X-ray flare commenced at 22:34 UT on November 15 1991 in active region NOAA 6919 (S14W19). The GOES class of this event was X1.5 and the H_α importance 2B. *Yohkoh* observed this flare from the start until the end of the HXR emission above 20 keV at 22:44 UT. Flare mode was triggered at 22:34:38 UT. This event has been studied extensively in hard X-rays by Sakao (1994). The white-light flare emission began around 22:36:40 UT as can be seen in fig. 5.5. Figure 5.13 and fig. 5.14 show grey scale images of the white-light emission at 22:37:52 UT overlaid with contours of the corresponding hard X-ray sources at 22:37:30 UT and 22:38:00 UT respectively. This event showed double source structure both in hard x-rays and in white-light. For further discussion

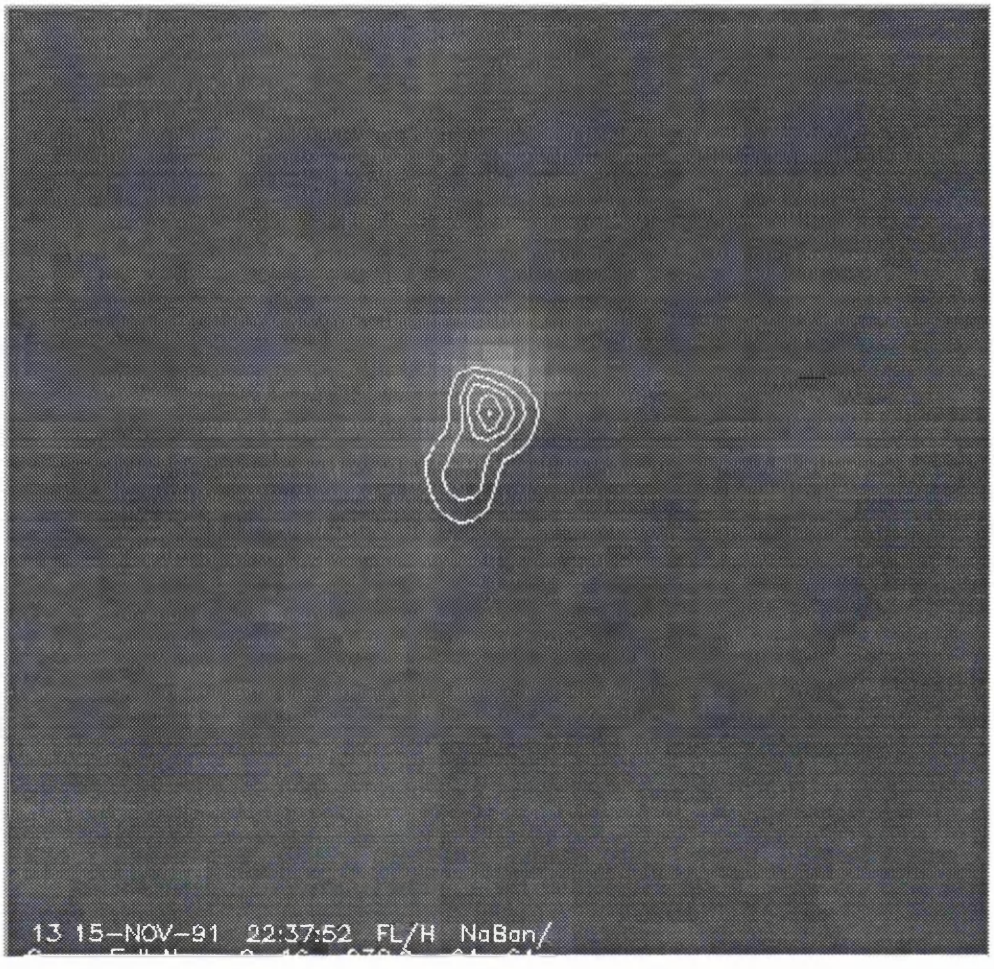

Figure 5.13: Grey-scale image of the white-light flare emission of November 15 1991 at 22:37:52 UT overlaid with HXR contours from the HI channel at 22:37:30 UT.

these sources have been labelled A and B, as indicated in fig. 5.15, which shows the hard X-ray footpoints in the M2 channel.

We can see from fig. 5.14 and fig. 5.13 that there is a close spatial correspondence btween the white-light and hard X-ray emission, suggestive of a connection between the origins of the two emissions. A comparison of fig. 5.4 and fig. 5.5 shows the temporal relationship between the two.

Sakao (1994) showed that the footpoints of the double hard X-ray source were located on either side of the magnetic neutral line, and that the brighter of the hard X-ray sources, B, is located in a region of positive polarity with longitudinal magnetic field strength, $\mathbf{B} \sim +200G$, whilst the dimmer source, A, is located in a region of negative polarity with longitudinal field strength $\mathbf{B} \sim -400G$ (Sakao, 1994). However, the footpoints can be seen to brighten simultaneously to within 0.1s at the 1σ level (Sakao, 1994).

As the double sources that we observe in hard X-rays are most reasonably explained as the footpoints of a magnetic loop the disparity between the brightness of these footpoints suggests

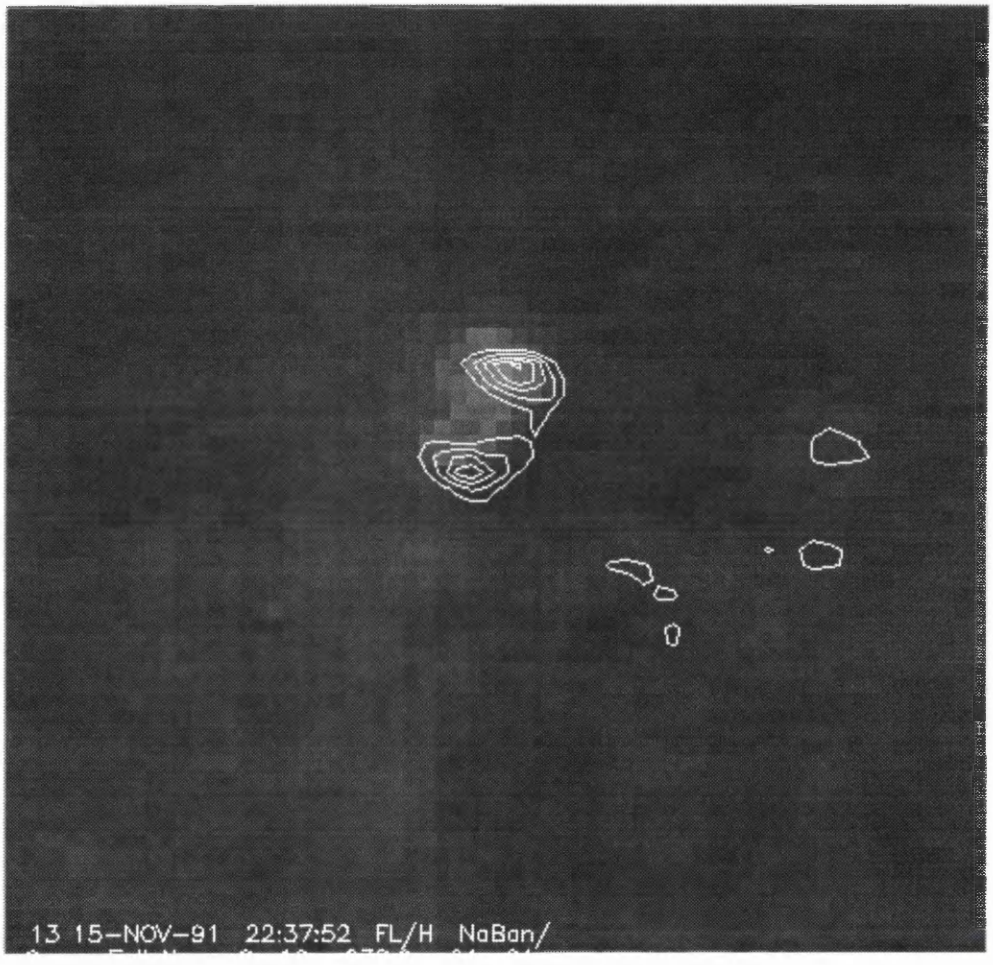

Figure 5.14: As fig. 5.13 with M2 channel contours at 22:38:00 UT.

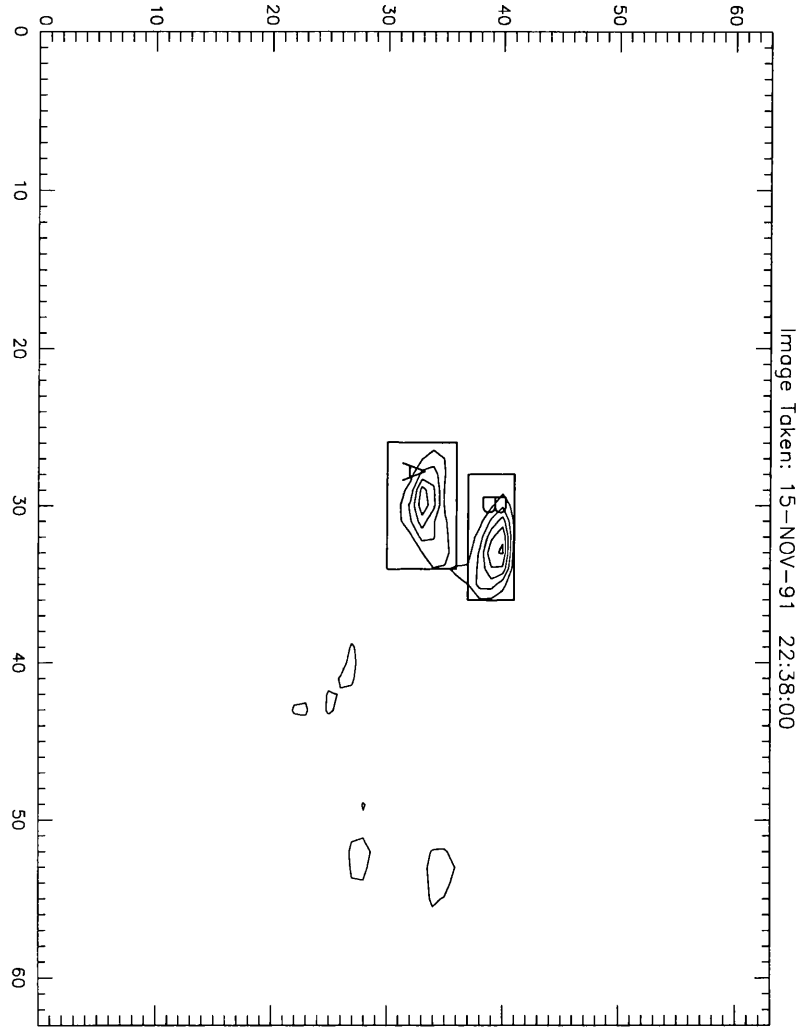

Figure 5.15: Hard X-ray sources *A* and *B*, as indicated, for November 15 1991 shown in the M2 channel at 22:38:00 UT.

that the footpoint with the stronger magnetic field also has stronger magnetic field convergence and hence less electron precipitation as a result of magnetic mirroring.

Melrose and Brown (1975) studied the hard X-ray energy spectra from loop tops, where the electrons are trapped, and from loop footpoints where electrons precipitating from the trap interact with the cold, dense ambient plasma. They assumed that precipitation is caused by Coulomb scattering into the loss cone and that this scattering can be described in terms of diffusion in pitch angle of the trapped electrons. Trubnikov (1965) showed that pitch angle diffusion occurs at a rate $\nu_D = 2\nu_E$ where ν_E is the rate of energy loss due to Coulomb collisions, viz.,

$$\frac{dE}{dt} = -\nu_E E \tag{5.15}$$

where $\nu_E \simeq 5 \times 10^{-9} n_i E^{-3/2}$ when E is given in keV.

In the weak diffusion limit (i.e. low precipitation) where scattering into the loss cone is not dominant then the precipitation rate, ν_p, is given by

$$\nu_p \sim \nu_D \propto E^{-3/2} \tag{5.16}$$

which gives a smaller precipitation rate for higher energy electrons.

We can see that this is indeed the case when we look at the light curves of the double source in the M2 (32.7-52.7 keV) and HI (52.7 - 92.8 keV) channels, see fig. 5.16 and fig. 5.17. The emission in the HI channel begins $\sim$ 1 minute after that in the M2 channel.

Figure 5.18, fig. 5.21, fig. 5.19 and fig. 5.22 show the evolution of R throughout the event. Beneath fig. 5.18 and fig. 5.19 we show the light curves of the white-light sources corresponding to the hard X-ray footpoints, fig. 5.18 and fig. 5.20. Also, in figures 5.18-5.22 ($R = v_D/v_{is}$ vs time for these two sources) show that the possible onset of the ion-acoustic instability ($R > 1$) in the lower source (higher magnetic field) does not occur until some 15 seconds later than in the top source. Since this ratio depends on the electron flux we might expect that a reduced precipitation rate due to a converging field would produce such a result.

We now examine the correspondence between the white-light flare and the onset of the ion-acoustic instability, i.e. the point where the drift speed, v_D exceeds the ion-sound speed v_{is}.

In all cases R has been calculated at the level in active region P model of Basri et al. (1979) in which the return current was shown to be most unstable to the onset of ion-acoustic wave generation in the previous chapter. For this level we have $N = 5.004 \times 10^{20}$, $n_H = 3.476 \times 10^{13} cm^{-3}$, $x = 1.784 \times 10^{-3}$ and $T = 5.35 \times 10^3 K$. Note that the fact that this is not a flare atmosphere will be discussed later on.

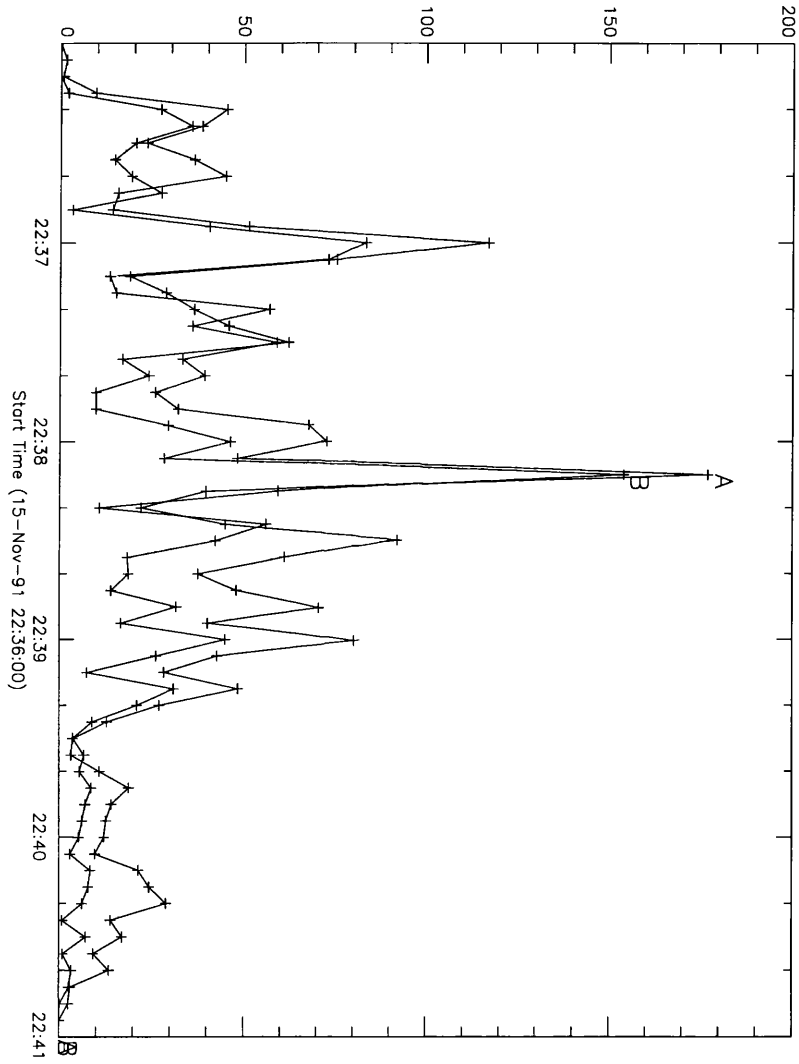

Figure 5.16: Light curves of the footpoint sources A and B of November 15 1991 in the M2 channel. We see that these begin to brighten at the beginning of the time interval.

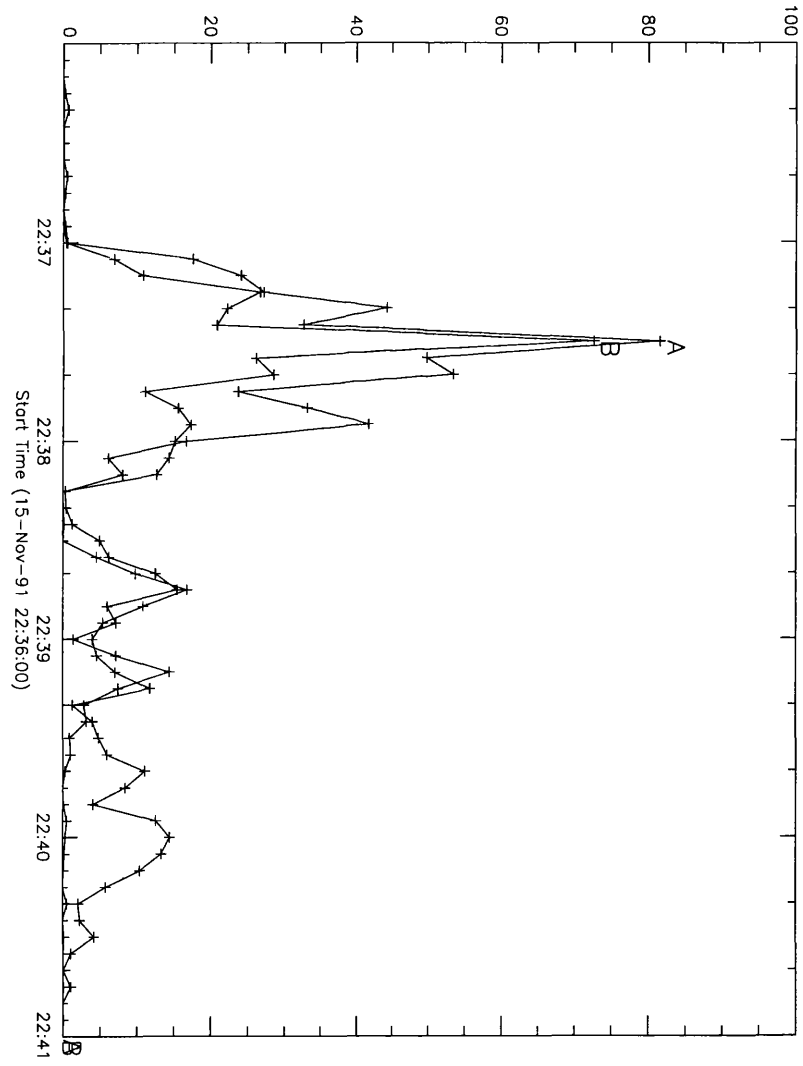

Figure 5.17: As fig. 5.16 but in the HI channel. We see that here the footpoints do not begin to brighten until $\sim 22:37:00$ UT, about a minute after the M2 channel.

Source B

We see that the white-light emission in this footpoint begins at 22:36:40 UT (fig. 5.18), although there is not a significant rise until about 22:36:50 UT. We can see from fig. 5.18 that the criterion $R > 1$ is satisfied at around 22:36:40 UT, within the error limits given by the determination of v_D, the same time as the onset of the white-light flare. The white-light emission reaches its peak at $\sim 22:37:40$ UT, whilst R reaches its maximum at 22:37:35 UT. By 22:41:00 UT the HXR emission has returned to background levels in all but the lowest channel of HXT (see fig. 5.4) and we see that the white-light emission has also returned to background levels.

Source A

Again we see that the white-light emission begins at 22:36:40 UT (see fig. 5.20 with the same steep rise occurring at 22:36:50 UT. From the HXR analysis we see that $R > 1$ is satisfied at 23:07:05 UT, somewhat after the onset of the white-light flare. If this is the case then clearly a return current instability could not be responsible for the white-light emission. However, we see from the errors on the determination of v_D that in fact $R > 1$ can be satisfied as early as 22:36:20 UT. The peak value of R is attained at 22:37:30 UT in this case and the maximum of the white-light at 22:37:40 UT.

5.6 January 26 1992 - Results

The flare began at 15:23 UT in NOAA active region 7012 (S16W66). The GOES class of this event was X1.0 with H_α importance 3B. *Yohkoh* observed this flare until 15:43 UT. This event showed five white-light flare patches, A, B, C, D and E as can be seen in figure. 5.24, and seven hard X-ray sources as can be seen in fig. 5.25.

Source A

The whitelight emission in this location began at $\sim 15:26:50$ UT, reaching a peak between 15:28:30 - 15:29:10 UT (see fig. 5.26). We see from the hard X-ray emission in this location that $R > 1$ is satisfied at $\sim 15:26:40$ UT, (see fig. 5.26) within the error limits. R attains its peak value at 15:28:30 UT and has tailed off by 15:29:30. The white-light emission is still significant, however, until 15:32:00.

Source B

The white-light emission in this kernel began at $\sim 15:27:20$ UT, somewhat after that from patch A. It reached a maximum at around 15:28:30 UT, as shown in fig. 5.28. Figure 5.27 shows the variation of $R = v_D/v_{is}$ for this source throughout the event. We see that within the error limits $R > 1$ is attained at $\sim 15:27:05$ UT, reaching a peak value at 15:28:20 UT. The overall shape of both the white-light curve and the variation of R are very similar in this case.

Source C

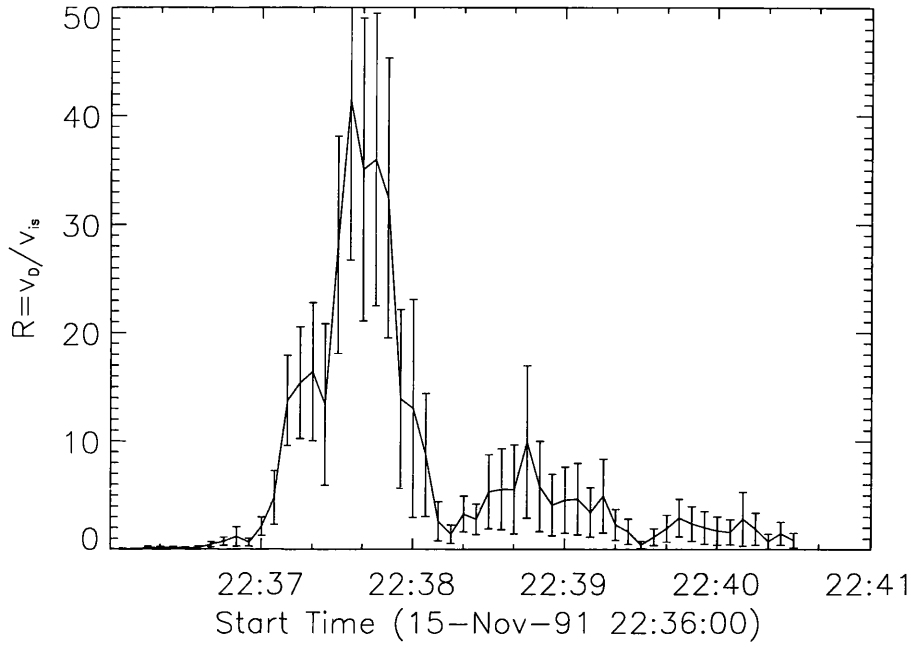

(a)

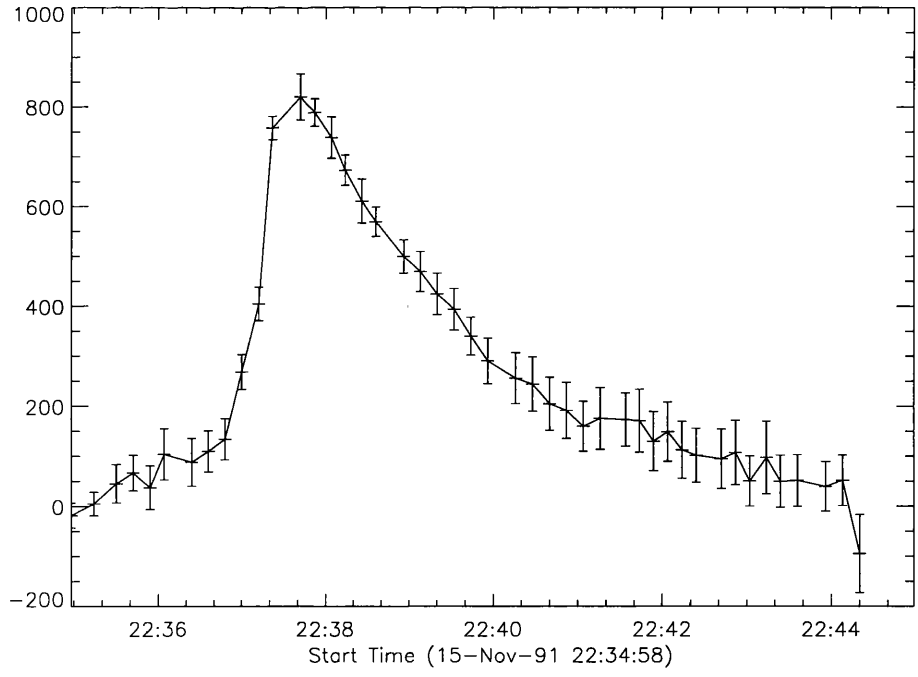

(b)

Figure 5.18: a)The variation of $R = v_D/v_{is}$ with time for footpoint B of November 15 1991, calculated at the $N = 5.004 \times 10^{20} cm^{-2}$ level in model atmosphere P of Basri et al. (1979) and b)The light curve of the white-light emission from source B of November 15 1991.

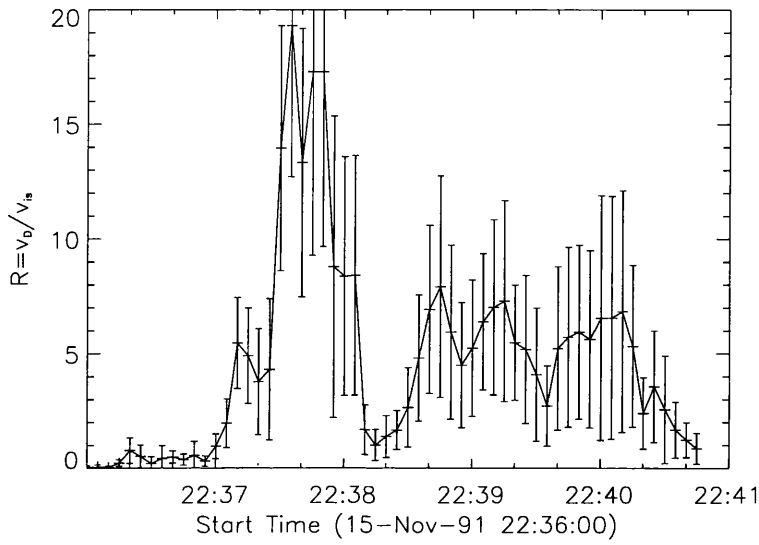

Figure 5.19: The variation of $R = v_D/v_{is}$ with time for footpoint A of November 15 1991, calculated at the $N = 5.004 \times 10^{20} cm^{-2}$ level in model atmosphere P of Basri et al. (1979).

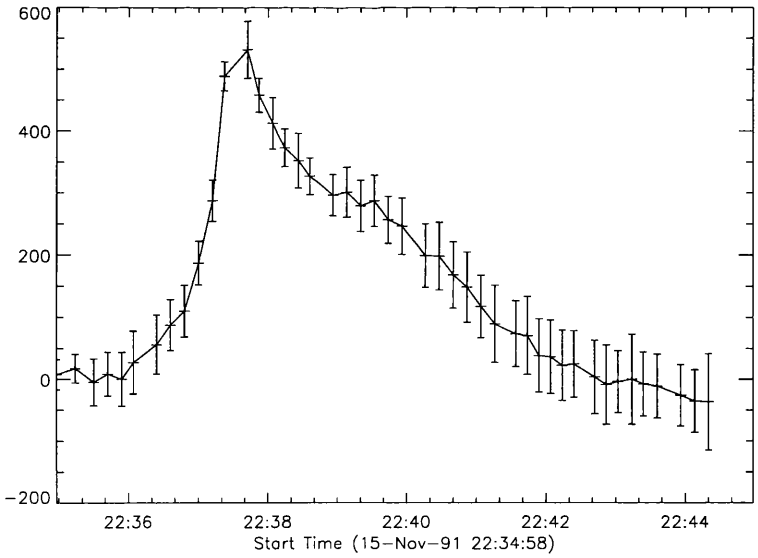

Figure 5.20: The light curve of the white-light emission from source A of November 15 1991.

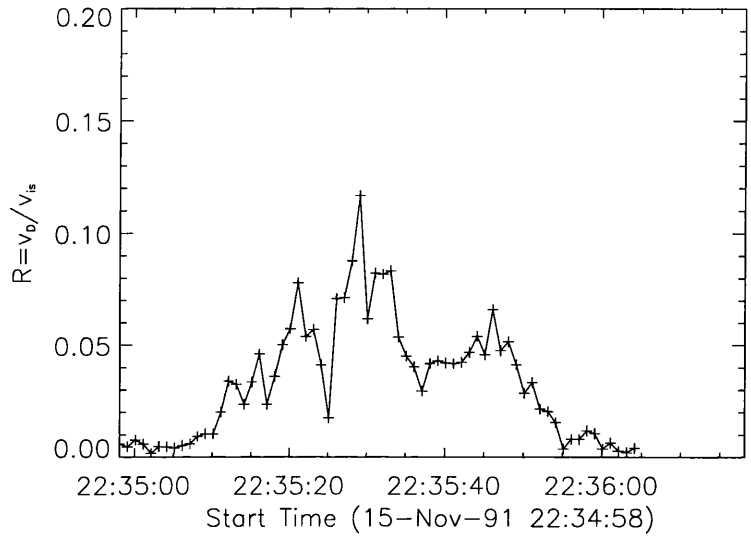

Figure 5.21: High time resolution plot of the variation of R in the early stage of the flare for footpoint B of Nov. 15 1991.

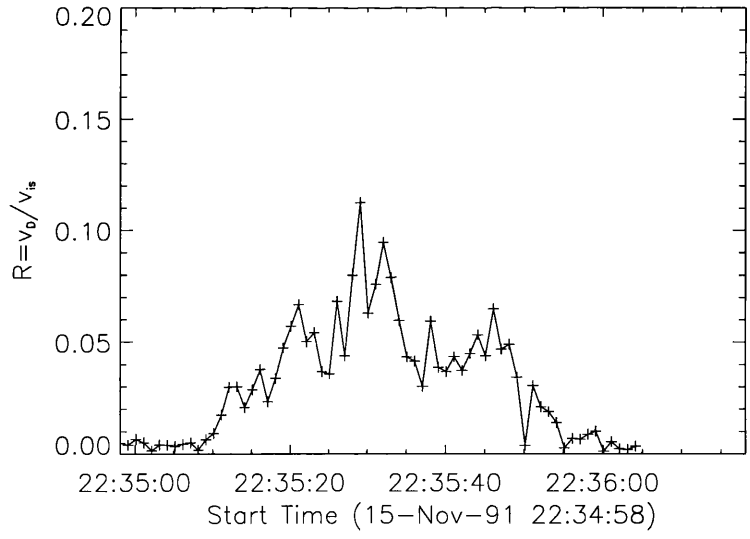

Figure 5.22: High time resolution plot of the variation of R in the early stage of the flare for footpoint A of Nov. 15 1991.

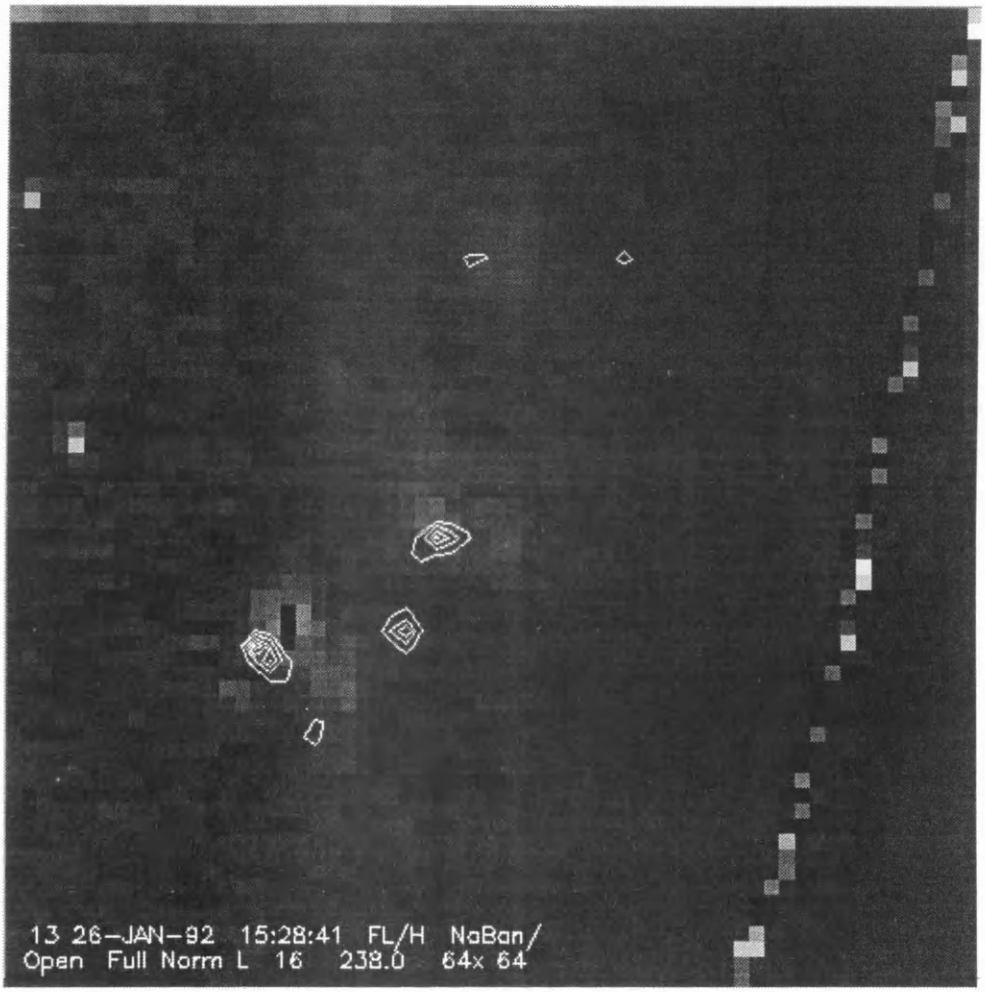

Figure 5.23: Grey-scale image of the white-light flare emission of January 26 1992 at 15:28:41 UT overlaid with HXR contours from the HI channel at 15:28:40 UT.

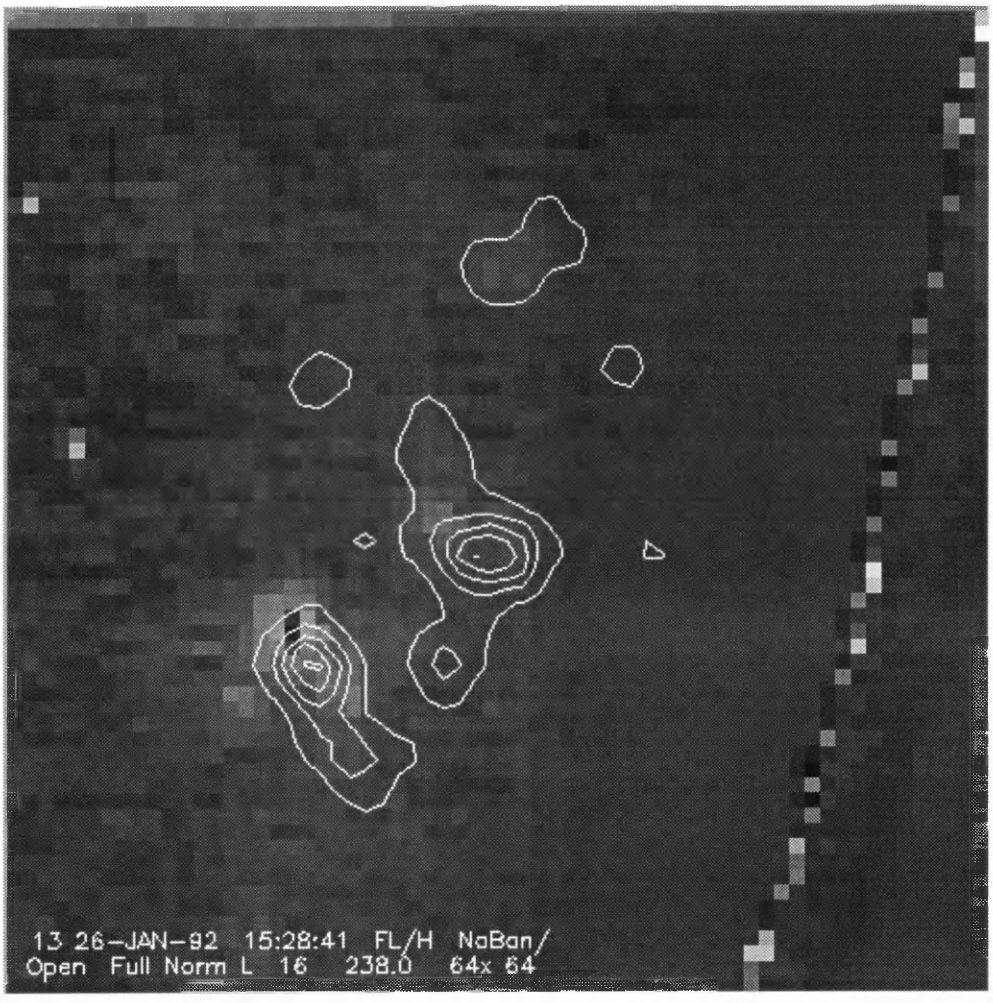

Figure 5.24: As fig. 5.23 with M2 channel contours at 15:27:14 UT.

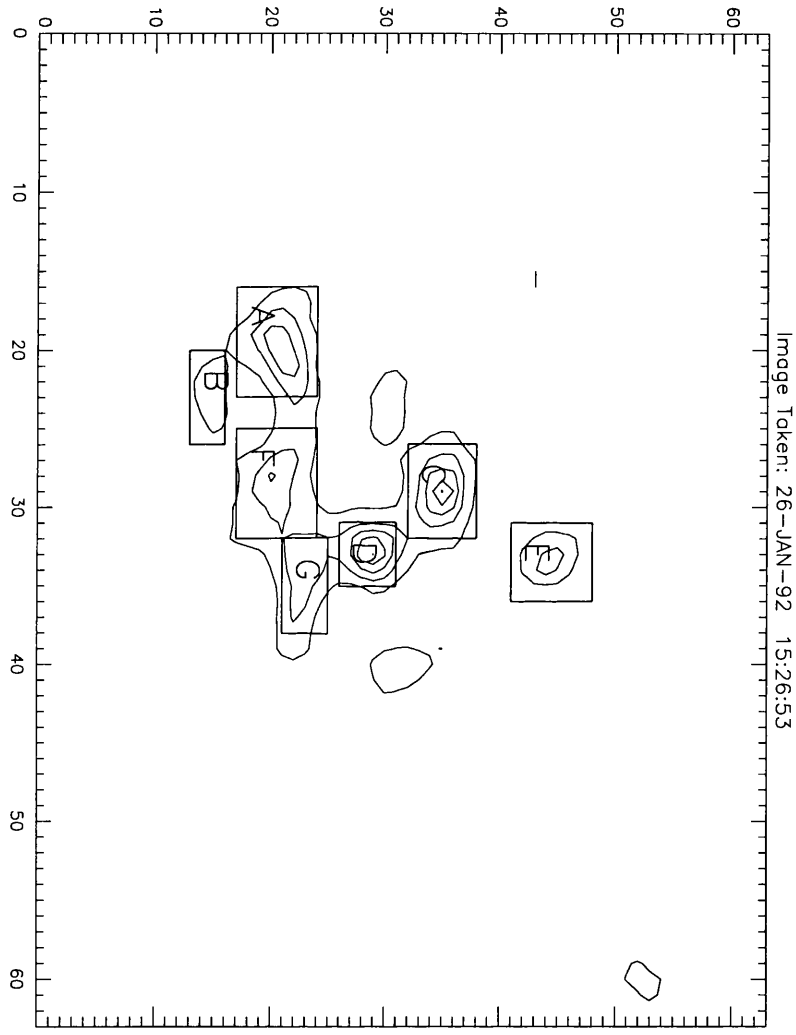

Figure 5.25: Hard X-ray sources A, B,C,D,E,F and G as indicated for January 26 1992, shown in the M1 channel at 15:26:53 UT.

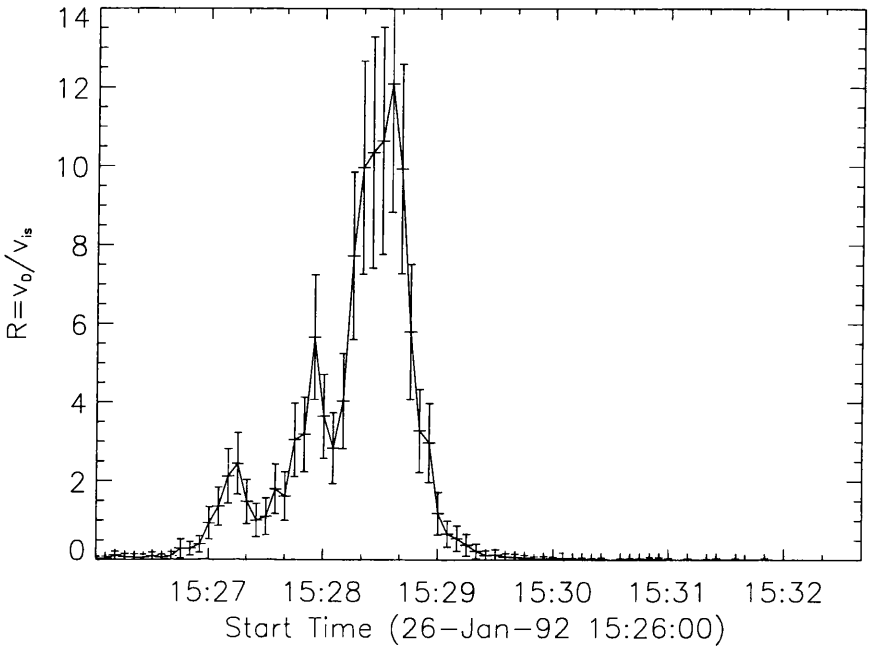

(a)

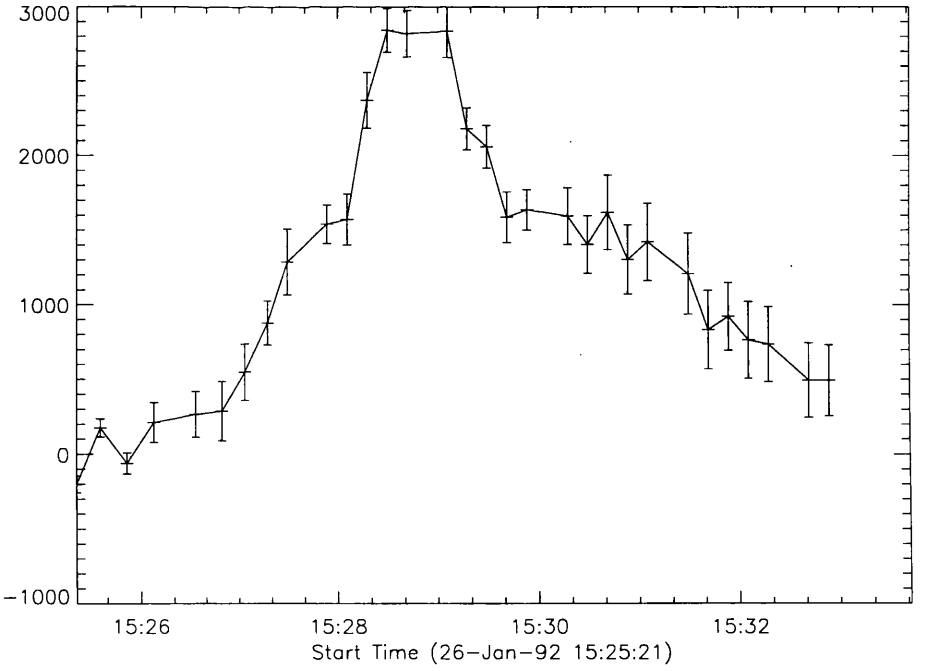

(b)

Figure 5.26: a) The variation of $R = v_D/v_{is}$ with time for footpoint A of January 26 1992, calculated at the $N = 5.004 \times 10^{20} cm^{-2}$ level in model atmosphere P of Basri et al. (1979). and b) The light curve of the white-light emission from source A of January 26 1992.

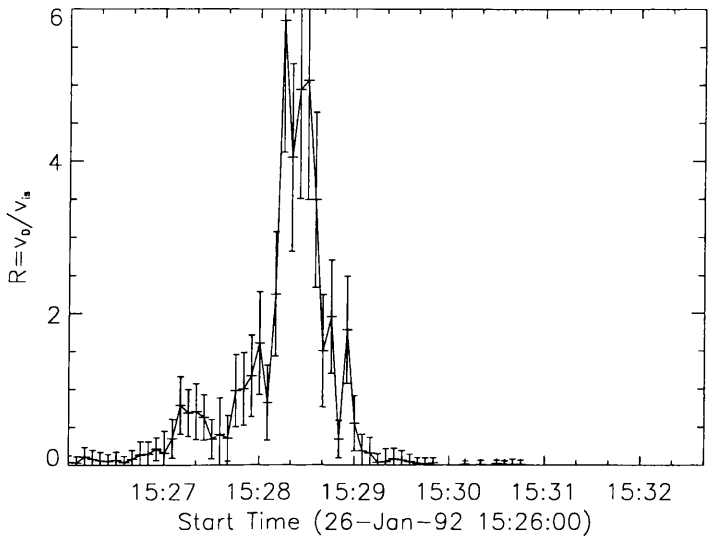

Figure 5.27: The variation of $R = v_D/v_{is}$ with time for footpoint B of January 26 1992, calculated at the $N = 5.004 \times 10^{20} cm^{-2}$ level in model atmosphere P of Basri et al. (1979).

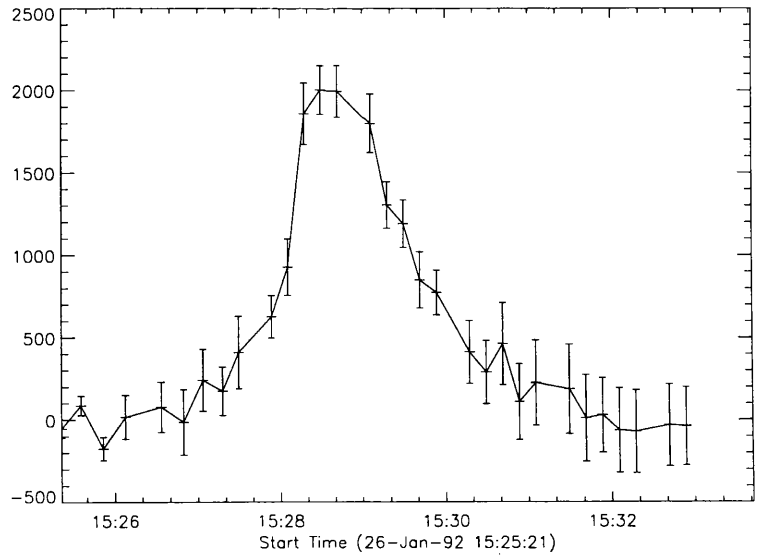

Figure 5.28: The light curve of the white-light emission from source B of January 26 1992.

In this location the white-light emission began at $\sim$ 15 : 27 : 10 UT, rising to a maximum at 15:28:40 UT, as can be seen in fig. 5.29. The corresponding hard X-ray emission shows the criterion $R > 1$ is satisfied at 15:27:05 UT, within error limits, reaching its peak value at 15:28:40 UT, coincident with the peak in white-light emission (see fig. 5.29).

Source D

The white-light emission in kernel D began at 15:26:50 UT, reaching its peak signal level at 15:28:30 UT, as can be seen in fig. 5.31. The corresponding hard X-ray source shows the criterion for ion-acoustic instability ($R > 1$) is satified at 15:26:45 UT within the limits of the errors on the determination of v_D. The peak value of R is attained at 15:28:40 UT, viz. fig. 5.30.

Source E

The white-light emission in kernel E began at 15:28:00 UT, showing a marked dip before a steep rise to its maximum at 15:29:10 UT, fig. 5.33. The hard X-ray emission indicates that $R > 1$ is satisfied at 15:27:50 UT within the error limits, reaching its peak value at 15:28:40 UT, as shown in fig. 5.32.

Sources F and G

There are two other hard X-ray sources, F and G which are indicated in fig. 5.25. These sources do not show corresponding white-light emission at these locations despite satisfying the criterion $R > 1$, as shown in fig. 5.34 and fig. 5.35.

5.7 October 27 1991 - Results

The flare began at 05:37 UT and flare mode was triggered at 05:37:35 UT. However, for HXT the flare began during a data gap and the first hard X-ray data available is from 05:47:00 UT. This flare also ended during a data gap, which explains the sharp fall off in both R and the white-light emission at $\sim$ 05 : 41 UT. This event occurred in NOAA active region 6891 (S13E15) and was a GOES class X6.1 flare with H_α importance 3B.

The hard X-ray emission displayed five sources, A, B, C, D and E, as indicated in fig. 5.38. The white-light flare also displayed five sources in positions coincident with the hard X-ray emission. This coincidence can be seen in fig. 5.36, which shows a grey-scale image of the white-light emission at 05:40:47 UT overlaid with HXR contours from the HI channel at 05:40:56 UT.

Source A

The white-light emission in this patch began at 05:39:41 UT and reached its peak value at 05:40:40 UT, see fig. 5.39. As noted above, the very sharp fall off is due to the fact that the data for this event is incomplete and this characteristic is present for all individual patches of emission studied in this event. The hard X-ray footpoint corresponding to this white-light patch shows emission which satisfies the criterion $R > 1$ at 05:39:41 UT, reaching a peak value at 05:40:25 UT,

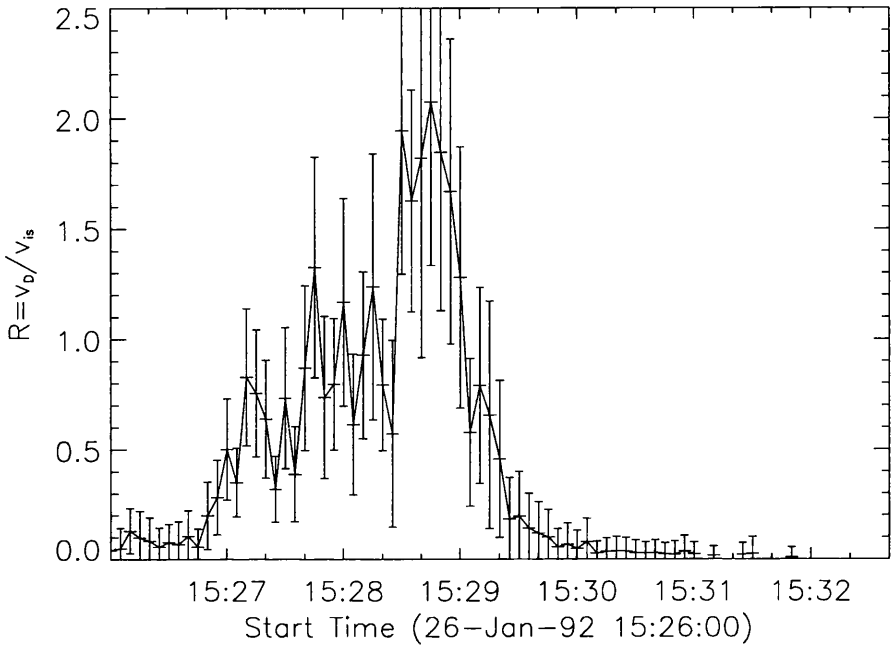

(a)

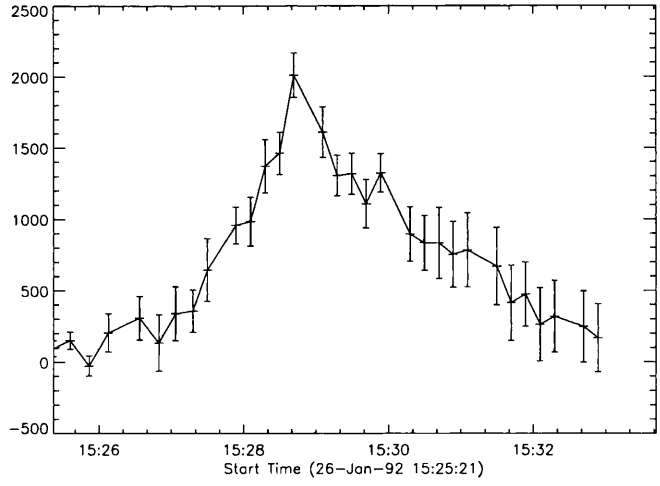

(b)

Figure 5.29: a) The variation of $R = v_D/v_{is}$ with time for footpoint C of January 26 1992, calculated at the $N = 5.004 \times 10^{20} cm^{-2}$ level in 26 1992.

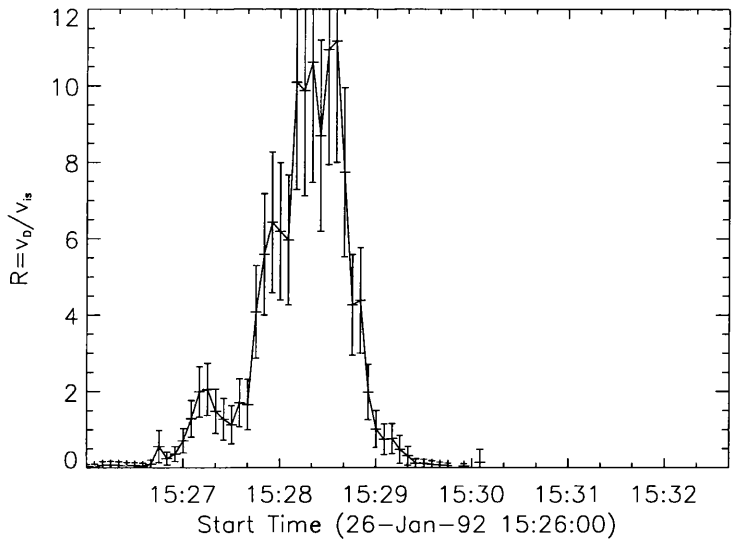

Figure 5.30: The variation of $R = v_D/v_{is}$ with time for footpoint D of January 26 1992, calculated at the $N = 5.004 \times 10^{20} cm^{-2}$ level in model atmosphere P of Basri et al. (1978).

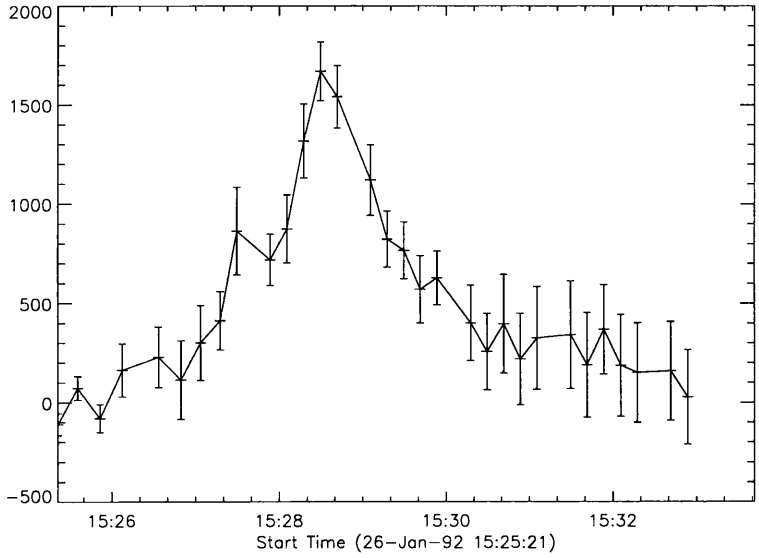

Figure 5.31: The light curve of the white-light emission from source D of January 26 1992.

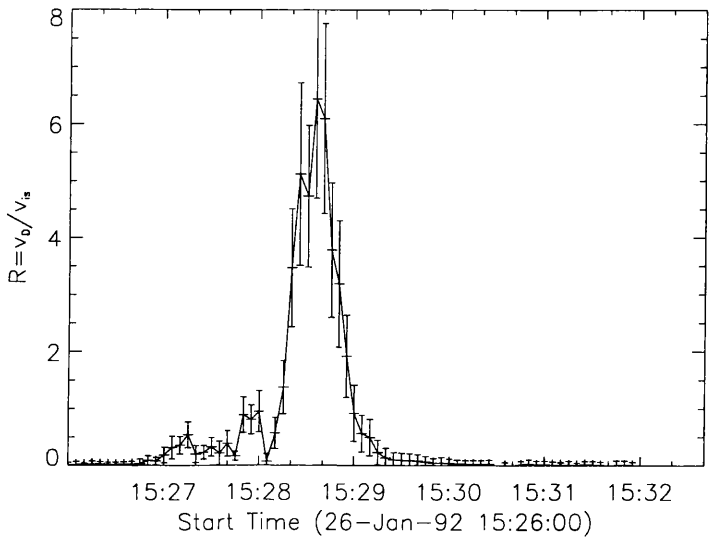

Figure 5.32: The variation of $R = v_D/v_{is}$ with time for footpoint E of January 26 1992, calculated at the $N = 5.004 \times 10^{20} cm^{-2}$ level in model atmosphere P of Basri et al. (1979).

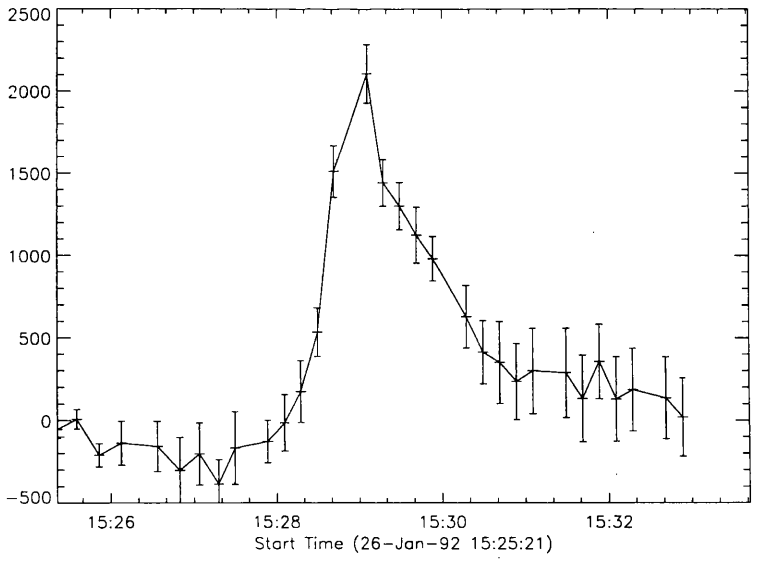

Figure 5.33: The light curve of the white-light emission from source E of January 26 1992.

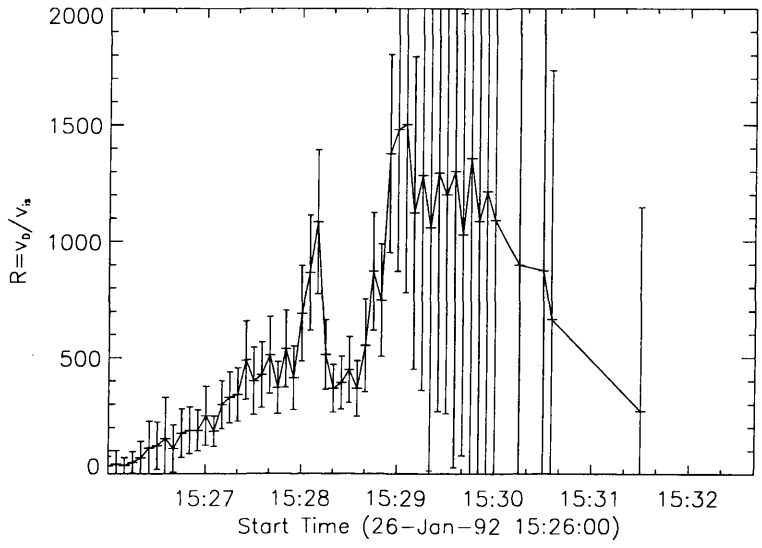

Figure 5.34: The variation of $R = v_D/v_{is}$ with time for footpoint F of January 26 1992, calculated at the $N = 5.004 \times 10^{20} cm^{-2}$ level in model atmosphere P of Basri et al. (1979).

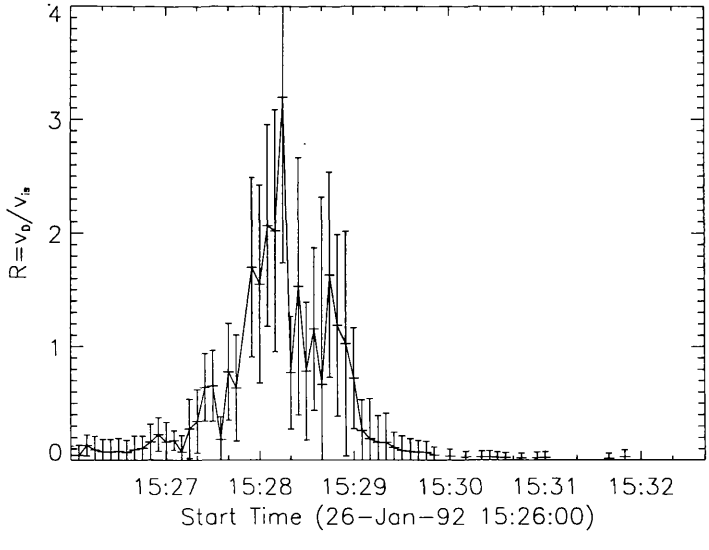

Figure 5.35: The variation of $R = v_D/v_{is}$ with time for footpoint G of January 26 1992, calculated at the $N = 5.004 \times 10^{20} cm^{-2}$ level in model atmosphere P of Basri et al. (1979).

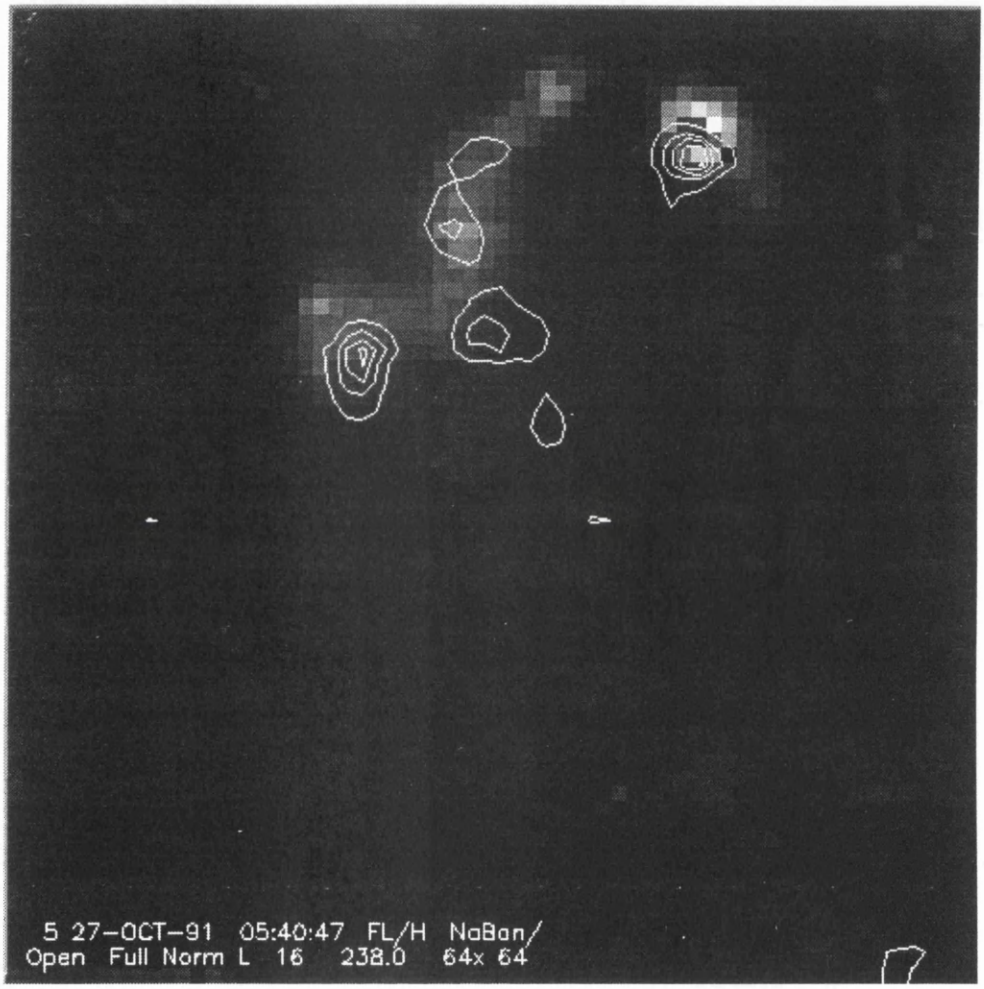

Figure 5.36: Grey-scale image of the white-light flare emission of October 27 1991 at 05:40:47 UT overlaid with HXR contours from the HI channel at 05:40:56 UT.

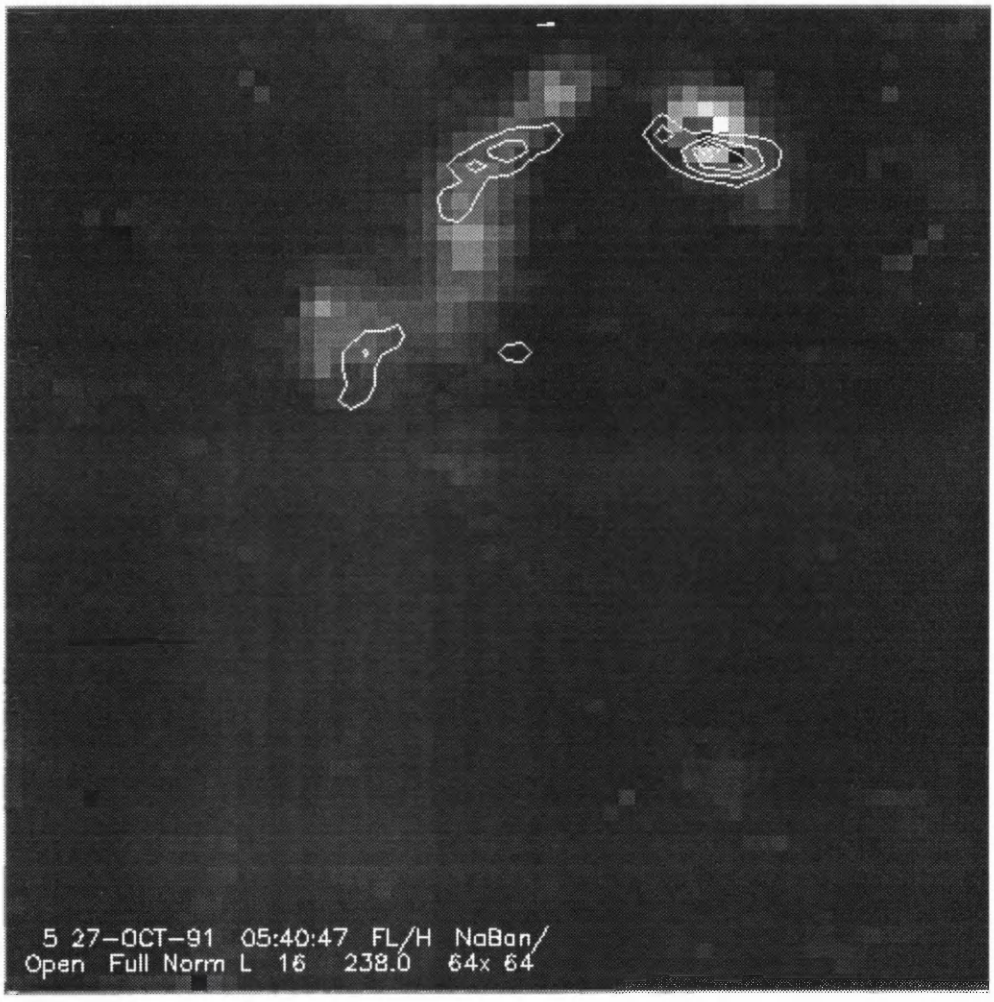

Figure 5.37: As fig. 5.36 with M2 channel contours at 05:41:12 UT.

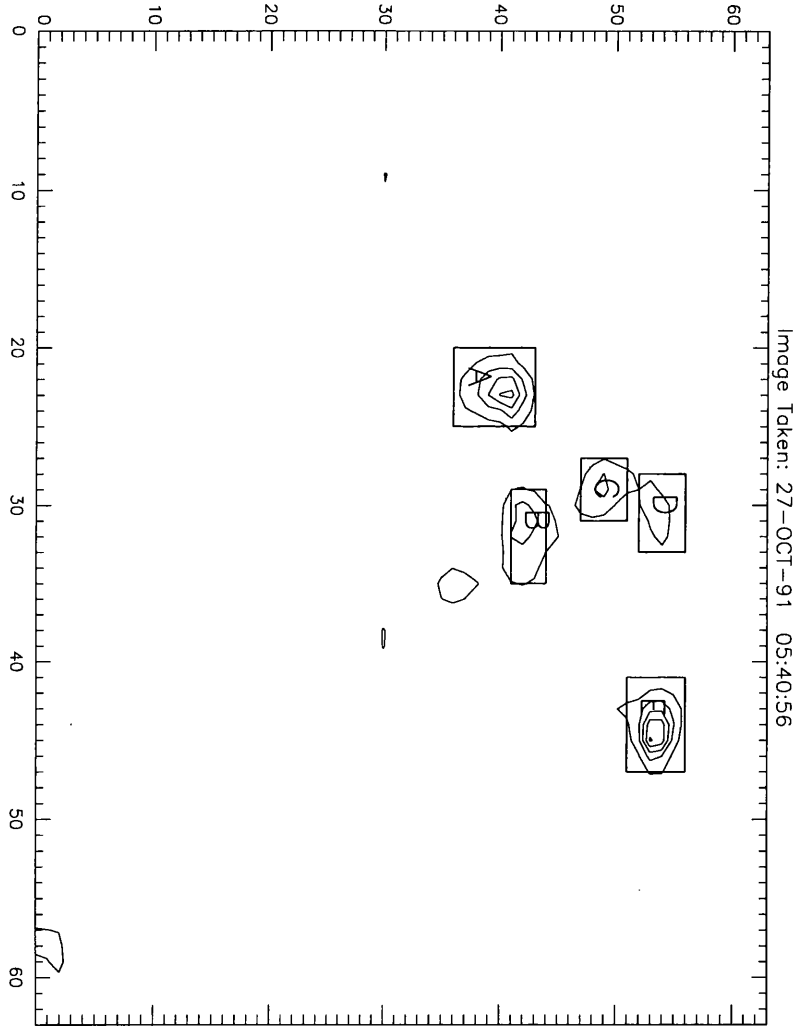

Figure 5.38: Hard X-ray sources A, B,C,D and E as indicated for October 27 1991, shown in the HI channel at 05:40:56 UT.

fig. 5.39.

Source B

The white-light emission in location B began at 05:40:15 UT, reaching its peak signal between 05:40:45 and 05:40:50 UT, as may be seen in fig. 5.41. Consideration of the hard X-ray spectrum from the coincident hard X-ray footpoint indicates that the $R > 1$ criterion is first exceeded at 05:39:40 UT, with the peak value of R being attained at 05:41:15 UT, fig. 5.40. The shape of these two curves, however, is noticeably different from one another.

Source C

From the hard X-ray emission in this footpoint we can see that the criterion $R > 1$ is satisfied at 05:39:40 UT, reaching a peak at 05:40:00 UT, see fig. 5.42. The corresponding white-light emission began at 05:39:41 UT, rising to a maximum value which was maintained between 05:40:45-05:40:50 UT, fig. 5.42.

Source D

In this location the white-light emission began at 05:39:41 UT peaking at around 05:41:10 UT, as indicated in fig. 5.45. The hard X-ray spectrum for this footpoint shows that the drift speed first exceeds the ion-sound speed at 05:39:40 UT rising to a maximum value at 05:41:15 UT. We can see that the overall shape of the white-light curve and the variation of R is very similar, fig. 5.44.

Source E

Source E showed white-light emission above background levels from 05:39:41 UT which reached a peak level between 05:40:45 and 05:40:50 UT, where it remained at a fairly steady value until 05:41:10 UT when it fell off sharply due to the data gap (see fig. 5.47). The hard X-ray spectrum of this footpoint indicates that $R > 1$ is first attained at 05:39:40 UT, reaching a maximum value at 05:41:10 UT. the shape of these curves is not very similar.

5.8 February 14 1992 - Results

The flare of February 14 1992 began at 23:04 UT and ended during a data gap after 23:10 UT. It occurred in NOAA active region 7056 (S13E02), and was of GOES class M7.0 with H_α importance 2B. This is an interesting white-light event from the point of view that it is an M flare, indicating that white-light emission is more common than has been previously thought. Traditionally these events have been associated with very energetic X class flares, but here we see that this is most likely a detection threshold selection effect.

This event also showed five distinct sources in both hard X-rays and white-light, as can be seen in fig. 5.52 and fig. 5.48. Figure 5.53 also shows how the hard X-ray spectral index for each footpoint evolves throughout the event.

Source A

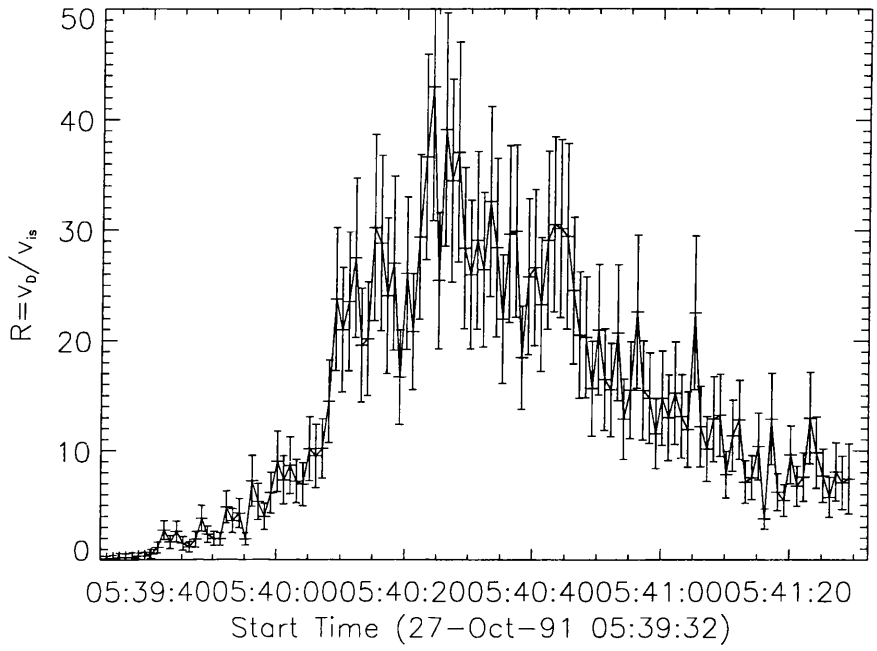

(a)

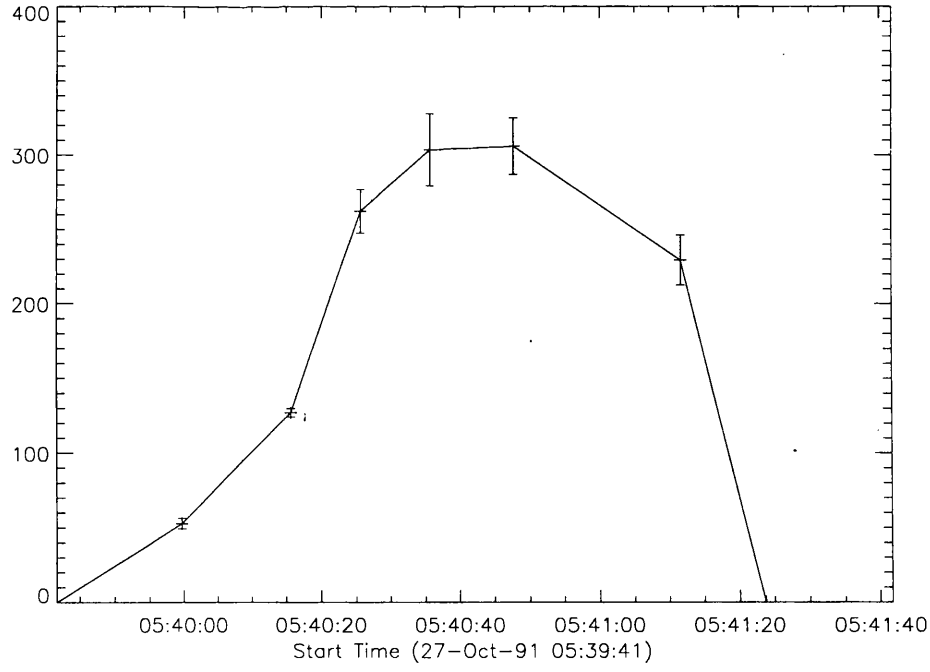

(b)

Figure 5.39: a) The variation of $R = v_D/v_{is}$ with time for footpoint A of October 27 1991, calculated at the $N = 5.004 \times 10^{20} cm^{-2}$ level in model atmosphere P of Basri et al. (1979) and b) The light curve of the white-light emission from source A of October 27 1991.

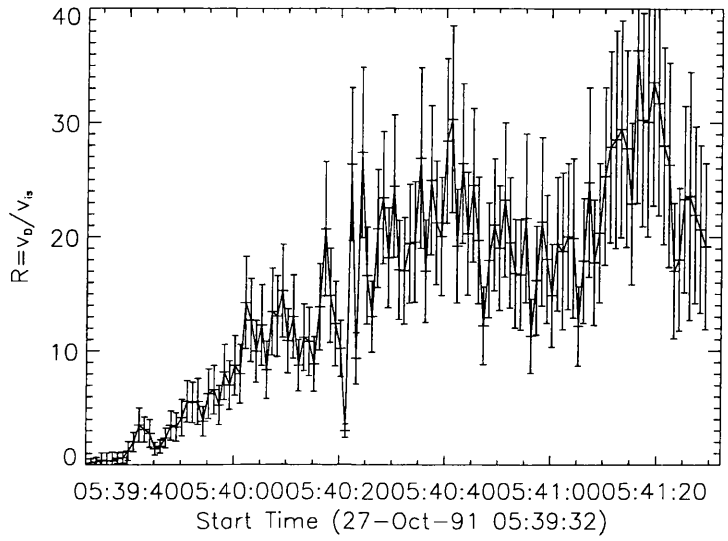

Figure 5.40: The variation of $R = v_D/v_{is}$ with time for footpoint B of October 27 1991, calculated at the $N = 5.004 \times 10^{20} cm^{-2}$ level in model atmosphere P of Basri et al. (1979).

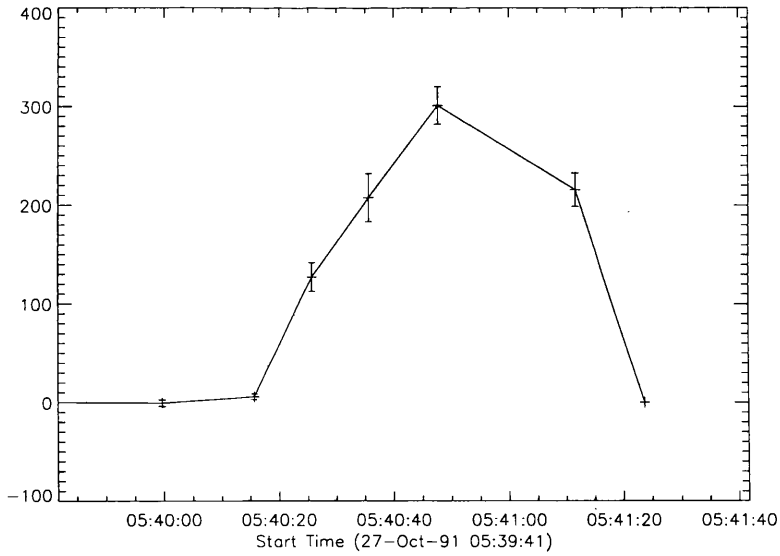

Figure 5.41: The light curve of the white-light emission from source B of October 27 1991.

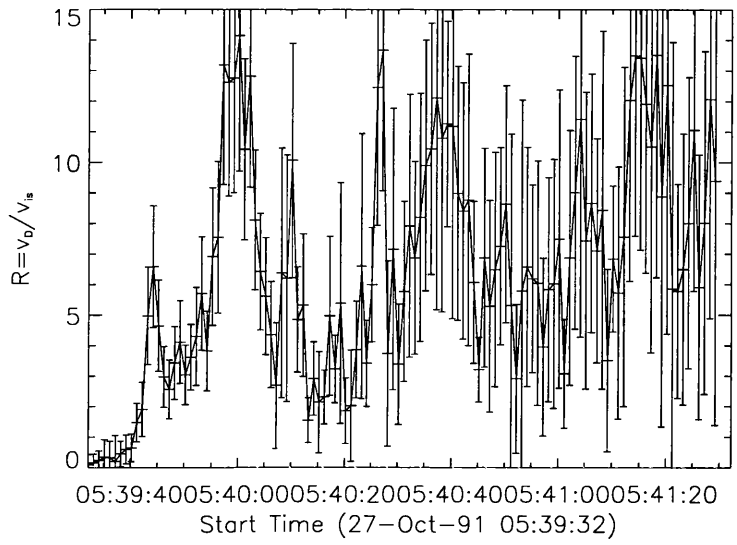

Figure 5.42: The variation of $R = v_D/v_{is}$ with time for footpoint C of October 27 1991, calculated at the $N = 5.004 \times 10^{20} cm^{-2}$ level in model atmosphere P of Basri et al. (1979).

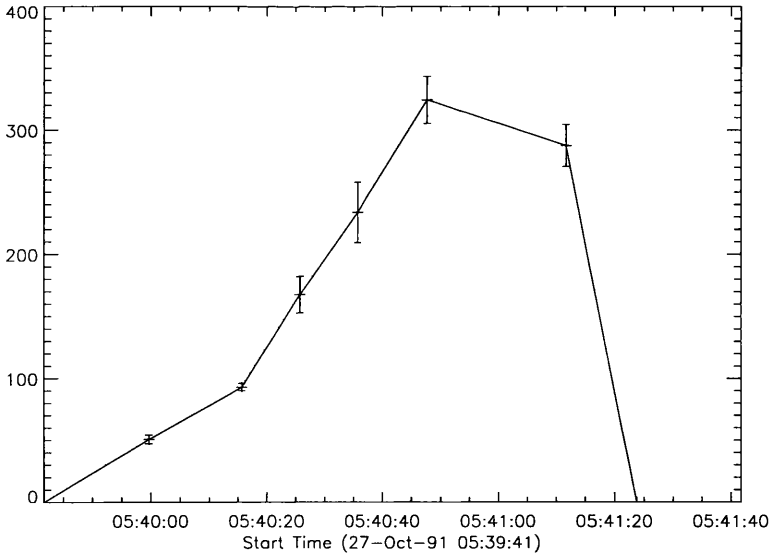

Figure 5.43: The light curve of the white-light emission from source C of October 27 1991.

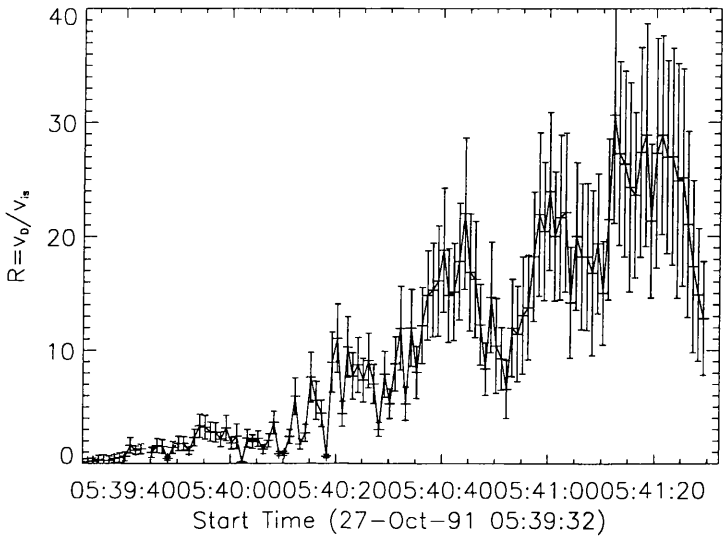

Figure 5.44: The variation of $R = v_D/v_{is}$ with time for footpoint D of October 27 1991, calculated at the $N = 5.004 \times 10^{20} cm^{-2}$ level in model atmosphere P of Basri et al. (1979).

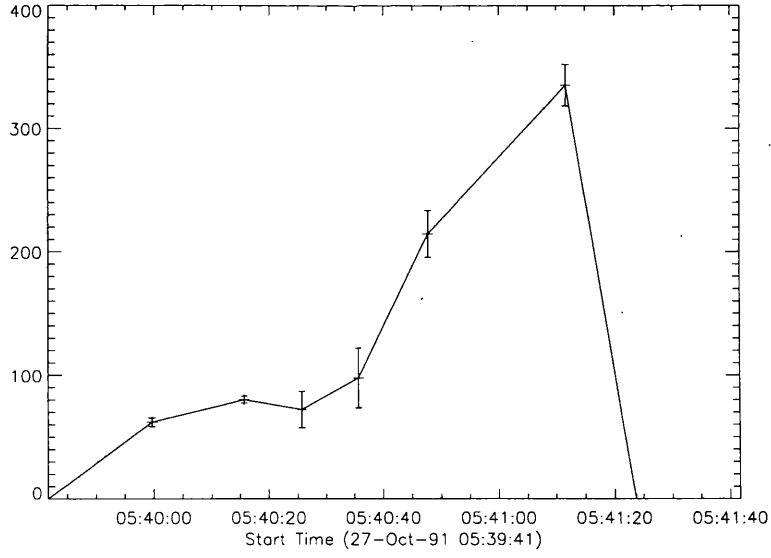

Figure 5.45: The light curve of the white-light emission from source D of October 27 1991.

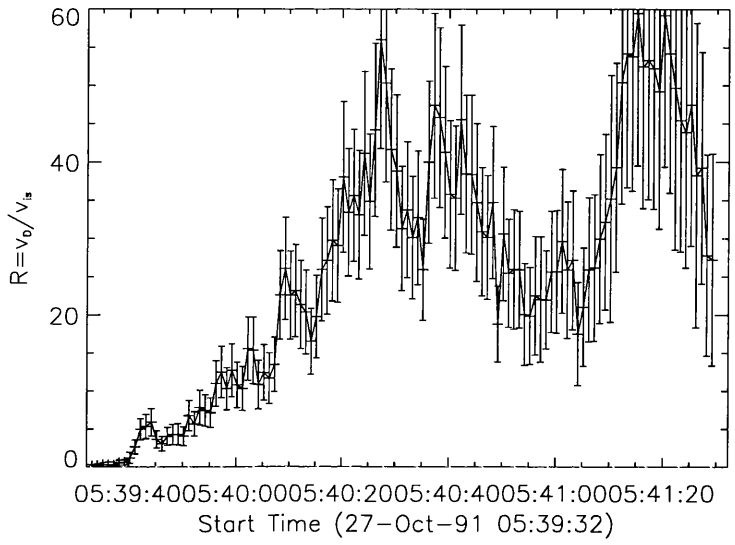

Figure 5.46: The variation of $R = v_D/v_{is}$ with time for footpoint E of October 27 1991, calculated at the $N = 5.004 \times 10^{20} cm^{-2}$ level in model atmosphere P of Basri et al. (1979).

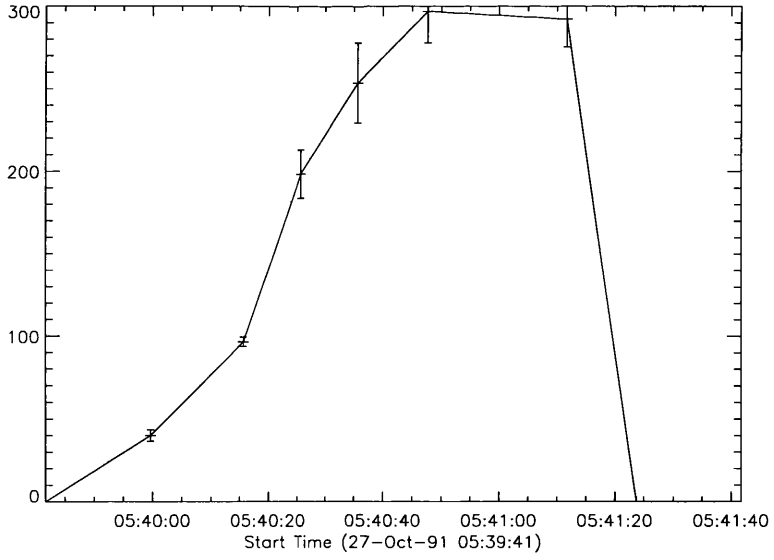

Figure 5.47: The light curve of the white-light emission from source E of October 27 1991.

Figure 5.48: Grey-scale white-light image of the event February 14 1992 at 23:07:48 UT. Overlaid are contours of the corresponding hard X-ray sources in the M2 channel at 23:07:45 UT

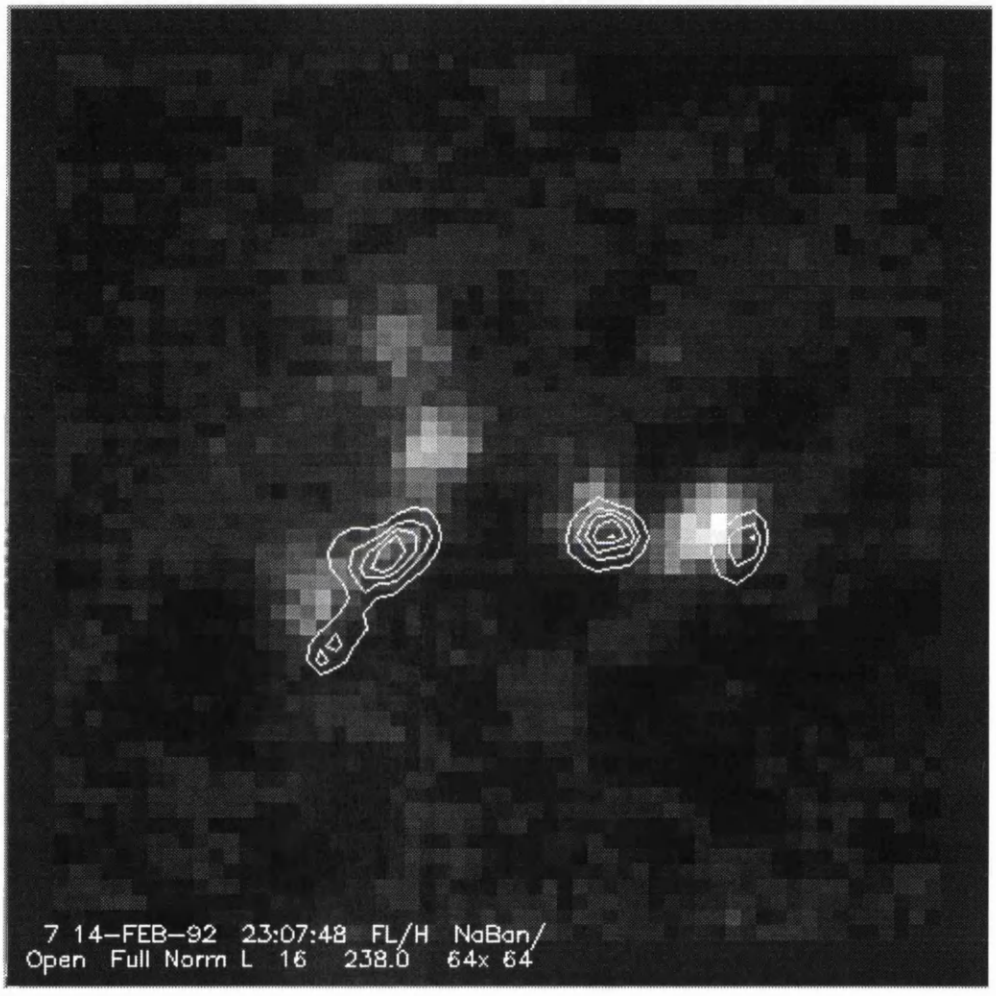

Figure 5.49: Grey-scale white-light image of the event Feb. 14 1992 at 23:07:48 UT with M2 channel HXR contours from 23:07:31 UT.

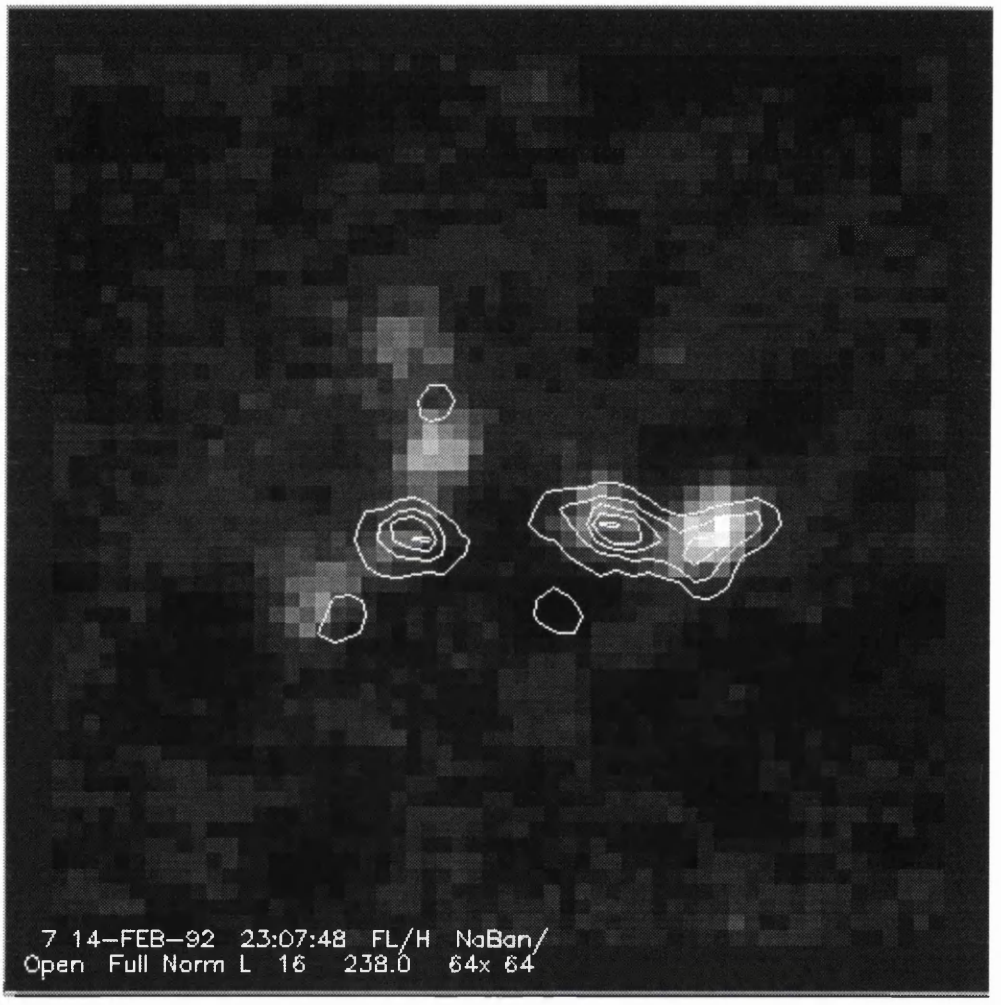

Figure 5.50: As fig. 5.48 and fig. 5.49 but with hard X-ray contours from M1 overlaid at 23:07:39 UT

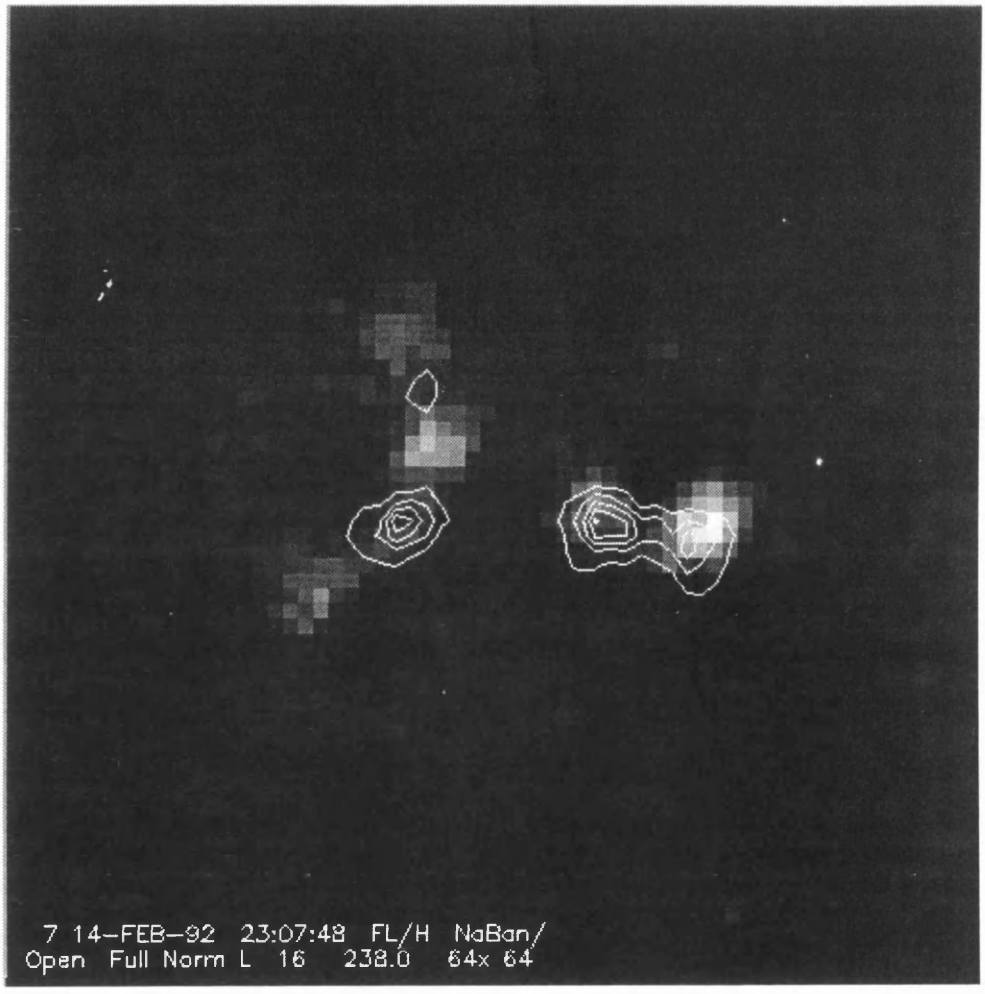

Figure 5.51: As fig. 5.50 with M1 channel contours at 23:07:41 UT.

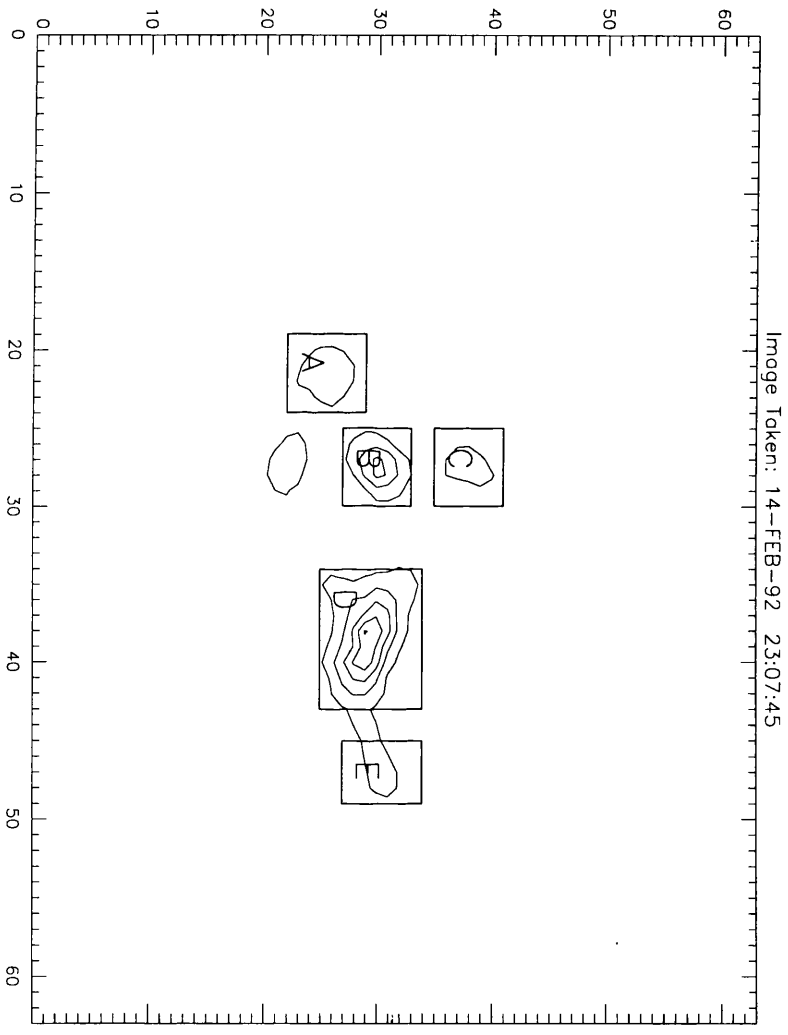

Figure 5.52: Hard X-ray sources *A*, *B*, *C*, *D* and *E* as indicated for the event of February 14 1992, shown in the M2 channel at 23:07:45 UT.

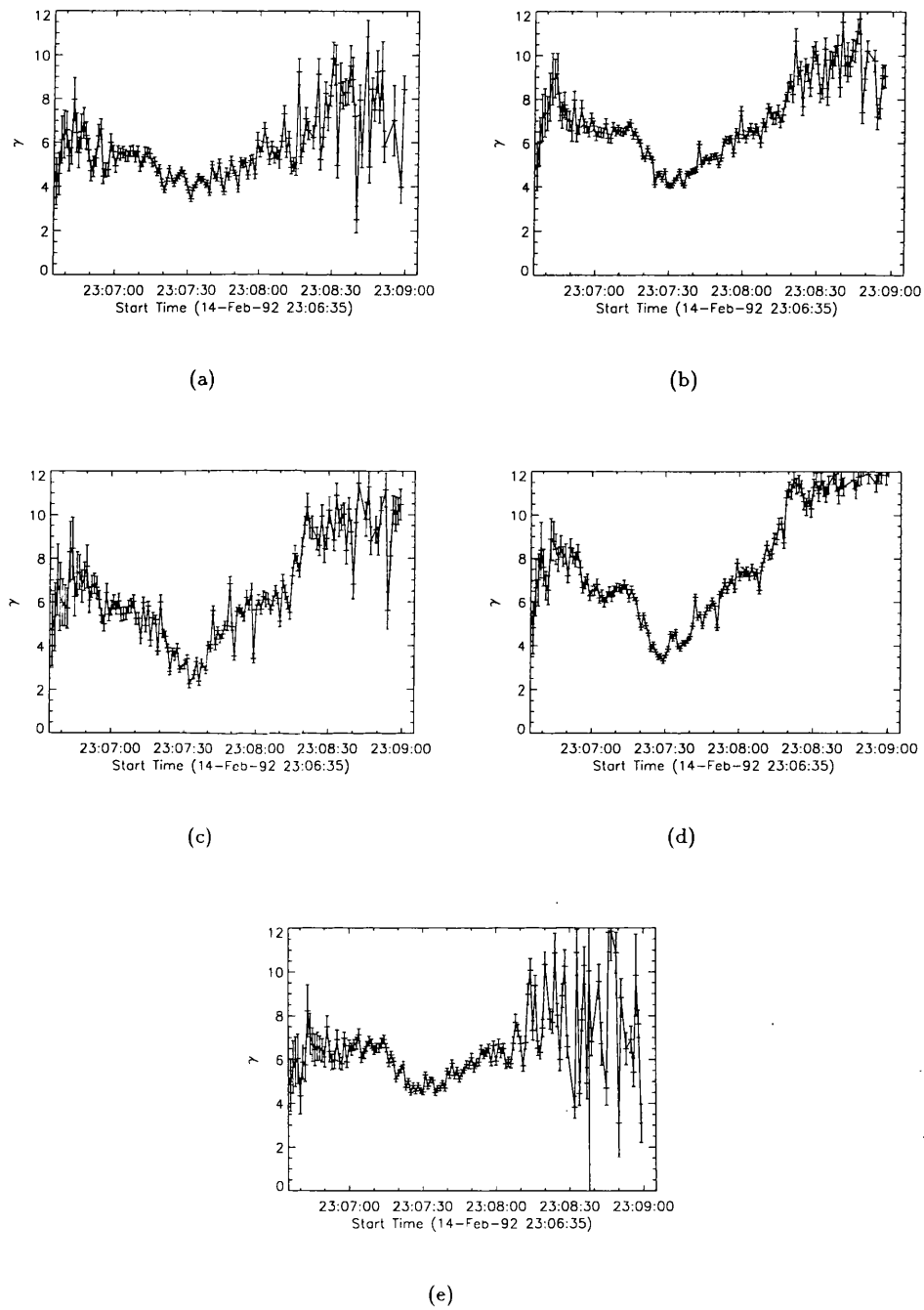

Figure 5.53: The evolution of the hard X-ray spectral index, γ, throughout the event of February 14 1992, derived from images reconstructed using ME methods. Figure a) corresponds to source A, figure b) to source B and so on.

The white-light emission in this source began at $\sim 23:07:15$ UT, rising to a peak at 23:07:40 UT, as shown in figure. 5.54b. The hard X-ray spectrum of this footpoint shows $R > 1$ is attained first at 23:06:40 UT, within the error limits, reaching its maximum value at 23:07:35 UT, fig. 5.54. The overall shape of both these curves is very similar.

Source B

The white-light flare in kernel B began at 23:06:50 UT and reached its peak signal at 23:07:50 UT. The corresponding hard X-ray emission in this location indicates that $R > 1$ is not achieved until 23:06:56 UT, within the error limits. Clearly, if this is the case then the white-light emission in this case cannot be produced by an instability of the beam-return current system. However, we will see later that the same footpoint when imaged using Pixon reconstruction methods shows $R > 1$ from 23:06:50 UT and that within the error limits R is already high at 23:06:35 UT, falling and then rising again. This initial dip corresponds well to a similar dip observed in the white-light emission, fig. 5.56. R reaches its maximum value at 23:07:30 UT (see fig. 5.55), whilst the peak in the white-light emission is attained at 23:07:50 UT.

Source C

White-light emission in this location begins at 23:06:50 UT, reaching maximum signal at 23:07:50 UT, see fig. 5.58. The corresponding hard X-ray emission in this case can be seen to show $R > 1$ at 23:06:35 UT within the error limits, reaching a peak value at 23:07:45 UT. However, as we can see from fig. 5.57 the errors on R are particularly large in this case. This is largely due to the fact the the errors on the constant A, where $I(\epsilon) = A\epsilon^{-\gamma}$ for the hard X-ray spectrum, are $\sim 50\%$ in some cases.

Source D

In this case the white-light emission begins at 23:06:50 UT, reaching a maximum at 23:07:45 UT as shown in fig. 5.60. The corresponding hard X-ray emission indicates $R > 1$ first at 23:06:45 UT within the error limits, rising to a peak at 23:07:30 UT (see fig. 5.59).

Source E

The white-light emission in this kernel began at 23:06:50 UT with the peak of the emission occurring at 23:07:50 UT, fig. 5.62. The hard X-ray spectrum of the emission from this footpoint shows that the first instant at which the drift velocity exceeds the ion-sound speed is at 23:06:50 UT within the error limits. The peak value of R is attained at 23:07:30 UT (see fig. 5.61).

5.8.1 February 14 1992 - Pixon images

The event of February 14 1992 was also reconstructed using the Pixon methods developed by Metcalf et al. (1995). This method of reconstruction has been described above and has been shown to produce fewer spurious sources than MEM algorithms. We can see from a comparison of fig. 5.63 and fig. 5.64 with fig. 5.52 however, that whilst all five hard X-ray sources are visible in the

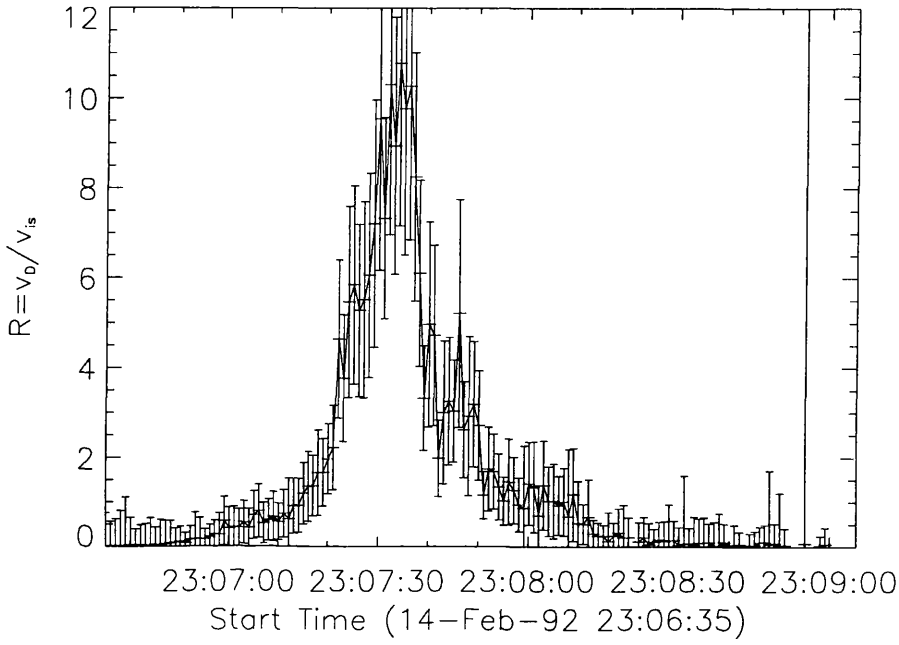

(a)

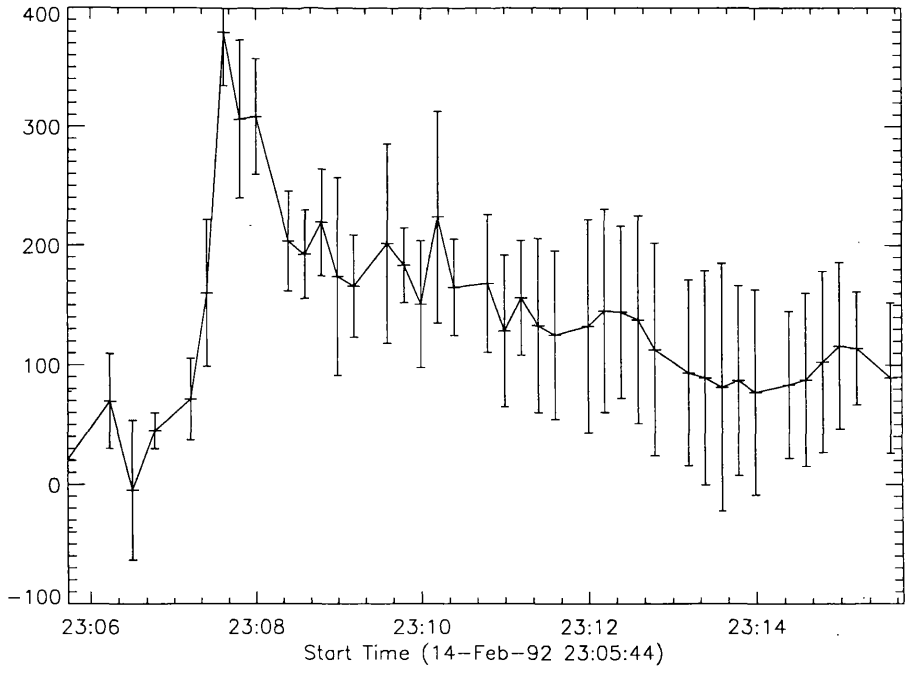

(b)

Figure 5.54: a) The variation of $R = v_D/v_{is}$ with time for footpoint A of February 14 1992, calculated at the $N = 5.004 \times 10^{20} cm^{-2}$ level in model atmosphere P of Basri et al. (1979) and b) The light curve of the white-light emission from source A of February 14 1992.

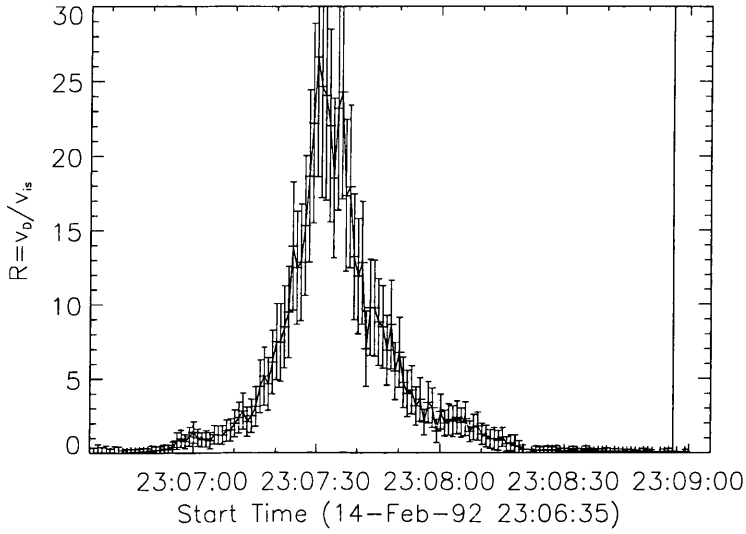

Figure 5.55: As fig. 5.54 for footpoint B.

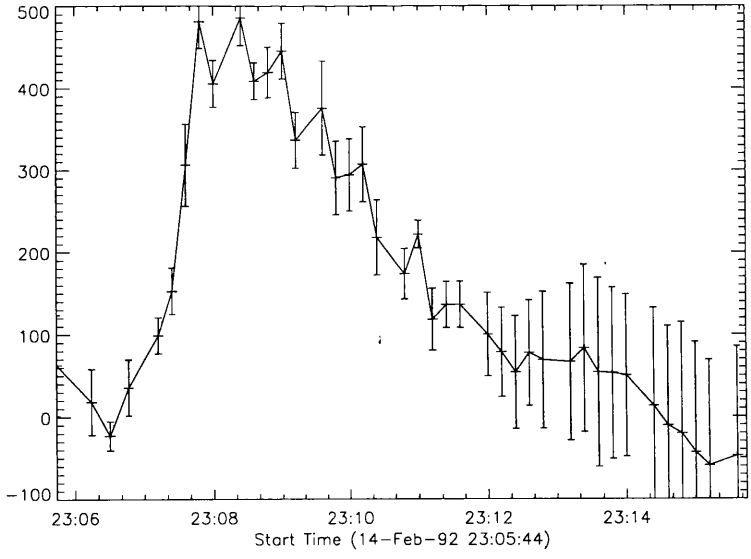

Figure 5.56: As fig 5.54b for source B.

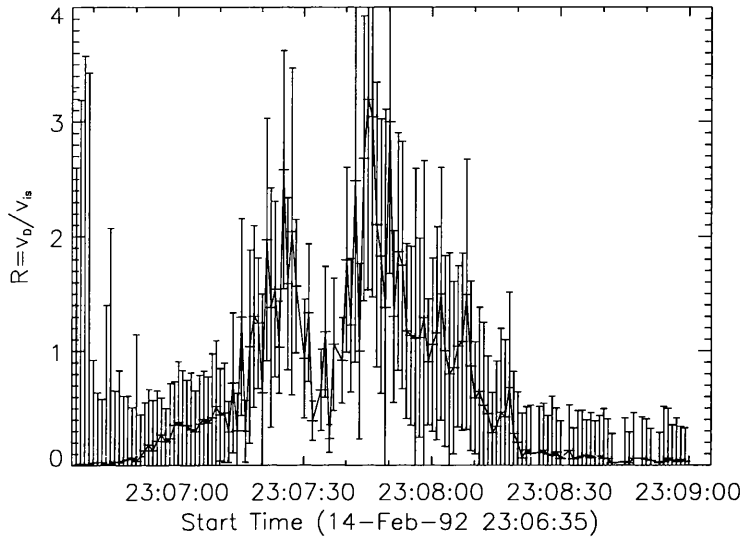

Figure 5.57: As fig. 5.54 for footpoint C.

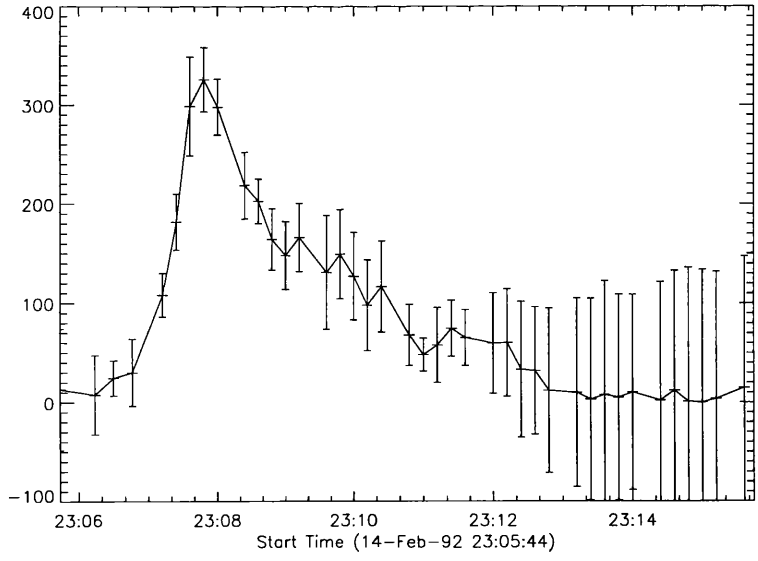

Figure 5.58: As fig. 5.54b for source C.

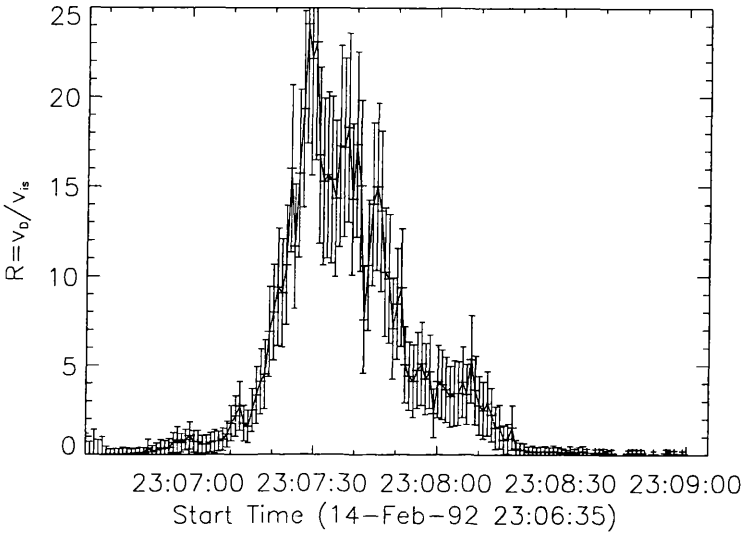

Figure 5.59: As fig. 5.54 for footpoint D.

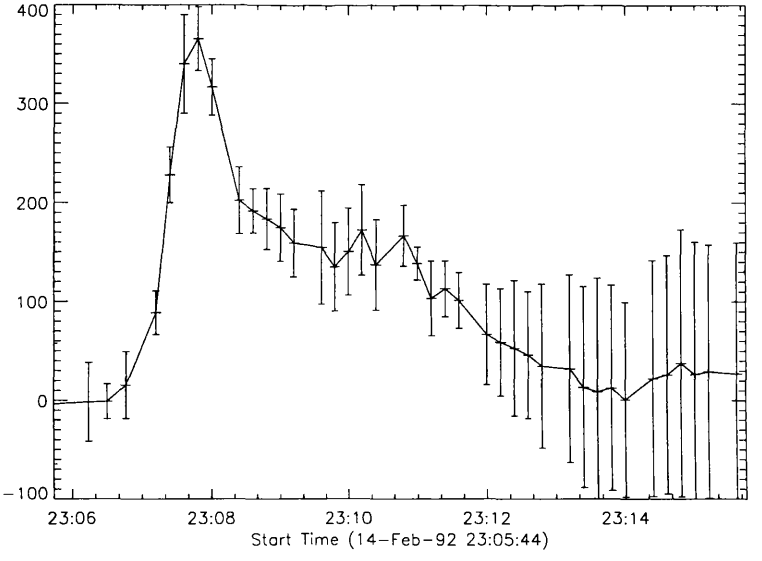

Figure 5.60: As fig. 5.54b for source D.

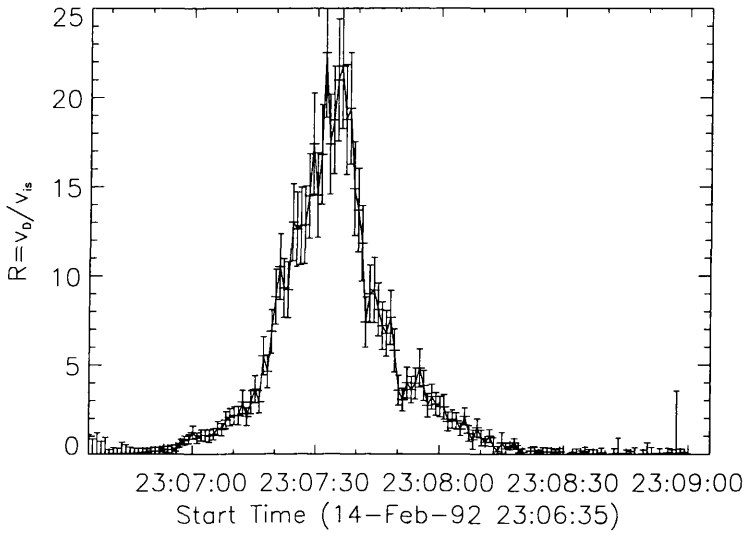

Figure 5.61: As fig. 5.54 for footpoint E.

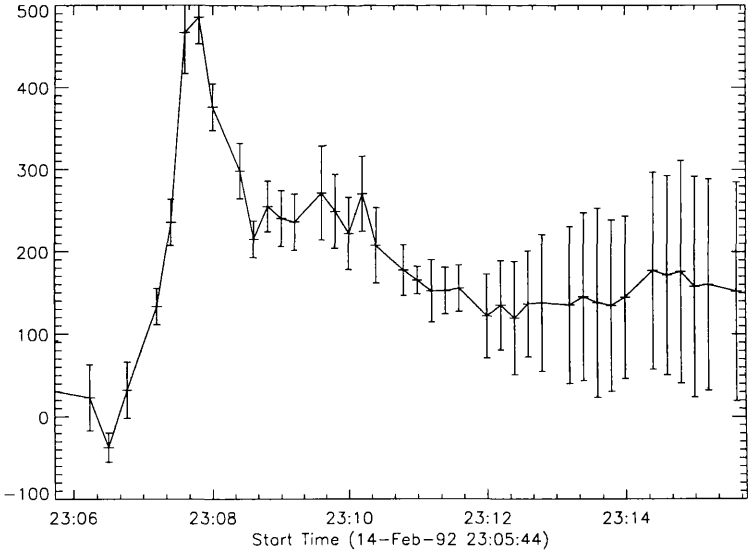

Figure 5.62: As fig. 5.54b for source E.

MEM map, at these contour levels, (fig. 5.52) of the M2 channel at 23:07:45 UT only four sources are visible in each of the pixon maps, fig. 5.63, from the M2 channel at 23:07:50 UT and fig. 5.64, from the M1 channel at 23:06:55 UT, at the same contour level. The 'missing' sources in these cases are indicated by an empty box. It should be noted however, that the light curves of these 'empty' boxes do in fact indicate that there is a hard X-ray source in these locations i.e. a peak,like that observed in the MEM map can be seen. Also, we see that although source C is not visible in the M1 channel (fig. 5.64) it is visible in M2 (fig. 5.63) and vice versa with source A. However, since an estimation of the area of the hard X-ray emission is necessary for this analysis evidence from the light curve is insufficient. In general though, the images from pixon methods were much cleaner and sharper. Figure 5.53 which shows the evolution of spectral index, γ, derived from the MEM reconstructions can also be compared with fig. 5.65 showing those derived from pixon images. Obviously though, since the accumulation times used in the MEM and pixon reconstructions of this event were in fact different, it is not valid to draw any definite conclusions between these two methods on the basis of these results. In order to do this would require that identical accumulation times were used in each case. We should also note that the use of the contours in this context is primarily to identify the location of footpoints. For the actual analysis the light curve of the hard X-ray patches was used to determine the source.

Source A

The white-light emission for this location began at 23:07:15 UT, reaching its peak at 23:07:40 UT, as shown in fig. 5.54b. The hard X-ray emission shows that $R > 1$ is satisfied at 23:07:15 UT, with the peak value of R being attained at 23:07:30 UT (see fig.5.66). The general character of these results is very similar to that obtained from the MEM images, the main difference being the extra structure that is observed in the MEM results (fig. 5.54). This is primarily due to the fact that the image accumulation time is one second for the MEM images whilst it is five seconds for the pixon images. Memory and time constraints prevented pixon reconstruction with the higher time resolution. One other difference is that the values of R are seen to be lower from the pixon images than from the MEM reconstruction.

Source B

The white-light emission in source B began at 23:06:50 UT, preceded by a dip at $\sim 23:06:30$ UT, and rising to a peak at 23:07:45 UT, see fig. 5.56. The corresponding hard X-ray emission shows $R > 1$ at 23:06:35 UT rising to a small peak at 23:06:40 UT, falling again to a minimum at 23:06:45 UT and then rising to a maximum at 23:07:35 UT, see fig. 5.67. The major difference between the results from the pixon image synthesis, fig. 5.67 and those from the MEM image synthesis is the small peak which is observed at the beginning of the interval for the pixon results. Although there is certainly a dip in the white-light emission at the beginning of the event, this occurs at $\sim 23:06:30$ UT, before the dip observed in R. In this case, also the values of R are

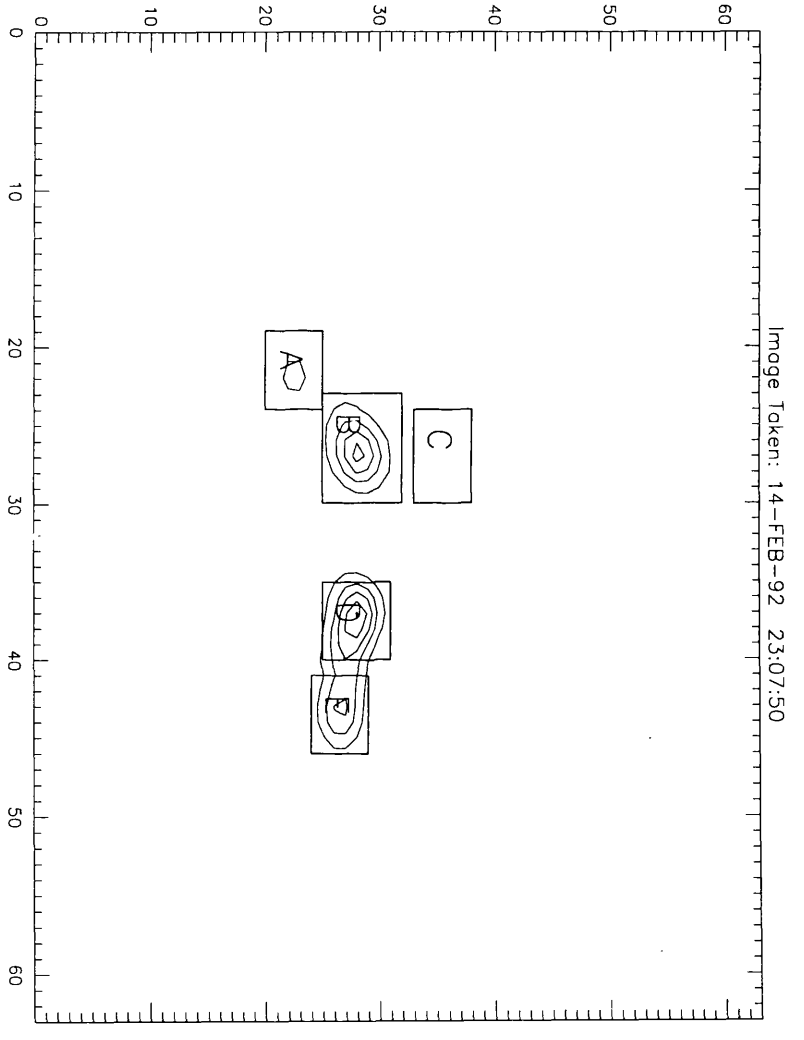

Figure 5.63: Hard X-ray sources *A*, *B*, *C*, *D* and *E*, as indicated, shown in the M2 channel at 23:07:50 UT on February 14 1992.

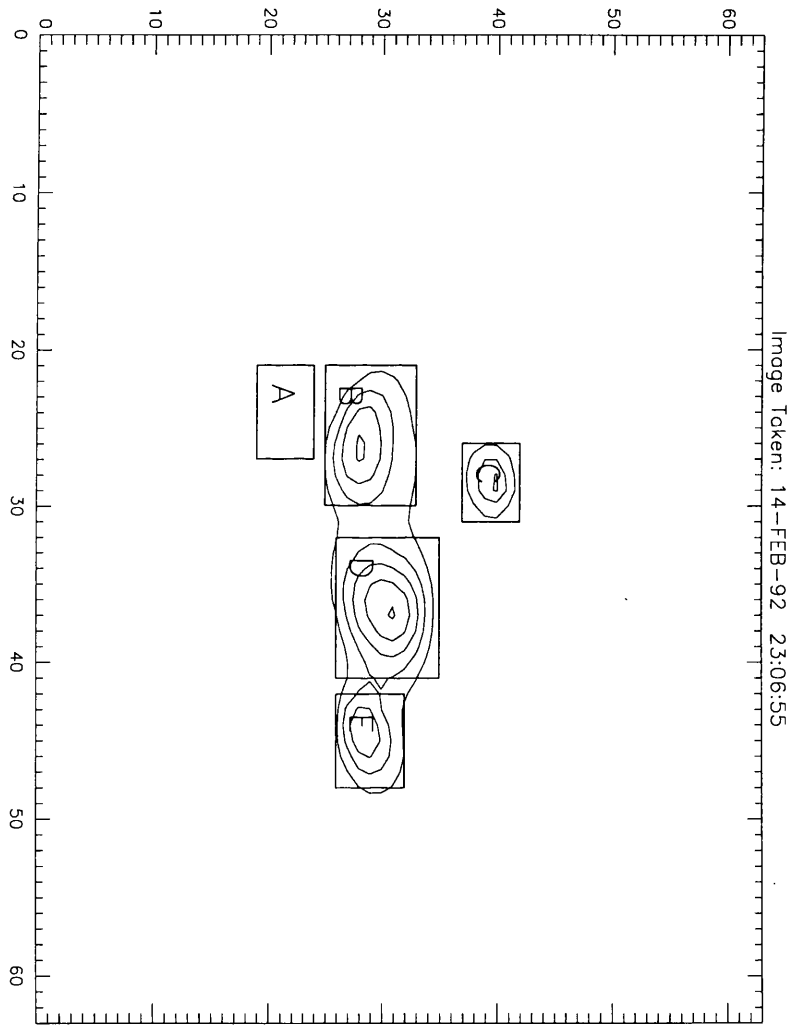

Figure 5.64: As fig. 5.63 but in the M1 channel at 23:06:55 UT.

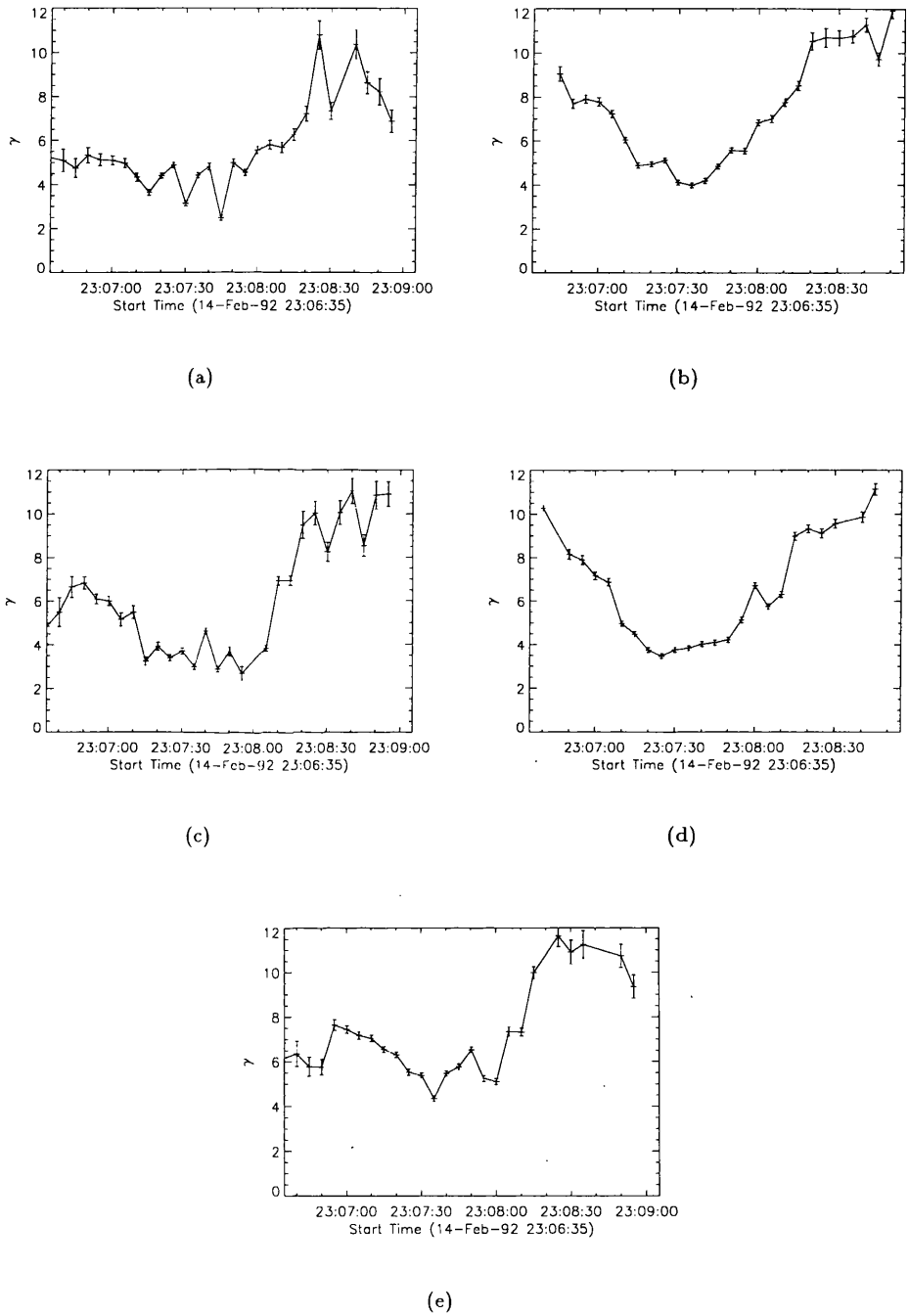

Figure 5.65: The evolution of the hard X-ray spectral index, γ, throughout the event of February 14 1992, derived from images reconstructed using pixon methods. Figure a) corresponds to source A, figure b) to source B and so on.

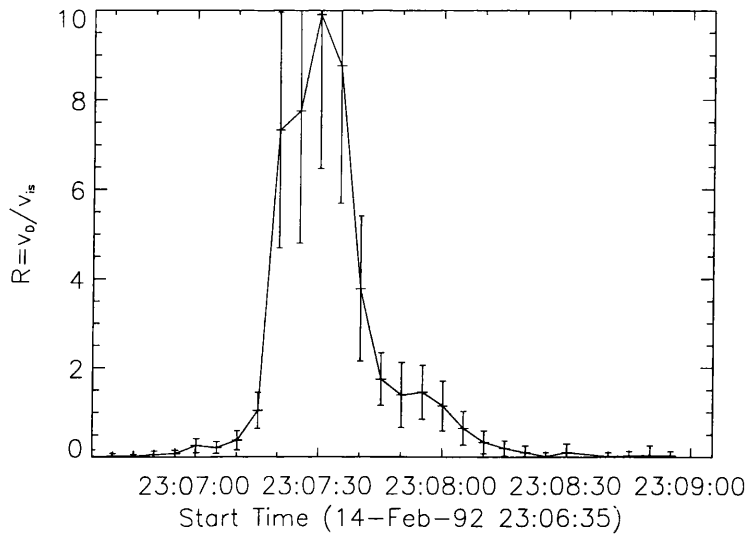

Figure 5.66: The variation of $R = v_D/v_{is}$ with time for footpoint A of February 14 1992, calculated at the $N = 5.004 \times 10^{20} cm^{-2}$ level in model atmosphere P of Basri et al. (1979). Pixon image synthesis.

less than those derived from the MEM images.

Source C

The white-light flare in location C begins to brighten at 23:06:50 UT, reaching a peak at 23:07:40 UT (fig. 5.58). Corresponding hard X-ray emission in this area shows that R does not exceed 1 until 23:07:20 UT, clearly quite some time after the onset of the white-light flare. This was also the case for the MEM results (see fig. 5.57) althought the errors in the determination of the drift velocity in that case were so large as to make it impossible to rule out $R > 1$ being attained earlier. However, it would appear from the pixon reconstruction (fig. 5.68) that the white-light emission almost certainly does commence before the possible onset of an ion-acoustic instability in this case. Again the R values derived from the pixon images are less than those derived from the MEM images.

Source D

As described above for the MEM case, the white-light emission began at 23:06:50 UT, reaching its peak signal at 23:07:50 UT (fig. 5.60). Fig. 5.69 shows that within the error determination, $R > 1$ occurs first at 23:06:50 UT, rising to a peak at 23:07:25 UT. Apart from lower values of R derived from pixon images and the lower time resolution, the general character of fig. 5.69 is very similar to that of fig. 5.59, showing the MEM results.

Source E

The white-light emission began at 23:06:50 UT reaching a peak at $\sim$ 23 : 07 : 45 UT see fig. 5.62. The hard X-ray spectral parameters derived from the pixon images indicate that $R > 1$

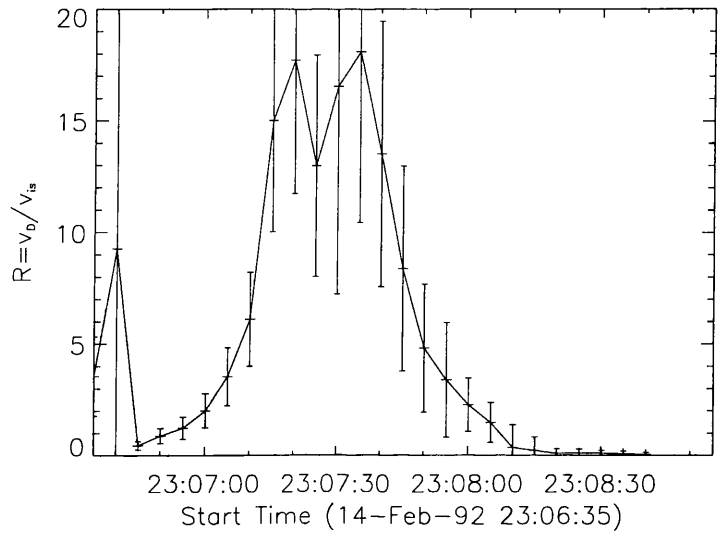

Figure 5.67: The variation of $R = v_D/v_{is}$ with time for footpoint B of February 14 1992, calculated at the $N = 5.004 \times 10^{20} cm^{-2}$ level in model atmosphere P of Basri et al. (1979). Pixon image synthesis.

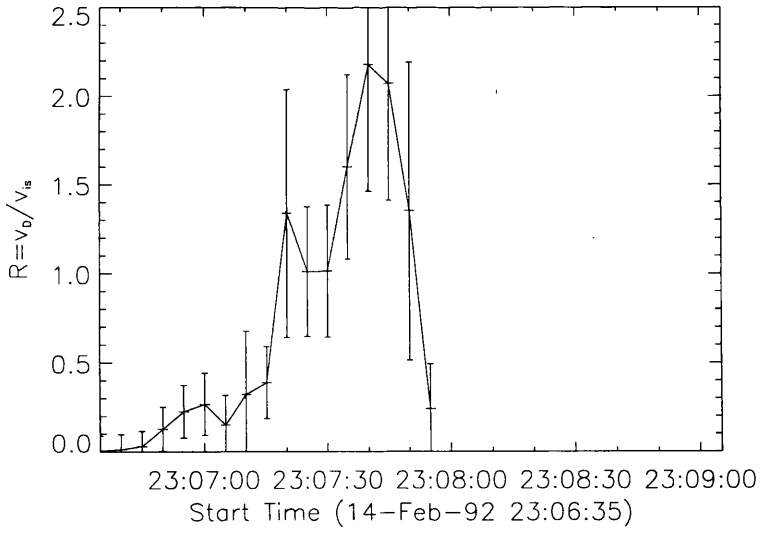

Figure 5.68: The variation of $R = v_D/v_{is}$ with time for footpoint C of February 14 1992, calculated at the $N = 5.004 \times 10^{20} cm^{-2}$ level in model atmosphere P of Basri et al. (1979). Pixon image synthesis.

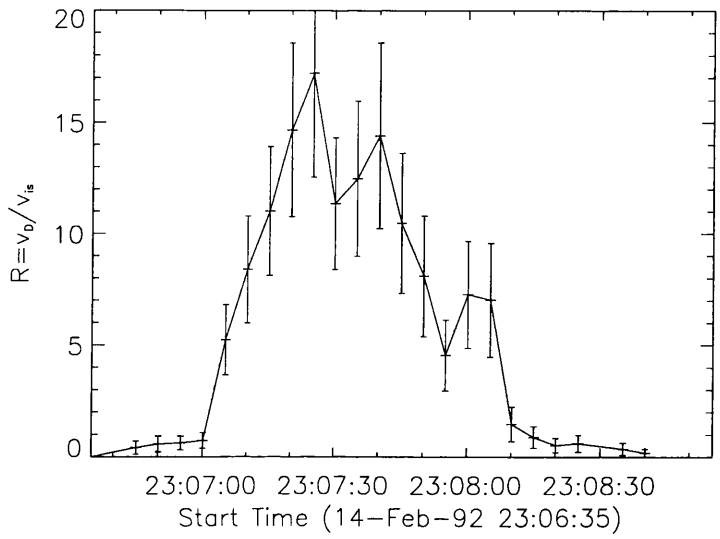

Figure 5.69: The variation of $R = v_D/v_{is}$ with time for footpoint D of February 14 1992, calculated at the $N = 5.004 \times 10^{20} cm^{-2}$ level in model atmosphere P of Basri et al. (1979). Pixon image synthesis.

is satisfied at 23:06:40 UT, within the error limits, reaching a peak value at around 23:07:25 UT. Again we see the main difference between the results from the pixon images, fig. 5.70, and those from the MEM images (fig. 5.61) is the lower time resolution and consistently lower values of R attained.

5.9 Conclusions

The main driving force behind this analysis was the idea that if, as shown in the previous chapter, the return current associated with a hard X-ray producing electron beam can be unstable to the generation of ion-acoustic turbulence in the deep chromosphere then the anomalous Joule heating associated with this could heat the atmosphere sufficiently to account for the white-light flare. It is obvious from the temporal and spatial coincidences between the white-light and hard X-ray flares that the probability that both these phenomena are produced by the same electron distribution is high and so it would not appear to be an unreasonable suggestion that a beam-return current instability might be a viable mechanism for the white-light flare.

The results of the spectral analysis of the individual footpoints of the hard X-ray emission when compared to the corresponding white-light patches also do not by themselves rule out this possibility; although there are certainly cases for which the white-light emission appears to begin before the onset of an ion-acoustic instability. However, there are several points which must be addressed.

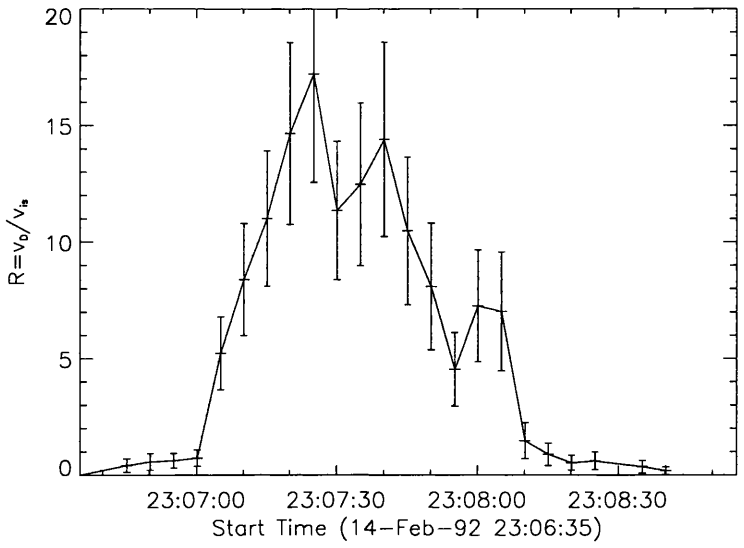

Figure 5.70: The variation of $R = v_D/v_{is}$ with time for footpoint E of February 14 1992, calculated at the $N = 5.004 \times 10^{20} cm^{-2}$ level in model atmosphere P of Basri et al. (1979). Pixon image synthesis.

Firstly, the excitation of ion-acoustic waves does not necessarily guarantee their growth to the point where anomalous resistivity sets in and is maintained. There are several other possibilities. The onset of anomalous resistivity tends to lead to rapid heating which increases the electron temperature, increasing the ion-sound speed and thus reducing the ratio $R = v_D/v_{is}$ once again to a sub-critical level. On longer time-scales the heated plasma can undergo further collisional ionization which leads to an increase in the number of free electrons, ie. an increase in x, the degree of ionization, which again leads to a decease in R, switching off the instability. A further effect of anomalous resistivity is a strong increase in the return current driving electric field, since $\underline{\mathbf{E}} = \eta j_b$. When the resistivity η increases, E necessarily increases and the beam is strongly decelerated. If the resistivity does remain anomalous for a sufficiently long time then the beam will be stopped over a very short distance and we would expect there to be a significant energy deposition at this point. However, the calculation of the ion-acoustic wave growth rate for a partially ionized plasma is definitely necessary before anything definitive can be said about a connection between a return current instability and the white-light flare.

Secondly, the drift speed has only been calculated at one level of a semi- empirical active region model atmosphere. Although, this is appropriate at the beginning of the flare it would be interesting to calculate how the atmosphere would evolve if the anomalous resistivity did persist. There are now several model atmospheres for white-light flares (e.g. Mauas et al., 1990, Ding et al., 1994) with which such a calculation might be compared. Below we consider the time and distance over which the beam is stopped for typical values from the data at $N = 5.0 \times 10^{20} cm^{-2}$ and the

increased heating rate which would result from this. If we assume a pre-flare energy content for a loop we can also calculate the maximum temperature increase at this level that anomalous heating can create (van den Oord, 1990), which can be compared with typical temperatures found in the white-light flare models.

From van den Oord (1990), if anomalous resistivity develops, then

$$\nu_{eff} \simeq 10^{-2}\omega_p \tag{5.17}$$

where ν_{eff} is the effective collision frequency and ω_p is the plasma frequency. The rate of return current dissipation in this case is given by,

$$W_R \simeq 10^{34}\beta\tau \tag{5.18}$$

and the beam energy is dissipated on a time scale of

$$\tau_{stop} = (\frac{n_p}{n_b})\frac{2}{\nu_{eff}} \simeq 10^{-9}\frac{n_p}{n_b}\ s. \tag{5.19}$$

where n_p is the ambient plasma density and n_b is the beam density. For a beam density of a few times $10^8 cm^{-3}$, and $n_p = 3.5 \times 10^{13} cm^{-3}$ at $N = 5.0 \times 10^{20} cm^{-2}$ in the active region model P of Basri et al. (1979), this gives a stopping time of $\sim 1.1 \times 10^{-4} s$.

The distance over which the beam is stopped is then also given by van den Oord (1990), viz.,

$$v_b \tau_{stop} \simeq 30\beta(\frac{n_p}{n_b})\ cm \tag{5.20}$$

which, for an average electron energy of 50 keV, gives a stopping distance of $\sim 10^6 cm$, indicating that significant energy deposition would occur in this layer of the atmosphere.

The anomalous Ohmic heating rate is given approximately by $W_R \simeq 10^{34}\beta\tau$ where τ is the duration, and $\beta = v/c$ (van den Oord, 1990). If the beam is stopped over a distance of $10^6 cm$, then this gives an anomalous heating rate over this distance of $\sim 10^{29} ergs^{-1}$. If we consider that the pre-flare energy content of this layer of the atmosphere is given by $\epsilon = 1.5 n k_B T \times volume \simeq 1.3 \times 10^{25}$ we can estimate the maximum temperature which can be obtained over the distance that the beam is stopped by considering the energy balance of this layer without radiative and conductive losses. By solving the equation $\frac{d\epsilon}{dt}$ and allowing the resistance to vary with temperature (van den Oord, 1990), the maximum temperature, T, attainable is given by:

$$T = T_0(1 + 5/2(W_R/\epsilon)t)^{2/5} \tag{5.21}$$

where we take t to be the beam stopping time. In this case we find that the maximum temperature attainable is $\sim$ 9600 K. Typical temperatures at an equivalent column density in the white-light flare model atmospheres of Mauas et al. (1990) are about 7000 K. However, the estimated value

of W_R does not take into account the fact that the resistance depends on temperature, $\sim T^{-3/2}$, and as the plasma starts to heat up , the heating rate will decrease. We have also neglected both radiative and conductive losses. Clearly, though, anomalous heating in the layer at which the beam is stopped is capable of producing significant temperature increases.

Thirdly, and most importantly, are the problems with the data analysis. For all of these events spatially resolved spectra were calculated from images produced using maximum entropy methods. The biggest problem with deriving quantitative results from this type of map is that MEM is a non-linear procedure. The errors on the counts in the restored map are no longer purely Poisson and are much harder to deal with; the upshot of this being that it is very difficult to produce reliable χ^2 statistics quantifying the fit. Even before this the energy resolution on HXT is rather crude with only four channels. Also, the errors associated with the determination of the constant associated with the power law tend to be somewhat high.

For the February 14 1992 event the hard X-ray data was also reconstructed using the pixon methods developed by Metcalf et al. (1995). Although these maps certainly had much less spurious structure than the MEM images, the spectral results differed significantly only in the fact that they produced consistently lower values for the drift velocity.

The biggest source of uncertainty in this study lies in the spectral analysis of the hard X-ray footpoints. Potentially, the initial 'dirty map', as described above, would provide more reliable results for the spatially resolved spectra since the Fourier transform is linear and the errors in this case remain Poisson. However, determination of the area of the source is likely to be much harder in this case than with the cleaner images. Sakao (1994) describes a Gaussian fitting procedure with a linear characteristic for image reconstruction. This works by approximating the hard X-ray distribution by a number of circular Gaussian sources. It has several advantages over the maximum entropy method: it has a linear characteristic and so handles quantitative values of the hard X-ray sources properly; the results of the fitting can be properly evaluated with χ^2 statistics and it gives satisfactory results for count rates as low as 30-50 cts/subcollimator. This latter point would be a significant advantage in studying the earliest phases of the flare. Its main drawback, though, is that it is not suitable for obtaining the precise shape of the hard X-ray sources, although this is not a problem for nearly circular double sources like the November 15 1991 event.

In conclusion, although it cannot be claimed that this mechanism is the unique answer to the origin of the white-light flare, it seems at this stage that it cannot be dismissed out of hand without some further investigation of the kind discussed above. Another interesting possibility that might be addressed is the effect of the magnetic field on the development of a return current instability. We saw for the November 15 1991 event that the stronger magnetic field in one footpoint led to delayed emission in the highest energy channel, it is possible then that in these circumstances the white-light emission in areas of high magnetic field strength might be delayed, or might be dimmer.

Chapter 6

Conclusions and Future Work

The purpose of this short chapter is to provide an overall conclusion to the results described in the preceding chapters in order to provide a more coherent overview of what has been achieved, the limitations of particular pieces of work, in particular those results of Chapters 3 and 5, and the possibilities for improving and moving forward in these areas.

A large chunk of the work that forms this thesis has involved the analysis of data. Inevitably, in my opinion, there are always better ways to handle data analysis, which one learns through experience, both personal and from other people, and there will most certainly be improvements in the quality of data as technology continues to progress. Bearing this in mind, I will outline some of the improvements which I would like to make in repeating and improving some of these analyses, particularly those of Chapter 5, and the improvements in the data which I would also like to be able to make. However, theory and data analysis should not, as they largely tend to be, be separate disciplines and we will discover some theoretical possibilities as well.

6.1 Nonthermal Line broadening in γ-ray flares

In Chapter 3 we investigated the possibility of a direct correlation between the nonthermal line broadening that is observed in the soft X-ray lines from flares and the γ ray line spectrum. Specifically, we assumed a model of particle acceleration due to the presence of MHD turbulence and, by appealing to energy conservation, considered the decay of the turbulent energy density to particle kinetic energy. Whilst it is obvious from the results presented in Chapter 3 that this model cannot be the only mechanism responsible for the observed line broadening, since it is unable to account for the observed rise in v_{nt} after about 30 seconds, it is certainly interesting from the point of view of being a self consistent model which can account for quite disparate phenomena on some level.

The model used in this work is limited in several respects. Firstly, the accelerator has been assumed to be 100% efficient in the sense that no other energy losses from the waves have been

included. While this will affect the validity of the model from the point of view of proton acceleration, it will not affect the soft X-ray analysis. Secondly, the wavenumber spectrum has been allowed to decay uniformly in wave number. It is more likely that the higher wave numbers will decay on longer timescales than those with lower k values since there are more particles at lower energies to resonate with the waves (Alexander - private communication). To treat this problem properly requires a quasi-linear treatment to describe the the wave particle interactions and the effect of the back reaction of the accelerated particles on the turbulence. Bogdan et al. (1991) have presented the first rigorous theory for stochastic second order Fermi acceleration of particles in which the back reaction of the accelerated particles on the turbulence is considered. In this model the sum of the fluctuation and the particle energy is conserved and the theory is based on quasi-linear theory and the assumption that the relevant waves are transverse hydromagnetic waves propagating parallel to the magnetic field. The wave particle interaction is therefore governed by the cyclotron-resonance condition (e.g. Melrose, 1980). If the energy density of the energetic particles is larger than that of the fluctuation power in the resonant frequency range then the derived energetic particle spectrum differs greatly from that derived in linear theory, in which the wave intensities are specified. A treatment of a similar nature should be applied to the proton acceleration problem.

Thirdly, only particles with velocities in excess of the Alfvén speed can be accelerated by the waves. For conditions in the flaring corona this implies that the protons have to gain energy in excess of 25 keV before they can resonate with the waves. In order to achieve this a first step acceleration process would be required. It is conceivable that the reconnection events which are thought to indicate the initial energy release could provide this acceleration (Antonucci et al., 1986). However, in this case the time between the initial flare energy release and the decay of the wave energy should be characterized by either large constant or increasing line widths (Alexander and MacKinnon, 1993).

Without performing the type of analysis described above there is little more of great interest to be gained from the application of this model, as it stands, to further data. Having said this, it would be interesting to study a simple loop flare on the limb which has a simple 'face-on' geometry. In this case all upflow velocities will be perpendicular to the line-of-sight and should not contribute a component to the Doppler velocity, thus providing an event which is free from hydrodynamic effects. In this case we would, hopefully, be looking at pure nonthermal effects and we may find a better fit of the wave decay to the nonthermal velocity decay.

In Chapter 3 we also considered one γ-ray event observed by *Yohkoh*. Although this was far from an ideal event to study, for the reasons described in Chapter 3, the BCS instrument on board *Yohkoh* does potentially provide a wider ion coverage than that on SMM. It appears from all the events considered in Chapter 3 that there is an ion dependence associated with the nonthermal line

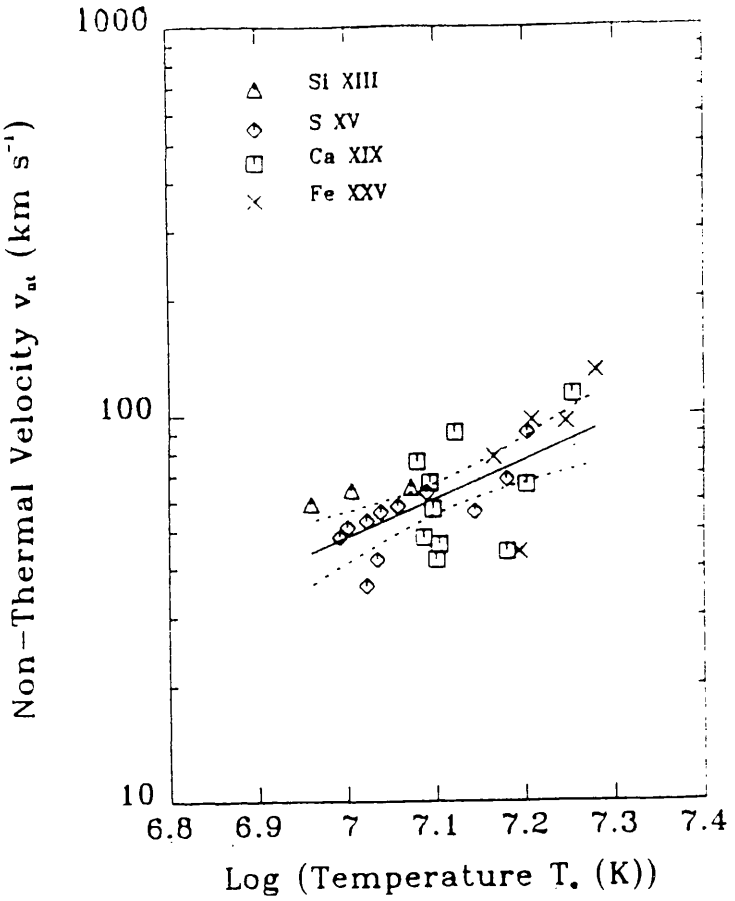

Figure 6.1: Nonthermal velocities derived from soft X-ray lines formed in the 'hot' component of the flare plasma, plotted as a function of the temperature of line formation (from Antonucci and Dodero, 1995).

broadening. Indeed, Mariska (1992) and Antonucci and Dodero (1995) have indicated that non-thermal velocities observed in the flaring corona depend on the temperature of line formation and that systematically higher velocities have been found for e.g Fe XXV (peak emission temperature 5×10^7K) than for S XV (peak emission temperature 1.6×10^7 K).

This temperature dependence was first suggested by Saba and Strong (1991b) and the general trend for v_{nt} to increase from the chromosphere to the corona has been confirmed by the results of Antonucci and Dodero (1995), Saba and Strong (1991a) and Dere and Mason (1993) (see fig. 6.1). This result suggests that there is a direct relation between the nonthermal velocity and the degree of plasma heating. This is inconsistent with the Alfvén wave broadening being able to account for the whole of the observed excess line width.

Khan et al. (1995) used limb occultation to investigate the correlation between the nonthermal velocity and the hard X-ray count rate but were unable to reach any definite conclusions. Presently, the potential correlation between spatially resolved hard X-ray sources observed by HXT on *Yohkoh* and the temporal behaviour of the non-thermal line broadening is underway (Alexander, Khan, Harra-Murnion and Matthews). We hope in this study to test for a source dependent component

in the nonthermal velocity and to determine whether there is a direct response in the nonthermal broadening to the energy deposition associated with the hard X-ray emission. Ideally we would like to be able to separate what is really 'nonthermal' in the line broadening, i.e. we are examining soft X-ray lines which are an indirect product of the initial energy release through plasma heating, this heating being a convolution of the energy input with the ambient plasma properties and we then use the thermal emission to determine the nonthermal component, i.e $T_D - T_e$.

6.1.1 Line narrowing

Finally, on the subject of nonthermal line broadening it is worth mentioning the problem of line narrowing inherent in the BCS on *Yohkoh*.

When an X-ray photonenters a proportional counter window, an atom of the counter gas is ionized, then a cloud of positively ionized gas atoms begin to drift toward the cathode and the resulting distribution of ions can be calculated if the electric field in the detector is known. When a detector is illuminated by a narrow beam or point, then a sheet of ions is produced in the drift regions and this charge generates an electric field which has a component perpendicular to the plane of the sheet. Primary electrons are attracted to this region as they drift toward the anode (Trow et al., 1994). The amount of lateral drift depends on the density of ions in the sheet, the location of the primary ionization, and the drift velocity of the electrons. Since the sites of the initial ionization occur at a range of depths, it is expected that a distribution of lateral drifts will be observed for a particular initial perpendicular distance from the ion sheet (Trow et al., 1994).

The practical consequences of this are as follows. Each point in an image produces its own positive ion sheet which can affect electron trajectories in all other parts of the detector. The result is that bright regions in any image will attract one another, and the degree of attraction will be a function of the count rate (Trow et al., 1994). Certain regions in the image will increase in intensity and other parts may decrease, although the overall number of counts remains unchanged. Distortions cause the profile to remain symmetrical but decrease in width; this being the line narrowing which is observed in the BCS data. It has been observed in all three of the most commonly used channels, S XV, Ca XIX and Fe XXV and while temperature measurements are unaffected by it (the total count is unchanged), the calculation of nonthermal velocity is, and as a result can only be considered to be a lower estimate of the true value.

Trow et al. (1994) developed a numerical model of the image distortion effect and found that their modelled results were well approximated by a family of exponential functions describing the position shift as a function of distance from the central bright region, viz.,

$$shift = A\exp(-x/d) \tag{6.1}$$

where A is a parameter depending on the count rate, x is the distance of the test peak from the

bright region and $d = 8.3$ is a scale length parameter.

However, they found that the modelled shifts were not large enough to account for the distortions which are seen in practice and the exponential law was not confirmed in experiment.

To undertake a detailed study of nonthermal velocities observed in the soft X-ray lines observed by *Yohkoh* it seems important that we should be able to make some kind of estimate for the line narrowing, if only in terms of its variation with the count rate, in order that we can either compensate for its effect or at least place a more rigorous boundary on the derived v_{nt} values.

6.1.2 γ-ray analysis

Although it appears that there have been no observable γ-ray flares on the Sun since January 1992 (Kosugi, 1994) there are nevertheless a number of events which were observed by *Yohkoh* between its launch and this time. To date, only three of these events have been analyzed in any detail. In Chapter 3 we considered one of these events, using the inferred spectral parameters of Yoshimori et al. (1994) and Kawabata et al. (1994). However, in order to exploit fully further γ-ray data from *Yohkoh* it will be necessary to fit the data.

An observed pulse height count distribution is a convolution of the incident photon spectrum with the instrumental response. Generally, the incident spectrum is recovered by one of two methods. The first of these involves the deconvolution of the count distribution from the instrument response using some type of inversion technique. The second, and mostly commonly applied, involves convolving a trial spectrum with the instrument response and comparing this spectrum with the observed spectrum. Ultimately, we are interested in the parent proton, or electron spectrum responsible for the γ-ray emission. For the proton spectrum the fluence in any one line will tell us the number of interacting protons for that event, and the ratio of the fluence in e.g. the 2.223 MeV neutron capture line to that in the 4-7 Mev band can tell us the shape of the proton spectrum (see Chapter 3 for more details). This approach is, however, model dependent.

The possibility of inverting the incident γ-ray spectrum to obtain the parent proton spectrum is an intriguing prospect, although a rather daunting one. The most difficult aspects of this problem are fitting the continuum satisfactorily and getting the correct abundances. The continuum is composed of both an electron bremsstrahlung componet ($\lesssim 1$ MeV) and a mixture of broad nuclear lines and the level of it is rather uncertain. In order to make the problem tractable it is probably necessary to perform some kind of hybrid fitting in which a form for the continuum is assumed (MacKinnon -private communication). Even with this simplification other problems still exist, including the overlap of many of the nuclear cross sections, which will still make the problem very difficult. If it could be achieved though, it could provide us with unique insights into the process of particle acceleration in flares, from a virtually model independent point of view.

6.2 Beam driven return current instabilities

In Chapter 4 we established that as the degree of hydrogen ionization decreases deep in the chromosphere there is a possibility that the return current associated with a thick target electron beam can become unstable to the generation of ion-acoustic waves, which can in turn lead to the onset of anomalous resistivity and the disintegration of the beam. This is important from a few points of view. Firstly, the layers of the atmosphere in which $R(N) > 1$ would be the layers where the beam propagation ceases and strong energy deposition occurs, but it would also be the position where the beam/return current closes.

The treatment in this chapter is time independent, and as such we can only speculate as to what will happen when the anomalous resistivity sets in. As discussed in Chapter 4 there are several possibilities, including fast heating which lead to an increase in the electron temperature, a corresponding rise in the ion sound speed, v_{is}, and a switching off of the ion-acoustic instability; on longer timescales the heated plasma can collisionally ionize further leading to an increase in the number of free electrons, an increase in $(x + x_M)$ and a decrease in $R(N)$, again switching off the instability. To be able to qualify further whether the beam will be stopped by the onset of anomalous resistivity, we have to calculate the ion-acoustic wave growth rate in a weakly ionized plasma. For a fully ionized plasma we have the dispersion relation for ion-acoustic waves given by (Galeev and Sagdeev, 1973)

$$0 = 1 - \frac{\Omega_p^2}{\omega^2} + \frac{\Omega_p^2}{k^2 v_{is}^2}\left\{1 + i\left(\frac{\pi m}{2M}\right)^{1/2}\left(\frac{\omega}{k v_{is}} - \frac{\mathbf{k}.\mathbf{v_d}}{k v_{is}}\right)\right\} \tag{6.2}$$

and the growth rate, γ, given by the imaginary part of the dispersion relation, viz.,

$$\gamma \simeq \sqrt{\frac{\pi m}{8M}}\left(\frac{\omega}{k v_{is}} - \frac{k v_d}{k v_{is}}\right) / \left(1 + \frac{k^2 v_{is}^2}{\Omega_p^2}\right) \tag{6.3}$$

where v_{is} is the ion sound speed, Ω_p is the plasma frequency, ω is the wave frequency, k is the wavenumber, m the electron mass and M the ion mass. The growth rate is essentially the ion plasma frequency reduced by a factor equal to the ratio of the electron drift velocity to the electron thermal speed.

Also, the threshold for the onset of the ion-acoustic instability depends heavily on the ratio of the electron temperature to the ion temperature. While this is well known for a fully ionized plasma this treatment has not considered what this value is in a partially ionized plasma, such as the deep chromosphere. Almost certainly incorporating this dependence will increase the threshold for the onset of the instability above the value $R = 1$. From the point of view of the stability of the beam through the corona this can only improve the results since it permits the possibility of somewhat larger beam fluxes than the $10^{17} cm^{-2} s^{-1}$ which were considered in these cases.

The big question with this problem is whether the mechanism can persist once the flare is

well established. The results obtained using the atmospheric parameters of Machado and Linsky's (1975) flare model 1 (see fig. 4.6) are rather discouraging from this point of view. However, it is possible that the flare is highly filamented and that these atmospheric parameters are only averages, in this case one might find that the instability occurs in some filaments but not others. Also, it appears that the beam/return current system is most susceptible to the onset of instability at the beginning when the atmosphere is still relatively cool and least dense. If this is so then the generation of ion-acoustic waves early on may affect how the flare progresses. To answer this question requires numerical calculation of the response of a model atmosphere to energy input in the form of an electron beam taking into account losses due to the anomalous Ohmic heating caused by the generation of ion-acoustic waves.

As a first approximation we can calculate the beam energy deposition with column density allowing for arbitrary ionization and return current losses (e.g. Emslie, 1980), viz.,

$$I_B(N) = n \int_{E_0^*}^{\infty} F_0(E_0) \left| \frac{dE}{dN} \right| (E_0, N) dE_0 \tag{6.4}$$

where

$$\frac{dE}{dN} = -\left\{ \frac{2\pi e^4}{\mu E} [x\Lambda_c + (1-x)\Lambda_c'] + \frac{\eta e^2 F_{00}}{n} \left(1 + \frac{E_0^*}{E_{00}} \right)^{1-\delta} \right\} \tag{6.5}$$

with Λ_c and Λ_c' as in Chapter 4 and Emslie (1978), x the degree of ionization and E_0^* the injection energy corresponding to $E = 0$ at column density N.

$$F_0(E_0) = (\delta - 1) F_{00} \frac{E_{00}^{\delta - 1}}{(E_{00} + E_0)^{\delta}} \; electrons \; cm^{-2} \; s^{-1} \; keV^{-1} \tag{6.6}$$

is the differential energy spectrum of the beam with E_{00} and δ constants and F_{00} the total injected flux. The classical resistivity for a plasma of arbitrary ionization is given by Spitzer (1962),

$$\eta = \frac{7.26 \times 10^{-9} x}{T^{3/2}} ln \left[\frac{3}{2e^3} \left(\frac{k^3 T^3}{\pi n} \right)^{1/2} \right] + \frac{7.6 \times 10^{-18} (1-x) T^{1/2}}{x} \tag{6.7}$$

We can then calculate the beam energy deposition with column density for those model atmospheres considered in Chapter 4 (e.g. active region models of Basri et al., 1979), setting the resistivity to an anomalous value at the levels where we expect the return current to be unstable. However, of more interest would be to take an initial model atmosphere and calculate the hydrodynamical response of this atmosphere to energy input in the form of a beam taking into account all of these losses (see e.g Nagai and Emslie, 1984), including those due to anomalous Joule heating before the beam breaks up and see whether the resultant atmosphere is similar to the white-light flare semi-empirical model atmospheres of Mauas et al. (1990) and Ding et al. (1994).

6.3 White-light flares

In Chapter 5 we examined four white-light flares observed by the the SXT Aspect Camera on board the *Yohkoh* satellite from the point of view of establishing whether the anomalous Joule heating caused by the return current instability was capable of powering the white-light emission. For all of the events considered it is obvious that there is a spatial and temporal coincidence between the white-light and hard X-ray flares, which provides a strong case for assuming that the same electron distribution is responsible for both of these emissions. We can also see that in general the light curve of the white-light flare in each footpoint has similar general trends to the plots of the evolution of the ratio of the return current drift speed to the ion sound speed, and that the onset of an ion-acoustic instability coincides well with the onset of the white-light flare within the error limits imposed by the determination of the drift speed.

We mentioned briefly in the conclusions to Chapter 5 the problems associated with image synthesis by the Maximum Entropy method and deriving spectral quantities from this restored map. Ideally, the solution to this problem would be to calculate exactly what the errors on the restored counts are, since they are certainly no longer Poisson. A more reliable estimate of these errors would give more reliable determinations of the spectral parameters and hence of the drift velocity. Alternative methods would be to apply the spectral fitting routine to the so called 'dirty map', as described in Chapter 5, since the inverse Fourier transform is linear and the errors on this map are Poisson. This in itself has problems though in that the spurious structure that will inevitably be generated by this method will make the estimation of the area of the hard X-ray emission even more subjective than it is now.

Sakao (1994) describes a Gaussian fitting procedure which has a linear characteristic. Essentially this procedure works by approximating the hard X-ray source distribution by a number of two-dimensional Gaussian sources. Since this procedure is linear the results of spectral fitting can be properly evaluated using χ^2 statistics and it also has the virtue of providing satisfactory results for time integrated count rates around 30-50 cts/SC, as opposed to the 100 cts/SC that are required to produce statistically significant images with MEM. It does have a drawback from the point of view that it is not suitable for obtaining the shape of the hard X-ray source, which could hamper area estimation, but for nearly circular sources this is not a problem.

From Sakao (1994), the ith Gaussian source B_i can be expressed as:

$$B_i(x, y; S_i, w_i, X_i, Y_i) = \frac{S_i}{2\pi w_i^2} exp\left\{-\frac{(x - X_i)^2 + (y - Y_i)^2}{2w_i^2}\right\} \tag{6.8}$$

where (X_i, Y_i) is the centre position and w_i is the size of the source. Then the hard X-ray brightness distribution, B_{HXR} is assumed to be a collection of N circular Gaussian sources,

$$B_{HXR}(x,y) = \sum_{i=1}^{N} B_i(x,y;S_i,w_i,X_i,Y_i) \tag{6.9}$$

The hard X-ray counts from each of the 64 subcollimators are then compared with the background subtracted observed counts and best fit parameters for each of the Gaussian sources (such as the location (X_i, Y_i) and the hard X-ray flux, S_i) are obtained using a linear least squares method. Applying this Gaussian fitting in two adjacent channels of HXT for the same data set allows the spectral hardness of the source to be derived (Sakao, 1994), viz.,

$$H_i^{m/n} = \frac{S_i^m}{S_i^n} \tag{6.10}$$

where S_i^m and S_i^n are the hard X-ray fluxes from the ith Gaussian component in energy bands m and n, respectively.

The application of this image restoration procedure may also provide more reliable spectral parameters, and thus more reliable estimates of the drift speed. However, the fact still remains that the energy resolution available with HXT is rather crude, with only four energy bands. Ideally, a much higher energy resolution instrument, also with imaging capabilities, would provide the best data for this particular analysis. Unfortunately, this will probably not be available until the launch of HESSI.

Finally, there are about a dozen other white-light flares which have been observed by *Yohkoh* (van Driel-Gesztelyi et al., 1994) and are suitable for the kind of analysis which was carried out in Chapter 5. Also, of interest would be to obtain ground-based spectral data for these white-light flares which would also us to identify the level in the atmosphere that the emission originated from, and should also allow comparison of the total power radiated in the white-light flare with that deposited by anomalous Joule heating.

Bibliography

Abourdarham J. and Hénoux J.C.: 1986, Astron. Astrophys., *156*, 73.

Achterberg A.:1981, Astron. Astrophys., *97*, 259.

Acton L.W., Culhane J.L., Gabriel A.H., Bentley R.D., Bowles J.A., Firth J.G., Finch M.L., Gilbreth C.W. et al.: 1980, Solar Phys., *65*, 53.

Acton L.W.:1968, ApJ, *152*, 305.

Acton L.W., Tsuneta S., Ogawara Y., Bentley R.D., Bruner M., Canfield R., Culhane J.L., Doschek G. et al.:1992, Science, *258*, 618.

Akioka M., Acton L.W. and Hudson H.S.:1994, X-Ray Solar Physics from Yohkoh, eds. Y. Uchida et al., 241.

Alexander D. and MacKinnon A.L.: 1993, Solar Phys., *144*, 155.

Alexander, D., Dunphy P.P. and MacKinnon A.L.: 1994, Solar Phys., *151*, 157.

Alexander D. et al.:1994, Proc. of the Third SOHO Workshop-Solar Dynamic Phenomena and Solar Wind Consequences, ESA SP-373, 187.

Alexander D. and Matthews S.A.:1994, Solar Phys., *154*, 157.

Alfvén H.:1939, The Physical Review, *55*, No.5, 425.

Anders E. and Grevesse N.: 1989, Geochim. Cosmochim. Acta, *53*, 197.

Antonuuci E., Gabriel A.H., Acton L.W., Leibacher J.W., Culhane J.L., Rapley C.G., Doyle J.G., Macahdo M.E. and Orwig L.E.:1982, Solar Phys., *78*, 107.

Antonucci E.: 1984, Mem. S. A. It., *55*, 699.

Antonucci E., Rosner R. and Tsinganos K.:1986, ApJ., *301*, 975.

Antonucci E.: 1989, Solar Phys., *121*, 31.

Antonucci E., Malvezzi M., Ciminiera L., Angrilli F., Bruner M., Perona G., Dodero M., Evans B. et al.:1992, Electromechanical coupling of the solar atmosphere: Proceedings of the OSL Workshop, 126.

Axford W.I., Leer E. and Skadron G.:1978, 15th International Cosmic Ray Conference, Volume 11, 132.

Bai T. and Ramaty R.:1979, ApJ, *227*, 1072.

Bai T. and Dennis B.R.:1985, ApJ, *292*, 699.

Barbosa, D.D.: 1979, ApJ., *233*, 383.

Basri G.S, Linsky J.L, Bartoe J.-D., Brueckner G.E. and Van Hoosier M.E.:1979, ApJ, *230*, 924.

Batchelor D.A., Crannell C.J., Wiehl H.J. and Magun A.:1985, ApJ, *295*, 258.

Benka S. and Holman G.D.:1992, ApJ, *391*, 854.

Bennett W.H.:1934, Physical Review, *45*, 890.

Bentley R.D., Doschek G.A., Simnett G.M., Rilee M.L., Mariska J.T.,Culhane J.L., Kosugi T. and Watanabe T.:1994, ApJ., *421*, L55.

Benz A.O.:1986, Solar Phys., *104*, 99.

Benz A.O.:1993, Plasma Astrophysics, Kluwer.

Bogdan, T.J., Lee, M.A. and Schneider, P.: 1991, J. Geophys. Res., *96*, 161.

Boischot A. and Denisse J.F.:1957, C.R. Acad. Sci., *245*, 2194.

Bornmann P.:1987, ApJ., *313*, 449.

Bradt H., Gamire G., Oda M., Spada G., Sreekantan B.V., Gorenstein P. and Grusky H.:1968, Space Sci. Rev., *8*, 471.

Brown J.C.:1971, Solar Phys., *18*, 489.

Brown J.C.: 1972, Solar Phys., *26*, 441.

Brown J.C.: 1973 Solar Phys., *31*, 143.

Brown J.C. and Hayward J: 1982, Solar Phys., *80*, 129.

Brown J.C. and Hayward:1980, Solar Phys., *73*, 121.

Brown J.C. and Melrose D.B.: 1977, Solar Phys., *52*, 117.

Brown J.C., Melrose D.B. and Spicer D.S.:1979, ApJ, *228*, 592.

Brown J.C.:1976, Phil. Trans. Roy. Soc. Lond. A., *281*, 473.

Brown J.C., Smith D.F. and Spicer D.S.:1981, The Sun as a Star, NASA, 181.

Brown J.C.:1974, Coronal Disturbances, ed. G. Newkirk, IAU Symp. No. 57.

Brown J.C., Spicer D.S. and Melrose D.B.:1979, ApJ, *228*, 592.

Brown J.C.:1991, Phil. Trans. Roy. Soc. Lond. A., *336*, 413.

Brown J.C. and Bingham R.:1984, Astron. Astrophys., *131*, L11.

Brown J.C. and Craig I.J.:1983, Astron. Astrophys.

Brown J.M., Zink L.R., Jennings D.A., Evenson K.M. and Hinz A.:1986, ApJ., *307*, 410.

Brueckner G.E. and Bartoe J.-D.F.:1983, ApJ, *272*, 329.

Canfield R.C., Pasachoff J.M., Stencel R.E. and Beckers J.M.:1978, Solar Phys., *58*, 263.

Canfield R.C., Bely-Dubau F., Brown J.C., Dulk G.A., Emslie A.G., Enome S., Gabriel A.H., Kundu M. et al.:1986, Energetic Phenomena on the Sun, edS. M. Kundu and B. Woodgate, NASA CP 2439, Chap. 3.

Canfield R.C., Brown J.C., Craig I.J.D., Brueckner G.E., Cook J.W., Doschek G.A., Emslie A.G., Machado M.E., Hénoux J.-C. and Lites B.W.:1980, Solar Flares: A Monograph from Skylab

Solar Workshop II, 231.

Carmichael H.:1964, AAS-NASA Symposium on the Physics of Solar Flares, ed. W.N. Hess, NASA SP-50, 451.

Chen F.F.:1974, Introduction to Plasma Physics, Plenum Press.

Cheng C.-C., Pallavicini R., Acton L.W. and Tandberg-Hanssen E.:1985, ApJ., *298*, 887.

Cheng C.-C. and Widing K.G.:1975, ApJ, *201*, 735.

Cheng C.-C., Doschek G.A. and Karpen J.T.:1984, ApJ., *286*, 787.

Cheng C.-C., Rilee M. and Uchida Y.:1994, Proc. Kofu Symposium, NRO Report No. 360, eds. S.Enome and T. Hiryama, 213.

Chubb T.A., Kreplin R.W. and Friedman H.:1966, J. Geophys. Res., *71*, 3611.

Chupp, E.L.: 1990, ApJ. Suppl., *73*, 213.

Chupp E.L., Forrest D.J., Ryan J.M., Heslin J., Reppin C., Pinkau K., Kanbach G., Reiger E. and Share G.H.:1982, ApJ Letts., *263*, L95.

Chupp E.L., Forrest D.J., Higbie P.R., Suri A.N., Tsai C. and Dunphy P.P.:1973, Nature, *241*, 333.

Chupp E.L., Forrest D.J. and Suri A.N.:1975, Solar Gamma, X- and EUV Radiation, ed. S.R. Kane, IAU Symp. No. 68, 341.

Chupp E.L.:1984, Ann. Rev. Astron. Astrophys., *22*, 359.

Cliver E.W., Dennis B.R., Kiplinger A.L., Kane S.R., Neidig D.F., Sheeley N.R. JR. and Koomen M.J.:1986, Ap.J., *305*, 920.

Craig I.J.D. and Brown J.C.:1976, Astron. Astrophys., *49*, 239.

Crannell C.J., Joyce G., Ramaty R. and Werntz C.:1976, ApJ., *210*, 582.

Crannell C.J., Frost K.J., Saba J.L., Maetzler C. and Ohki K.:1978, ApJ, *223*, 620.

Culhane, J.L., Hiei E., Doschek G.A., Cruise A.M., Ogawara Y., Uchida Y., Bentley R.D., Brown C.M. et al.: 1991, Solar Phys.,*136*, 89.

Culhane J.L., Phillips A.T., Pike C.D., Fludra A., Bentley R.D., Bromage B.J., Doschek G.A., Hiei E. et al.:1993, Adv. Space Res., *13*, 303.

Davis L.:1956, Phys. Rev., *101*, 351.

De Jager C.:1985, Solar Phys., *98*, 267.

Dennis B.R.:1982, OSO-8 Internal Technical Memorandum, NASA.

Dennis B.R. et al.:1986, MAX '91, An Advanced Payload for the Exploration of High Energy Processes on the Active Sun, Report of MAX '91 Science Study Committee, NASA.

Dennis B.R. and Schwartz R.A.:1989, Solar Phys., *121*, 75.

Dennis B.R.:1985, Solar Phys., *100*, 465.

Dennis B.R., Holman G.D., Hudson H.S., Kosugi T., Strong K.T. and Zarro D.M.:1994, Proc. Kofu Symposium, NRO Report No. 360, eds. S. Enome and T. Hiryama, 217.

Dermer C.D. and Ramaty R.:1986, ApJ., *301*, 962.

Ding M.D., Fang C., Gan W.Q. and Okamoto T.:1994, ApJ., *429*, 890.

Donati-Falchi A., Falciani R. and Smaldone L.A.:1986, The Lower Atmosphere of Solar Flares, ed. D.F. Neidig.

Donnelly R.F.:1976, J. Geophys. Res., *81*, 4745.

Donnelly R.F. and Kane S.R.:1978, ApJ, *222*, 1043.

Doschek G.A., Kreplin R.W. and Feldman U.:1979, ApJ. Lett., *233*, L157.

Doschek G.A. et al.: 1986, NASA Conference Publ. 2439, 4-1/4-42.

Doschek G.A., Kreplin, R.W. and Feldman, U.: 1979, ApJ., *233*, L157.

Doschek G.A., Mariska J.T., Watanabe T., Hiei E., Lang J.R., Culhane J.L., Bentley R.D., Brown C.M., Feldman U. and Phillips A.T.: 1992, Publ. Astron. Soc. Japan, *44*, L95.

Doschek G.A., Feldman U., Landecker P.B. and McKenzie D.L.:1981, ApJ., *249*, 372.

Doschek G.A., Feldman U., Kreplin R.W. and Cohen L.:1980, ApJ, *239*, 725

van Driel-Gesztelyi L., Hudson H.S., Anwar B. and Hiei E.:1994, Solar Phys., *152*, 145.

Dröge F.:1977, Astron. Astrophys., *57*, 285.

Duijveman A., Hoyng P. and Machado M.E.:1982, Solar Phys., *81*, 137.

Dulk G.A., Bastian T.S. and Kane S.R.:1986, ApJ, *300*, 438.

Dulk G.A. and McLean D.J.:1978, Solar Phys., *57*, 279.

Dunphy P.P. and Chupp E.L.:1992, Particle Accleration in Cosmic Plasmas, eds. G.P. Zank and T.K. Gaisser, AIP, 253.

Efimov Y.E. and Kocharov G.E.:1985, Proc. of 19th ICRC, *4*,154.

Ellis G.R.A.:1969, Aust. J. Phys., *22*, 177.

Emslie A.G.: 1978, ApJ, *224*, 241.

Emslie A.G.: 1980, ApJ, *235*, 1055.

Emslie A.G.: 1981, ApJ, *249*, 817.

Emslie A.G. and Brown J.C.:1985, ApJ, *295*, 648.

Emslie A.G., Brown J.C and Donnelly R.F.:1978, Solar Phys., *57*, 175.

Emslie A.G. and Nagai F.:1985, ApJ., *288*, 779.

Emslie A.G. and Smith D.F.:1984, ApJ., *279*, 882.

Emslie A.G. and Alexander D.:1987, Solar Phys., *110*, 295.

Emslie A.G. and Sturrock P.A.:1982, Solar Phys., *80*, 113.

Feldman U., Hiei E., Phillips K.J.H., Brown C.M. and Lang J.:1994, ApJ, *421*, 843.

Fang C. and Ding M.D.:1995, Astron. Astrophys. Supp., *110*, 99.

Fermi E.:1949, Phys. Rev., *75*, 1169.

Fletcher L. and Brown J.C.:199 , Astron. Astrophys., *259*, L43.

Forman M.A., Ramaty R. and Zweibel E.G.:1986, Physics of the Sun, Volume II: The Solar Atmosphere, eds. P.A. Sturrock et al.

Forrest D.J.:1983, Positron-electron Pairs in Astrophysics, Vol. II, eds. M.L. Burns et al. AIP

Forrest D.J., Vestrand W.T., Chupp E.L., Rieger E. and Cooper J.:1986, Adv. Space Res., *6*, 115.

Frieden B.R.:1972, J. Opt. Soc. Am., *62*, 511.

Frost K.J.:1969, ApJ Letts, *158*, L159.

Frost K.J. and Dennis B.R.:1971, ApJ, *165*, 655.

Fürth H.P., Killeen J. and Rosenbluth M.N.:1963, Phys. Fluids, *6*, 459.

Gabriel A.H., Phillips K.J.H., Acton L.W., Wolfson C.J., Culhane J.L., Rapley C.G., Bentley R.D., Kayat M.A., Jordan C. and Antonucci E.:1981, ApJ. Lett., *244*, L147.

Gary D.E.:1985, ApJ., *297*, 799.

Gold T. and Hoyle F.:1960, Mon. Not, R.A.S., *120*, 89.

Grineva Y.I., Karev V.I., Korneev V.V., Krutov V.V., Mandlestam S.L., Vainstein L.A., Vasilyev B.N. and Zhitnik I.A.:1973, Solar Phys., *29*, 441.

Gull S.F. and Daniell G.J.:1978, Nature, *272*, 686.

Gurman J.:1987, NASA's Solar Maximum Mission: A Look at a New Sun, NASA.

Gurman J.:1992, The Sun: A Laboratory for Astrophysics, NATO ASI, *373*, 221.

Hanaoka Y.:1994, ApJ., *420*, L37.

Harrison R.A.:1986, Astron. Astrophys., *162*, 283.

Hénoux J.C., Chambe G, Smith D., Tamres D., Feautrier N, Rovira M. and Sahal-Brechot S.:1990, ApJ. Supp., *73*, 303.

Hénoux J.-C. and Chambe G.:1990, Journal of Quantitative Spectroscopy and Radiative Transfer, *44*, 193.

Heristchi D.:1986, ApJ, *311*, 474.

Heyvaerts J.H., Priest E. and Rust D.M.:1977, ApJ, *216*, 123.

Hiei E., Hundhausen A.J. and Sime D.G.:1993, Geophys. Res. Letters, *20*, 2785.

Högbohm J.A.:1974, Astron. Astrophys. Supp., *15*, 417.

Holman G.D.:1985, ApJ, *293*, 584.

Holman G.D., Eichler D. and Kundu M.R.:1980, Radio Physics of the Sun, eds. M. Kundu and T. Gergely, IAU Symp. No. 86, 457.

Hoyng P.: 1975 Ph.D. Thesis University of Utrecht.

Hoyng P., Brown J.C. and van Beek H.F.:1976, Solar Phys., *48*, 197.

Hua X.M. and Lingenfelter R.E.:1987b, ApJ, *319*, 555.

Hua X.M. and Lingenfelter R.E.:1987a, Solar Phys., *107*, 351.

Hudson H.S.:1991, Bull. Am. Astron. Soc., 23, 1064.

Hudson H.S.:1994, Proc. of Kofu Symposium, NRO Report No. 360, 1.

Hudson H.S., Strong K.T., Dennis B.R., Zarro D.M., Inda M., Kosugi T. and Sakao T.:1994, ApJ., *422*, L25.

Hudson H.S., Acton L.W., Hirayama T. and Uchida Y.:1992, Publ. Astron. Soc. Japan, *44*, L77.

Hudson H.S.:1994a, X-ray Solar Physics from Yohkoh, eds. Y. Uchida et al., 143.

Hurley K., Sommer M., Atteia J.-L., Boer M., Cline T., Cotin F., Hénoux J.-C., Kane S.R., Lowes P. and Niel M.:1992, Astron. Astrophys. Supp., *92*, 401.

Hynecek J.:1979, IEEE IEDM Tech. Dig., *611*.

Ibragimov I.A. and Kocharov G.E.:1977, Sov. Astron. Lett., *3*(5), 221.

Janesick J., Hynecek J. and Blouke M.:1981, Proc. SPIE, Solid State Imagery for Astronomy, *290*, 165.

Johns C.M. and Lin R.P.:1992, Solar Phys., *137*, 121.

Kahler S.W.:1992, Ann. Rev. Astron. Astrophys., *30*, 113.

Kai K., Kosugi T. and Nitta N.:1985, Publ. Astron. Soc. Japan, *37*, 155.

Kane S.R.:1969, ApJ Letts., *157*, L139.

Kane S.R.:1974, 'Coronal Disturbances', (ed. G. Newkirk), IAU Symp. No.57.

Kane S.R. and Donnelly R.F.:1971, ApJ, *164*, 151.

Kane S.R. and Anderson K.A.:1970, ApJ, *162*, 1003.

Kane S.R., Chupp E.L., Forrest D.J., Share G.H. and Rieger E. :1986, ApJ., *300*, L95.

Kane S.R., Kai K., Kosugi T., Enome S., Landecker P.B. and Mc Kenzie D.L.:1983, ApJ., *271*, 376.

Kaufmann P., Correia E., Costa J.E.R., Dennis B.R., Hurford G.J. and Brown J.C.:1984, Solar Phys., *91*, 359.

Kawabata K., Yoshimori M., Suga K., Morimoto K., Hiraoka T., Sato J., Ohki K.:1994, ApJ Suppl., *90*, 701.

Khan J.I., Uchida Y., Mc Allister A.H. and Watanabe Ta..:1994, X-ray Solar Physics From Yohkoh, eds. Y. uchida, K. Shibata, T. Watanabe, H.S. Hudson, 201.

Khan J.I., Harra-Murnion L.K., Hudson H.S., Lemen J.R. and Sterling A.C.:1995: ApJ., *425*, L153.

Klimchuk J., Acton L.W., Harvey K.L., Hudson H.S., Kluge K.L., Sime D.G., Strong K.T. and Watanabe Ta.:1994, X-ray Solar Physics From Yohkoh, eds. Y. uchida, K. Shibata, T. Watanabe, H.S. Hudson, 181.

Knight J.W. and Sturrock P.A.:1977, ApJ, *230*, 924.

Knight J.W. and Sturrock P.A.:1977, ApJ., *218*, 306.

Korchak A.A.:1967, Astron. Zh., *44*, 328.

Korchak A.A.:1971, Solar Phys., *18*, 284.

Kocharov G.E.:1983, Proc. of 18th ICRC, *12*, 235.

Kosugi T., Dennis B.R. and Kai K.:1988, ApJ, *324*, 1118.

Kosugi T., Makishima K., Murakami T., Sakao T., Dotani T., Inda M., kai K., Masuda S. et al.:1991, Solar Phys., *136*, 17.

Kosugi T.:1994, Proceedings of the Kofu Symposium, NRO Report No. 360, eds. S. Enome and T. Hirayama, 11.

Kosugi T., Sakao T., Masuda S., Hara H., Shimizu T. and Hudson H.S.:1994, Proceedings of the Kofu Symposium, NRO Report No. 360, eds. S. Enome and T. Hirayama, 127.

Krüger A.:1979, Introduction to Solar Radio Astronomy and Radio Physics, 330.

Kulsrud R.M. and Ferrari A.:1971, Ap. Space Sci., *12*, 302.

Kundu M.R.:1983b, Solar Phys., *83*, 385.

Kundu M.R. and Woodgate B.:1986, (eds.) Energetic Phenomena on the Sun, The Solar Maximum Mission Flare Workshop Proceedings, NASA, Conf. Publ. 2439.

Kundu M.R.:1985, Solar Phys. *100*, 491.

Lang J., Bentley R.D., Brown C.M., Culhane J.L., Doschek G.A., Watanabe Te., Hiei E., Deslattes R. et al.:1992, Publ. Astron. Soc. Japan, *44*, L55.

Lang J. et al.:1993, RAL Publication RAL-93-035.

Lawson J.D.:1957, J. Electr. Contr., *3*, 587.

Leighton R.B.:1960, 4th Symposium on Cosmical Gas Dynamics.

Lifshitz M.A. and Tomozov V.N.:1974, Soviet Astron. AJ, *18*, 331.

Lin R.P.:1974, Space Sci. Rev., *16*, 189.

Lin R.P., Schwartz R.A., Pelling R.M. and Hurley K.C.:1981, ApJ Letts., *251*, L109.

Lin R.P. and Schwartz R.A.:1987, ApJ, *312*, 462.

Lin R.P.:1985, Solar Phys., *100*, 537.

Linford G.A. and Wolfson C.J.:1989, ApJ., *331*, 1036.

Lingenfelter R.E. et al.:1965, J. Geophys. Res., *70*, 4077 and 4087.

Lingenfelter R.E. and Ramaty R.:1967, High Energy Nuclear Reactions in Astrophysics, ed. B.S.P. Shen, 99.

Livshits M.A. and Tsytovich V.N.:1970, Nuclear Fusion, *10*, 241.

Lu E. and Hamilton R.J.:1991, ApJ., *380*, L89.

McAllister A.:1992, Publ. Astron Soc. Japan, *44*, L205.

McClements K.G.:1987b, Solar Phys., *109*, 355.

McClements K.G., Harrison R.A. and Alexander D.:1991, Solar Phys., *131*, 41.

McDonald F.B. and van Hollebecke M.A.I.:1985, ApJ., *290*, L67.

McGuire R.E., von Roesenvinge T.T. and McDonald F.B.:1986, ApJ., *301*, 938.

McKenzie D.L., Broussard R.M.. Landecker P.B., Rugge H.R., Young R.M., Doschek G.A. and Feldman U.:1980, ApJ., *238*, L43.

MacKinnon A.L., Brown J.C. and Hayward J.:1985, Solar Phys., *99*, 231.

MacKinnon A.L.:1991, Vistas in Astronomy, *34*, 331.

McTiernan J.M., Kane S.R., Loran J.M., Lemen J.R., Acton L.W., Hara H., Tsuneta S. and Kosugi T.:1993, ApJ Letts., *416*, L91.

McTiernan J.M., Kane S.R., Loran J.M., Lemen J.R., Acton L.W., Hara H., Tsuneta S. and Kosugi T.:1994, X-Ray Solar Physics from Yohkoh, eds. Y. Uchida et al., 255.

McTiernan J.M.:1994, Yohkoh Analysis Guide, Lockheed Palo Alto Research Laboratory, M. Morrison.

Machado M.E. and Linsky J.L.:1975, Solar Phys., *42*, 395.

Machado M.E., Emslie A.G. and Brown J.C.:1978, Solar Phys., *58*, 363.

Machado M.E., Emslie A.G. and Mauas P.J.:1986, Astron. Astrophys., *159*, 33.

Machado M.E., Moore R.L., Hernandez Ana M., Rovira M.G., Hagyard M.J. and Smith J.B. JR.:1988a, ApJ, *326*, 451.

Makishima K., Miyamoto S., Murakami T., Nishimura J., Oda M., Ogawara Y. and Tawara Y.:1978, New instrumentation for Space Astronomy, eds. K. Van Hucht and G.S. Vaiana., 277.

Mandzhavidze N. and Ramaty R.:1993, ApJ., *289*, 739.

Mariska J.T. and Poland A.I.:1985, Solar Phys., *96*, 317.

Mariska J.T., Doschek G.A. and Bentley R.D.:1993, ApJ, *419*, 418.

Mariska J.T.:1992, The Solar Transition Region, CUP.

Marsh K.A. and Hurford G.J.:1980, ApJ Letts., *240*, L111.

Marsh K.A., Hurford G.J., Zirin H., Dulk G.A., Dennis B.R., Frost K.J. and Orwig L.E.:1981, ApJ., *251*, 797.

Martens P.C.H., van den Oord G.H.J. and Hoyng P.:1985, Solar Phys., *96*, 253.

Martens P.C.H.:1988, ApJ., *330*, L131.

Masuda S.:1994, PhD. Thesis, Univeraity of Tokyo.

Masuda S.:1994a, X-Ray Solar Physics from Yohkoh, eds. Y. Uchida et al., p.99.

Masuda S.:1994b, Proceedings of the Kofu Symposium, NRO Report No.360, eds. S. Enome and T. Hirayama, p.209.

Matsushita K., Masuda S., Kosugi T., Inda M. and Yaji K.:1992, Publ. Astron. Soc. Japan, *44*, L89.

Mauas P.J.D., Machado M.E. and Avrett E.H.:1990, ApJ., *360*, 715.

Melozzi M., Kundu M. and Shevgaonkar R.K.:1985, Solar Phys., *97*, 345.

Melrose D.B.:1970, Aust. J. Phys., *23*, 871.

Melrose D.B.:1974, Solar Phys., *37*, 353.

Melrose D.B. and Brown J.C.:1976, Mon. Not. R.A.S., *176*,15.

Melrose D.B. and Dulk G.A.:1982b, ApJ, *259*, L41.

Melrose D.B. and Dulk G.A.:1982, ApJ., *259*, 844.

Melrose D.B.:1980, Plasma Astrophysics, Gordon and Breach.

Metcalf T.R., Hudson H.S., Kosugi T., Puetter R.C. and Piña R.K.:1995, preprint.

Meyer J.P.:1985, ApJ. Supp., *57*,173.

Mikhailovskii A.B.: 1973, Theory of Plasma Instabilities.

Miller J.A., Guessoum N. and Ramaty R.:1990, ApJ., *361*, 701.

Miller J.A. and Ramaty R.:1989b, ApJ., *344*, 97.

Miller J.A. and Ramaty R.:1987 Solar Phys., *113*, 195.

Murphy R.J. and Ramaty R.:1984, Adv. Space Res., *4*, 127.

Murphy R.J., Ramaty R., Forrest D.J. and Kozlovsky B.:1985, Proc. 19th ICRC, *4*, 249.

Murphy R.J., Dermer C.D. and Ramaty R.:1987, ApJ. Supp., *63*, 721.

Murphy R.J., Kozlovsky B. and Ramaty R.:1988, ApJ., *331*, 1029.

Murphy R.J., Share G.H., Letaw J.R. and Forrest D.J.:1990, ApJ., *358*, 298.

Neidig D.F. and Cliver E.W.:1983a, Air Force Geophysics Lab. Technical Report AFGL-TR-83-0257.

Neidig D.F.:1989, Solar Phys., *121*, 361.

Neidig D.F. and Wiborg D.H.:1984, Solar Phys., *94*, 217.

Neidig D.F.:1986, The Lower Atmosphere of Solar Flares, ed. D.F. Neidig.

Ogawara Y., Takano T., Kato T., Kosugi T., Tsuneta S., Watanabe T., Kondo I. and Uchida Y.:1991, Solar Phys., *136*, 1.

van den Oord G.H.J.: 1990, Astron. Astrophys., *234*, 496.

van den Oord G.H.J.:1994, Fragmented Energy Release in Sun and Stars: the interface between MHD and Plasma Physics, Kluwer.

Orrall F.Q. and Zirker J.B.:1976, ApJ., *208*, 616.

Orwig L.E. and Woodgate B.E.:1986, The Lower Atmosphere of Solar Flares, ed. D. Neidig, NSO, p.306.

Pallavicini R., Serio S. and Vaiana G.S.XS:1977, ApJ, *216*, 108.

Papadopoulos K.:1977, Rev. Geophys. Sp. Sci., *15*, 113.

Parker E.N.:1975, Cosmical Magnetic Fields.

Parker E.N.:1988, ApJ, *330*, 474.

Parker E.N. and Tidman D.A.:1958, Phys. Rev., *111*, 1206.

Petschek H.E.:1964, 'AAS-NASA Symp. Phys. Solar Flares', ed. W.N. Hess.

Piana M.:1994, Astron. Astrophys., *288*, 949.

Piana M., Brown J.C. and Thompson A.M.:1995, Solar Phys., *156*, 315.

Pike C.D., Phillips K.J.H., Lang J., Sterling A.C., Watanabe T., Hiei E. and Culhane J.L.:1996,

Adv. Sp. Res., *17*, 51.

Piña R.K. and Puetter R.C.:1993, Publ. Astron. Soc. Pacific, *105*, 630.

Poland A.I., Orwig L.E., Mariska J.T., Auer L.H. and Nakatsuka R.:1984, ApJ, *280*, 457.

Priest E.R., Hood A.W. and Anzer U.:1991, Solar Phys., *132*, 199.

Prince T.A., Forrest D.J., Chupp E.L., Kanbach G. and Share G.H.:1983, Proc. of the 18th Internaional Cosmic Ray Conference, *4*, 79.

Prince T.A., Hurford G.J., Hudson H.S. and Crannell C.J.:1988, Solar Phys., *118*, 269.

Puetter R.C.:1995, International Journal of Image Systems and Technology.

Ramaty R., Kozlovsky B. and Suri A.N.:1977, ApJ., *214*, 617.

Ramaty R. and Murphy R.J.:1987, Space Science Rev., *45*, 213.

Ramaty R., Kozlovsky B. and Lingenfelter R.E.:1979, ApJ. Supp., *40*, 487.

Ramaty R., Murphy R.J., Kozlovsky B. and Lingenfelter R.E.:1983a, Solar Phys., *86*, 395.

Ramaty R.:1986, Physics of the Sun, Vol. II: The Solar Atmosphere, eds. P.A. Sturrock et al., 291.

Ramaty R. and Murphy R.J.:1984, High Energy Transients in Astrophysics, ed. S. Woosley, AIP

Ramaty R., Murphy R.J., Kozlovsky B. and Lingenfelter R.E.:1983b, ApJ., *273*, L41.

Ramaty R., Murphy R.J. and Dermer C.D.:1987, ApJ., *316*, L41.

Ramaty R. and Mandzhavidze N.:1994, High Energy Solar Phenomena- A New Era of Spacecraft Measurements, AIP Conf. Proc. *294*, 26.

Rieger and Marschhäuser:1990, Proc. of the 3rd MAX '91/SMM Workshop on Solar Flares: Observations and Theory, eds. R.M. Winglee and A.L. Kiplinger, 68.

Rieger E., Reppin C., Kanbach G., Forrest D.J., Chupp E.L. and Share G.H.,:1983, Proc. 18th ICRC, *10*, 338.

Rieger E.:1989, Solar Phys., *121*, 323.

Roberts J.A.:1958, Australian J. Phys., *12*, 327.

Rosner R., Tucker W.H. and Vaiana G.S.:1978, ApJ, *220*, 643.

Ryan J.M., Chupp E.L., Forrest D.J., Matz S., Rieger E., Reppin C., Kanbach G. and Share G.H.:1983, ApJ., *227*, L61.

Saba J.L.R. and Strong K.T.:1991, Adv. Space Res., *11*, 117.

Sakao T., Kosugi T., Masuda S., Inda M., Makishima K., Canfield R.C., Hudson H.S., Metcalf T.R., Wuelser J.-P. and Acton L.W.:1992, Publ. Astron. Soc. Japan, *44*, L83.

Sakao T.:1994, PhD. Thesis, University of Tokyo.

Sakurai T.:1983, Solar Phys., *86*, 339.

Sakurai T.:1985, Solar Phys., *95*, 311.

Schmeleva O.P. and Syrovatskii S.I.:1973, Solar Phys., *33*, 341.

Shevgaonkar R.K. and Kundu M.R.:1985, ApJ., *292*, 733.

Shibata K., Ishido Y., Acton L.W., Strong K.T., Hirayama T., Uchida Y., McAllister A.H., Matsumoto R. et al.:1992, Publ. Astron. Soc. Japan, *44*, L173.

Shibata K. et al.: 1994, The Sun as a Variable Star: Solar and Stellar Irradiance Variations, eds. J.M. Pap, C. Fröhlich, H.S. Hudson and S. Solanki, CUP.

Shimizu T., Tsuneta S., Acton L.W., Lemen J.R., Ogawara Y. and Uchida Y.:1994, ApJ., *422*, 906.

Simnett G.M.:1986, Solar Phys., *106*, 165.

Simnett G.M. and Haines M.G.:1991, Solar Phys., *130*, 253.

Simnett G.M.:1991, Phil. Trans. Roy. Soc. Lond. A., *336*, 439.

Slottje C.:1978, Nature, *275*, 520.

Smith D.F. and Lilliequist C.G.:1979, ApJ, *232*, 582.

Smith D.F. and Brecht S.H.:1989, ApJ., *334*, 1004.

Smith D.F.:1990, Basic Plasma Processes on the Sun, IAU Symp.,*142*, eds. E.R. Priest and V. Krishan, 375.

Somov B.V.:1981, Solar Max. Year, Vol. 1, 155, U.S.S.R. Academy of Sciences.

Sonnerup B.V.O.:1970, J. Plasma Phys., *4*, 161.

Sonnerup B.V.O.:1973, High Energy Phenomena on the Sun, eds. R. Ramaty and R.G. Stone, NASA SP-342, 357.

Spicer D.S.:1976, NRL Report 8036.

Spicer D.S.:1977, Solar Phys., *53*, 305.

Spicer D.S.:1981, Solar Phys., *70*, 115.

Spicer D.S. and Sudan R.N.:1984, ApJ., *280*, 448.

Spicer D.S. and Brown J.C.:1980, Solar Phys., *67*, 385.

Spitzer L.:1962, 'Physics of Fully Ionized Gases', Interscience.

Strong K.T., Harvey K.L., Hirayama T., Nitta N., Shimizu T. and Tsuneta S.:1992, Publ. Astron. Soc. Japan, *44*, L161.

Sturrock P.A.:1968, 'Structure and Development of Solar Active Regions', ed. K.O. Kiepenheuer, IAU Symp. No. 35.

Sturrock P.A.:1980, Solar Flares - A Monograph from Skylab Solar Workshop II, ed. P.A. Sturrock.

Sturrock P.A., Kaufman P., Moore R.L. and Smith D.F.:1984, Solar Phys., *94*, 341.

Sturrock P.A.:1974, IAU Symp. *57*, 437.

Suri A.N., Chupp E.L., Forrest D.J. and Reppin C.:1975, Solar Phys., *43*, 415.

Svéstka Z.:1986, The Lower Atmosphere of Solar Flares: Proceedings of the Solar Maximum Symposium, p.332.

Sweet P.A.:1958, 'Electromagnetic Phenomena in Cosmical Physics', ed. B. Lehnert, IAU Symp. No. 6.

Sweet P.A.:1969, Ann. Rev. Astr. Ap., *7*, 149.

Syrovatskii S.I.:1966, Soviet Astron., *10*, 270.

Syrovatskii S.I.:1969, Solar Flares and Space Research, eds. C. de Jager and Z. Švestka, 346.

Takakura T. and Kai K.:1966, Publ. Astr. Soc. Japan, *18*, 57.

Takakura T.:1969, Solar Phys., *6*, 122.

Takakura T. et al.:1982, Proc. Hinotori Symp. on Solar Flares, Tokyo.

Tanaka K.:1983, Activity in Red-Dwarf Stars, eds. P.B. Byrne and M. Rodonō, IAU Coll. *71*, 307.

Tanaka K.:1987, Publ. Astron. Soc. Japan, *39*, 1.

Tanaka K. et al.:1982, Proceedings of Hinotori Symposium on Solar Flares, 43.

Tandberg-Hanssen E. and Emslie A.G.:1988, Physics of Solar Flares

Tang F.:1985, Solar Phys., *102*, 131.

Thompson A.M., Brown J.C., Craig I.J.D. and Fulber C.:1992, Astron. Astrophys., *265*, 278.

Trow M.W., Bentley R.D. and Culhane J.L.:1989, SPIE 1159 EUV, X-ray and Gamma Ray Instruments for Astronomy and Atomic Physics, 252.

Trow M.W., Bento A.C. and Smith A.:1993, Nucl. Inst. and Meth. A., *348*, 232.

Trubnikov B.A.:1965, Particle Interactions in a Fully Ionized Plasma, Consultants Bureau, Vol I., New York.

Tsuneta S., Takakura T., Nitta N., Ohki K., Tanaka K., Makishima T., Oda M. and Ogawara Y.:1984a, ApJ, *280*, 887.

Tsuneta S., Takakura T., Nitta N., Ohki K., Tanaka K., Makishima T., Oda M. and Ogawara Y.:1984b, ApJ, *284*, 827.

Tsuneta S., Acton L.W., Bruner M., Lemen J.R., Brown W., Caravalho,R., Catura R., Freeland S. et al.:1991, Solar Phys., *136*, 37.

Tsuneta S., Takahashi T., Acton L.W., Bruner M.E., Harvey K.L. and Ogawara Y.:1992, Publ. Astron. Soc. Japan, *44*, L211.

Tsuneta S., Hara H., Shimizu T., Acton L.W., Strong K.T., Hudson H.S. and Ogawara Y.:1992a, Publ. Astron. Soc. Japan, *44*, L63.

Tsuneta S.:1985, ApJ., *290*, 353.

Tsytovich V.N.:1970, Nonlinear Effects in Plasma, Plenum.

Tsytovich V.N.:1972, An Introduction to the Theory of Plasma Turbulence, Pergamon.

Tverskoi B.A.:1967, Soviet Phys. JETP, *25*, 317.

Uchida and Hudson H.S.:1972, Solar Phys., *26*, 414.

Uchida Y., McAllister A.H., Strong K.T., Ogawara Y., Shimizu T., Matsumoto R. and Hudson H.S.:1992, Publ. Astron. Soc. Japan, *44*, L155.

Velusamy T. and Kundu M.R.:1982, ApJ, *258*, 388.

Vernazza J.E., Avrett E.H. and Loeser R.:1973, ApJ., *184*, 605.

Vestrand W.T., Forrest D.J., Chupp E.L., Rieger E. and Share G.H.:1987, ApJ, *322*, 1010.

Vlahos L. and Papadopoulos K.:1979, ApJ., *233*, 717.

Vlahos L. and Rowland H.K.:1984, Astron. Astrophys., *139*, 263.

Wang H.T. and Ramaty R.:1974, Solar phys., *36*, 129.

Watanabe Ta., Kozuka Y., Ohyama M., Kojima M., Yamaguchi K., Watari S., Tsuneta S., Joselyn J.A., Harvey K.L. and Acton L.W.:1992, Publ. Astron. Soc. Japan, *44*, L199.

Watanabe Te. et al.:1994, Proceedings of the Kofu Symposium, NRO Report No., 360.

Widing K.G. and Cheng C.-C.:1974, ApJ, *194*, L111.

Wild J.P.:1950, Aust. J. Sci. Res., Ser. A, *3*, 399.

Wild J.P. et al.:1963, Ann. Rev. Astron. Astrophys., *1*, 291.

Willingdale R.:1981, Mon. Not. R.A.S., *194*, 359.

Winglee R.M., Kiplinger A.L., Zarro, D.M., Dulk G.A. and Lemen J.R.:1992, ApJ, *375*, 366.

Winglee R.M., Dulk G.A. and Pritchett P.L.:1988a, ApJ., *327*, 968.

Winglee R.M., Dulk G.A. and Pritchett P.L.:1988b, ApJ., *329*, 440.

Wolfson C.J., Leibacher J.W., Doyle J.G. and Phillips K.J.H.:1983, ApJ., *269*, 319.

Wu S.T., Krall K.R., Hu Y.Q., Hagyard M.J. and Smith J.B. JR. :1984, Solar Phys., *90*, 117.

Yaji K., Kosugi T., Sakao T., Inda-Koide M. and Hanaoka Y.:1994, Proceedings of the Kofu Symposium, NRO Report No.360, eds. S. Enome and T. Hirayama, p.143.

Yoshimori M., Okudaira K., Hirasima Y., Igarashi T., Akasaka M., TaKai Y., Morimoto K., Watanabe T. et al.:1991, Solar Phys., *136*, 69.

Yoshimori M., Takai Y., Morimoto K., Suga K., Ohki K., Watanabe T., Yamagami T., Kondo I. and Nishimura J.:1992, Publ. Astron. Soc. Japan, *44*, L51.

Yoshimori M., Suga K., Morimoto K., Hiraoka T., Sato J., Kawabata K. and Ohki K.:1994, ApJ Supp., *90*, 639.

Zarro D.M., Canfield R.C., Strong K.T. and Metcalf T.R.:1988, ApJ., *324*, 582.

Zirin H.:1988, Astrophysics of the Sun, CUP.

Zwaan C.:1981, The Sun as a Star, ed. S. Jordan, , NASA SP-450, 163.